

UNIVERSITY OF STRATHCLYDE
DEPARTMENT OF PHYSICS

**Optimisation and measurement
of bremsstrahlung and
synchrotron radiation in
ultra-intense laser-solid
interactions**



by

Alana G. Horne

in partial fulfilment of the requirements for the degree of Doctor of
Philosophy in Physics

2024

Copyright Declaration

This thesis is the result of the author's original research. It has been composed by the author and has not been previously submitted for examination which has led to the award of a degree.

The copyright of this thesis belongs to the author under the terms of the United Kingdom Copyright Acts as qualified by University of Strathclyde Regulation 3.50. Due acknowledgement must always be made of the use of any material contained in, or derived from, this thesis.

Signed: 

Date: March 29, 2025

Abstract

This thesis reports on experimental and numerical investigations to optimise and measure bremsstrahlung and synchrotron x-ray production in ultra-intense laser-solid interactions. The aim of the work is to better understand the processes behind the generation of synchrotron and bremsstrahlung x-rays within laser-solid interactions and to be able to resolve and differentiate between x-ray distributions from such interactions. This study also significantly advances understanding of a key diagnostic for measuring x-ray emission in these interactions.

First, a numerical investigation of the influence of laser focal spot size, focusing geometry, and pulse energy on bremsstrahlung and synchrotron x-ray production is presented. PIC simulations indicate that bremsstrahlung emission is highly dependent on pulse energy, whereas synchrotron production is highly spot-size and intensity dependent. An increase in synchrotron photon numbers with small spot size is attributed to greater hole-boring for higher laser intensities, as there is a larger volume within which electrons can interact directly with the laser fields.

Building on this, an experimental investigation of the influence of laser focal spot size, focusing geometry, and pulse energy on electron and bremsstrahlung x-ray production is reported. While the data do not strongly indicate a focusing geometry effect, electron and bremsstrahlung production is found to be highly dependent on pulse energy. This is consistent with the previous numerical results.

Finally, the focus moves to the development of x-ray diagnostics which would enable improved measurements of the x-ray spectrum. Measurements of bremsstrahlung x-rays for laser intensities up to $3 \times 10^{21} \text{ Wcm}^{-2}$ were analysed. Such laser intensities were achieved through the use of F/1 focusing plasma optics which enabled higher intensities to be reached than otherwise achievable with

the Vulcan laser. Through analysis of these measurements and extensive PIC and Monte Carlo modelling, an existing absorption-based x-ray spectrometer is characterised. It is found that there is a high degree of uncertainty in spectral deconvolution with the current spectrometer design, and several improvements are designed and numerically tested. Additionally, through analysis of the total x-ray spectrometer signal and analytical modelling, with comparison to Cu K- α x-ray measurements, our results suggest the presence of lower fast electron temperatures than many published electron temperature scalings predict. This highlights a critical challenge: the combined effects of low-resolution detector design and unexpected physical behavior complicates x-ray measurements in the high-energy part of the spectrum. Consequently, this thesis work underscores the need for more focused efforts on improving signal-to-noise ratios in this region, for example, through dual-spectrometer designs, to better measure high-energy x-rays.

Acknowledgements

This degree took me the best part of seven years. Longer than the average, to say the least. That time, as it is for most people in some way, was tinged with personal tragedy and strife! This experience has been a lesson in determination and in shining in the face of adversity. For good or bad, people have moved in and out of my life over this time. Thank you for everything you forced me to learn.

Firstly, thank you to Coherent Scotland for giving me a job when nobody else would. I couldn't have finished this thing otherwise. I pretty much told you that I had no clue about fiber lasers but you had faith in my ability to learn!

Speaking of, hello and thank you to all of the amazing people I have met at Coherent! Raphael, Daniele, Iacopo, Adrian, Leigh, Lenny, George... the list could go on and on. You are all fantastic and it is actually a privilege to work with you all.

Egle, Jesel, Ewan, Matt; you all made this experience more enjoyable. Experiments were a lot more bearable with you around.

Matt K., congratulations to you and your amazing partner, Hannah. Joanna is gorgeous. I want updates.

Chris, I owe so much of this work to you. Thank you for all of your guidance and your input. I hate to say it but, I'm a lot better at Python now thanks to having to unravel your code! Three temperature inputs? "F- off" indeed!

To my supervisors Ross, Paul, and the late Dave Neely. Thank you for not giving up on me entirely. And Ross, I still want Kerouac and restaurant recommendations. Tim and Martin, thank you both for your inputs and contributions (and for putting up with having me in your office for 6 months).

Muriel. Thank you for your support over the years. I hope you're well.

Tanya and Jason. I don't think you'll read this but, thanks for taking in a weird 23 year old when you were two weeks away from having a child. Having a family to come back to every evening when I was at RAL for my Masters - and you genuinely *did* made me feel like family - was everything. But Tanya, I am never getting in a car with you again - the Italian half is too strong!

The rest of these acknowledgements are going to be me telling everyone how much I love them. Feel free to skip to your section. If I missed you erroneously, fight me.

To all my buds from the old days of copying each other's coursework frantically in the common room on a Monday. The days of the Old Bar and Wetherspoons. I love you all.

Kalila. Born in the same hospital and having lived strangely parallel lives, I think we're connected in some woo-woo, spiritual way. You can take the girl out of Croydon, but can you really take the Croydon out of the girl? Remains to be seen for both of us... I love you.

Gerrard and Dorcas. You have always been a haven for me in this hectic and busy life. I'm so glad I met you both and am fortunate enough to still have you in my life. Thank you. I love you both.

To my Grandmothers, Frances and Ursula. Frances, you've supported me as far back as I can remember. I still think of you when I see the moon. I love you to pieces. Ursula, you'll never be able to read this (and as I write this travelling down to England on the train, looking out at the bleak North Sea, I'm hit again by our loss). You gave me your scientific mind and musical soul.

Man, last but not least, my parents. Sue and Tim. Momma and Timo. I'll be seeing you this evening! It can't have been easy having your only daughter move steadily further north, further and further from home. When are you moving to Scotland? I love you both. Thank you for everything.

P.S. Dad, stop showing off that you have the next-gen Apple Pencil. Some of us need more money for...sandwiches.

P.P.S My favourite comment from my supervisors throughout this process

(thank you both for putting up with my shoddy proof reading): “the sentence is confusion”. I’m sure it was.

Role of Author

The results presented in this thesis are the work of the author. The experimental results were achieved over several experimental campaigns, performed as part of a team of researchers led by Prof. P. McKenna. The author had a primary role in the execution, data analysis, numerical simulations and interpretation of results.

Chapter 5: PIC simulations were carried out by the author, supported by Dr Martin King, and analysed by the author.

Chapter 6: The author was closely involved in the planning and execution of the experimental campaign reported in this chapter. The author contributed to the digitisation of the IP data and calibration of the IP scanner. Analysis codes were developed by the author (supported by Dr Ross Gray) to extract the data into a manageable ‘dataframe’ format. The author developed a focal spot size measurement code, used to analyse the laser focal spot measurements made during the experiment.

Chapter 7: The author contributed to the execution of the experiment. PIC simulations were carried out by the author and Dr Martin King, and analysed by the author. Analytical modelling was performed by the author, using codes developed both by the author and by Dr Ross Gray. Monte Carlo simulations were performed by the author and Dr Chris Armstrong, and analysed by the author. Analysis of the x-ray spectrometer data was performed using code developed by Dr Chris Armstrong and modified by the author. The K- α diagnostic was designed and set up by Drs. Jonathan Jarrett and Robbie Wilson. Analysis of the K- α data was performed by Dr Timothy Frazer.

Contents

Abstract	i
Acknowledgements	iii
Role of Author	vi
List of Figures	xiii
List of Tables	xix
1 Introduction	1
1.1 Applications	2
1.1.1 Inertial confinement fusion	3
1.1.2 Laser driven x-ray radiography	6
1.2 Thesis outline	9
2 Fundamentals of laser-solid interactions	11
2.1 Introduction	11
2.2 Electromagnetic fields	12
2.2.1 Maxwell's equations	12
2.2.2 Single particle motion	13
2.2.3 Particle motion in inhomogeneous fields	15
2.3 Ionisation	16
2.3.1 Collisional ionisation	17
2.3.2 Collisionless ionisation	17
2.3.3 Field ionisation	17

2.3.4	Single and multi-photon ionisation	19
2.3.5	Barrier suppression ionisation	20
2.4	Plasma	21
2.4.1	Laser propagation in plasma	22
2.4.2	Dispersion relation	22
2.4.3	Scale length	24
2.4.4	Self focusing	25
2.5	Absorption of laser energy	25
2.5.1	Collisional absorption	26
2.5.2	Collisionless absorption	26
2.6	Electron transport in solid targets	29
2.6.1	Sheath Development	30
2.6.2	Electron populations and distributions	31
2.6.3	Holeboring, plasma channelling and relativistically-induced transparency (RIT)	35
2.6.4	Conclusion	37
3	X-ray production and interactions with matter	38
3.1	Introduction	38
3.2	X-ray Production	38
3.2.1	Line emission	39
3.2.2	Bremsstrahlung production	41
3.3	Synchrotron production	42
3.3.1	Synchrotron emission in ultra-intense laser-solid interac- tions	46
3.3.2	Skin-depth emission	46
3.3.3	Edgeglow	47
3.3.4	Reinjected electron synchrotron emission (RESE)	47
3.4	X-ray attenuation	48
3.5	Experimentally distinguishing synchrotron and bremsstrahlung ra- diation	50

3.6	Summary	52
4	Methodology	53
4.1	Lasers	53
4.1.1	Laser architecture	54
4.1.2	Mode locking	54
4.1.3	Q -switching	55
4.1.4	Amplification	55
4.1.5	Chirped pulse amplification	56
4.1.6	Laser parameters	57
4.1.7	Focusing optics, spot size and encircled energy	58
4.1.8	Wavefront diagnostics and optimisation	60
4.1.9	Temporal intensity contrast	61
4.1.10	Plasma mirrors	63
4.1.11	Focusing Plasma Mirrors	66
4.1.12	Vulcan Petawatt laser	66
4.1.13	PHELIX laser	69
4.2	Detectors	71
4.2.1	Image plate	71
4.2.2	Scintillators	73
4.2.3	CMOS and CCD Cameras	74
4.3	Diagnostic methods	75
4.3.1	Linear absorption x-ray spectrometer	76
4.3.2	Spectrometer image analysis	78
4.3.3	Electron spectrometer	80
4.3.4	$K\text{-}\alpha$ x-ray imaging	82
4.4	Numerical modelling	83
4.4.1	Monte Carlo modelling	83
4.4.2	Particle-in-cell modelling	84
4.4.3	Summary	90

5	The role of focal spot size and pulse energy in bremsstrahlung and synchrotron production in thick targets	91
5.1	Introduction	91
5.1.1	Optimising synchrotron emission	93
5.1.2	Laser focal spot size and pulse energy in LPIs	95
5.1.3	‘Defocusing’ to investigate spot size effects	96
5.2	Modelling	98
5.2.1	Spot size and energy dependence of electron acceleration and bremsstrahlung emission	101
5.2.2	Fixed Intensity Modelling	101
5.2.3	Fixed Energy Simulations	107
5.2.4	Bremsstrahlung modelling for fixed energy and fixed intensity pulses	112
5.2.5	Spot size and energy dependence of bremsstrahlung and synchrotron emission	114
5.3	Conclusion	121
6	Experimental investigation of the role of focal spot size and pulse energy in bremsstrahlung production in thick targets	124
6.1	Introduction	124
6.2	Experimental method	125
6.2.1	Laser focal spot size measurements	128
6.3	Experimental results	129
6.3.1	Focusing geometry	131
6.3.2	Energy on target for fixed spot size	133
6.3.3	Comparison of spot size and energy effects	136
6.4	Conclusion	139
7	Linear absorption spectrometer characterisation using bremsstrahlung x-rays	140
7.1	Introduction	140
7.2	Experimental method	144

7.2.1	Intensity enhancement using focusing plasma mirror .	145
7.2.2	X-ray spectrometer deconvolution	147
7.3	Experimental results	148
7.3.1	X-ray energy deposition scaling with incident laser intensity	149
7.3.2	Cu K- α results	152
7.3.3	Analytical modelling	153
7.3.4	Consideration of two temperature component Boltzmann photon distributions	153
7.3.5	X-ray temperature measurements	159
7.4	Modelling using PIC and Monte Carlo simulations	168
7.4.1	Generation of electron spectra	168
7.4.2	Generation of x-ray spectra	170
7.4.3	X-ray spectra	173
7.5	The characterisation of the existing spectrometer design	177
7.5.1	Custom spectral fitting	177
7.5.2	Generating synthetic data	178
7.6	High-resolution hard x-ray spectrometer designs	182
7.6.1	Extension of current design	182
7.6.2	Spectrometer signal and flux modelling	186
7.6.3	Extended spectrometer design summary	187
7.6.4	Complementary high energy design (LAS-HX)	187
7.7	Conclusions	190
7.8	Future work	193
8	Conclusions	194
8.1	The role of laser focal spot size and pulse energy in bremsstrahlung and synchrotron production in thick targets	195
8.2	Experimental investigation of the role of laser focal spot size and pulse energy in bremsstrahlung production in thick targets	197

8.3	Linear absorption spectrometer characterisation using bremsstrahlung x-rays	198
8.4	Further work	200
	Bibliography	202

List of Figures

1.1	Illustration of direct and indirect drive inertial confinement fusion	4
1.2	Illustration of example x-ray radiography setup	9
2.1	Illustration of electron motion in electromagnetic fields	15
2.2	Illustration of four ionisation processes, relevant to laser-solid interactions	18
2.3	Illustrations of laser energy absorption mechanisms	27
2.4	Example electron spectral distribution functions	32
2.5	Example electron temperature scalings as a function of laser intensity	33
2.6	Illustration of holeboring into a solid target	36
3.1	Illustration of field line discontinuity for moving charges	39
3.2	Illustrations of three x-ray production mechanisms	40
3.3	Attenuation cross-section as a function of photon energy for tungsten	50
4.1	Illustrations of regenerative and multi-pass laser amplifiers	56
4.2	Illustration of the principle of CPA	57
4.3	Schematic of Gaussian beam focusing	59
4.4	Schematic illustrating the principle of a Shack-Hartmann wavefront sensor	61
4.5	Illustration of temporal laser pulse features	63
4.6	Illustration of the principle of planar plasma mirror operation	64

4.7	Layout of the Vulcan laser facility	67
4.8	Layout of the PHELIX laser facility	70
4.9	Illustration of typical IP composition and the relevant electron transitions leading to PSL	72
4.10	Energy level diagram showing electron transitions in an inorganic scintillator.	74
4.11	Quantum efficiency curves for a CMOS camera	75
4.12	Example LAS x-ray spectrometer setup	77
4.13	Example LAS x-ray spectrometer analysis flow	78
4.14	Example LAS x-ray spectrometer merit grid	79
4.15	Example LAS x-ray spectrometer image processing	79
4.16	Schematic of a typical electron spectrometer	81
4.17	Trajectory of an electron in a typical electron spectrometer	81
4.18	Schematic of a typical K- α x-ray imaging diagnostic	83
4.19	Illustration and flowchart of an example PIC algorithm.	87
5.1	Simulated front surface, rear surface, and internal to target electron spectra for fixed pulse intensity	102
5.2	Simulated front surface electron temperatures for fixed pulse intensity	103
5.3	Simulated front surface electron numbers and total energy for fixed pulse intensity	104
5.4	Simulated internal to target electron temperatures for fixed pulse intensity	105
5.5	Simulated internal to target electron numbers and total energy for fixed pulse intensity	106
5.6	Simulated front surface, rear surface, and internal to target electron spectra for fixed pulse energy	108
5.7	Simulated front surface electron temperatures, numbers and total energy for fixed pulse energy	109

5.8	Simulated internal to target electron temperatures, numbers and total energy for fixed pulse energy	110
5.9	Simulated bremsstrahlung x-ray numbers for fixed intensity and pulse energy, independently	113
5.10	Simulated synchrotron and bremsstrahlung x-ray numbers for fixed pulse intensity and energy, independently	116
5.11	Simulated electron density plots for different laser intensities	118
5.12	Simulated electron, synchrotron, and bremsstrahlung x-ray density plots	118
5.13	Simulated combined E -field and electron density plot	119
5.14	Simulated holebore volume as a function of laser intensity, for two laser focal spot sizes	120
5.15	Simulated synchrotron spectra for different pulse energies	121
6.1	Example laser focal spots close to, and far from, focus	127
6.2	Plots showing process of laser focal spot measurement code testing	130
6.3	Plots showing process of laser focal spot measurement code on experimental data	131
6.4	Plots illustrating the investigated pulse energy and focal spot size ranges	132
6.5	X-ray spectrometer signal normalised by energy on target as a function of intensity	133
6.6	X-ray spectrometer signal as a function of energy on target	134
6.7	Electron spectrometer signal as a function of energy on target	135
6.8	X-ray spectrometer signal as a function of laser intensity for fixed pulse energy and fixed spot area	136
6.9	Electron spectrometer signal as a function of laser intensity for fixed pulse energy and fixed spot area	138
6.10	Maximum electron energy as a function of laser intensity for fixed pulse energy and fixed spot area	138

7.1	X-ray attenuation cross-sections for tungsten	142
7.2	Schematic of focusing plasma mirror	145
7.3	Schematic and images of LAS x-ray spectrometer	148
7.4	LAS x-ray spectrometer response matrix	149
7.5	X-ray spectrometer signal as a function of energy on target .	150
7.6	X-ray spectrometer signal as a function of laser intensity . .	151
7.7	Copper K- α x-ray signal as a function of laser intensity . . .	152
7.8	Comparison of LAS x-ray spectrometer signal and numerical mod- elling for Haines <i>et al.</i> electron temperatures	155
7.9	Comparison of LAS x-ray spectrometer signal and numerical mod- elling for Wilks electron temperatures	155
7.10	Flow of radiative numerical modelling	157
7.11	Comparison of LAS x-ray spectrometer signal and numerical mod- elling of refluxing electrons for Wilks, Haines and Beget <i>et al.</i> electron temperatures	158
7.12	Initial, deconvolved x-ray temperatures as a function of laser in- tensity	160
7.13	Distributions of spectral fitting parameters for experimental spec- tral deconvolution	162
7.14	Merit grids from initial experimental spectral deconvolution	163
7.15	Reconstructed x-ray spectrometer signals constrained by deconvo- lution merit value	164
7.16	Reconstructed x-ray spectrometer signals constrained by experi- mental standard deviation	165
7.17	Reconstructed x-ray spectral distributions constrained by experi- mental standard deviation	165
7.18	Reconstructed x-ray spectral distributions constrained by experi- mental standard deviation with extended response matrix . .	167
7.19	Simulated electron spectral distributions for fixed pulse energy	169
7.20	Comparison of simulated electron temperatures and several typical electron temperature scalings	170

7.21	GEANT4-generated electron to x-ray spectral heatmap. . . .	171
7.22	Simulated bremsstrahlung x-ray spectral distributions with comparisons to other methods	172
7.23	Simulated bremsstrahlung x-ray spectra for fixed pulse energy simulations	173
7.24	Simulated bremsstrahlung x-ray temperatures	173
7.25	Boltzmann temperature fits to simulated bremsstrahlung x-ray spectra	175
7.26	Maxwell-Boltzmann temperature fits to simulated bremsstrahlung x-ray spectra	176
7.27	Comparison of Boltzmann and Maxwell-Boltzmann temperature fits to simulated bremsstrahlung x-ray spectra	176
7.28	Custom spectral deconvolution of experimental x-ray spectrometer data	178
7.29	Reconstructed spectral distributions from custom spectral deconvolution of experimental x-ray spectrometer data	179
7.30	Merit grids from spectral deconvolution of synthetic data . .	180
7.31	Reconstructed spectral distributions from spectral deconvolution of synthetic data	181
7.32	$N_1T_1:N_2T_2$ ratios for simulated bremsstrahlung x-ray spectra	181
7.33	Schematic of proposed linear 20-layer x-ray spectrometer . .	183
7.34	Merit grids from spectral deconvolution of synthetic data with extended spectrometer design	184
7.35	Reconstructed spectra from spectral deconvolution of synthetic data with extended spectrometer design	185
7.36	Merit grids from spectral deconvolution of synthetic data with extended design	185
7.37	Synthetic spectrometer signals for extended spectrometer design as a function of laser intensity	187
7.38	Schematic and response matrix of the proposed LAS-HX spectrometer design	188

7.39 Merit grids from spectral deconvolution of synthetic data with LAS-HX spectrometer design	189
7.40 Synthetic spectrometer signals for LAS-HX spectrometer design as a function of laser intensity	189

List of Tables

5.1	The spot size parameters for fixed energy and intensity EPOCH 2D simulations	98
5.2	Parameters for the 2D and 3D EPOCH simulations performed.	99
5.3	Parameters for the EPOCH 3D simulations performed, for both the fixed energy and fixed intensity scans.	100
6.1	Beam sizes and F -numbers ($F/\#$) achieved through the use of apodisers.	126
6.2	Flow of code used to calculate laser focal spot areas and encircled energies from focal spot data.	128

Chapter 1

Introduction

Since the invention of the laser in 1960 [1], advances in technology have led to the capability for relativistically intense pulses, with intensities above 10^{18} Wcm^{-2} to be routinely generated within the laboratory. The chirped pulse amplification (CPA) technique [2], for which Strickland and Mourou shared in the Nobel Prize in physics in 2018 [3], provided the technology to amplify ultrashort pulses to petawatt-power. Since the invention of CPA, the interactions between ultra-intense lasers and solids have been investigated as a driver for high energy ions [4–6], x-ray sources [7–9], and high harmonic generation [10]. Additionally, with ultra-intense laser-solid interactions, it is possible to achieve conditions that are analogous to those found in astrophysical environments [11, 12]. The understanding of the physics gained from these investigations has the potential to be exploited in applications of significant societal benefit, notably in proton oncology [13, 14], x-ray radiography [15, 16], and inertial confinement fusion [17–19]. It is clear that the study of laser-solid interactions has significant potential value due to the numerous applications of the technology. This has motivated extensive research in the field over the last few decades.

In recent years, new technologies have enabled higher-power lasers to be designed and built, such as the ELI-Nuclear Physics 10 PW laser in Romania [20, 21]. As available lasers reach intensities of 10^{22} - 10^{23} Wcm^{-2} , laser-solid interactions are expected to become highly relativistic. In these ultra-intense laser-solid interactions, quantum electrodynamic (QED) effects can start to be-

come observable due to the high strength electromagnetic fields involved, leading to phenomena that go beyond classical electrodynamics [22, 23]. When laser intensities exceed a certain threshold, the electric fields can be comparable to the critical field of QED, the Schwinger limit ($1.32 \times 10^{18} \text{ Vm}^{-1}$) [24, 25]. The intensity threshold for this is around 10^{29} Wcm^{-2} , which is many orders of magnitude higher than is available with current laser systems. However, as electrons are accelerated to high velocities in a counter-propagating geometry with an ultra-intense laser pulse, they experience boosted electric field strengths in their rest frame, which become comparable to the Schwinger limit. Under these conditions, quantum effects like photon-photon scattering can occur [26, 27]. Electrons can emit high-energy photons in an ultra-intense laser field through a process called synchrotron radiation [28, 29]. At extreme intensities of 10^{22} Wcm^{-2} , the force exerted on electrons from the emission of this radiation can significantly alter the electron momentum, a phenomenon known as radiation reaction [27, 30, 31]. Additionally, ultra-intense lasers can produce conditions where photon-photon interactions can lead to the creation of electron-positron pairs [28, 32, 33]. This process is known as Breit-Wheeler pair production and is a direct manifestation of a QED interpretation [34]. Understanding these highly-relativistic interactions is key for applications such as synchrotron x-ray generation. In order to perform experimental investigations of high-field phenomena, it is imperative to be able to optimise the interaction to increase the signal to noise of synchrotron emission to other x-ray production mechanisms, and to be able to measure synchrotron x-ray signals.

1.1 Applications

There are three prominent potential applications discussed in the literature: hadron therapy [13, 14], inertial confinement fusion (ICF) [17–19], and the non-destructive testing and imaging of material with x-rays [15, 35–37]. As ion acceleration is not directly related to the core material of this thesis, more detailed descriptions can be found in [38]. This section will instead focus on ICF and

x-ray radiography schemes, which are directly related to the work presented in this thesis.

1.1.1 Inertial confinement fusion

Since the 1950's, there has been a large effort to harness fusion reactions as a clean and plentiful source of energy [39, 40]. Nuclear fusion involves fusing two lighter nuclei into a single heavier, and more stable, nucleus. The difference in rest mass between the original and final products is released as energy in a process that is similar, but opposite, to fission, which involves the splitting of nuclei. The biggest challenge is to overcome the electrostatic repulsion between the two lighter nuclei, which involves providing them with large amounts of energy [40]. For fusion reactions to become a viable energy source, ignition, the term given to a fusion reaction where the reaction heats the fuel mass more rapidly than it cools, is necessary. Not only does it involve a large amount of energy, it also requires the confinement of a plasma, characterised by the confinement time, τ_E , which is a measure of the rate of energy loss from a system to its surroundings. Furthermore, the criteria of ignition, known also as the extended Lawson criterion, is given by a minimum value of the 'triple product'. The minimum of the triple product for ignition is given by $nT\tau_E \geq 2.76 \times 10^{21}$ keV.s.m⁻³, where n is the fuel number density and T is the fuel temperature [40].

There are two main avenues of fusion research: low density with long confinement times, and high densities and temperatures with short confinement times. These two schemes are magnetic confinement fusion (MCF) and inertial confinement fusion (ICF), respectively. Although MCF has been the point of focus for many fusion studies, with tokamak reactors located across the globe, it proves difficult to confine a plasma for long periods of time due to particle drifts and magnetic instabilities [41, 42]. With this in mind, ICF has also been a popular field of study, considering the short confinement times required.

ICF has been a major driver in laser-plasma research since the invention of the laser [1, 43]. In principle, lasers can be used to drive controlled fusion reactions as a means to generate power. In most ICF schemes, lasers are used to heat

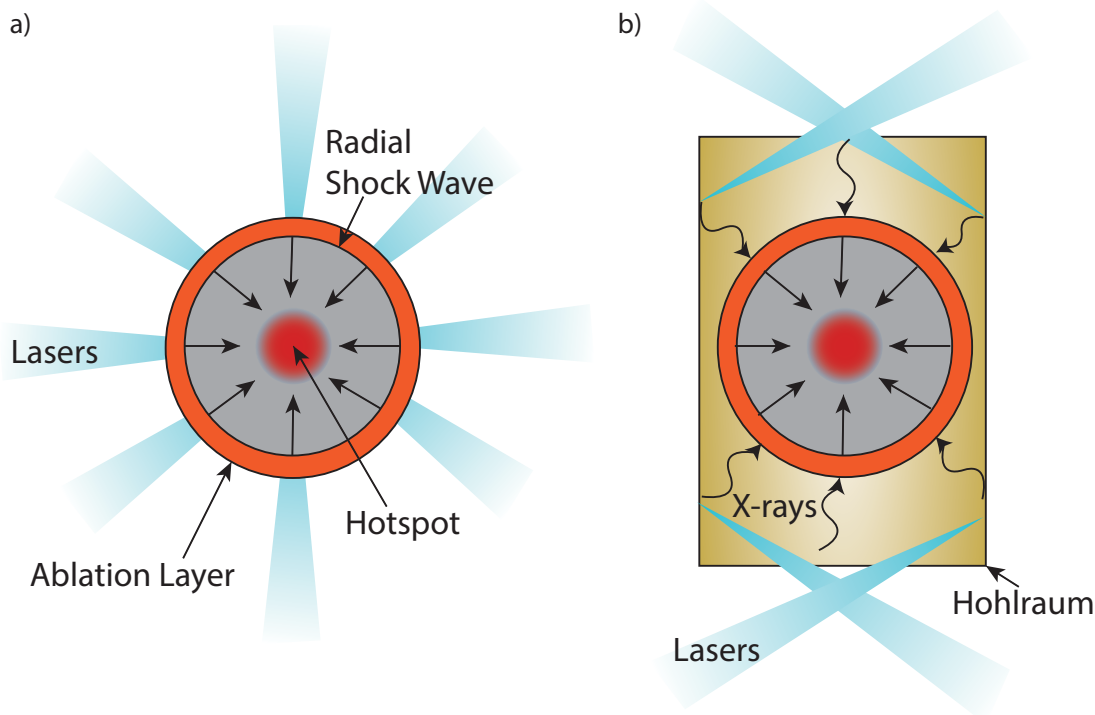


Figure 1.1: Schematic showing the principles of (a), direct drive ICF and, (b), indirect drive ICF. In (a), lasers are uniformly irradiating a fuel capsule which acts to compress and heat the fuel, generating a central hot spot. In (b), lasers irradiate the inside of a gold *hohlraum*, which generates x-rays which compress and heat the fuel, generating a central hot spot.

and compress a fuel target with the intention of igniting a fusion reaction. The initial proposals in Kidder [18] and Nuckolls [17] described a theoretical scheme within which a gas cell would be heated by an incident laser. The resultant ablation pressure would then drive a wave of increased density and temperature to the core. The heated outer layer of the gas cell would gain momentum from the laser, and act to confine and compress the remaining fuel. More recent ICF schemes typically involve the heating of a hybrid solid and gas fuel capsule either directly, or indirectly, using a suite of lasers.

Direct drive involves the direct heating and compression of a fuel capsule, where lasers directly interact with the outermost layers to drive the compression, shown in Figure 1.1(a) [44]. However, this method is particularly susceptible to non-uniform compression of the fuel, due in part to non-uniform irradiation, surface irregularities on the fuel capsule, and plasma instabilities [45, 46]. A method to circumvent this is to use lasers indirectly to drive compression of the fuel.

In indirect drive fusion, the fuel capsule is instead heated within a cylindrical container, known as a *hohlraum*, which is irradiated internally through apertures at either end, shown in Figure 1.1(b) [45]. The x-rays generated in the interaction between the lasers and the *hohlraum* irradiate the fuel capsule directly, which also drives an inward ablation pressure through the fuel. Whilst this method lessens the impact of non-uniformity on the interaction, it is still a highly inefficient process. Not only are the lasers frequency tripled, both in direct and indirect drive schemes, (to reduce fast electron heating as $T_e \propto I\lambda^2$ [47, 48]), which is an inefficient process, the laser light is then converted into x-rays through interaction with the *hohlraum*.

A more recent branch of ICF looks to lessen the requirements on fuel compression. Fast ignition (FI) fusion combines the method of indirect drive fusion with the application of a particle beam into the capsule to produce a hot spot [19, 49]. The most common method of achieving this is the application of a gold cone into the target: the centre of the tip is irradiated by laser light to produce x-rays and fast electrons in a concentrated region [50]. As these penetrate the fuel, it is heated to high temperatures [48, 51–53].

Not only are x-rays used to induce compression in indirect drive fusion, they are also a key diagnostic tool. Experiments relating to fast ignition typically centre on the heating of fast electron populations, which are difficult to directly measure. For this purpose, the K- α and bremsstrahlung x-rays produced by fast electrons have been used to indirectly measure the characteristics of the population, including the temperature [54–56] and divergence [57, 58] of accelerated electron beams. One of the main challenges in the FI scheme is the efficient transfer of energy from the driver to the ignition region [49]. A key measurement of this is the x-ray emission from the electrons within the cone, which can indicate the fraction of laser energy delivered to the electrons.

This highlights the importance of understanding the physics of high-energy x-ray generation for use in diagnostic techniques. The characterisation and development of a hard x-ray spectrometer is reported in this thesis. With this diagnostic, the spectral distributions of bremsstrahlung emission from fast elec-

trons can be resolved, which is key to diagnosing the fast electron distribution in FI applications.

1.1.2 Laser driven x-ray radiography

Another application of interest is the potential for laser-solid interactions to become a feasible source of high-energy x-rays for the fast imaging and non-destructive inspection of large and/or dense objects. This technology is of interest to the security and industrial sectors, such as aerospace, nuclear, and advanced manufacturing. Laser-solid interactions offer high brightness and energy, short duration, and small emission area ($\ll 1\text{mm}^2$) point sources [36], which make them unique from conventional sources such as cathode ray x-ray tubes and linac sources, which cannot simultaneously achieve all of the above properties in a single source. Not only can a laser-driven source achieve all of these qualities, it can also be a compact option which could eventually be employed on-site in industrial units.

For example, a study demonstrated that laser-driven x-ray sources can achieve source sizes in the range of a few micrometers, which facilitates high-resolution radiography and imaging applications [59]. In contrast, conventional x-ray tubes typically have larger source sizes, often on the order of millimeters, which can limit the spatial resolution of the radiographs.

Another important property of laser-driven x-ray sources is their ability to generate ultrashort pulses. These sources can produce x-ray pulses with durations in the femtosecond (10^{-15} seconds) to picosecond (10^{-12} seconds) range. Such brief pulses are beneficial for capturing ultrafast processes, such as molecular interactions or ultrafast reactions, with high precision. An example of this is the imaging of shockwave propagation [45]. In comparison, conventional x-ray sources like x-ray tubes generally produce continuous radiation or longer-duration pulses that are not suitable for time-resolved imaging or other applications requiring rapid temporal resolution [60].

Laser-driven x-ray sources generally offer superior brightness with a smaller footprint compared to conventional x-ray sources. The brightness of an x-ray

source is typically defined as the flux of photons per unit area, per unit solid angle, and per unit energy, and it is an important factor in many imaging and analysis techniques.

Laser-driven x-ray sources, particularly those based on laser wakefield acceleration (LWFA) or compact laser-driven plasma sources, can achieve extremely high peak brightness. For example, peak brightness values of laser-driven sources can be on the order of (10^{24} photons ($\text{mm}^2 \cdot \text{mrad}^2 \cdot \text{s} \cdot 0.1\%$ bandwidth)), which are several orders of magnitude higher than those of conventional x-ray tubes or synchrotron light sources [60]. For comparison, conventional x-ray tubes typically exhibit brightness values around ($10^{14} - 10^{15}$ photons ($\text{mm}^2 \cdot \text{mrad}^2 \cdot \text{s} \cdot 0.1\%$ bandwidth)), meaning that laser-driven x-ray sources can offer up to a million times higher brightness than conventional x-ray tubes, making them suitable for applications requiring high spatial and temporal resolution, such as ultrafast imaging and time-resolved spectroscopy.

Synchrotron sources, while brighter than x-ray tubes, still fall short of the peak brightness levels achievable by laser-driven sources. Synchrotrons typically produce x-rays with brightness values in the range of ($10^{18} - 10^{19}$ photons/ $(\text{mm}^2 \cdot \text{mrad}^2 \cdot \text{s} \cdot 0.1\%$ bandwidth)) [61]. This is still significantly lower than the values achieved by laser-driven sources, which can provide highly intense, short-duration pulses ideal for capturing fast phenomena.

While laser-driven x-ray sources offer enhanced spatial resolution and temporal resolution, they typically face challenges such as lower overall efficiency and high operational costs due to the need for high-power laser systems (although not as high as for synchrotrons or x-ray free-electron lasers (XFELs)). However, ongoing advancements in laser technology are continuously improving their performance and making them a promising, low-cost and small-footprint alternative to traditional x-ray sources in various scientific, medical, and industrial applications.

Many experimental demonstrations of x-ray radiography have been performed, both for the imaging of industrial objects [36, 37], shown in Figure 1.2, and as backlighters for ICF research [16, 62–64]. High pulse energy systems, such as

the Vulcan Petawatt laser (offline for upgrade as of 2023), could deliver upwards of 100 J of energy onto a solid target. This can result in a bright x-ray source, which has been used to perform single-shot radiography on a range of objects [37]. Such Nd:glass-based lasers are currently only able to produce high energy pulses every twenty minutes. Ti:sapphire lasers, such as the Astra Gemini laser [65, 66], can deliver pulses of Joule-level energies with pulse durations of tens of femtoseconds at Hz repetition rates. However, laser systems that utilise diode-pumped amplifiers can operate at up to tens of Hz repetition rates [67–69], which could allow for the fast imaging and non-destructive testing of objects. Such lasers would be able to generate high repetition-rate, highly penetrative x-ray beams, which can probe the density variations in components as they go through stress processes.

With higher intensity lasers becoming available, high-field effects can be utilised to generate synchrotron emission. A laser-driven synchrotron source has the potential to be a bright, highly directional source of x-rays, which is ideal for imaging and testing [28, 29, 70, 71]. For such a source to become viable, it must be characterised. The characterisation of a laser-driven synchrotron source both requires the optimisation of synchrotron production with respect to other emission mechanisms, such as bremsstrahlung, and the ability to detect and measure the synchrotron emission spectrum. At the highest laser intensities achievable at present (10^{22} - 10^{23} Wcm^{-2}), the x-ray emission spectrum is dominated by bremsstrahlung production, which renders it difficult to detect and measure synchrotron x-rays [72, 73]. The work presented in Chapters 5 and 6 addresses the optimisation of synchrotron emission at currently available laser intensities, to make it possible to detect. Chapter 7 then focuses on the measurement of hard x-ray spectra, which are, by nature, difficult to spectrally resolve. With the findings presented in this thesis, it should be possible to experimentally characterise laser-driven synchrotron emission, with the intention of producing an ultra-bright, highly collimated synchrotron x-ray source.

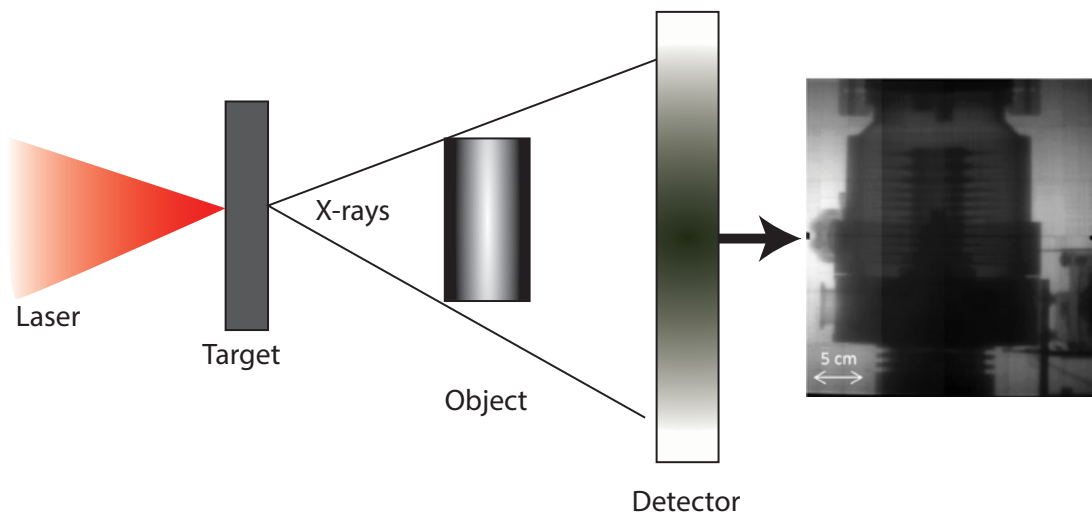


Figure 1.2: Schematic for x-ray radiography of a sample with internal structure. Laser accelerates electrons through a target, these electrons generate x-rays as they interact with the target. These x-rays illuminate the object, and as they are highly penetrative, variations in the density can be probed. Example radiography image from [36].

1.2 Thesis outline

This thesis reports on experimental and numerical investigations exploring the role of laser parameters in the optimisation of bremsstrahlung and synchrotron x-ray production. Additionally, the characterisation and development of an absorption-based x-ray spectrometer for effective spectral measurements of x-rays generated at laser intensities above 10^{21} Wcm^{-2} is reported. The outline of the remainder of the thesis is as follows:

- **Chapter 2:** The physics underpinning laser-solid interactions is reviewed, which provides an essential foundation for the understanding of the underlying dynamics described and reported in the following chapters.
- **Chapter 3:** The key x-ray generation mechanisms are reviewed, notably line, bremsstrahlung, and synchrotron emission, the x-ray emission mechanisms that form the bulk of the discussions within this work.
- **Chapter 4:** Presented in this chapter are the key experimental and numerical methodologies employed in the investigations reported in this thesis, including the details of laser architecture and laser systems, diagnostic techniques, and simulation tools.

- **Chapter 5:** The optimisation of synchrotron and bremsstrahlung emission with respect to pulse energy and laser focal spot size for laser-solid interactions with laser intensities between 10^{20} and 10^{22} Wcm^{-2} is reported, with the intent of experimentally enhancing synchrotron emission at currently available laser intensities.
- **Chapter 6:** The effects of pulse energy and laser focal spot size on bremsstrahlung emission investigated in the previous chapter are investigated experimentally.
- **Chapter 7:** The characterisation and development of a linear absorption x-ray spectrometer with respect to diagnosing bremsstrahlung x-rays generated in laser-solid interactions with laser intensities from 10^{21} Wcm^{-2} and beyond is reported.
- **Chapter 8:** The results and interpretations presented in Chapters 5, 6, and 7 are summarised, with the impact on the wider research field of laser-solid interactions highlighted. Potential future avenues of research are also discussed.

Chapter 2

Fundamentals of laser-solid interactions

2.1 Introduction

The interaction between lasers and solid material is a complex and nuanced one, with many aspects and variables at play. In this chapter, a review of laser-solid experiments, and the fundamental mechanisms and physics, are reported. Firstly, due to the electromagnetic nature of a laser pulse, Maxwell's equations of electromagnetism and the descriptions of charged particle motion in electromagnetic fields are discussed, with a view to understanding the effect of these fields on particles in the target. This is followed by a discussion of target ionisation mechanisms and the methods by which a laser pulse can ionise target material. From there it is appropriate to discuss the nature and characteristics of plasma, and the propagation of light in such a medium. With the fundamental building blocks of laser-plasma interactions reviewed, the complex processes of the absorption of laser energy, electron transport and temperature scalings, and field evolution within the target can be introduced.

2.2 Electromagnetic fields

Before discussing the nature of interactions between laser pulses and electrons, the classical laws of electrodynamics are introduced, alongside their relation to ultra-intense laser pulses. Here, Maxwell's equations are introduced, which describe the evolution of electric and magnetic fields, as well as the Lorentz equation for the motion of a charged particle in electromagnetic (EM) fields.

2.2.1 Maxwell's equations

Maxwell's equations are essential to the description of the interaction of electromagnetic waves with matter. Gauss' laws, in Equations 2.1a and 2.1b, describe the gradients of the electric and magnetic fields, \vec{E} and \vec{B} . They describe how the electric field is related to the particle charge density, ρ , the behaviour of magnetic field lines forming closed loops. ϵ_0 here describes the permittivity of free space.

$$\nabla \cdot \vec{E} = \frac{\rho}{\epsilon_0} \quad (2.1a)$$

$$\nabla \cdot \vec{B} = 0 \quad (2.1b)$$

The Maxwell-Faraday law, in Equation 2.2a, dictates that the electric field of a loop is dependent on the evolution of the magnetic field within that loop. Ampere's law, in Equation 2.2b, states that the magnetic field is related both to the current density, \vec{j} , inducing it, and to the evolution of the electric field.

$$\nabla \times \vec{E} = -\frac{d\vec{B}}{dt} \quad (2.2a)$$

$$\nabla \times \vec{B} = \mu_0 \vec{j} + \frac{1}{c^2} \frac{d\vec{E}}{dt} \quad (2.2b)$$

Here, μ_0 is the permeability of free space and c is the speed of light in vacuum.

In addition to Maxwell's laws, it is essential to be able to describe a laser pulse, which is an electromagnetic wave solution to Maxwell's equations, characterised by a spatially and temporally varying electric and magnetic field. A laser pulse has

a number of characteristics, such as its wavelength, λ , intensity, I_L , and energy, E_L . Such a pulse will be focused to a spot of size r_L . The field propagation can be shown to be

$$\nabla^2 \vec{E} = \frac{1}{c^2} \frac{d^2 \vec{E}}{dt^2} \quad (2.3)$$

using Maxwell's equations above. The relationship between the electric and magnetic fields can be shown to be

$$|B_0| = \frac{1}{c} |E_0| \quad (2.4)$$

using the Maxwell-Faraday law. The laser intensity is related to the electric field strength as given by

$$I_L = \frac{c\epsilon_0}{2} |\vec{E}|^2 \quad (2.5)$$

Another important parameter of a propagating laser pulse is polarisation, which describes the electric field oscillation. There are many types of polarisation. However, solely linear polarisations are considered in this thesis. The linear polarisations, s- and p-, describe the oscillation of the electric field transversely and parallel to the plane of incidence to the target, respectively.

2.2.2 Single particle motion

The acceleration of electrons is the driving force within this field of research. However, before the acceleration of electrons by a laser pulse can be discussed, the basics of electron motion in EM fields need to be understood. The Lorentz force equation that governs the dynamics of a charged particle subject to electric and magnetic fields is given by

$$\frac{d\vec{p}}{dt} = -q_e \left(\vec{E} + \vec{v} \times \vec{B} \right). \quad (2.6)$$

In this equation, $\vec{p} = m_e \vec{v}$ is the particle momentum, which can be relativistically corrected to $\vec{p} = \gamma m_e \vec{v}$, where $\gamma = \left(1 + \frac{v^2}{c^2}\right)^{\frac{1}{2}}$ is the relativistic factor. Here, m_e , q_e , and v are the mass, charge and velocity of the electron, respectively, and t is

time. In the presence of a plane-wave electric field, electrons will begin to move in the oscillation direction of the electric field. When the $\vec{v} \times \vec{B}$ force is negligible, the Lorentz equation reduces to

$$\frac{d\vec{p}}{dt} = -q_e \vec{E}. \quad (2.7)$$

If only the temporally varying aspect of the electric field is considered, such that $|\vec{E}| = E_0 \sin(\omega t)$ and by using the relationship $\vec{p} = m_e v$, the Lorentz equation becomes

$$m_e \frac{d\vec{v}}{dt} = -q_e E_0 \sin(\omega t). \quad (2.8)$$

Now, one can see that the velocity with which an electron oscillates or ‘quivers’ in an electric field is given by

$$v_{quiver} = \frac{q_e E_0}{m_e \omega} \cos(\omega t) \quad (2.9)$$

An electron that is initially at rest will begin to oscillate in the transverse direction to the propagation of the electric field, along the axis of polarisation. In the classical regime, the maximum quiver velocity that electrons can reach is $v_{quivermax} = \frac{eE_0}{m_e \omega}$ and the frequency with which it oscillates is equal to that of the driving electric field, ω .

In the presence of a magnetic field there is an additional force in the $\vec{v} \times \vec{B}$ direction, i.e. in the direction of wave propagation, and transverse to both the electric and magnetic fields. At low electron velocities - at non-relativistic values far lower than the speed of light - this $\vec{v} \times \vec{B}$ component is small compared to that of the electric field and can generally be ignored. However, at high laser intensities (with irradiances above $I\lambda^2 > 1.37 \times 10^{18} [\text{Wcm}^{-2}\mu\text{m}]$), where the electron velocity moves into the relativistic regime, the force due to the magnetic field becomes comparable to that of the electric field. The normalised vector potential,

$$a_0 = \frac{q_e E_L}{m_e c \omega_0} = \sqrt{\frac{q_e^2}{2\pi^2 \epsilon_0 m_e^2 c^5} \lambda_0^2 I_0} \quad (2.10)$$

is an indicator of the strength of the laser field. For $a_0 \geq 1$ the electron oscillatory velocity will approach c and the electron motion will be relativistic. In this case, the additional Lorentz force component due to the magnetic field needs to be considered. Here we consider only the temporally varying component of the force, for simplicity. At laser intensities larger than the limit given above, the $\vec{v} \times \vec{B}$ force becomes non-negligible and results in a longitudinal motion, with a velocity of magnitude

$$v_{longitudinal} = \frac{q_e^2 E_0^2}{4m_e^2 c \omega^2} \cos(2\omega t), \quad (2.11)$$

and a frequency twice that of the transverse quiver motion and field oscillation frequency. The combination of these motions result in a figure-of-eight trajectory in the reference frame following the average motion, which can be seen in Figure 2.1.

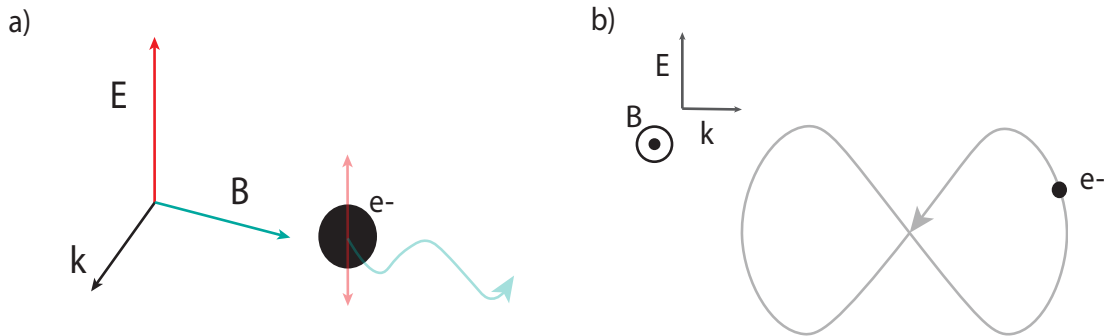


Figure 2.1: An illustration showing the joint effects of electric and magnetic fields on electron motion. In a) the separate longitudinal and quiver velocities can be seen in relation to the fields responsible. In b) the combined ‘figure-of-eight’ trajectory of these motions in the transverse plane can be seen.

2.2.3 Particle motion in inhomogeneous fields

In laser-plasma interactions we are not considering the interaction of an electron with an infinite homogeneous field, but one that is inhomogeneous, both spatially and temporally. A temporal envelope of the form

$$\vec{A}(x, t) = a_0 f(t) \cos \phi \quad (2.12)$$

where $f(t)$ is a slower-varying function compared to the EM field oscillation, such that $df/dt \ll \omega f$, can be used to describe the pulse, and ϕ is the phase.

In such an inhomogeneous electromagnetic field, with either spatial or temporal gradients, the ponderomotive force - the time averaged oscillation potential - becomes important. Gibbon [74] gives the relativistic ponderomotive force, f_p , as:

$$f_p = -mc^2 \nabla \langle \gamma \rangle \quad (2.13)$$

where $\langle \gamma \rangle$ is the time averaged relativistic factor. In an infinite, homogeneous field an electron will not gain any net energy. However, this is not realistic. In an inhomogeneous field, i.e. in a laser pulse where the fields are higher in the centre of the focal spot than in the outer edges, the electrons experience a force that ejects them from the centre of the beam. The first half wave cycle of the electric field acts to move the electrons away from the centre of the laser spot to an area of lower field strength. In the second half wave the electron experiences a smaller restoring force, which results in a drift toward areas of lower field strength. Overall, this results in a net force and a net transfer of energy from the EM field to the electron.

For lower intensity pulses ($a_0 < 1$) where $\vec{v} \times \vec{B}$ is insignificant, electrons are ejected at 90° to the direction of laser propagation [75]. However, at relativistic intensities where there is a longitudinal drift present, the electron will be ejected diagonally at some angle to the laser propagation. Considering the electron momenta in each plane gives an emission angle, θ , of

$$\cos \theta = \sqrt{\frac{\gamma - 1}{\gamma + 1}} \quad (2.14)$$

from the longitudinal axis [75].

2.3 Ionisation

It is important to discuss the ionisation of material as, in laser-solid interactions, the solid target material is ionised and becomes plasma. In this section a number

of ionisation mechanisms are introduced.

Ionisation, partial or total, occurs when electrons are released from the bond to their parent nuclei. For this to happen, an energy above the binding energy of an electron has to be deposited for the electron to overcome the electrostatic bonds attracting it to the atomic nucleus. Such an energy is known as the ionisation potential, I_p .

2.3.1 Collisional ionisation

In collisional ionisation, energy is imparted to the electron through a collision with another charged particle. The collision frequency is given by

$$\nu_{CI} \approx n_e v_e 4\pi a_b^2 \left(\frac{I_H^2}{I_p k_B T_e} \right) \ln \left(\frac{k_B T_e}{I_p} \right) \quad (2.15)$$

where I_H is the ground state ionisation potential of hydrogen (= 13.6 eV), v_e is the electron velocity, a_b is the Bohr radius, k_B is the Boltzmann constant, and n_e and T_e are the electron number density and temperature, respectively [76, 77]. This ionisation mechanism is relevant when electrons are already liberated from their atoms, and can then go on to liberate other electrons. Such electrons can be ionised by the following mechanisms.

2.3.2 Collisionless ionisation

Depicted in Figures 2.2(a) - 2.2(d) are four different collisionless ionisation mechanisms: single and multi-photon ionisation, and two barrier suppression mechanisms: quantum tunneling and over-the-barrier, respectively. In each, an electron is initially bound within a potential well, with potential $V(x)$ and ionisation potential, I_p .

2.3.3 Field ionisation

Electrons can be freed from their atoms by the presence of an external electric field, such as that supplied by a laser. By substituting the Bohr radius into

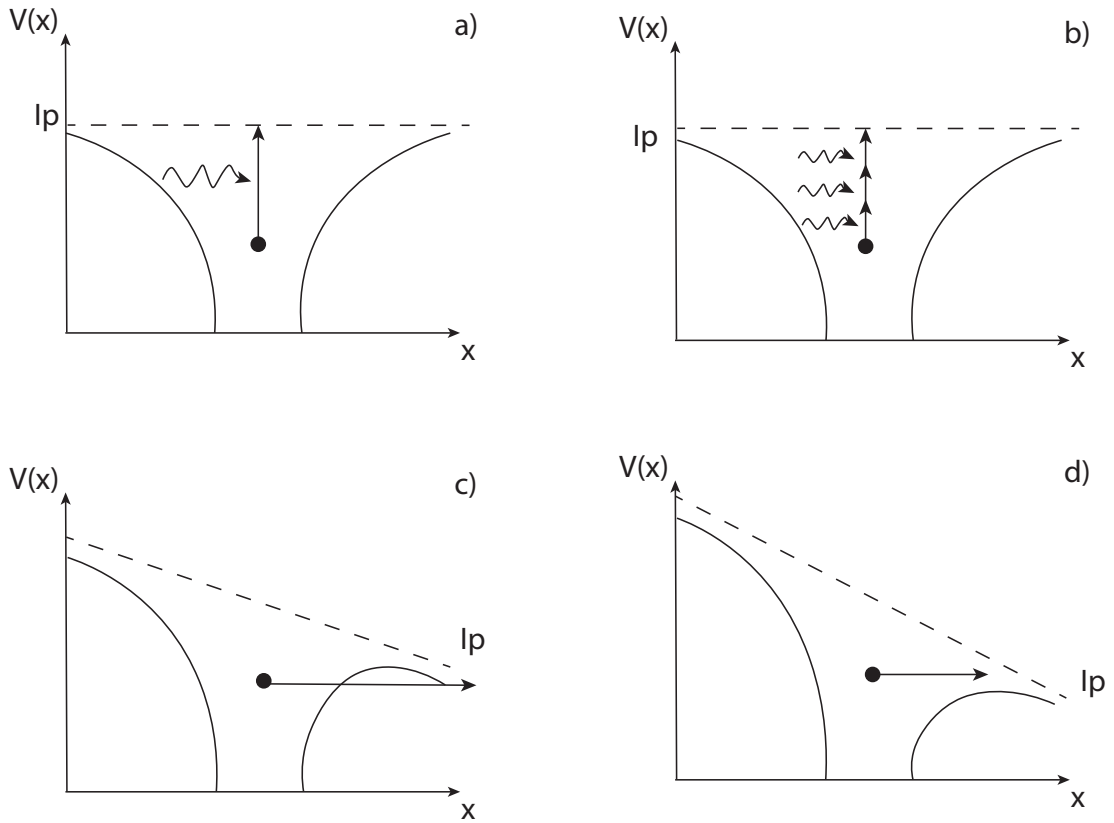


Figure 2.2: Potential energy as a function of position, x , with ionisation potentials, I_p , denoted by dashed lines. (a) and (b) show single and multi-photon ionisation respectively. In these the ionisation potential remains fixed and the electron is liberated from the atom through deposition of energy greater than the ionisation potential. (c) and (d) represent the barrier suppression ionisation mechanisms, quantum tunneling and over-the-barrier ionisation, respectively. In both the ionisation potential has been altered by an external electric field, which is shown by the change in gradient of I_p .

Coulomb's law one can determine the strength of electric field that binds an electron to the nucleus. Such a field strength, E_a is given by:

$$E_a = \frac{q_e}{4\pi\epsilon_0 a_b^2} \quad (2.16)$$

and yields a value of $\approx 9 \times 10^{11} \text{ Vm}^{-1}$ for atomic hydrogen. By relating electric field strength to laser intensity using Equation 2.5, for $\eta = 1$ in vacuum, the required intensity is $I_a \approx 3.5 \times 10^{16} \text{ Wcm}^{-2}$. We however see ionisation at lower laser intensities than this, which indicates the existence of other ionisation mechanism that operate at lower laser intensities [78, 79]. Such a mechanism is multi-photon ionisation.

2.3.4 Single and multi-photon ionisation

Common ionisation mechanisms occur when incident photons interact with an electron. Illustrations of these processes can be seen in Figures 2.2(a) and 2.2(b). The energy from the photon is absorbed by the electron and can either be promoted to a higher energy level or be completely freed from the atom. Because of the discrete nature of atomic energy levels, only photons of a specific energy can be absorbed, and only photons above a certain energy can cause the release of an electron. In the case of atomic hydrogen, the minimum photon energy required for ionisation is 13.6 eV, which corresponds to a wavelength of 91 nm, which is an order of magnitude smaller than the mid infra-red (IR) laser wavelengths used in this thesis.

It is possible, within short timescales of a few nanoseconds [80], for multiple photons to contribute to the excitation of an electron. Such a mechanism is known as multi-photon ionisation (MPI) and is enabled by the existence of short-lived virtual states [80, 81]. Photons that do not have the required energy to boost an electron to an excited state can instead excite the electron to a virtual state. The lifetime of the virtual state can be determined using the uncertainty principle and is given by

$$\Delta t = \frac{\hbar}{\Delta E} = \frac{\lambda_L}{2\pi c} \quad (2.17)$$

If the rate of arrival of photons, or intensity, is high enough for a second photon to be absorbed within this time frame the electron will be excited again, either to another virtual or real state. Otherwise the electron will decay to its original state. For the flux of photons to be high enough this ionisation mechanism is only feasible at intensities above 10^{12} Wcm^{-2} , for the photon wavelengths considered in this thesis (1053 nm). The ionisation rate is proportional to the laser intensity and is given by

$$W_{MPI}^n = \sigma_{MPI}^n I_L^n \quad (2.18)$$

where σ_{MPI}^n is the cross-section for multi-photon ionisation and n is the order of ionisation.

2.3.5 Barrier suppression ionisation

The above ionisation mechanisms rely on there being a fixed potential required to liberate an electron from the atom. However, this is not always the case. As the incident electric field strength, or laser intensity, increases, the potential well holding the electron is altered, as shown in Figures 2.2(c) and 2.2(d) [79, 82]. The Coulomb potential, $V(x)$, under the influence of an external field, E_{ext} , can be described as

$$V(x) = -\frac{Zq_e^2}{4\pi\epsilon_0x} + q_eE_{ext}x \quad (2.19)$$

where Z is the atomic number. The additional E_{ext} term represents the electric field of the laser light. It is possible for electrons to tunnel through the reduced suppressed barrier, in a process known as quantum tunnelling. The probability for this to occur is given by the Keldysh parameter, γ_K , which can be written in terms of the ionisation and ponderomotive potentials, I_p and ϕ_p [83, 84]:

$$\gamma_K = \left(\frac{I_p}{2\phi_p}\right)^{1/2} \quad (2.20)$$

For $\gamma_K \approx 1$, MPI and quantum tunneling will equally contribute to ionisation. Above one, MPI dominates and below, quantum tunnelling dominates.

As the laser field strength increases further, it is possible for the potential to be suppressed enough for the electron to spontaneously be freed. This is known as over the barrier (OTB) ionisation, which is shown in Figure 2.2(d). For this to occur, the barrier potential at $x_{max} = Ze/E$ (the barrier position in x), is equal to I_p . This gives an minimum required external field strength equal to $I_p^2/4Ze^3$, which corresponds to a laser intensity of

$$I_{app} = 4 \times 10^9 \left(\frac{I_p}{\text{eV}}\right)^4 Z^{-2} [\text{Wcm}^{-2}] \quad (2.21)$$

For atomic hydrogen, this gives a minimum laser intensity of $1.4 \times 10^{14} \text{ Wcm}^{-2}$ [38].

2.4 Plasma

In the previous section, the ionisation mechanisms that result in the creation of plasma are discussed. Here it is imperative to explain what the plasma state of matter is and some of its important characteristics. A plasma is a quasi-neutral ionised gas that exhibits collective behaviour. A fundamental parameter of plasma is the Debye length, λ_D , which is a measure of the electric field screening effects of a plasma, also known as Debye screening or shielding. It is defined as the distance over which a charge's field strength drops to $1/e$, where e is Euler's number, within a plasma and is given by

$$\lambda_D = \sqrt{\frac{\epsilon_0 k_B T_e}{q_e^2 n_e} + \sum z_i^2 T_i / n_i} \quad (2.22)$$

where ϵ_0 is the permittivity of free space, k_B is Boltzmann's constant, q_e is the charge of an electron, n_e and T_e are the density and temperature of the electrons, and z_i and n_i are the charges and densities of the ion species within the plasma. However, as the ion mass is considerably larger than the electron mass and therefore ion movement and reactions to field changes are far slower, the ion terms are typically discarded leaving

$$\lambda_D = \sqrt{\frac{\epsilon_0 k_B T_e}{n_e q_e^2}}. \quad (2.23)$$

Another important parameter is the plasma frequency, ω_p . It is the frequency of collective electron oscillation within a plasma. This oscillation occurs due to the displacement of electrons from the positively charged ions. The Coulomb force acts to pull the electrons toward the ions. However, they overshoot and oscillate about the ions. When disregarding ion motion the plasma frequency is given as

$$\omega_p = \sqrt{\frac{n_e q_e^2}{m_e \epsilon_0}}, \quad (2.24)$$

where m_e is the electron rest mass. To be defined as an ideal plasma, the plasma must fit three criteria:

- The size of the plasma, L , must be larger than Debye length in order for Debye screening to occur;
- The number of particles must be much larger than 1 within any Debye radius, for collective effects to occur;
- The plasma frequency, ω_p must be larger than collision frequency, ν_{CI} , so that collective behaviour will dominate over collisional behaviour.

2.4.1 Laser propagation in plasma

Once the laser pulse has ionised the solid target and generated a plasma, the laser can then interact and start to propagate through it, when the plasma is below a critical density. Plasmas, by definition, act to screen out external electric fields through collective screening effects. This affects the propagation of the laser pulse through the medium. To describe the propagation of an EM wave through a plasma medium it is appropriate to consider the dispersion relation.

2.4.2 Dispersion relation

To begin to understand the interaction between lasers and plasma one must consider the propagation of light through such a medium; specifically, one must look at the dispersion relation, which describes the relationship between the frequency and wavenumber of a wave that can propagate in a plasma. The dispersion relation for an unmagnetised plasma, in which c is the speed of light, and ω is the frequency of a plasma wave, is given by

$$\omega^2 = \omega_p^2 + c^2 k^2, \quad (2.25)$$

where ω_p represents a cut-off frequency below which the plasma wave is damped and cannot propagate. This also means that electromagnetic waves cannot propagate in a plasma where the laser frequency, ω_L , is smaller than ω_p . The plasma density at which the plasma frequency equals the laser frequency is known as the

critical density. The critical density is given by

$$n_c = \frac{\epsilon_0 m_e}{q_e^2} \omega_L^2 \quad (2.26)$$

where ω_L is the laser frequency. This equates to a critical density of

$$n_c = 1.1 \times 10^{21} \lambda_{\mu m}^{-2} [\text{cm}^{-3}] \quad (2.27)$$

where $\lambda_{\mu m}$ is the laser wavelength in microns. Densities above and below this critical density are known as overdense and underdense, respectively and the corresponding density contour is known as the critical surface.

The laser pulse is not completely reflected at this surface of critical density. For overdense plasmas the wavevector, k , becomes complex. Physically, this corresponds to an evanescent decay of the EM field into the plasma. This decay has a characteristic scale length known as the skin depth, l_s , and is given by

$$l_s = \frac{c}{\sqrt{\omega_p^2 - \omega_L^2}} \quad (2.28)$$

For cases where the plasma density is far higher than the critical, this tends toward $l_s = \frac{c}{\omega_p}$. Haines *et al.* [48] adapted the skin depth for relativistic intensities to be

$$l_s \approx \frac{c}{\omega'_p} \left(\frac{\omega_L}{\omega'_p} \right)^{2/3} a_0^{1/3} \quad (2.29)$$

where a_0 is the normalised vector potential. The plasma frequency also has a relativistic correction [85] in the form of

$$\omega_p'^2 = \frac{n_e q_e^2}{\epsilon_0 \gamma m_e} \quad (2.30)$$

At non-zero angles of incidence, the laser is reflected at a different density which is itself dependent on the angle of incidence, θ_i . The density at which the laser is reflected is determined by the refractive index of the medium, which for

a plasma is

$$\eta = \sqrt{1 - \frac{\omega_p^2}{\omega_L^2}} = \sqrt{1 - \frac{n_e}{n_c}} \quad (2.31)$$

The non-relativistic refractive index of plasma is related to its density, and as such the laser is reflected by the density ramp at the target front surface. At relativistic laser intensities, where the plasma density becomes $n'_c = \gamma n_c$, the refractive index becomes dependent on the laser intensity (as $\gamma = \sqrt{1 + a_0^2}$). Using Snell's law, the density at which the laser is reflected is

$$n_f = n_c \cos^2 \theta_i \quad (2.32)$$

Therefore, at non-zero angles of incidence the laser is reflected at densities lower than the critical density. This occurs where there is a density ramp in the plasma, as the laser pulse will refract.

2.4.3 Scale length

As the laser light begins to interact with, and ionise, the front of the target, the plasma starts to expand into the vacuum. This occurs typically during the rising edge of the laser pulse, a few picoseconds prior to the pulse [86]. This phenomenon, known as preplasma, typically has an exponential density profile of the form

$$n_e(z) = n_0 e^{(-zL_s^{-1})} \quad (2.33)$$

where L_s is known as the plasma scale length, n_0 is the target density, and z is the axis of plasma expansion. This parameter is given by

$$L_s^{-1} \sim \frac{1}{n_e} \frac{dn_e}{dz} \quad (2.34)$$

and is the length over which the density drops by $1/e$. As we have seen, ionisation of the target can occur at intensities as low as 10^{12} Wcm^{-2} . This means that not only can the rising edge of the pulse ionise the target, but so can any pre-pulses or pedestals that are intense enough [87]. This can have unwanted effects, such

as producing large quantities of preplasma which can inhibit the interaction.

2.4.4 Self focusing

In underdense sections of plasma, the ponderomotive force will eject electrons quicker from regions of higher intensity, which decreases the electron density within those regions. This causes an increase in refractive index along the laser axis, decreasing radially, which causes the plasma to act as a positive lens and can focus the laser pulse as it propagates. The minimum or critical power for self focusing to occur is given by

$$P_{crit} = 17.5 \left(\frac{\omega_L}{\omega_p} \right)^2 \text{ [GW]} \quad (2.35)$$

and is derived by considering the “cavitation”, or lowering, of the electron density along the laser propagation axis [88, 89].

2.5 Absorption of laser energy

In the previous section, the propagation of a laser pulse through plasma was discussed. Most importantly, the presence of a critical surface within the plasma of density n_c was described, beyond which the laser pulse cannot propagate and is reflected. The electromagnetic field evanescently decays beyond the critical surface. This behaviour is critical for the absorption of laser energy by overdense plasma.

The absorption of laser energy by a plasma is generally split into two types: collisional and collisionless. Collisional absorption mechanisms involve the collisions of electrons, whereas collisionless ones do not. It is important to note that each absorption mechanism is present for a particular set of laser parameters, although more than one absorption mechanism can prevail.

2.5.1 Collisional absorption

Collisional absorption, or inverse bremsstrahlung, is a process where electrons collide with ions after the electrons have been accelerated by the laser field. As a collisional process it relies on the mean free path of the electrons being low and the frequency of collisions being high [90]:

$$\nu_{CI} \propto \frac{n_e Z_i}{T_e^{3/2}}. \quad (2.36)$$

Therefore, as the electron temperature increases with laser intensity, this collisional mechanism becomes less dominant.

2.5.2 Collisionless absorption

There are three main collisionless absorption mechanisms: resonance absorption, vacuum or Brunel heating, and $j \times B$ heating. Each mechanism relies on the inability of the laser pulse to propagate past the critical surface of the plasma. This phenomenon allows the plasma electrons to carry laser energy into the target where they experience a weaker restoring force, in the region where the field evanescently decays. As such, the electrons do not return back to the underdense area in front of the critical surface. The three collisionless absorption mechanisms are depicted in Figures 2.3(b), 2.3(c), and 2.3(d), which shows an incident laser pulse with incidence angle, θ_i , being reflected from the exponential density ramp of an expanding target, an example profile of which is shown in Figure 2.3(a). For resonance absorption and vacuum heating, the plasma density ramp for which the mechanisms apply is very different, with vacuum heating requiring a much steeper increase in density than is shown in Figure 2.3(a).

For larger density scale-lengths ($L_s \gg \lambda_L$), the mechanism known as ‘Resonance Absorption’ is prevalent. In resonance absorption, electron plasma waves are resonantly excited at the critical surface and the laser energy becomes coupled to them. The breaking of the plasma waves then injects electrons into the target. For this to occur, the scale length of the front-surface plasma (the distance over

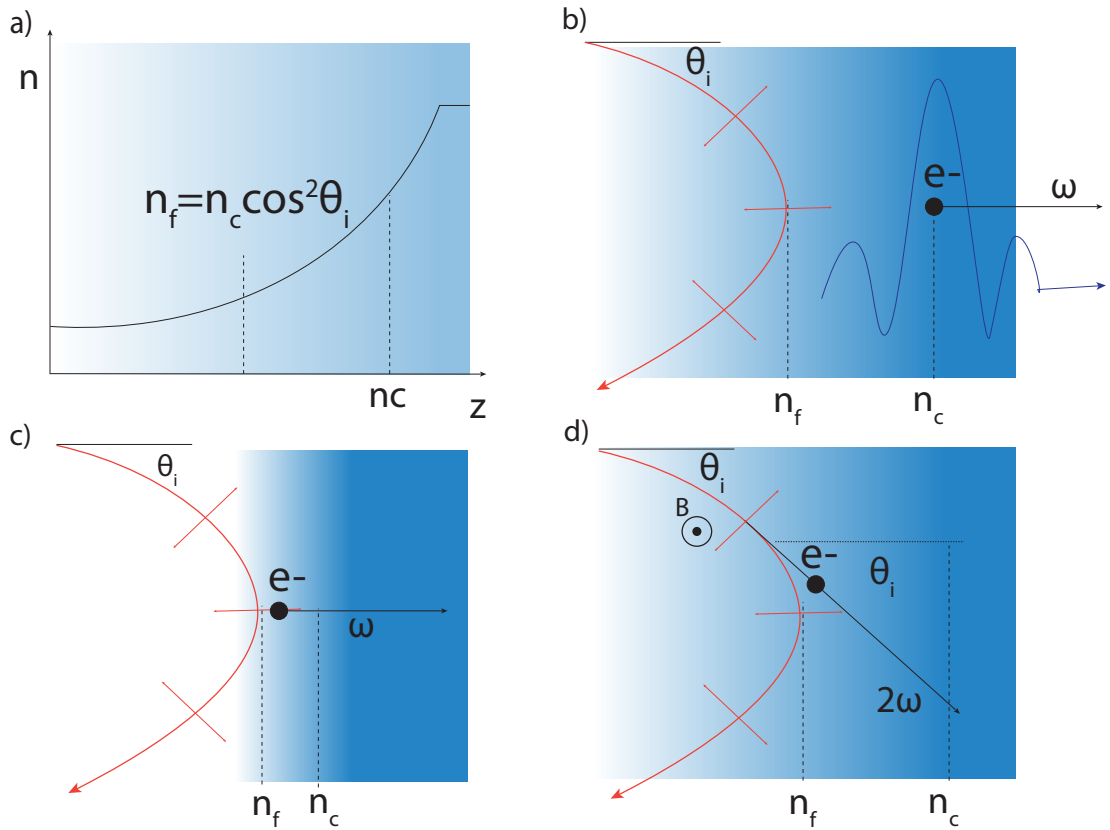


Figure 2.3: Illustrations depicting: (a), the exponential density ramp into the target, the point at which the laser is reflected, n_f , and the critical density surface, at n_c , and the three collisionless absorption mechanisms occurring in the density ramp (b), resonance absorption, (c), vacuum or Brunel heating, and (d), $j \times B$ heating. In each the laser, in red, can be seen reflecting from the surface with density n_f , with incidence angle θ_i , and with polarisation indicated by arrows.

which the density drops to $1/e$, must be larger than the laser wavelength. This is required so that plasma waves have the space to form in the laser field. The formation of a plasma wave within the preplasma is shown in Figure 2.3(b). The laser field extends to the critical density and electrons are resonantly excited at the critical surface. In Figure 2.3(b), the plasma wave that forms at the critical surface is represented by the dark blue wave. As this process relies on a plasma wave being driven by the laser light, at least some portion of the polarisation must be in the direction of the density gradient. The efficiency of this process is dependent on the laser angle of incidence and plasma scale length which both determine how far away from the critical surface the laser gets reflected at. Additionally, the efficiency is also dependent on the polarisation of the laser pulse.

Vacuum heating (Brunel heating, or not-so-resonant resonance absorption) is

where electrons are pushed past the critical surface by the laser's electromagnetic field [91]. Once the electrons pass the critical surface, where the laser field decays, they experience a weaker restoring force. This results in a net acceleration of electrons into the target. However, it only occurs in areas of high density gradient where the plasma density decreases steeply into the vacuum. The laser field at first drags the electrons into the vacuum before accelerating them back into the target, where they pass the critical surface. For this mechanism, the electrons are accelerated in the direction perpendicular to the critical surface, which is typically normal to the target. The direction of electron acceleration in this mechanism is shown in Figure 2.3(c), where it can also be seen that the density gradient is steeper than for resonance absorption, in Figure 2.3(b).

$\mathbf{j} \times \mathbf{B}$ heating is similar to the vacuum heating mechanism in that electrons are pushed past the the critical surface by the laser field, only to experience a weaker restoring field. However, at high laser intensities ($a_0 > 1$) where the $\vec{v} \times \vec{B}$ component of the Lorentz force becomes large, electrons experience another force in the laser propagation direction. As this motion is driven by the electron quiver motion, and therefore the field and electron motion both change sign twice per laser cycle, the electrons are accelerated into the target twice, at $2\omega_L$. Kruer and Estabrook [92] gives the ponderomotive force for linear polarisation as

$$f_p = -\frac{m_e}{4} \frac{\partial v_{quiver}^2(x)}{\partial x} (1 - \cos 2\omega_L t) \quad (2.37)$$

where the first and second terms represent the spatial variation in electron quiver velocity and twice-a-cycle acceleration of the electron along the laser axis, respectively, shown in Figure 2.3(d).

Vacuum heating and resonance absorption can accelerate electrons past the critical surface no more than once per laser oscillation cycle, due to the oscillation of the electric field. In $\mathbf{j} \times \mathbf{B}$ heating, the electrons are injected twice per cycle. Additionally, the centre of the accelerated electron distribution may point in different directions, depending on the mechanism, which allows the mechanisms to be identified experimentally where the laser incidence angle is non-zero.

2.6 Electron transport in solid targets

Now the mechanisms of electron acceleration by the laser pulse have been discussed, the transport of electrons through the target is considered. Each of the above absorption mechanisms launches a current of fast electrons into the target, typically in the mega-Ampere range. The Alfvén current limit dictates that beams current higher than I_a will induce magnetic fields large enough to filament electron beams [93]. Alfvén [93] gives this limit as

$$I_a = \frac{\beta\gamma m_e c^3}{q_e} \quad (2.38)$$

where β is the normalised particle speed v/c . For MeV energy electrons, as generated in laser solid interactions, this limit is in the order of 50 kA, which is far lower than the fast electron currents in laser-solid interactions, shown in Bell *et al.* [94] to be in the order of tens of MA. As such high currents are impossible without completely fragmenting the electron beam through the self-generation of magnetic fields, there is a mechanism to allow for charge neutrality. To preserve charge neutrality, the fast forward-going electron current pulls a cold electron current, with a higher number of electrons, through charge separation in the opposite direction. This results in a forward-going fast electron current, \vec{j}_{fast} , and a cold return current, \vec{j}_{cold} , such that

$$\vec{j}_{fast} + \vec{j}_{cold} \approx 0 \quad (2.39)$$

This allows the *net* current to be lower than the current limit, whilst maintaining high fast electron currents. The fast electron beam generates magnetic fields according to

$$\frac{\partial \vec{B}}{\partial t} = \eta_e \left(\nabla \times \vec{j}_{fast} \right) + \nabla \eta_e \times \vec{j}_{fast} \quad (2.40)$$

given by Maxwell's equations, where η_e is the plasma electrical resistivity and the higher order terms, for example those relating to magnetic diffusion, are negligible and are ignored. In plasmas, in the Spitzer regime, the resistivity inversely scales

with electron temperature ($\eta_e \propto k_B T_e^{-3/2}$) [51], so that the resistivity is higher in cooler regions within the target and will have a larger effect on the B -field rate of change. The right hand side terms in Equation 2.40 correspond to the opposing collimation and divergence of the electron beam. The first term represents the change in magnetic field due to spatial gradients in fast electron current, which generates a magnetic field to pinch the beam [51, 95]. Consequently, the pinching of the beam causes an increase in the current density, \vec{j}_{fast} , which can cause the beam to filament and become unstable [95]. The second term relates to the gradient in plasma resistivity which, in the Spitzer regime, increases radially from the centre of the beam due to the inverse relationship of resistivity to electron temperature, as electron heating is highest on-axis.

From this it is clear that the generation of magnetic fields within the target is complex and ever-evolving. It can be seen experimentally that the electron beam is overall divergent. However, there is no singular divergence of the electron beam as it is dynamic throughout the interaction [96].

2.6.1 Sheath Development

Initially, as electrons travel toward the rear of the target they are largely prevented from leaving the target as there is no longer material from which to draw a return current. The small population that does escape the target has a current that is below the Alfvén current limit. This results in a charge separation occurring as the electrons leave the target, leaving the target slightly net positive. This charge separation induces an electric field on the rear of the target, known as a sheath field. This field acts to deflect electrons back into the target (as do magnetic fields that are generated by the lack of return current in vacuum). It also acts to confine electrons within the target. Such electrons will be reflected by the field and will travel back into the target until they reach the front surface, where a similar sheath field will be set up. The electrons can be reflected back and forth between the front and rear target sheath fields, which can result in electrons making many passes of the target, in a mechanism known as electron refluxing or recirculation [97]. As the electrons recirculate to the front of the target, they

have the opportunity to interact again with the laser field, if the laser focus is wide enough and the pulse long enough [98]. Additionally, as the electrons make many passes of the target, they interact with more target material as a whole and lose more energy to x-ray production. Recirculating electrons tend to spread laterally as they recirculate, due to being injected with an angular spread into the target, and this can be seen in the emitted x-rays [99–102]. Ions and protons can be accelerated by a mechanism known as target normal sheath acceleration (TNSA), which was observed in high energy proton beams from the rear surface of targets [103, 104]. Ions and protons are accelerated normally from the rear surface by target sheath fields that develop [105]. Ions originating from the target rear surface are accelerated quickly over a few micrometers from the rear of the target [105]. Several factors can influence the efficiency and characteristics of TNSA. Laser parameters such as intensity, pulse duration, and focal spot size play crucial roles in determining the strength of the sheath field and the resulting particle acceleration [106–111]. Target properties, including material composition, thickness, and density gradients, also affect TNSA dynamics [112, 113]. Accelerated ions have been found to originate from contaminants on the target surface [114] as well as target constituent ions.

2.6.2 Electron populations and distributions

It can be useful to describe the distributions of electrons generated in laser-plasma interactions. There are a number of statistical distributions that can describe the energy spectrum of fast electrons. The three most common of which are the Boltzmann, Maxwell-Boltzmann (also known as Maxwellian), and Maxwell-Juttner distributions, each of which are shown in Figure 2.4 [115–118]. Both the Boltzmann and Maxwell-Boltzmann distributions are characterised by the electron temperature, which is defined as the average electron energy. The Maxwell-Boltzmann distribution is given as

$$f(E) = 2N_f \sqrt{E/\pi} (1/k_B T)^{\frac{3}{2}} e^{(-E/k_B T)} \quad (2.41)$$

where E is the electron energy and N_f is the total number fast electrons within the distribution. As the laser intensity increases and electron motion becomes relativistic, another expression is required to describe the spectral shape of the accelerated electrons as the electron mass is relativistically increased. Such a distribution is called the Maxwell-Juttner distribution and is given by

$$f(\gamma) = N_f \frac{\gamma^2 \beta}{\epsilon_T K_2(\epsilon_T)} e^{(-\gamma/\epsilon_T)} \quad (2.42)$$

where ϵ_T is the normalised temperature $k_B T/mc^2$ and $K_2(\epsilon_T)$ is a modified Bessel function of the second kind [118]. In this distribution, the gradient is given by the inverse of the normalised fast electron temperature, when considered in terms of γ .

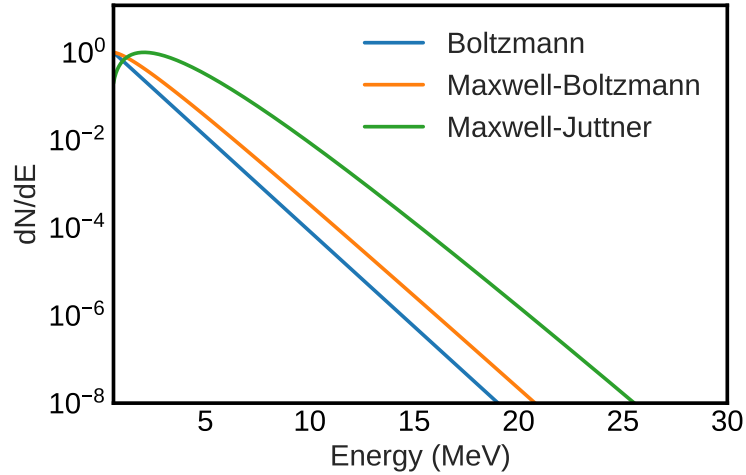


Figure 2.4: Electron energy spectra of temperature $k_B T = 1$ MeV with Boltzmann [115], Maxwell-Boltzmann [116, 117], and Maxwell-Juttner [118] distributions.

As electron temperature is a convenient way to describe the distribution of the fast electron population, there have been many studies to quantify the scalings of electron temperature with laser irradiance (equal to $I\lambda^2$). In Wilks [47] simulations of the interaction of ultraintense ($I\lambda^2 > 10^{18} \text{W}\mu\text{m}^2\text{cm}^{-2}$) short pulse lasers with solid-density plasma are reported. Through consideration of the electron energy gain through the ponderomotive potential the hot electron temperature is given by:

$$k_B T_e = \left[(1 + I\lambda_\mu^2 / 1.4 \times 10^{18})^{1/2} - 1 \right] \times 511 \text{ [keV]} \quad (2.43)$$

where $I\lambda_\mu^2$ is the irradiance with the laser wavelength in micrometers. This scaling can also be written in terms of a_0 :

$$k_B T_e = (1 + a_0^2)^{1/2} - 1 \text{ [keV]} \quad (2.44)$$

Beg *et al.* [54], reports an experiment to investigate electron temperatures for laser intensities up to 10^{19} Wcm^{-2} . Through the use of x-ray and ion diagnostics, a slower than expected scaling of electron temperature with intensity ($\propto (I\lambda^2)^{1/3}$) was reported [119–121]:

$$k_B T_e = 215 (I_{18} \lambda_{\mu\text{m}}^2)^{1/3} \text{ [keV]} \quad (2.45)$$

which can also be written in terms of a_0

$$k_B T_e \approx 0.47 a_0^{2/3} \text{ [keV]} \quad (2.46)$$

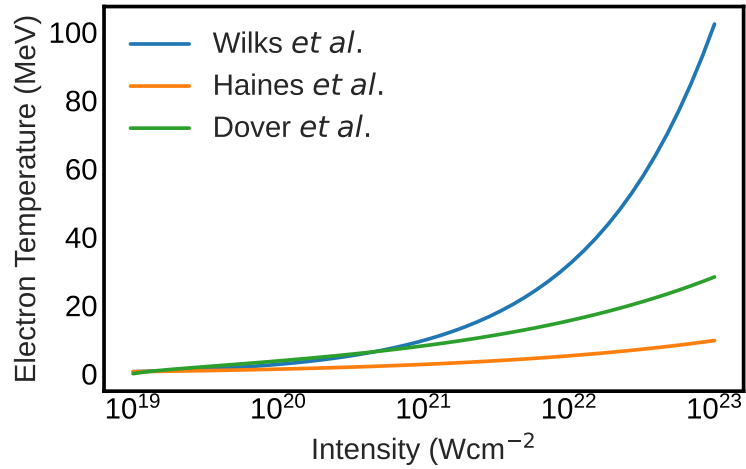


Figure 2.5: Electron temperature as a function of laser intensity for Wilks [47], Haines *et al.* [48], and Dover *et al.* [110] scalings. The temperatures given by the Dover *et al.* scaling are calculated for a near diffraction-limited spot size of $1.5 \mu\text{m}$ and laser wavelength of $1 \mu\text{m}$.

In Haines *et al.* [48], the discrepancy between the Wilks [47] and Beg *et al.* [54] scalings was reported, stating that the reason the electron temperatures were lower than those predicted by the ponderomotive scaling was that electrons were only experiencing a fraction of the pulse as, at high intensities, electrons were being accelerated well past the skin depth before experiencing even a quarter of a

wavelength. Therefore, the electrons were not experiencing anywhere near the full ponderomotive potential. A modification for the description of the collisionless skin depth for large amplitude EM waves was given:

$$l'_s \approx \frac{c}{\omega_p} \left(\frac{\omega_L}{\omega_p} \right)^{2/3} a_0^{1/3} \quad (2.47)$$

for $a_0 \gg 1$. In Haines *et al.* [48], it is noted that this explanation is only applicable for short scale length plasmas and that those with an extended preplasma region will allow the electrons to experience the full ponderomotive potential.

More recently, in Dover *et al.* [110], an experiment on the J-KAREN-P laser to investigate electron heating at intensities up to $5 \times 10^{21} \text{ Wcm}^{-2}$ is reported. By increasing the intensity through decreasing the laser focal spot size they were able to investigate the influence of tight focusing on electron heating. The Wilks [47] or ‘ponderomotive’ scaling of electron temperature, T_e , can be written in terms of the transverse electron momentum, p_y

$$T_e = m_e c^2 \left[\left(1 + \left(\frac{p_y}{m_e c} \right)^2 \right)^{1/2} - 1 \right] \quad (2.48)$$

where

$$p_y = a_0 m_e c \left[1 - \left(1 - \frac{w_0}{y_0} \right)^2 \right]^{1/2} \quad (2.49)$$

y_0 is the transverse acceleration distance, and w_0 is the focal spot full-width half-maximum (FWHM). It was found, through simulation, that for spot sizes smaller than the transverse acceleration distance, the transverse electron momentum would be limited. This in accordance with with the saturation in electron temperature seen experimentally with small spot sizes. At larger spot sizes, however, it was found that the electron temperature followed the ponderomotive scaling.

The work in this thesis considers the measurement of bremsstrahlung x-rays to determine electron temperature (Chapter 7) and as such, there will be detailed discussions of fast electron temperature, drawing on the physics presented in this

section. Much of the discussion in this work will focus on the presence of two distinct temperature components in both the electron and x-ray energy spectra, one of lower temperature and higher flux, and another of higher temperature with fewer particles. Additionally, in Chapters 5 and 6, there will be discussions of the behaviours of different electron populations with regards to the effects of spot size and pulse energy on bremsstrahlung and synchrotron emission, for which this is relevant.

2.6.3 Holeboring, plasma channelling and relativistically-induced transparency (RIT)

As the intensities in experimental laser facilities are increasing (up to intensities of $1 \times 10^{23} \text{ Wcm}^{-2}$), other laser-driven effects can take place. In each of the descriptions to follow, the laser is able to propagate further into the target than previously possible. The mechanisms discussed here are holeboring, plasma channelling, and relativistically-induced transparency (RIT).

As photons interact with, and are reflected by, the target, they impart momentum into the plasma. In Wilks *et al.* [122], the presence of radiation pressure induced boring into the target was shown. The light pressure, P_L , is given by

$$P_L = 2I/c \tag{2.50}$$

which is in the order of 100 Gbar for a $1 \times 10^{21} \text{ Wcm}^{-2}$ pulse [122, 123]. This assumes perfect reflectivity, R , of the target, i.e. $R=1$, which is not the case in reality as laser energy is absorbed by the target. This equation can be corrected for the reflection, absorption, A , and transmission, T by the target, where $R + A + T = 1$:

$$P_L = \frac{I}{c} (2R + A). \tag{2.51}$$

Transmitted light does not contribute to the radiation pressure on the surface, as the momentum is transferred through the surface. So, the contribution of transmitted light to the radiation pressure is zero and as such there is no T term

in Equation 2.51.

Due to the presence of radiation pressure, it is possible at high laser intensities for the laser to bore into a solid target, in a process known as ‘holeboring’.

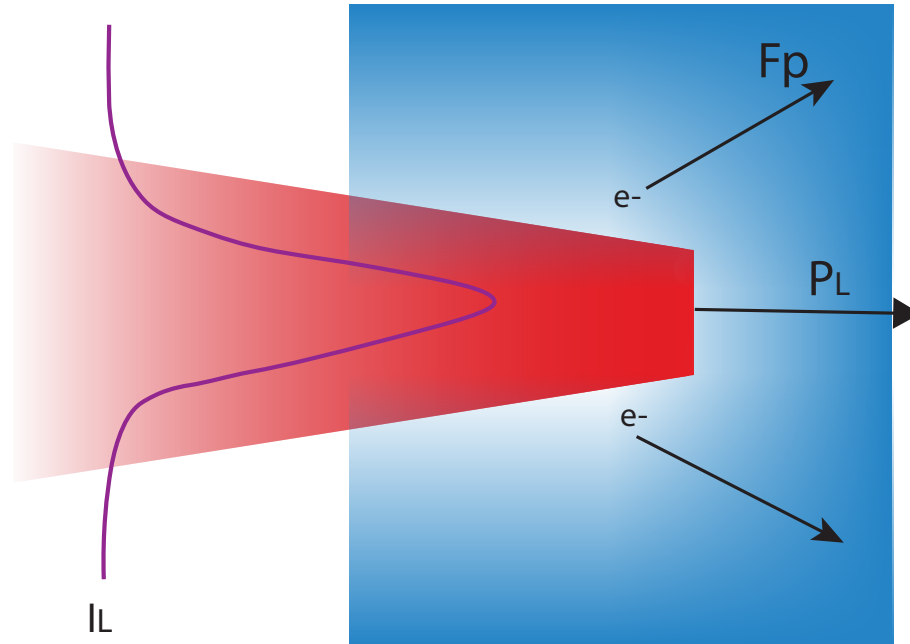


Figure 2.6: Illustration of a laser pulse propagating into a partially transparent target. Shown are the directions of the radially-acting ponderomotive force, F_p , and radiation pressure, P_L , which both act to eject electrons from the laser path. The purple Gaussian curve represents the radial intensity profile of the laser which is driving the radial ponderomotive potential.

Another phenomenon seen in underdense plasmas is driven by the ponderomotive ejection of electrons from the centre of the focal spot, due to the radial intensity gradient. This can cause a hole, or channel, to form within the target [124, 125]. Figure 2.6. shows an illustration of the radiation pressure and ponderomotive force incident on target electrons. Electrons are ejected from the most intense region of the laser by the ponderomotive force, F_P , which partially channels through the target. The laser then interacts with a critical surface and reflects, imparting the radiation pressure, P_L .

Finally, as electron motion becomes relativistic, the electron mass becomes relativistically increased ($m'_e = \gamma m_e$), and as such the critical density of the plasma is also increased ($n'_c = \gamma n_c$). As previously mentioned, the critical density surface tends to lie in an exponential ramp in density from vacuum towards the solid target. Because of this, more of the target is transparent to the laser, and

the laser can propagate further into the plasma. This is known as relativistically-induced transparency (RIT) [126]. There are two ways in which the electron density, n_e , can become lower than the relativistically-increased critical density n'_c : either n'_c increases due to higher laser intensities inducing relativistic electron motion and higher γ factors or a decrease in n_e due to thermal expansion of the target into the vacuum or from aforementioned ponderomotive expulsion of electrons from the laser focal region.

In Chapter 5, there is a discussion of the effects of holeboring and plasma channelling on bremsstrahlung and synchrotron production, specifically to compare the effects of laser intensity, spot size, and pulse energy on these mechanisms.

2.6.4 Conclusion

The fundamentals of laser-solid interactions are discussed, starting with a review of charged particle motion in electron magnetic fields and ending with laser-induced transparency of solid targets. The discussions in this chapter are by no means exhaustive, as the interactions between lasers and solids are complex and dependant on many variables. However, the key physics and mechanisms relevant to the investigations presented in Chapters 5, 6 and 7 are summarised to help the understanding of further discussions.

Chapter 3

X-ray production and interactions with matter

3.1 Introduction

In the previous chapter, the interaction between laser pulses and solid targets and the acceleration and transport of fast electrons is described. In this chapter the interaction of electrons with the target material is discussed. More specifically, the energy loss of electrons and the emission and absorption of x-rays is reported.

3.2 X-ray Production

An important aspect of electron acceleration in laser-solid interactions is the generation of radiation. This radiation is not limited to the x-ray energies presented here; photons in the THz and XUV spectral ranges can be produced and are their own fields of study [127–130]. However, the emission and detection of x-rays is at the core of this thesis and so this is the focus of this chapter.

The generation of x-rays by electrons is directly related to the acceleration, or deceleration, of electrons. As energy is lost by an electron, it is emitted as radiation, the power of which can be described by Larmor’s formula:

$$P = \frac{2}{3} \frac{q_e^2 a^2}{4\pi\epsilon_0 c^3} \quad (3.1)$$

where P is the power emitted by and a is the acceleration of the particle [131, 132]. A charged particle moving at constant speed has electric field lines that emerge radially from the particle, as shown in Figure 3.1(a). As the charged particle experiences acceleration, the field lines emerging radially from the particle can't keep up due to the limited speed of information transfer (the speed of light) and become discontinuous. The field lines bridge the gap, depicted by the red lines in Figure 3.1(b), between those emerging from the particle and those left behind resulting in a perpendicular component of the field of magnitude

$$E_{\perp} = \frac{q_e a \sin \theta}{rc^2} \quad (3.2)$$

where r is the radius about the particle, equal to ct , and correlates to the speed of information transfer (depicted by the innermost circle in Figure 3.1(b)), θ is the polar angle with respect to the instantaneous acceleration vector, \vec{a} , and q_e is the electron charge [132].

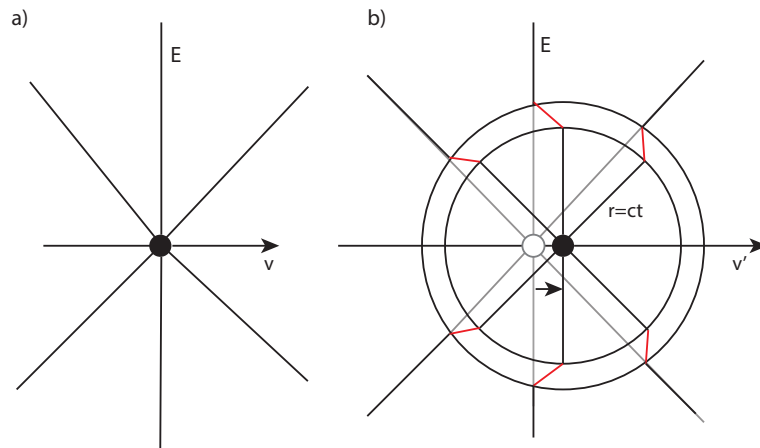


Figure 3.1: (a) Field lines of a charged particle travelling at constant speed and, (b), the discontinuous field lines of an accelerating particle, where the innermost circle has radius $r = ct$. The red lines represent the discontinuity in the electric field of the particle, caused by the acceleration of the particle.

3.2.1 Line emission

Line emission is the emission of an x-ray photon that occurs when electrons transition from a higher energy state to a lower energy state. Line emission tends to occur as a by-product of ionisation, wherein lower energy level, bound electrons

are liberated from their atoms. This leaves empty energy levels for higher energy bound electrons to decay into. These electrons lose energy in the form of x-ray photons in order to fill the lower energy shells. The frequency, f , of the emitted photon is given by the change in energy of the electron, ΔE , which is equal to the difference between the energy levels (here named E_1 and E_2). This can be described by the following:

$$hf = \Delta E = E_2 - E_1 \quad (3.3)$$

where h is Planck's constant. This mechanism is shown in Figure 3.2(a). A commonly used emission line in laser-solid interactions is the K- α line of copper, with an x-ray energy of 8.04 keV [133], due to the relative ease of the manufacture of copper targets (or the insertion of copper layers in targets), high K- α x-ray yield, and easy detection. In this transition an electron is liberated from the lowest energy shell (K shell) resulting in an L shell electron decaying into the lowest state.

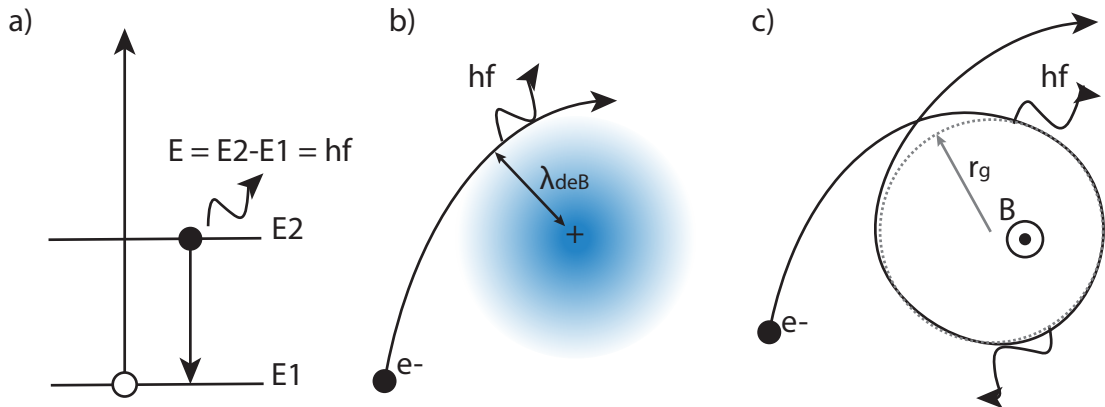


Figure 3.2: (a), Line emission, (b), bremsstrahlung emission, and (c), synchrotron emission, mechanisms. In (a), an electron is shown to be ionised from energy level E_1 so that the electron in E_2 can decay and produce line emission. (b) shows the acceleration of an electron in the field of a positive charge, indicated by the blue region, with the de Broglie wavelength, λ_{deB} , as the minimum interaction distance. The curved motion of an electron about magnetic field lines is seen in (c), with characteristic gyroradius, r_g .

3.2.2 Bremsstrahlung production

Bremsstrahlung, originating from the term ‘braking radiation’ in German, is the name given to the x-rays emitted by a charged particle that is accelerated in the field of an atomic nucleus. In laser-solid interactions, electrons generate bremsstrahlung as they pass through the ionised and solid portions of the target, generating a broad spectrum of x-rays that can extend into the tens of MeV [36, 134].

The acceleration of an electron, specifically in the vicinity of an ion, is given by Coulomb’s Law

$$F = \frac{z_i q_e^2}{4\pi\epsilon_0 m_e r^2} \quad (3.4)$$

where r is the distance between the electron and the ion and z_i is the atomic number of the ion. The minimum distance is called the ‘closest approach’ or impact factor, b , and corresponds to the position in which the electron feels the strongest force from the atom. This geometry is shown in Figure 3.2(b). From Larmor’s formula [131] (Eq. 3.1) and Equation 3.4, the power radiated by the electron is

$$P_e = \frac{q_e^2}{6\pi\epsilon_0 c^3} \left(\frac{z_i q_e^2}{4\pi\epsilon_0 m_e r^2} \right)^2 \quad (3.5)$$

By taking the electron spatial distribution to be uniform about the plasma ions, the total emission by the electrons surrounding the ion is [135]

$$P = \frac{8\pi z_i^2 q_e^6 n_e}{3(4\pi\epsilon_0)^3 m_e^2 c^3} \int_{r_{min}}^{\infty} \frac{dr}{d^2} = \frac{8\pi z_i^2 q_e^6 n_e}{3(4\pi\epsilon_0)^3 m_e^2 c^3 r_{min}} \quad (3.6)$$

As the above function diverges at $r = 0$, a lower limit is imposed. One can take the de Broglie wavelength, λ_{deB} , the distance below which an electron cannot be considered a classical particle, as the minimum interaction distance r_{min} . For a thermal electron, the de Broglie wavelength is given by

$$\lambda_{deB} \sim \frac{\hbar}{\sqrt{m_e k_B T_e}} \quad (3.7)$$

and thus the power is given by

$$P \simeq \frac{8\pi z_i^2 q_e^6 n_e}{3(4\pi\epsilon_0)^3 m_e c^3 \hbar} \left(\frac{k_B T_e}{m_e} \right)^{1/2}. \quad (3.8)$$

For an ion density of n_i , the total bremsstrahlung power radiated per unit volume of plasma is [135]

$$P \simeq \frac{8\pi}{3} \frac{z_i^2 q_e^6 n_e}{m_e c^3 \hbar} \left(\frac{q_e^2}{(4\pi\epsilon_0)^3} \right) \left(\frac{k_B T_e}{m_e} \right)^{1/2} = 5.34 \times 10^{-37} z_i^2 n_e n_i T_e^{1/2} [(\text{keV}) \text{Wm}^{-3}] \quad (3.9)$$

The power radiated is proportional to z_i^2 and the square root of the electron temperature, as well as to the electron and ion densities. Due to this, in laser-plasma interactions the total bremsstrahlung power is increased with the use of a higher- Z target and with higher electron temperatures although, in reality, as the electron temperature increases, more electrons will escape the target sheath fields and no longer contribute to bremsstrahlung emission. Additionally, as electrons approach energies in the order hundreds of keV to a few MeV, they become less collisional and tend to lose energy through radiative processes instead [40, 136].

The influence of electron temperature, as well as electron and ion densities, on bremsstrahlung emission are key to the arguments presented later in this thesis. The influence of electron temperature on x-ray emission is relevant to the results in Chapters 5, 6 and 7. The influence of holeboring, and hence ion and electron densities, on bremsstrahlung production is discussed in Chapter 5.

3.3 Synchrotron production

Synchrotron emission is the emission of x-rays by a charged particle that is subject to an acceleration perpendicular to its velocity. The momentum lost in the electron direction of motion is emitted in the form of an x-ray photon, shown in Figure 3.2(c). In laser-solid interactions, this can occur when electrons directly experience the influence of the laser magnetic field and rapidly change direction.

The following derivations can be found in [137], for an electron in the presence

of a uniform static magnetic field. The synchrotron motion of an electron in an oscillating EM field, such as a laser, is complex and as such this case is considered for simplicity. The equation of motion for an electron is

$$\frac{d}{dt}(\gamma m_e \vec{v}) = q_e (\vec{v} \times \vec{B}) \quad (3.10)$$

When considering the full form of the Lorentz factor, $\gamma = (1 - (\vec{v} \cdot \vec{v})/c^2)^{-1/2}$, the left hand side can be expanded to

$$m_e \frac{d}{dt}(\gamma \vec{v}) = m_e \gamma \frac{d\vec{v}}{dt} + m_e \gamma^3 \vec{v} \frac{\vec{v} \cdot \vec{a}}{c^2} \quad (3.11)$$

For a charged particle orbiting magnetic field lines the acceleration is always perpendicular to the particle velocity, and as such the final term in Equation 3.11. is equal to zero. This simplifies the equation of motion to

$$\gamma m_e \frac{d\vec{v}}{dt} = q_e (\vec{v} \times \vec{B}) \quad (3.12)$$

One can consider the parallel and perpendicular components, v_{\parallel} and v_{\perp} of the particle velocity such that the pitch angle, θ_p , is given by $\tan \theta_p = v_{\perp}/v_{\parallel}$. The pitch angle is the angle between the vectors \vec{v} and \vec{B} , which is the angle between the particle velocity and the magnetic field direction. v_{\parallel} is parallel to the magnetic field and is therefore unchanging as the magnetic field direction does not change. Considering only the component of motion perpendicular to the magnetic field the equation of motion becomes

$$\gamma m_e \frac{d\vec{v}}{dt} = q_e v_{\perp} |\vec{B}| (\vec{i}_v \times \vec{i}_B) = q_e |\vec{v}| |\vec{B}| \sin \theta_p (\vec{i}_v \times \vec{i}_B) \quad (3.13)$$

where \vec{i}_v and \vec{i}_B are unit vectors in the directions of \vec{v} and \vec{B} . Due to the $(\vec{i}_v \times \vec{i}_B)$ term, the acceleration is always perpendicular to the plane containing both the direction of magnetic field and the electron velocity. This acceleration drives circular motion around the magnetic field direction. By considering the equation for centripetal motion, one can equate the perpendicular velocity and radius of

motion, r_g , to

$$\frac{v_{\perp}^2}{r_g} = \frac{q_e |\vec{v}| |\vec{B}| \sin \theta_p}{\gamma m_e}, \quad (3.14)$$

giving

$$r_g = \frac{\gamma m_e |\vec{v}| \sin \theta_p}{q_e |\vec{B}|}. \quad (3.15)$$

We can see that the motion of an electron about static, uniform magnetic field lines is a spiral path with a constant velocity parallel to the magnetic field direction and constant pitch angle. In this motion, r_g is often referred to as the gyroradius. The frequency of the electron's orbit about the magnetic field is known as the angular cyclotron frequency or angular gyrofrequency and is given by

$$\omega_g = \frac{v_{\perp}}{r_g} = \frac{q_e |\vec{B}|}{\gamma m_e} \quad (3.16)$$

The corresponding gyrofrequency, ν_g , is equal to

$$\nu_g = \frac{\omega_g}{2\pi} = \frac{v_{\perp}}{r_g} = \frac{q_e |\vec{B}|}{2\pi \gamma m_e} \quad (3.17)$$

and is the number of revolutions about the magnetic field per unit time [137].

In the time-varying field case, one can consider a non-relativistic particle. In this case, the field strength or magnetic flux density, \vec{B} , varies slowly with time such that $\Delta B/B$ has minimal change within the orbital period of the charged particle, $T = \nu_g^{-1}$. We can consider this with a physical approach; a charged particle gyrating about a magnetic field is essentially a current loop. The current here, i , is given by the number of times the particle passes a point in the loop per second [137]:

$$i = q_e \frac{v_{\perp}}{2\pi r_g} \quad (3.18)$$

and the magnetic moment, $\mu = iA$, where $A = \pi r_g^2$ is the area of the loop is

$$\mu = \frac{q_e v_{\perp}}{2} r_g \quad (3.19)$$

In the non-relativistic case, $r_g = m_e v_\perp / q_e B$ and so

$$\mu = \frac{m_e v_\perp^2}{2B} = \frac{w_\perp}{B} \quad (3.20)$$

where w_\perp is the kinetic energy of the charged particle in the direction perpendicular to the guiding centre [137].

A small change in magnetic flux density, ΔB , can now be considered. Because of this, an electromotive force, ϵ , is induced within the loop and the charged particle is accelerated. The work done by this force is

$$q_e \epsilon = q_e \pi r_g^2 \frac{dB}{dt} = q_e \pi r_g^2 \frac{\Delta B}{\Delta T} \quad (3.21)$$

where $\Delta T = 2\pi r_g / v_\perp$ is the period of one orbit. The change in kinetic energy in one orbit is therefore [137]

$$\Delta w_\perp = \frac{q_e r_g v_\perp}{2} \Delta B = \frac{m_e v_\perp^2}{2B} \Delta B = \frac{w_\perp}{B} \Delta B \quad (3.22)$$

The corresponding change in the magnetic moment throughout the loop is

$$\Delta \mu = \Delta \frac{w_\perp}{B} = \frac{\Delta w_\perp}{B} - \frac{w_\perp}{B^2} \Delta B = \frac{\Delta w_\perp}{B} - \frac{\Delta w_\perp}{B} = 0 \quad (3.23)$$

This shows that the magnetic moment of the particle is invariant in a slowly varying field. It can also be shown that the particle's centre of orbit will enclose a constant magnetic flux and as such the particle will remain tied to magnetic field lines [137].

It can be shown that the synchrotron radiation spectrum peaks at a critical frequency, ν_{crit} , that is related to the gyrofrequency and pitch angle. This critical frequency is given by

$$\nu_{crit} = \frac{3}{2} \gamma^2 \nu_g \sin \theta_p \quad (3.24)$$

as the particle velocity approaches c . The spectral distribution for a power-law

distribution of electron energies is of the shape

$$J(\nu) \propto \nu^{-\alpha} \quad (3.25)$$

where α is the spectral index and is related to the slope of the electron energy spectrum, p , where $a = (p - 1)/2$ [132]. For a distribution in thermal equilibrium, this would be equal to the electron temperature, T_e .

3.3.1 Synchrotron emission in ultra-intense laser-solid interactions

Moving to higher intensity laser pulses (10^{21} Wcm⁻² upwards) increases the electromagnetic field strengths experienced by electrons in laser-plasma interactions. This can cause electrons to become more efficient in emitting synchrotron radiation [73]. The effect of such field strengths can be expressed by non-classical terms, such as the electron quantum parameter, χ_e , which is given by

$$\chi_e = \frac{\gamma}{E_S} \sqrt{\left(\vec{E}_\perp + \vec{v} \times \vec{B}\right)^2 + E_\parallel^2/\gamma^2} \quad (3.26)$$

where $E_S = 1.32 \times 10^{18}$ Vm⁻¹ is the Schwinger field, \vec{E}_\perp and E_\parallel are the electric field strengths perpendicular and parallel to the electron motion, and \vec{B} is the magnetic field [24, 25, 138]. χ_e can be maximised by counter propagating electrons into the laser pulse, along the propagation axis, \vec{k} [73].

There are three mechanisms that have been identified for synchrotron emission in laser-solid interactions. Each occurs in a different situation depending on the density and transparency of the target material. These mechanisms are ‘skin-depth emission’, ‘edge-glow’, and ‘reinjecting electron synchrotron emission’ (RESE) [28, 70, 139–141].

3.3.2 Skin-depth emission

In Ridgers *et al.* [28] and Brady *et al.* [70], synchrotron emission is reported in PIC simulations considering overdense targets. It was found that, as the laser

penetrates the target skin depth and is reflected, a standing wave is formed. The backwards travelling component of this standing wave interacts with the forwards-travelling electrons which are accelerated into the target due to the ponderomotive potential. As noted above, the counter propagation of electrons with a laser field (parallel to \vec{k}) maximises the electron quantum parameter and, as such, there is a burst of synchrotron emission. This emission is characterised by a cone of emission along the laser axis, consistent with the relativistically boosted angle $\phi_{boost} = \cos^{-1}(v_{HB}/c)$, where v_{HB} is the velocity of the hole-boring surface [28, 70]. The relativistically corrected hole-boring velocity, v_{HB} , is proportional to $\sqrt{I}/(1 + \sqrt{I})$ [142], and as such the angle of synchrotron emission is dependent on the laser intensity.

3.3.3 Edgeglow

Edgeglow emission occurs in targets where the laser ponderomotive potential has cleared a plasma channel. The electrons that have been ejected from the focal spot are then accelerated back into edges of the laser profile by space charge fields that form [140]. This mechanism is not as efficient as skin-depth emission as the electrons are interacting with the lower-intensity edges of the laser. As the electrons are introduced into the laser field along the edges of the plasma channel, the photons are emitted in forward-facing lobes. It is reported in Brady *et al.* [70] that this emission is only seen in simulations for intensities above 10^{24} Wcm^{-2} .

3.3.4 Reinjecting electron synchrotron emission (RESE)

Reinjecting electron synchrotron emission (RESE) occurs in relativistically underdense targets [139]. In this mechanism, electrons from the front of the laser pulse are rapidly accelerated back into the laser field by space charge fields that build up [70]. This results in electrons propagating back into the counter-propagating laser field and a broad backwards emission of gamma rays.

Synchrotron production will be discussed in Chapter 5, and hence the various

production mechanisms outlined above will be of relevance.

3.4 X-ray attenuation

When measuring x-rays experimentally, one must consider the attenuation of x-rays by the target material and anything else along the path of propagation, such as vacuum chamber walls or windows. Typically, the lowest energies are attenuated most strongly, which results in the lower-energy region (below a few 100 keV) of the x-ray spectrum to be diminished and dominated by strong emission lines, rather than the broadband spectra produced by the bremsstrahlung and synchrotron mechanisms. The attenuation of x-rays through a material is described by the Beer-Lambert law:

$$I = I_0 \exp(-\rho l \sigma) \quad (3.27)$$

where I and I_0 are the intensities of the x-ray signals before and after the transmission through the absorbing material, ρ is the mass density, l is the length of transmitting material, and σ is the attenuation cross-section, which is energy and material dependent [133]. There are three main attenuation mechanisms: photoelectric absorption or the photo-electric effect (PE), elastic and inelastic scattering or Thomson and Compton scattering, respectively, and pair-production.

The photoelectric effect (PE) occurs when x-rays interact with electrons that are bound in atoms. The electrons absorb incident x-rays, thus gaining their energy, and transition to a higher energy level. This effect is prominent for x-rays with energies below 100 keV. However, the extent of the mechanism's efficiency is governed by the Z of the material, as higher- Z materials typically have higher electron densities and therefore more electrons present to interact with the x-rays. The cross-section for PE is given by

$$\sigma_{PE} \propto Z^n E_\gamma^3 \quad (3.28)$$

where E_γ is the x-ray energy and n is a scaling factor dependent on the material

[143].

At higher x-ray energies, the electron can re-emit the x-ray at some angle. This can be either an elastic or an inelastic process, wherein either the x-ray maintains its energy (Thomson scattering) or is reduced (Compton Scattering). In Thomson scattering, the electron is excited by the electric field of the x-ray photon and an equal frequency photon is emitted at an angle dependent on the polarisation angle of the incident x-ray. The more prolific mechanism of the two, Compton scattering, involves the ionisation of the electron which carries away a portion of the x-ray energy. Due to the loss of energy to the momentum of the electron the x-ray wavelength becomes red-shifted. The difference in wavelength, given by $\lambda' - \lambda$ is

$$\lambda' - \lambda = \frac{h}{m_e c} (1 - \cos \theta) \quad (3.29)$$

where θ is the angle of scattering. The x-ray energy, E'_γ , becomes

$$E'_\gamma = \frac{E_\gamma}{1 + \left(\frac{E_\gamma}{m_e c^2}\right) (1 - \cos \theta)} \quad (3.30)$$

where E_γ is the initial energy of the photon.

Pair production (PP) is the conversion of an x-ray photon to an electron-positron pair in the presence of an electromagnetic field. This field is typically that of atomic nuclei within the target. Since the rest mass energy of both electrons and positrons is 511 keV, this effect occurs at x-ray energies above 1.022 MeV, twice the rest mass energy. There are many different formulae for the pair-production cross-section depending on whether there is atomic screening, large interaction angles and extreme-relativistic energies (amongst other things). However, most have a $\sigma_{PP} \propto Z^2$ relationship [144].

The most prevalent electron-positron pair production is the Breit-Wheeler process [27, 34]. In this process, an electron-positron pair is created due to the collision of two photons, in this case an x-ray photon and a laser photon: $\gamma + \gamma_L = e^+ + e^-$. The pair creation length, L_p , is given by

$$L_p = cP_b^{-1} \quad (3.31)$$

where P_p is the pair-creation probability rate. The maximum pair-creation probability rate is proportional to the square root of the laser intensity [27].

The total cross-sections for materials can be found in the NIST XCOM database [133]. The attenuation curves for tungsten, plotted as a function of incident photon energy, are shown in Figure 3.3. Understanding the attenuation of x-rays is vital to their detection, and is key to the understanding of the linear absorption spectrometer that is used for measurements in Chapters 6 and 7. It will be shown in Chapter 7 that the ‘flat’ attenuation cross section for x-ray energies between 1 to 10 MeV can be detrimental to the energy-resolved measurement of x-rays, which is problematic for laser-solid interactions in the 10^{21} Wcm $^{-2}$ intensity range.

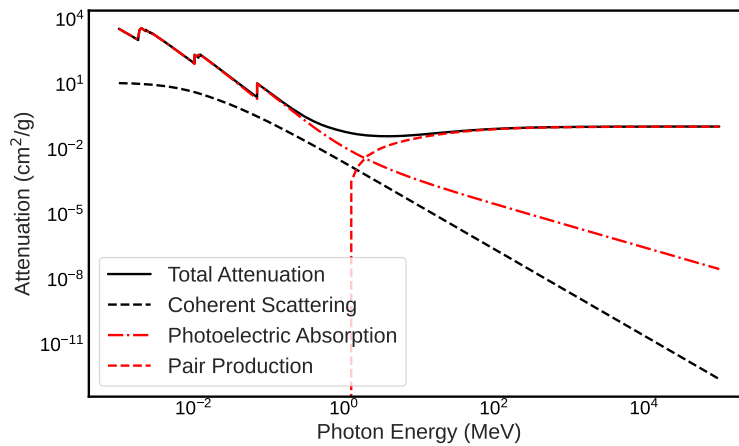


Figure 3.3: Attenuation cross-section for tungsten as a function of incident photon energy. The solid black line representing the total attenuation can be seen to be the sum of the cross sections of all the separate attenuation mechanisms: photoelectric Scattering, coherent or Compton scattering, and pair production.

3.5 Experimentally distinguishing synchrotron and bremsstrahlung radiation

In ultra-intense laser-plasma interactions, high-energy gamma-ray emission primarily arises from two mechanisms: synchrotron-like emission and bremsstrahlung radiation. These two processes differ significantly in their underlying physics, spectral characteristics, angular distributions, and dependence on target mate-

rial.

Synchrotron emission dominates at ultra-high intensities ($I \geq 10^{22} \text{ Wcm}^{-2}$), where electrons undergo rapid oscillations in the laser field [28, 70, 71, 145]. This leads to gamma-ray emission in a directional, beam-like structure. The angular distribution of synchrotron radiation is characterized by two prominent lobes with angles from the laser-propagation axis dependent on the holeboring velocity and therefore the laser intensity [70]. This feature, in skin-depth emission [28], can be attributed to the standing-wave field dynamics at the laser-plasma interface [28, 70], which governs the electron motion and enhances forward-directed radiation emission [71].

In contrast, bremsstrahlung emission results from the interaction of relativistic electrons with atomic nuclei in the target. As energetic electrons interact with and are decelerated by the atomic potential of high- Z nuclei, gamma-ray photons are emitted over a broad energy spectrum. Unlike synchrotron radiation, bremsstrahlung typically exhibits an isotropic angular distribution, with photon yield scaling as Z^2 , among other factors such as target density. This scaling implies that bremsstrahlung dominates in experiments using high- Z targets, particularly at moderate laser intensities, where electron-nucleus interactions are more frequent and the electron population is more collisional [71].

Experimentally, distinguishing between these two emission mechanisms relies on analyzing their distinct radiation signatures. One of the most feasible methods is angular distribution measurement. As mentioned previously, synchrotron radiation can be directional [70] and exhibit a characteristic lobe pattern. However, bremsstrahlung photons are emitted more isotropically. Their spectral characteristics provide little differentiation: both synchrotron emission and bremsstrahlung radiation are characterized by a continuous, quasi-exponential decay profile [71]. The choice of target material also plays a crucial role in modulating these emission mechanisms. While synchrotron emission is relatively independent of target composition it can be dependent on target density. However, bremsstrahlung is significantly enhanced in high- Z materials, making it dominant in thick, high-density targets [146]. This provides an experimental signature; measurements of

the radiation generation as a function of target material and thickness can be used to distinguish between the two emission mechanisms.

Another key experimental signature is the temporal evolution of the emitted radiation. Synchrotron radiation occurs on ultrafast timescales, closely correlated with the laser-electron interaction, whereas bremsstrahlung emission can persist for picoseconds as electrons undergo multiple scattering events and refluxing before losing energy completely [146]. Additionally, polarization measurements can provide further insight. Synchrotron photons are often linearly polarized due to their emission dynamics, whereas bremsstrahlung photons are typically unpolarized [147, 148]. High-energy gamma-ray polarimetry has been proposed as a method to distinguish between the two processes, as demonstrated in nonlinear Breit-Wheeler experiments [148].

Differentiating between synchrotron and bremsstrahlung emissions in ultra-intense laser-plasma experiments benefits from a combination of angular, spectral, material-dependent, temporal, and polarization diagnostics. By carefully selecting a range of target parameters and analyzing the emitted photon properties, it is possible to systematically identify the dominant emission mechanism, improving the understanding and optimization of laser-driven gamma-ray sources.

3.6 Summary

In summary, the three main x-ray production mechanisms in laser-plasma interactions are discussed: line emission, bremsstrahlung, and synchrotron, alongside the general theory of radiation by accelerating charged particles. Synchrotron emission mechanisms and their prevalence for different target densities are covered. Finally, the attenuation processes of x-rays are described, which are of importance to the x-ray spectrometer described in Chapter 4, which is used to make x-ray measurements presented in Chapters 6 and 7. The mechanisms of x-ray production will also guide the understanding of the results in Chapters 5, 6 and 7.

Chapter 4

Methodology

In the last two chapters, a broad description of the underpinning physics of laser-solid interactions was given, including the mechanisms that can produce secondary particles and radiation. In this chapter, the general methods used in the work presented in this thesis are covered. Chapter 7 focuses on the development of a new methodology related to the use of a linear absorption spectrometer for the detection of higher energy x-rays. Here, an overview of high-power, chirped pulse amplification (CPA), laser architecture, as well as the specifics of laser systems used are presented. Then, the suite of detectors used to diagnose laser-plasma interactions is introduced, including the details of diagnostic systems and detecting media, such as scintillators and imaging plate (IP). Finally, the modelling used to interpret the experimental data presented in this work is outlined.

4.1 Lasers

High-power, solid-state lasers have been used throughout the work in this thesis and, as such, it is important to give a summary of their architecture and operation, as well as the key parameters that are found to influence laser-solid interactions. In this chapter, the method of CPA will be described, which is key to attaining the high pulse energies and ultra-short pulse lengths used in this thesis. Chapters 5 and 6 focus on the effects of laser focal spot size and focusing geometry on electron acceleration and x-ray emission, so a detailed description of Gaussian

beam expansion and the dependence of spot size on focusing optic F -number is given.

4.1.1 Laser architecture

Solid-state lasers, like those used in this work, typically have an architecture that consists of an oscillator, pre-amplifier, pulse picking, and power amplifier, as well as the stretcher and compressor used in CPA.

The oscillator is a cavity containing a lasing or gain medium and features reflectors on either end. This gain medium is typically pumped either with flash lamps or lasers, which produces both stimulated and spontaneous emission within the gain medium. In order to generate pulsed light from the cavity, instead of continuous-wave (CW) emission, a method such as mode locking or Q -switching is used.

4.1.2 Mode locking

Mode locking is a technique that can generate ultra-fast pulse trains from an oscillator [149]. There are many different methods to achieve this which can be split into two categories: passive and active. A passive form of mode locking requires tuning the cavity length so that standing waves can be set up within the oscillator. Standing waves of many orders will then constructively and destructively interfere, resulting in a pulse train with a stable repetition rate. Another method employs the effect of Kerr lensing [150, 151]. Kerr lensing describes the phenomenon of intense light becoming focused due to the intensity dependent refractive index of the medium, which is ultimately related to the polarization and non-linear susceptibility of the chosen medium. This can be utilised within a laser cavity. As emission from the gain medium repeatedly bounces through the gain medium within the cavity it will increase in intensity. As the pulse intensity increases it is focused, through Kerr lensing, as it passes through and can then be emitted through a small aperture in the reflector on one side of the cavity. This means that only high intensity pulses are allowed to exit from the oscillator and

propagate towards the amplifier chain.

4.1.3 Q -switching

Q -switching is another technique to produce laser pulses from an oscillator that involves rapidly changing or switching the quality factor, Q , of the cavity [152, 153]. A high Q cavity will produce a large amount of stimulated emission, whereas a low Q cavity does not. One can take advantage of this to produce high energy pulses. The cavity Q is kept low whilst the gain medium is pumped, which increases the number of electrons in excited states within the material. Once the gain medium becomes saturated and enters a state within which no more electrons can be excited within the medium (known as population inversion), the cavity Q is then switched to be high so that the gain medium can then rapidly de-excite and produce a large amount of stimulated emission. Typically, in active Q -switching, the Q of the cavity can be switched by placing a variable attenuator within the cavity, which stops light emitted from the gain medium being reflected back into it. Passive Q -switching can be achieved using an intensity-dependent reflector such as a saturable absorber [154]. The transmission of such an optic decreases as the intensity of incident light reaches some threshold and as such the cavity is allowed to efficiently lase. This technique typically generates longer pulses and lower repetition rates than mode locking, due to the time it takes from the gain medium to reach population inversion and then effectively decay.

4.1.4 Amplification

There are two typical types of solid-state amplifier: regenerative and multi-pass. A regenerative amplifier can be used, which involves the pulse making several passes through the gain medium. Such an amplifier is used within the oscillator cavity in the PHELIX laser, which is used for the experiment presented in Chapter 6. An example regenerative amplifier is shown in Figure 4.1(a). An optical switch, typically consisting of an electro-optic modulator and polariser, can be used to control the number of round trips within the amplifier. The number of trips can

be very large and a large amount of energy can be gained from the amplifier. Another type of amplifier is a multi-pass amplifier, shown in Figure 4.1(b). In this regime, the beam takes multiple passes through the amplifier crystal before being directed out.

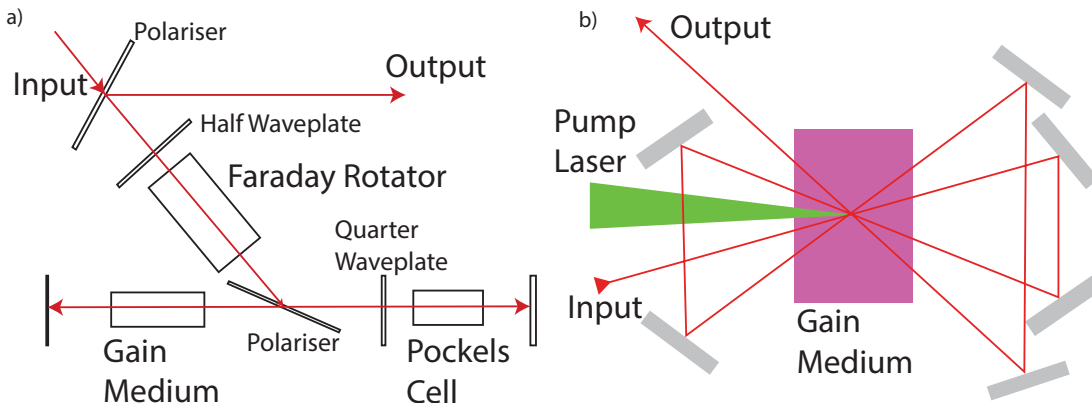


Figure 4.1: Illustrations of (a), a regenerative laser amplifier, and (b), a multi-pass amplifier.

4.1.5 Chirped pulse amplification

The pulses from the oscillator require amplification. High-power lasers require the pulse to be stretched, or chirped, in time to lower the incident intensity on optics. This has the benefit of achieving higher pulse energies without damaging optics within the laser chain. This process, known as CPA [2], requires the pulse to be stretched and compressed, typically by two sets of diffraction gratings, the process of which is shown in Figure 4.2. In Figure 4.2, a short, low energy pulse is shown passing through a set of gratings in order to temporally stretch the pulse. The stretched pulse is then amplified (signified by the dashed line) and is then compressed by another grating pair. The resulting pulse has a high pulse energy and a short pulse duration (in the order of 500-1000 fs for the Vulcan and PHELIX lasers). In order to reach the hundreds of Joules required for hundred-femtosecond petawatt lasers, amplification by optical parametric chirped pulse amplification (OPCPA) is required, and is used within the pre-amplifier sections of the Vulcan and PHELIX lasers. Alongside the CPA method, this uses optical parametric amplification (OPA) [155]. In OPA, a pump pulse and signal pulse interact within a non-linear medium to produce an idler pulse and amplified

signal pulse. The input pump and seed pulses of frequencies ω_{pump} and ω_{signal} are propagated into a non-linear crystal. The higher-frequency pump pulse is split into two photons, one of frequency equal to that of the signal pulse and another of lower frequency, ω_{idler} , which carries away the remaining energy. The original signal pulse is generated through optical parametric generation (OPG), wherein the pump pulse is converted by the non-linear medium into a signal and idler photon. The pulses at this stage typically have energies of mJ.

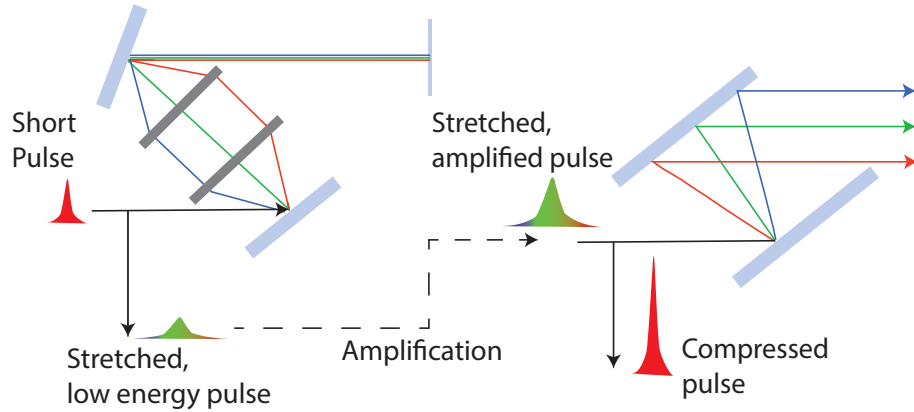


Figure 4.2: The stretching and compression stages of CPA, wherein a pulse is stretched and amplified before being compressed by a grating pair.

Once the pulse has been stretched and amplified, the pulse can be further amplified in the ‘main’ or ‘power’ amplifier. In the Vulcan and PHELIX lasers, this takes place within Nd:Glass amplifiers which are pumped using flash lamps. After this, the pulse needs to be compressed, which is typically done with a pair of diffraction gratings. The amplified and compressed pulse can then enter the interaction chamber, within which it is focused by a parabolic focusing optic (typically an off-axis parabola).

4.1.6 Laser parameters

The laser-plasma interaction physics explored in this thesis is sensitive to key laser parameters such as the energy, pulse duration, focal spot size, and, by extension, the laser intensity. In addition, other quantities such as the temporal intensity contrast and the wavefront quality play an important role in defining the dynamics of the interaction.

4.1.7 Focusing optics, spot size and encircled energy

In laser-solid experiments, the laser focal spot, given by the spatial-intensity profile of the pulse at focus, is critical. The size of the beam at focus influences not only the peak laser intensity, which itself has a significant effect on the interaction physics, but also has its own intensity independent effects, as reported in [98, 106, 110]. It is critical that the focal spot size and wavefront quality can be measured. This measurement is usually done on the beam at low power during alignment and optimisation of the OAP, using a camera and microscope objective, which is used to measure the size of the focal spot and the amount of energy contained within the area defined by the measured spot size, known as the encircled energy.

High-power laser beams are often focused down to micrometer-size focal spots in order to achieve the highest on-target intensities. Typically, a parabolic focusing optic is used to achieve this. An off-axis parabola (OAP) is used because the focus of the parabola does not overlap with the incoming beam and because reflecting parabolic optics avoid chromatic aberrations. The laser beam profile is spatially Gaussian in nature and thus focuses like a Gaussian beam. The focusing and expansion of a Gaussian beam can be described by several parameters: the beam waist, w_0 , the Rayleigh range or length, z_0 , the wavelength, λ , and the refractive index of the medium, η . Twice the beam waist, $2W_0$, is the beam diameter and describes the smallest beam cross-section. The beam waist is given by $W_0^2 = \lambda_L z_0 / \pi \eta$. The Rayleigh range or length is given as the distance from focus that the beam waist expands to $\sqrt{2}$ times the beam waist. At a distance of z along the propagation axis, the beam waist $W(z)$ is given by

$$W^2(z) = W_0^2 \left[1 + \left(\frac{z}{z_0} \right)^2 \right] \quad (4.1)$$

The size of focal spot achievable with an optic depends on the quality of the wavefront and the numerical aperture or F -number of the focusing optic. The divergence of the laser is often more usefully expressed in terms of the numerical aperture or the F -number or numerical aperture of the focusing system. The

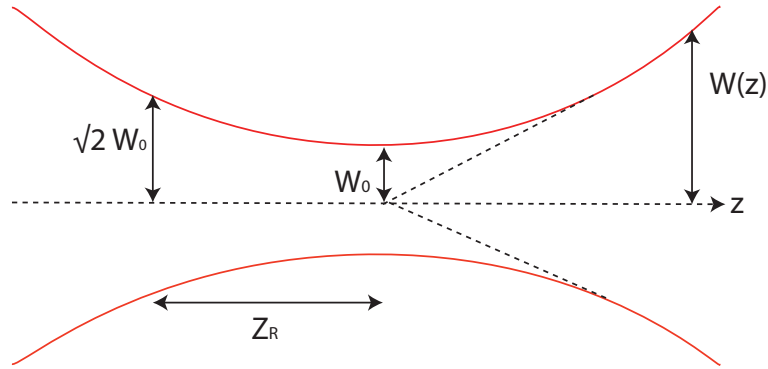


Figure 4.3: Schematic showing the geometry of focusing and expansion of a Gaussian beam as it propagates through focus.

F -number is given by $F/\# = f/D$, where f is the focal length of the optic and D is the beam diameter. In Chapter 6, the effective F -number of a focusing optic will be changed by reducing the beam size on the parabola. The beam radius is related to the F -number and is given by

$$2W_0 = 1.3 \frac{\lambda_L f}{D} = 1.3 \lambda_L F_{\#} \quad (4.2)$$

The size of a Gaussian beam is typically defined by finding the size at which the spatial intensity profile is at half its maximum (full-width half maximum or FWHM). The FWHM radius is approximately equal to $1.18W_0$. However, far from focus, if a beam is not perfectly Gaussian, the beam can appear to possess more of a flat-top profile, at which point the FWHM is not indicative of the beam size [156]. This is of particular prominence in the focal spots shown in Chapter 6, where many of the shots were taken with the target placed far from the beam focal plane. Instead, a method involving detecting the beam edges to directly compute the spot area was used, and is described in more detail in Chapter 6. The encircled energy for each spatial profile is found by calculating the amount of energy either inside the FWHM for a Gaussian-like beam or within the outer edge for a top-hat-like beam. For a Gaussian beam, encircled energies of 20-40% are typical, whereas, given the nature of the top-hat profile, the encircled energies tend towards 100% for largely defocused spots. Reductions in encircled energy, particularly for Gaussian-like spots, can occur due either to poor optimisation of, or damage to, the focusing optic, or from aberrations in the pulse wavefront,

which can arise from thermal effects.

4.1.8 Wavefront diagnostics and optimisation

In high-intensity systems with many stages of amplification, it is important to be able to compensate for wavefront distortions generated within the laser chain. It is critical to correct the wavefront when applying a tight focusing regime. This can be achieved by characterising and correcting for wavefront distortions.

Deviations from the ideal planar wavefront can arise anywhere within the laser chain. These aberrations are borne either from steady state or dynamic sources. Steady state sources include subtle misalignment of optics and optic surface imperfections, and are continually present within the laser chain. Dynamic sources change over time and can arise from either thermal or non-linear effects as the pulse propagates through the system. The most common aberrations caused are astigmatism, coma, tilt, and defocus, although higher-order aberrations are possible. The deviation of each aberration from the ideal planar wavefront can be described by the Zernike polynomials, Z_F [157, 158]. The sum of these polynomials can be used to describe highly complex wavefronts.

The defocus aberration is prevalent for high-pulse energy systems, including the Vulcan [159] and PHELIX [160] lasers used for measurements for the work reported in this thesis. This aberration is an unwanted curvature of the wavefront which can alter the divergence of the collimated beam. It can arise through a combination of both dynamic and steady state sources, which can make it difficult to compensate for. The defocus aberration causes a longitudinal displacement of the focal point along the laser propagation axis. A convex wavefront would displace the focal point further away from the nominal focus position. This offset, $\Delta\delta$, can be characterised using the Zernike coefficient, Z_F , laser wavelength, λ_L , and numerical aperture of the focusing optic, N_A using [158]

$$\Delta\delta = \frac{Z_F \cdot 4\lambda_L}{N_A^2} \quad (4.3)$$

Using this, the peak on-target intensity can be corrected, as the target is always

placed at the nominal focus position.

The Zernike coefficients can be measured experimentally using a Shack-Hartmann wavefront sensor [161, 162]. A Shack-Hartmann sensor consists of a CCD or CMOS chip (described later in Section 4.2.3), with an array of micro-lenses placed in front of the chip. This divides the incident beam into smaller beams, which are each focused onto the chip. If the wavefront of the incident beam is perfectly planar, each sub-beam will come to focus at the centre of the optical axis of each lens. However, if an aberrated wavefront is incident onto the lenses, the focal spots of each beam are offset, which results in a distorted grid of beams. The captured image can be used to reconstruct the wavefront of the incident beam, from which the Zernike coefficients can be calculated.

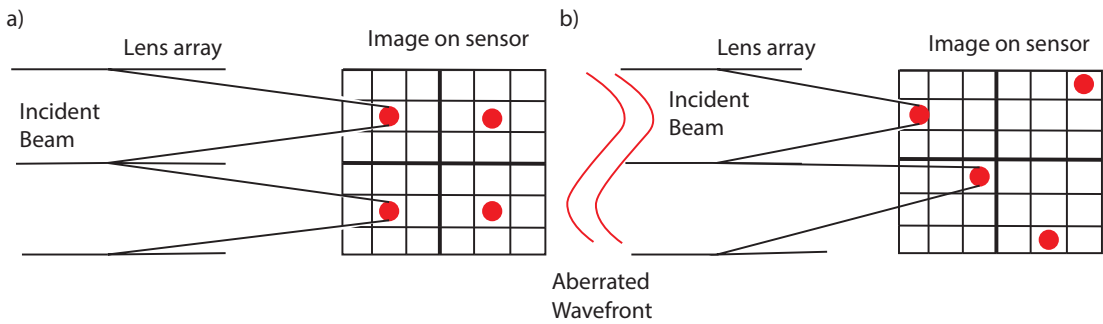


Figure 4.4: Schematic showing the basic principle of a Shack-Hartmann wavefront sensor. In (a), a perfectly planar wavefront is incident on the micro-lens array, which results in evenly spaced images of the separated beams on the sensor. Conversely, in (b), a deformed wavefront is incident on the micro-lens array, which results in a distorted grid of imaged beams on the sensor.

These sensors can often be found in adaptive optics (AO) systems, wherein the wavefront is measured before being corrected with a deformable optic.

4.1.9 Temporal intensity contrast

Laser pulses are often assumed to have a Gaussian temporal profile, with a pulse duration equal to the FWHM of the main pulse. This is typically not the case, with non-Gaussian features present, such as pulse pedestals and pre-pulses, in the temporal profile at much larger timescales than that of the main pulse. Such features can be present up to nanoseconds prior to the main pulse for nanosecond and picosecond pulses and can have a high enough intensity that they are able to

affect the interaction dynamics. A schematic of the intensity of a typical pulse as a function of time is shown in Figure 4.5. In this figure, the main laser pulse is preceded by a lower-intensity pedestal, pre-pulses, and a slow ramp up to the main pulse, typically caused by uncompensated dispersion. The low intensity pedestal is caused by amplified spontaneous emission (ASE), resulting from the amplification of spontaneous emission from the gain medium. This pedestal of ASE resides on the nanosecond scale around the main pulse. Pre- (or post-) pulses can be generated by back reflections within the laser chain or errors in pulse-picking. These pulses, arising from internal reflections within optics within the laser chain, typically have a duration similar to the main pulse or longer, due to the optic material dispersion. They can be minimised with the use of wedged optics, wherein the rear face of the optic is not parallel to the front face. This directs the reflections from the rear surface away from the main beam path. A post-pulse can become a pre-pulse under a number of conditions, either due to these pulses becoming delayed along long beam paths and interfering with ‘future’ pulses in the pulse chain or from interfering with the main chirped pulse and forming temporal modulation. This modulation can produce the pre-pulse after the compressor due to the B-integral in CPA [163]. Light preceding the main pulse can also be caused by uncompensated dispersion, which presents as a shallower rise in intensity of the main pulse. This can be caused by misaligned compressor optics or by other sources of dispersion and scattering [86].

With the prevalence of pre-pulses, ASE, and uncompensated dispersion, and the importance of these regarding the interaction, it is critical to define the quality of the pulse evolution in time. Such a parameter, known as temporal intensity contrast, describes the intensity of the laser pulse at a point in time prior to the main peak of the laser pulse. Measurements of temporal intensity contrast are normally taken at nanosecond and picosecond timescales before the peak of an ultrashort pulse and are quoted as a ratio of the measured intensity to that of the main pulse. This parameter is important as, for high-power lasers with many amplification stages, any emission prior to the main pulse can be intense enough to ionise a target. For the PHELIX laser, without improvements given by the

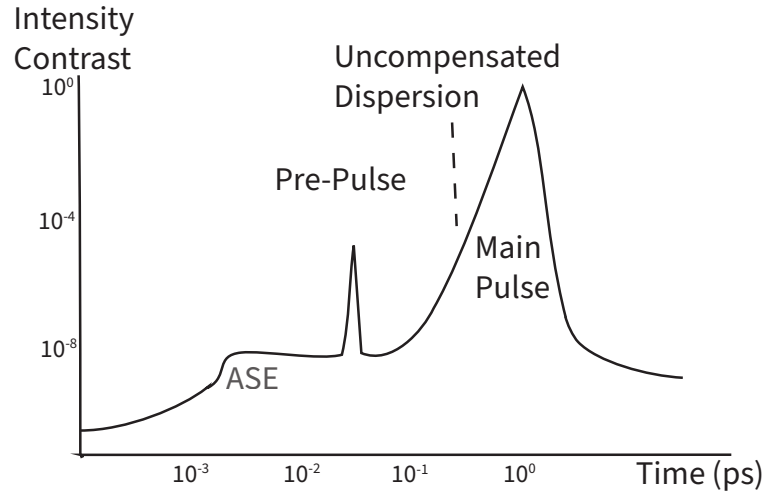


Figure 4.5: Schematic of the intensity as a function of time of a realistic laser pulse, featuring a pulse pedestal formed due to ASE, an example pre-pulse, and a shallow rise to the main pulse caused by uncompensated dispersion.

ultrafast optical parametric amplification (uOPA) technique (discussed later in Section 4.1.13), the temporal intensity contrast of the ASE is 10^{-6} which corresponds to an intensity of 10^{14} Wcm^{-2} , for a peak intensity of 10^{20} Wcm^{-2} [164]. Therefore, even the ASE is intense enough to cross the threshold for ionisation.

4.1.10 Plasma mirrors

Many of these temporal features cannot be fully removed within the laser chain and, as such, other *in situ* methods are required. A method of minimising the effect of pre-pulses and ASE on the interaction is to use a plasma mirror (PM) [38, 165, 166]. Plasma mirrors, usually made from anti-reflective coated glass, are transmissive until the incident light intensity is high enough to ionise its surface, producing an overdense plasma. The PM is set up such that this occurs within the rising edge of the main pulse. After this, the rest of the pulse is reflected from the plasma critical surface before propagating towards the target, a process which is shown in Figure 4.6. This has the effect of transmitting lower intensity ASE and pre-pulses before directing the main pulse to the target. The optic switches from transmissive to reflective on the sub-picosecond time scale [10], which reduces the possibility for instabilities to form in the PM plasma, which could otherwise distort the reflected beam. The downside of using a PM is that

a portion of the laser energy is absorbed by the plasma electrons within the PM, which can result in a decrease in interaction intensity of 15-30% when the PM is operating optimally.

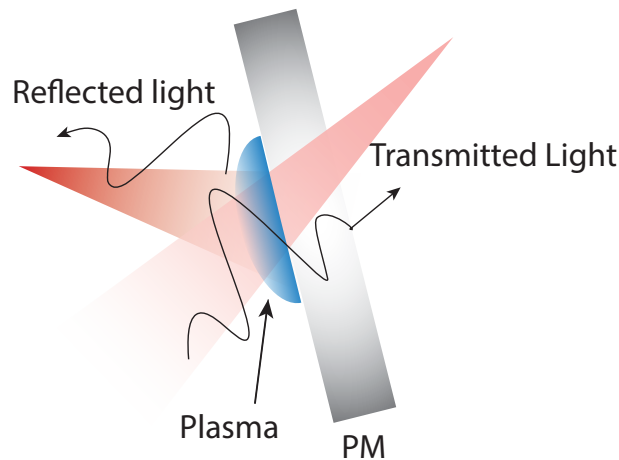


Figure 4.6: Illustration of the transmission and reflection of a plasma mirror. On the rising edge of the laser pulse the plasma mirror becomes reflective and the pulse is reflected.

Plasma mirrors, typically situated in the focusing beam, are slabs of anti-reflective (AR) glass that have been precision machined to a surface flatness of at least an eighth of the laser wavelength. The high surface flatness aids to prevent aberrations, and the AR coating (typically with a reflectivity of 0.25%) [167] prevents reflection of the laser pulse before the plasma mirror is ‘switched on’. The angle of the plasma mirror must be tuned to ensure maximum reflectivity once the mirror has been ionised, to ensure the highest possible intensity on-target [10]. Transmittance of the laser pulse before the PM is ionised can be maximised by positioning the PM at Brewster’s angle relative to the incident beam.

There are a few conditions that must be considered when using plasma mirrors: reduction in energy content of the pulse, plasma surface expansion, and potential degradation of the laser wavefront on reflection. The energy content of the beam after reflection from the PM can be lowered by around 20-30%, depending on the laser intensity, compared to the incident beam, which lowers the on-target intensity. The reduction in energy typically arises partly due to absorption of laser energy by plasma electrons within the PPM and partly due to transmission of part of the laser pulse. Additionally, as energy absorption by a plasma increases with incident laser intensity, peak specular reflectivity from

a PPM occurs at laser intensities of 10^{15} - 10^{16} Wcm^{-2} [10, 168]. Above these intensities, the plasma mirror switches on earlier in the interaction, which allows a greater amount of plasma expansion before the arrival of the peak of the pulse, and a greater degree of absorption as the absorption mechanisms become more efficient. This can act to decrease the specular plasma reflectivity and increase diffuse reflection as the plasma front expands and filaments [168]. Additionally, plasma processes, such as resonance absorption, become dominant at these intensities, which boosts the absorption of laser energy by the PM plasma electrons, leading to higher energy losses.

When using a PM, the beam should exhibit minimal degradation of the beam on reflection if triggered on sub-picosecond timescales. As previously mentioned, the surface of the glass is machined to precision flatness, however, the surface of the generated plasma also needs to remain as flat and as close to the surface of the glass as possible [10]. In order to achieve this, the ionisation of the PM must occur as close to the arrival (within a few picoseconds) of the main pulse as possible [168]. To ensure this, the plasma expansion must be smaller than the laser wavelength. This can be expressed as $c_s \Delta t < \lambda_L$, where c_s is the ion sound speed, Δt is the time of plasma formation before the main pulse, and λ_L is the laser wavelength. If this criterion is not met, the plasma expansion will be too large and the specular reflectivity will be reduced due to increased diffuse reflection. For a laser wavelength of $\approx 1 \mu\text{m}$, in the case of both the Vulcan and PHELIX lasers used for the work in this thesis, and an ion sound speed of $3 \times 10^5 \text{ ms}^{-1}$, the plasma must form less than 3.5 ps prior to the main pulse. This was verified experimentally and reported in Scott *et al.* [168].

With plasma mirrors, the effects of both ASE and pre-pulses can be suppressed [87, 169]. As such, for any work requiring high temporal intensity contrast, plasma mirrors are a useful tool. Plasma mirrors, both planar and focusing, are used for the work presented in Chapter 7.

4.1.11 Focusing Plasma Mirrors

In addition to planar plasma mirrors (PPMs), focusing plasma mirrors (FPMs) have been developed that can focus the pulse as well as provide temporal intensity contrast enhancement [170, 171]. In contrast to planar plasma mirrors, FPMs have a curved surface that generates a curved plasma, which acts to focus the reflected beam. Such optics can be used to enable tighter focusing than is achievable with permanent beamline optics, such as the F/3.1 focusing parabola in the Vulcan Petawatt laser, by providing lower F -number focusing. This is a relatively low cost method of increasing laser intensities on current systems without altering the existing, permanent beamline.

In Chapter 7, FPMs were used in the work to increase the maximum achievable intensity on the Vulcan Petawatt laser. These focusing plasma mirrors, developed by the McKenna group and reported in Wilson *et al.* [38, 166, 172], in addition to possessing the pulse-cleaning properties of a planar plasma mirror, are able to refocus the beam to a smaller spot than possible with the conventional focusing optic. The FPMs used in this work are ellipsoidally shaped, with two points of focus. The focus of the OAP is overlapped with the first focus of the plasma mirror and, upon reflection from the plasma surface, is refocused at a second focal point, with a demagnification of 2.51 times. This results in a $F/1.3$ focusing geometry and a near diffraction-limited spot size of $1.5 \mu\text{m}$ FWHM, which can result in an intensity enhancement of up to 3.6 times. This design was developed and characterised, as reported in [38, 166, 172], and is described in more detail in Chapter 7.

4.1.12 Vulcan Petawatt laser

The Vulcan facility (offline for upgrade in 2023), located at the Central Laser Facility in Oxfordshire, hosted two functioning target areas: Target Area West which offered up to 8 nanosecond-pulsed beam lines, and Target Area Petawatt, which provided a 500 fs petawatt-power beam and long-pulse nanosecond beam [173]. For the work presented within this thesis, only Target Area Petawatt was

used and, as such, the parameters discussed from now on will be those of the Petawatt arm of the facility. An experimental campaign at the Vulcan Petawatt facility was used to obtain results for Chapter 7 of this thesis. The layout of the Vulcan facility is shown in Figure 4.7 alongside photos of some of the disk amplifiers, in subset (a), and part of the compressor vacuum chamber in subset (b). The main laser chain and the Petawatt target area are highlighted in blue and red, respectively.

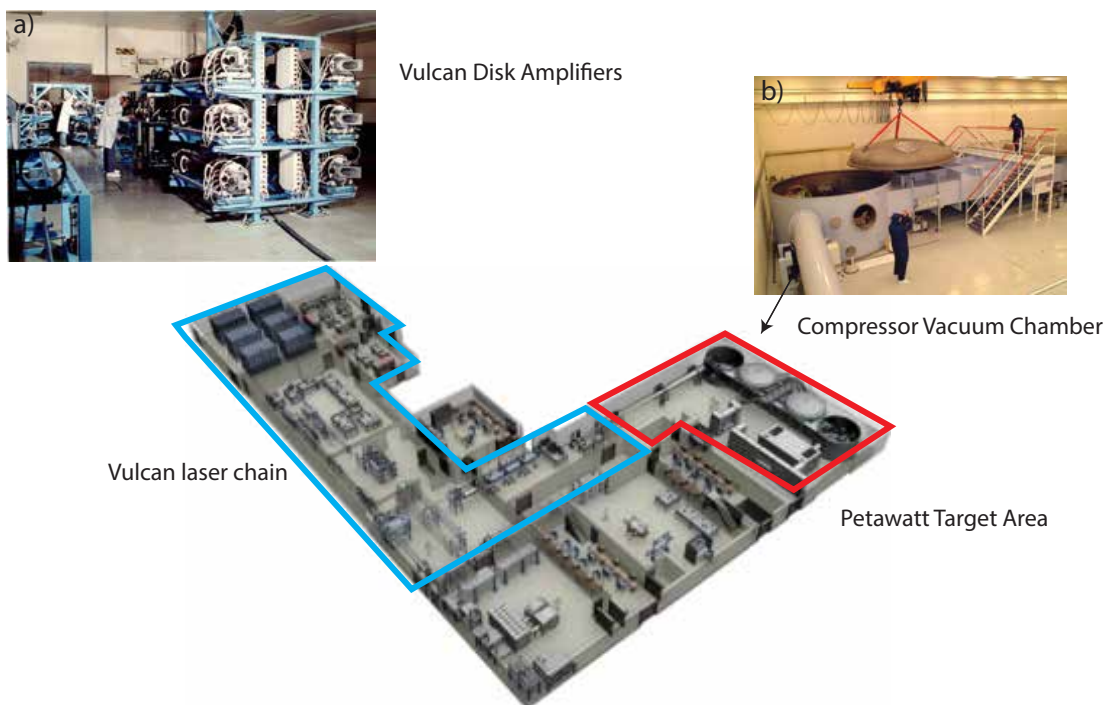


Figure 4.7: Schematic of the layout of the full Vulcan facility, taken from [174]. Subset (a) is a photograph of some of the disk amplifiers [175], and subset (b) is an image of part of the compressor vacuum chamber [176].

The front end of the Vulcan laser features OPCPA and an adaptive optics (AO) system to generate high intensity pulses [174]. The seed pulse of the Vulcan laser is produced using a commercial Ti-Sapphire oscillator. This oscillator is mode locked and the seed, typically 200 fs in duration and with a few nanojoules of energy, is selected from a train of pulses that have a central wavelength of 1053 nm. The first phase of OPCPA then occurs: the pulse is stretched to a duration on the order of a nanosecond using an Offner Triplet diffraction grating system, which consists of two holographic diffraction gratings and concentric mirrors of concave and convex geometry [173, 177, 178]. A linear chirp is applied across the

bandwidth, whilst spectral aberrations are minimised. The pulse is then amplified to a few millijoules using OPA within a non-linear crystal. From there the pulse is propagated through the main amplifier chain, composed of a set of rod and disk amplifiers, comprising doped neodymium glass. Phosphate and silicate are both used as dopants in order to avoid bandwidth narrowing of the pulse, as a narrower bandwidth would result in a longer pulse duration due to the time-bandwidth product. These amplifiers are pumped using broadband flash lamps. The adaptive optics system, consisting of a deformable mirror and wavefront sensor in a feedback loop, is used to improve the quality of the wavefront and allows for optimal compression of the pulse and focusing of the beam in the target chamber. The spatial quality of the beam is improved using a series of filters and an adaptive optic (AO) system, which lies within the final stages of amplification. In the AO system, a deformable mirror is used in conjunction with a Shack-Hartmann wavefront sensor to correct for astigmatism or lensing effects. After final amplification in the disk amplifier stage, the central wavelength of the pulse is 1053 nm and the pre-compressor pulse energy is around 600 J [177]. The pre-compressor energy measurement is taken from a leak in a turning mirror within the compressor and is characterised using a calibrated calorimeter. The throughput of the compressor is approximately 60%, which results in pulses of a maximum energy of 360 J entering the interaction chamber. When utilising plasma mirrors, as was the case for the work presented in Chapter 7, the energy on-target is further reduced (by 20-30%).

Within the target area the pulse is compressed, using a pair of diffraction gratings. The pulse duration, characterised using a second-order single-shot autocorrelator [174, 177], reaches around 500 fs before being directed into the target chamber. Within the target chamber is a 620 mm diameter F/3.1 off-axis parabola (OAP) which focuses the beam to a spot of around 5 μm FWHM, with an encircled energy of around 30-40% [179].

The temporal intensity contrast ratio has been measured to be approximately 10^{-10} at 500 ps, and 10^{-5} at 10 ps prior to the main pulse [180–182]. At the high intensities that the Vulcan laser is capable of (in the higher range of 10^{20} Wcm^{-2})

this correlates to intensities of 10^{15} Wcm⁻², 10 ps before the main pulse. This intensity sufficient to ionise a target, which is why plasma mirrors were used in the experimental campaign reported in Chapter 7.

Whilst steady state aberrations can be corrected for by the AO system, it can be much harder to correct for dynamic aberrations as these can change between the corrective action from the AO system and the pulse being delivered. Such aberrations are often caused by temperature-induced refractive index changes within the amplifier crystals, an issue that is intrinsic to systems generating high pulse energies. Measurements of the defocus aberration for the Vulcan Petawatt laser are reported in Frazer *et al.* [179], and were found to increase by around $1\lambda_L$ over a timespan of 15 minutes, before relaxing to the initial value after an hour, after thermal recovery had taken place. It was also found that the defocus measurement exhibited oscillatory behaviour, which was attributed to a 2 °C temperature fluctuation in the laser laboratory. This knowledge was used in order to better pre-compensate for the dynamic on-shot defocus aberrations.

4.1.13 PHELIX laser

The PHELIX laser is located at the GSI Laboratory near Darmstadt in Germany and was used to obtain the experimental results presented in Chapter 6. The PHELIX facility provides either a short or long pulse frontend on either femtosecond or nanosecond scales [183, 184]. The short pulse front end, seeded by a commercial laser oscillator, was used in the experimental reported in Chapter 6. An illustration of the facility, shown in Figure 4.8, shows the laser chain, compressor, and petawatt interaction chamber, which are all situated within the same laboratory.

The PHELIX laser is similar to Vulcan Petawatt and is also a Nd:Glass based system, operating at a wavelength of 1053 nm. The seed oscillator provides pulses of 20-30 mJ at a 10 Hz repetition rate which are stretched temporally before entering the pre-amplification phase. The PHELIX laser features an adaptive optic system within the pre-amplifier phase, which also contains flash-lamp pumped, double-pass neodymium amplifiers. The wavefront sensor for the AO system is

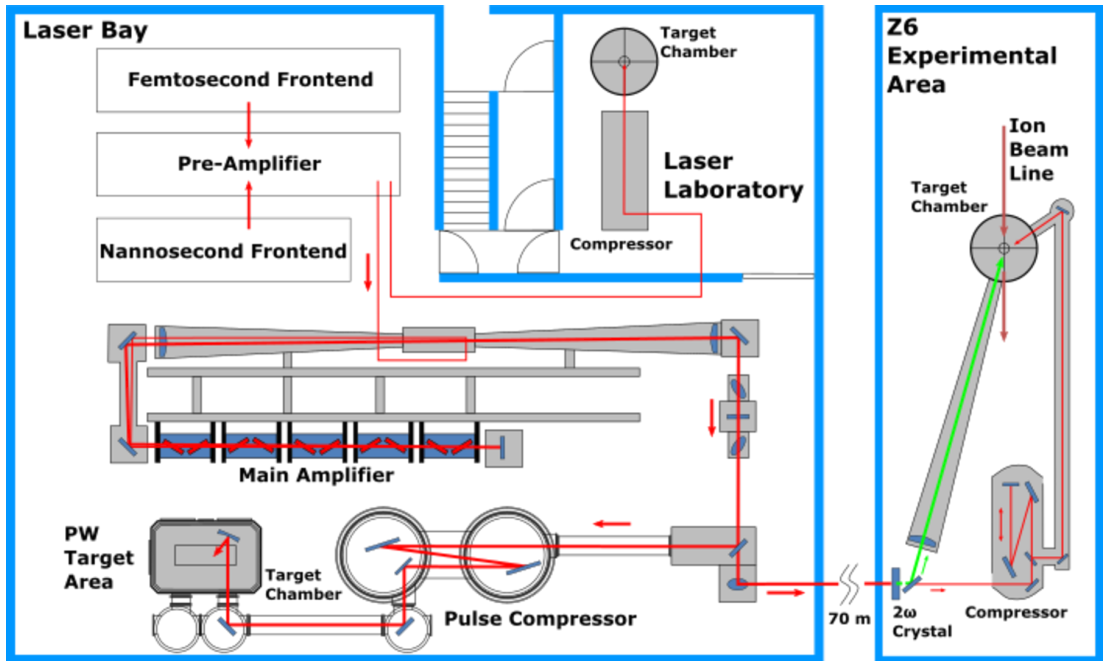


Figure 4.8: Schematic of the PHELIX front end, compressor chamber, and interaction chamber within the PHELIX laser laboratory [185].

situated after the main amplifiers and can therefore pre-compensate for aberrations introduced in the main amplifier. The main amplifier consists of five flash lamp-pumped neodymium-glass cassettes through which the pulse passes through twice. At this point the maximum pulse energy is 250 J. The pulse is then compressed by two single pass diffraction gratings to achieve powers of up to 500 TW with a minimum pulse length of 700 fs. The beam is then focused within the target chamber using an $F/1.7$ OAP to a minimum spot size of a few micrometers ($4\mu\text{m}$ FWHM), with post-compressor energies of around 100 J.

An ultrafast optical parametric amplification (uOPA) system is used to tune the pulse contrast of the PHELIX laser by increasing the signal of the main pulse above the ASE [164]. The temporal intensity contrast of the ASE is decreased to just below 10^{-10} for time periods above 100 ps prior to the main pulse. This method, however, also acts to amplify the prepulses, which are present at 300 and 200 ps prior to the pulse, with maximum temporal contrast ratios of 8×10^{-8} . The nanosecond contrast is estimated to be 10^{-12} [184]. A third-order single-shot autocorrelator is used to measure the temporal intensity contrast and the pulse duration [164, 186].

4.2 Detectors

This section will discuss the methods employed within this thesis to detect radiation arising from laser-solid interactions. The media of imaging plates and scintillators are described in detail, as well as the mechanisms used in CMOS and CCD detectors. The diagnostic techniques used in this thesis that utilise these detecting media are described later, in Section 4.3.

4.2.1 Image plate

Imaging plate (IP) was used within this thesis to detect electron and x-ray emission from the interaction. IP is most commonly used in medical imaging, specifically for the detection of x-rays. It is, however, sensitive to all forms of ionising radiation, including electrons and ions. It is therefore used in a variety of laser plasma diagnostics, including electron spectrometers and Cu K- α x-ray detectors, which are used for measurements reported within this thesis.

Imaging plate is a medium within which the energy from incident radiation is ‘stored’ by electrons which are excited into a metastable state. The long duration of this state, compared to short-lived phosphorescence, is important as it allows the signal to be kept for relatively long periods of time before the signal can be scanned and retrieved. The benefit of IP is its high dynamic range and extensive characterisation for multiple types of input radiation, including protons, electrons, and x-rays [187–189]. There are a few different types of IP (BAS-MS, BAS-SR, BAS-TR) that have differing compositions however, most contain an active layer (typically a BaF compound) laid between a protective CH layer and dark, magnetic backing, shown in Figure 4.9(a). The IP used for data collection in this thesis, most prominently in the electron spectrometer (Chapter 6), is predominantly BAS-TR, which does not feature a protective layer. This has the advantage of offering higher sensitivity to lower energy radiation due to the decreased attenuation before the detecting medium.

When IP is subjected to radiation, energy is deposited into the active medium which excites electrons into a metastable state. The signal from the IP can then

be retrieved by exposing the IP to a red laser which induces photo-stimulated luminescence (PSL), shown in Figure 4.9(b). This de-excites the electrons which emit photons that can then be detected. This process takes place in an IP scanner, wherein a 632 nm laser is scanned across the IP. The 390 nm PSL photons are then detected through a combination of photomultiplier tubes (PMTs) and amplifiers. The location and intensity of the emitted photons, detected by the PMTs as they are scanned across the IP, can then be used to generate an image of the incident radiation. This readout process removes from 60-90% of the stored signal, depending on the scanner [190]. The PSL signal is then converted to a digital image which indirectly represents the signal on the IP. The relationship between the photo-stimulated luminescence emission (PSL) and the signal on the IP, IP_{raw} , is given by

$$PSL = \left(\frac{Res^2}{100} \right) \left(\frac{4000}{S} \right) 10^{(L \frac{IP_{raw}}{2^{G-1}} - 0.5)} \quad (4.4)$$

where PSL is the intensity of the PSL emission, Res is the scanner resolution, S is the scanner sensitivity, L is the scanner latitude, and G is the scanner bit depth.

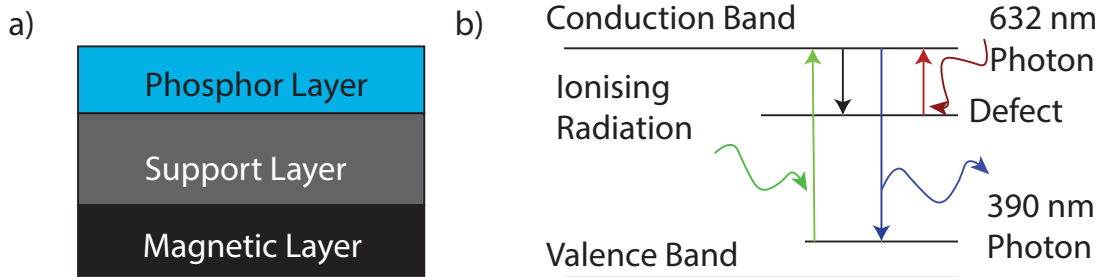


Figure 4.9: (a): schematic of the composition of BAS_TR image plate and, (b), a schematic showing the transition of electrons within metastable states when IP is subject to ionising radiation and laser light which stimulates PSL.

To process the signals from the imaging plate data, the image plate must be scanned until the charge-coupled device (CCD) within the scanner is no longer saturated by the PSL emission. By performing a calibration on the scanner to predict the signal loss on each scan, the original signal, $S(1)$, from the IP can be calculated. This formula has the form $S(1) = S(N)e^{-A(R_{\#}-1)}$ where $S(N)$

is the unsaturated signal, A is the rescan coefficient and $R_{\#}$ is the number of rescans required to retrieve an unsaturated signal. From this, the signal can be converted to the number of particles incident on the IP, depending on the particle and energy dependent sensitivity of the IP. Measurements of IP response to x-ray photons and electrons can be found in [187–189].

4.2.2 Scintillators

Scintillators are materials that are able to convert the energy from incident radiation into more readily detectable optical photons. Unlike IP, scintillators do not require a scanning phase to retrieve the data as, typically, the scintillation states are short-lived, and can therefore be used in ‘online’ diagnostics. This is beneficial as high-power lasers tend towards higher repetition-rates. Scintillators are typically split into two types: organic and inorganic [191]. In organic scintillators, it is the transition of electrons between internal energy levels that causes the emission of optical photons. Incident radiation excites electrons in higher energy states which then decay either directly in a process known as fluorescence, or through a longer-lifetime path through a triplet state, which is the process of scintillation. In inorganic scintillators, electrons are instead freed from their parent atoms and will go on to excite more electrons through collisions. These free electrons will eventually decay through an intermediary energy level, present because of impurities in the material, emitting optical photons. The impurities in inorganic scintillators are known as activators or dopants. The scintillation process of an inorganic scintillator is shown in Figure 4.10. In each mechanism, the electrons will eventually reset to the ground state, in timescales from nanoseconds to microseconds depending on the material [191]. Examples of inorganic scintillators are CsI and LYSO, the latter of which is employed in the x-ray spectrometer used and developed within this work.

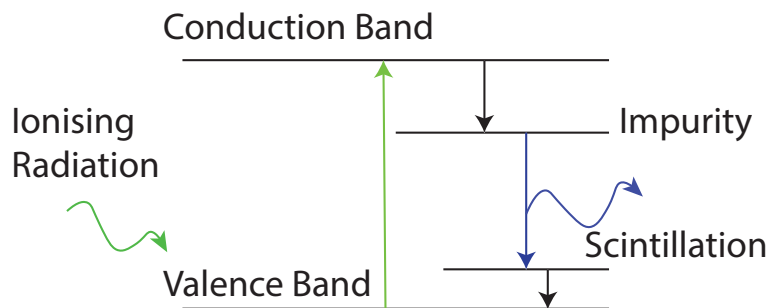


Figure 4.10: Energy level diagram showing the electron transitions in an inorganic scintillator.

4.2.3 CMOS and CCD Cameras

Complementary metal-oxide-semiconductor (CMOS) [192] and charge-coupled device (CCD) [193] sensors are used in diagnostics presented in this thesis. CMOS cameras are used to capture scintillator emission within the linear absorption spectrometer (LAS), used in the experiments reported in Chapters 6 and 7. CCD and CMOS cameras are commonly used as detectors in the diagnosis of laser-solid interactions.

Sensor chips are typically split into pixels, within which potential wells are contained. Both CMOS and CCD technologies utilise the photoelectric effect to convert incident photons into electrons. However, the main difference between them is that CMOS sensors have an amplifier within each pixel, whereas the charge is passed vertically through pixels in a CCD before being amplified in a single amplifier. CCD sensors are limited by the rate of charge transfer and suffer a lower dynamic range compared to CMOS sensors due to finite charge capacity within each pixel.

Each sensor has an intrinsic quantum efficiency (QE), which is defined as the number of electrons produced per incident photon. A QE of 100% would mean that one electron is produced for each incident photon. Typically, the QE of a sensor depends on the wavelength of light incident upon it. The QE curves, as a function of incident photon wavelength, for the CMOS camera used within the LAS x-ray diagnostic are shown in Figure 4.11 [194]. The maximum emission wavelength of LYSO, the scintillator used in the LAS is 420 nm, for which the CMOS sensor has a roughly 15% drop in QE compared to the peak at 500 nm

[195]. This is counteracted by the higher light yield from LYSO compared to other scintillators, such as BGO which emits green photons [101].

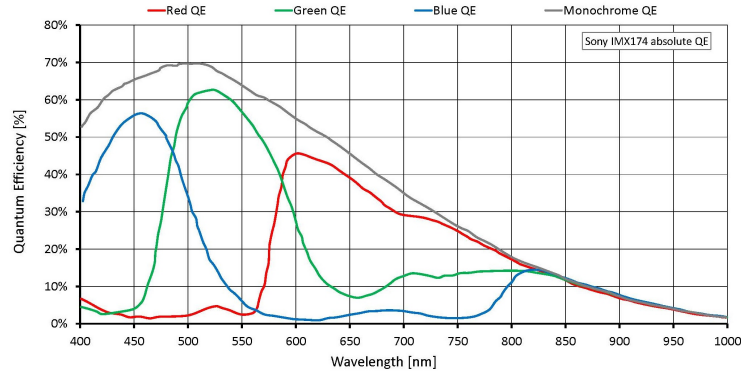


Figure 4.11: Quantum efficiency as a function of wavelength for the Allied Vision Manta G-235 camera, used in the LAS x-ray diagnostic [194].

4.3 Diagnostic methods

In the pursuit of understanding the physics of ultra-intense laser-solid interactions, precise diagnostic tools are essential. This section details the key diagnostic methods employed, including a linear absorption spectrometer, electron spectrometer, and $K\text{-}\alpha$ x-ray imaging diagnostic, each of which plays a critical role in capturing and characterizing high-energy emissions. Each of these methods utilise the detection methods detailed in the previous section. The linear absorption spectrometer, in particular, is an essential diagnostic in the work presented in this thesis. The development of this x-ray spectrometer, discussed in Chapter 7, is instrumental in refining the ability to deconvolve complex x-ray spectra, despite challenges related to signal uncertainties. Alongside this work, the electron spectrometer provides insight into fast electron populations, while the $K\text{-}\alpha$ x-ray diagnostic is crucial for spatially resolving characteristic x-ray emissions. Together, these diagnostic tools form a complementary suite for probing the complex dynamics of laser-driven interactions. It should be noted that there are many other methods relevant to the diagnosis of laser-solid interactions, such as proton and neutron detectors and reflected laser light diagnostics, which were

not used in the work reported in this thesis.

4.3.1 Linear absorption x-ray spectrometer

In order to characterise the x-rays originating from laser-solid interactions, an x-ray spectrometer was used. The spectrometer is a linear absorption spectrometer, first reported in Rusby *et al.* [196] and, later, in Armstrong *et al.* [197]. The spectrometer consists of an array of ten 2 mm LYSO scintillators separated by plastic spacers and, in the latter half of the array, 2 mm tungsten filtering. Each LYSO crystal is wrapped in white PTFE tape which acts to increase light yield by enabling multiple scatters within the crystal before exiting out of the face directed to the camera. The crystals and filtering are held within a 3D printed frame that keeps the emission of each individual crystal optically separate. A CMOS camera is used to capture the scintillator emission produced by incident x-rays. The lens used must have as high a numerical aperture as possible to maximise light collection. As such, the lens used in this diagnostic is an $F/0.95$ lens. The setup of the spectrometer, alongside images of the scintillator array, is shown in Figure 4.12.

A method of reconstructing incident x-ray spectra from the scintillator signals was reported in Armstrong *et al.* [197]. The process of extracting the data and the following algorithm for data analysis are shown in Figure 4.13. For the analysis of the spectrometer data presented in this work, it is assumed that an x-ray distribution comprising two or more temperature components is being measured. The method in [197] explicitly avoids using the generalised flux ratio of temperature components, R_{Chen} , proposed in Chen *et al.* [55, 198], by directly solving for each flux component. Using this method, the distribution of the incident spectrum, $F(E_\gamma)$, as a function of photon energy, E_γ , is treated as being the sum of multiple spectral shapes, where each component, f_i , is dependent on photon energy, photon flux, n_i , and a control parameter, T_i . This can be described by

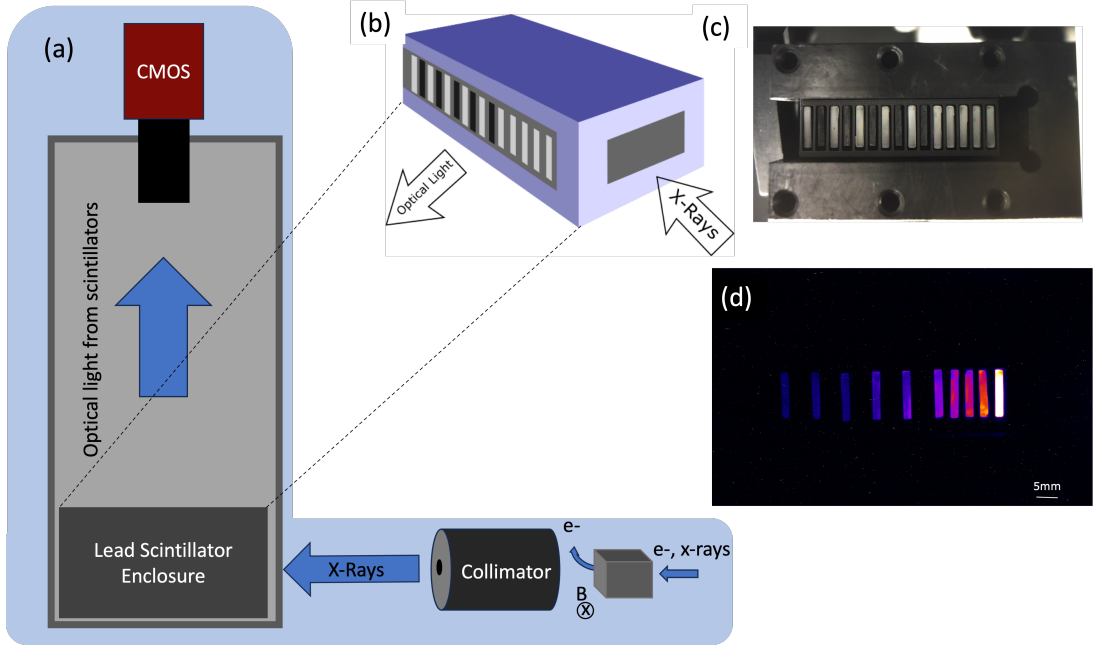


Figure 4.12: Example LAS x-ray spectrometer setup. (a) is a schematic of the spectrometer design showing the grey plastic housing with CMOS camera and lead enclosure for the scintillator crystals and filtering. External to the spectrometer housing is a magnet which is used to deflect electrons and a collimator which isolates x-rays from the interaction. (b) is a 3D schematic of the scintillators and lead housing. (c), photograph of the scintillator array, and (d) is an example measurement image from the spectrometer.

$$F(E_\gamma) = \sum_{i=1}^N n_i f_i(E_\gamma, T_i). \quad (4.5)$$

For Boltzmann and Maxwell-Boltzmann spectral shapes the control parameter is given by the temperature of the spectrum. It is noted in [197] that f_i has a subscript i to note that it is possible to consider multiple spectral shapes as well as components. This is important as the nature of the different possible components have different origins and hence different distributions.

The measured scintillator signals, M_k , are thereby a product of the above spectral shape and the response matrix, Γ , integrated over all energies and are given by

$$M_k = \int_0^\infty F(E_\gamma) \Gamma(k, E_\gamma) dE_\gamma, \quad (4.6)$$

where k is the crystal or scintillator layer. The fitting routine solves for $F(E_\gamma)$ by using a trial solution that is the combination of a predetermined number of

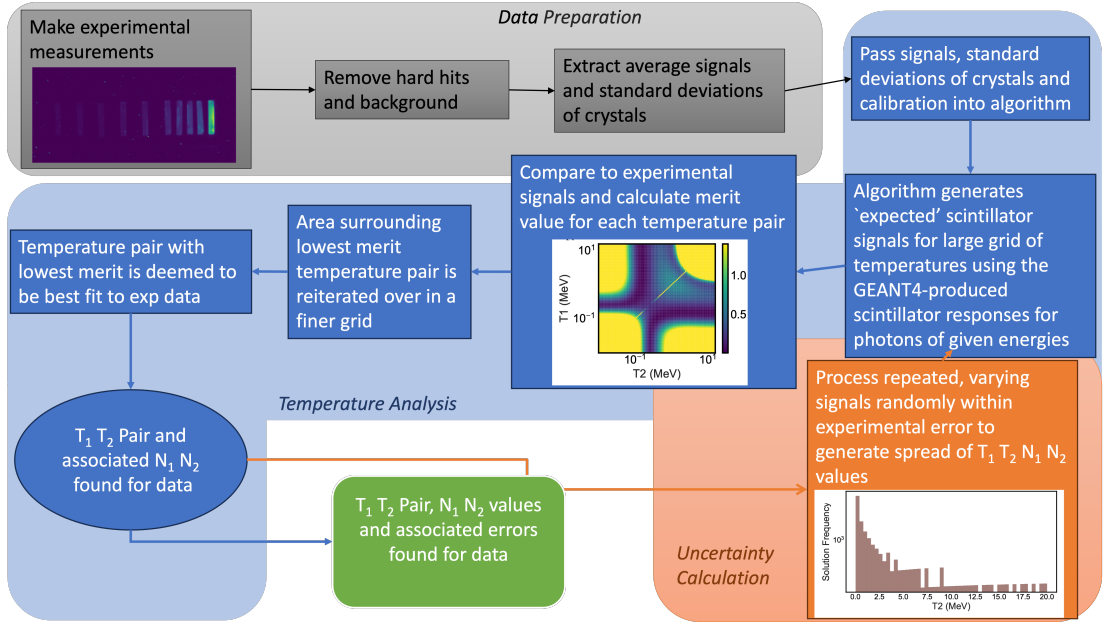


Figure 4.13: A flowchart illustrating the LAS analysis. Firstly, the experimental measurement of the scintillator emission is made with the CMOS camera and the images are then processed and analysed. Then, the average scintillator signals and uncertainties are passed to the analysis algorithm, which generates ‘expected’ scintillator signals for a grid of temperature pairs. These are compared to the experimental data and their fit (or merit) is quantified. A finer scan is performed about the area of lowest merit or best fit. The temperature pair with the best fit is then outputted by the algorithm. The uncertainty is calculated by performing this process with the scintillator signals varied randomly within experimental uncertainty. The spread of solutions gives the uncertainty in the output values.

components and spectral shapes.

In practice, this fitting routine is applied twice, once over the full temperature range given and again around the rough optima found by the first pass. The terminology used in Armstrong *et al.* [197] is ‘sparse’ and ‘fine’ reconstruction. An example sparse-reconstruction merit grid is shown in Figure 4.14, wherein the most-likely spectral solutions are found in the areas of lowest merit. Around this solution, a finer-resolution scan is performed to find the area of minimum merit in the localised region. An example flow chart illustrating the steps in the analysis process is shown in Figure 4.13.

4.3.2 Spectrometer image analysis

As the reconstruction error is dependent on the standard deviation of the scintillator crystals within the image, it is imperative to remove noise caused by direct x-ray and particle hits on the camera chip (so called ‘hard-hits’). In order to

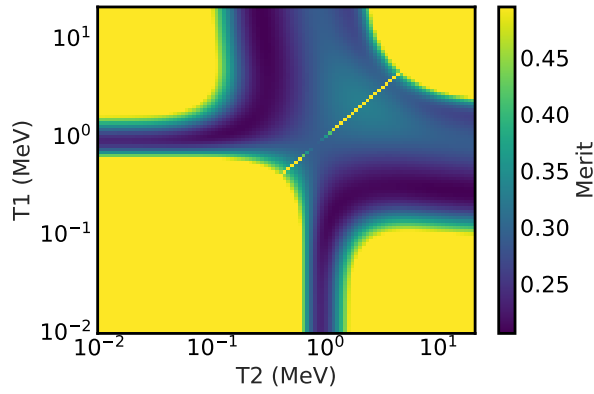


Figure 4.14: Example sparse-reconstruction LAS analysis merit grid, with merit value given as a function of T_1 and T_2 . Areas of low merit (darker) indicate more likely temperature solutions for the measured scintillator signals. In this phase of reconstruction, a large range of temperatures are considered, typically from 10 keV to around 25 MeV.

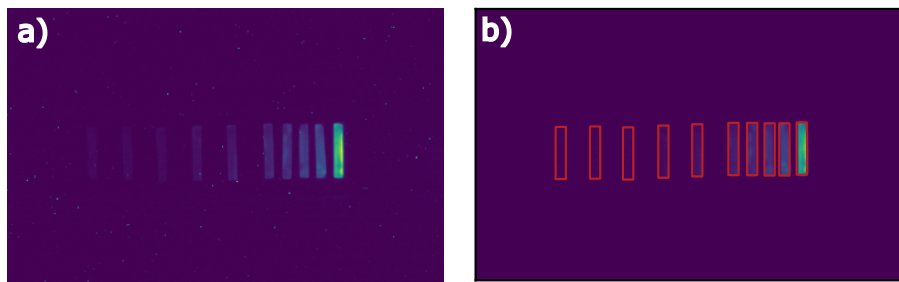


Figure 4.15: a) An example data image, with the scintillators lit up by incident x-rays, with bounding boxes overlaid to show the sample areas for the fitting. This image is prior to image processing and includes ‘hard-hits’ on the camera chip. (b) shows the image post-processing and the ROIs of each crystal in red.

do this, a high-pass filter is applied to the image to extract the bright regions caused by hard-hits, which is then subtracted from the original image. A section of the image not containing signal is then sampled for background noise from the camera chip and, more prominently, optical light leakage into the diagnostic. Once the image has been processed in this manner the crystal region of interests (ROIs) can be defined. To decrease the signal uncertainty it can be useful to ensure the ROI for each crystal remains spatially inside the crystal, so as to avoid a low background signal increasing the standard deviation. Examples of pre- and post-processing spectrometer images are shown in Figures 4.15(a) and 4.15(b).

The LAS x-ray diagnostic was used for bremsstrahlung x-ray measurements in experimental campaigns on both the Vulcan Petawatt and PHELIX lasers, presented in Chapters 6 and 7. Chapter 7 largely focuses on further development of

the spectrometer for higher intensity laser-solid interactions (above 10^{21} Wcm⁻²), where the bremsstrahlung x-ray spectrum tends towards temperatures that are not easily deconvolved with the current diagnostic design. As such, many of the results presented using this diagnostic focus on the total signal of the diagnostic, which directly corresponds to the total energy yield of bremsstrahlung x-rays, rather than direct spectral deconvolution. The focus of the final chapter is on the improvement of the diagnostic design to produce more accurate temperature reconstructions.

4.3.3 Electron spectrometer

In laser-solid experiments, a fraction of the electron population accelerated by the laser leave the rear of the target, escaping the target sheath fields. These electrons leave the target over an angular range centred on the the laser axis or target normal, depending on the method of electron acceleration [199]. It is possible to detect these electrons using an electron spectrometer. The electron spectrometer is an energy-resolving electron diagnostic, featuring a permanent magnet which produces a deflection in the trajectory of electrons which is dependent on their velocity, charge, and the magnetic field strength. The electron population is sampled through a pinhole in order to limit divergence of the beam that would result in a loss of energy resolution due to the spread of signal on the IP. Behind the magnet is a strip of BAS-TR image plate (IP) on a parabolic curve. As the electrons are deflected by the magnet they hit the IP, the geometry of which is shown in Figure 4.16. From the position of the signal on the IP a spectrum can be recovered. The PSL signal to number of incident electrons was calibrated, and is reported in Tanaka *et al.* [187] for BAS-TR IP.

In order to resolve the energy of the electrons from the IP data, the motion of the electrons as they pass through the magnet must be considered. The motion of an electron as it passes through the magnet is determined by the Lorentz force equation (Equation 2.6). The path of the electron in the plane perpendicular to the magnetic field can be shown to be a circle of radius $R_{elec} = v/\omega_g$. Therefore, as the electron exits the magnetic field, its angle is given by $\sin\theta = L_m/R_{elec}$,

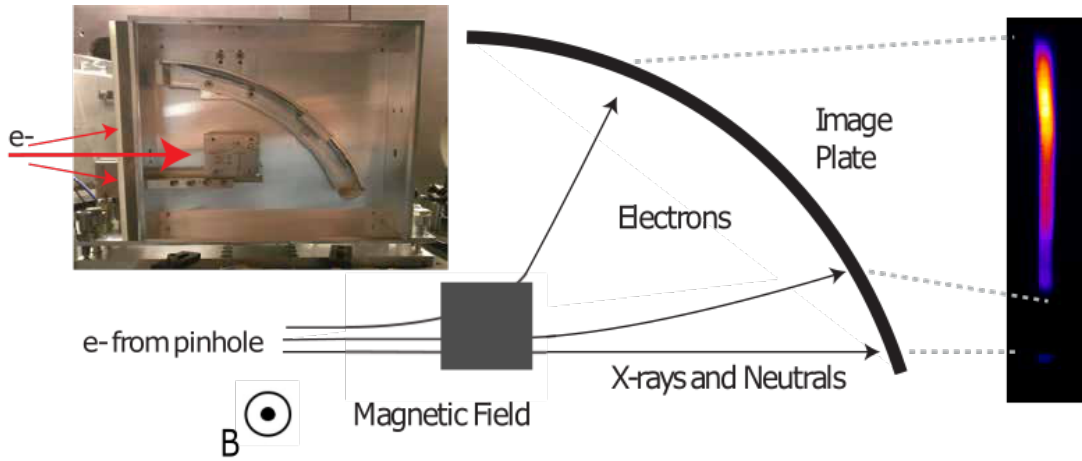


Figure 4.16: Image of an electron spectrometer, with accompanying illustration which shows the deflection of electrons according to their kinetic energy. Example data from the spectrometer is shown, which is extracted from the IP positioned on the parabolic curve.

where L_m is the length of the magnet. Using this, and the distance between the magnet and the curved imaging plate, the deflection of the electron along the IP can be calculated as a function of electron energy. The deflection of a 1 MeV electron as a function of distance is shown in Figure 4.17, with the position and strength of the magnetic field shown in the colour bar.

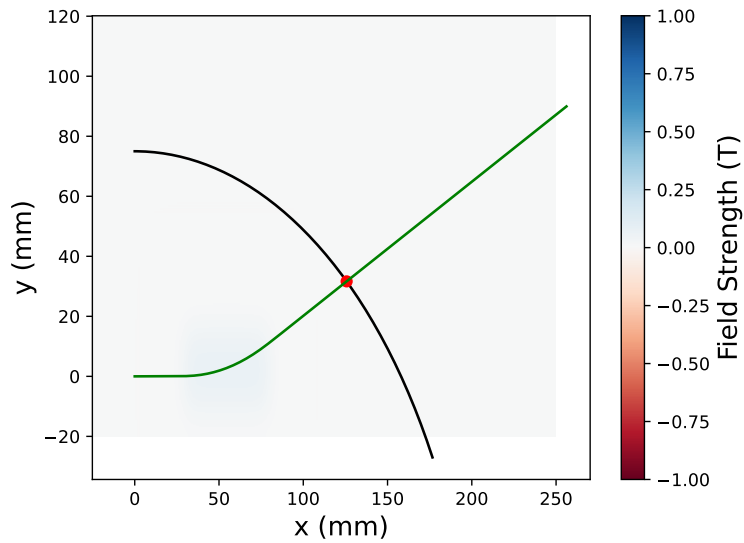


Figure 4.17: Deflection of a 1 MeV electron as a function of distance x and y as it travels through a magnet (green). The colour bar represents the strength and spatial position of the magnetic field and the black parabolic curve represents the position of the IP.

4.3.4 K- α x-ray imaging

In Frazer *et al.* [179], a copper K- α x-ray diagnostic was used to diagnose target electrons. This diagnostic is used to image the Cu K- α x-rays emitted from laser-plasma interactions and, by extension, to characterise the fast electron population within the target. For example, the diagnostic has been used to diagnose electron divergence [57, 58] and refluxing [99, 100, 200]. Additionally, K- α x-rays have been used to study the evolution of laser-solid interactions, with time-resolved diagnostics [201, 202]. K- α sources from laser-solid interactions have also been recognised as potential x-ray sources for radiography and imaging [35, 63, 120].

The targeted line emission is produced when an electron from the K-shell of an atom is ionised by a collision with a fast electron. An electron from the L-shell then decays, emitting a characteristic x-ray photon (with an energy of 8.048 keV for the copper K- α transition). Figure 4.18(a) shows the energy level transitions involved in this process.

K- α x-ray yield measurements from [179] are presented in Chapter 7 to aide the results discussion. The copper K- α imaging system, used in combination with the Vulcan Petawatt laser for the results presented, consists of a spherically bent Bragg crystal and an IP detector. K- α x-rays from the interaction are reflected and imaged onto the IP by the Bragg crystal. The energy of photons collected by the crystal is highly dependent on their incidence angle onto the crystal, with an angle given by the Bragg angle, $\theta_{Bragg} = \sin^{-1}(n\lambda_{K\alpha}/2d)$, where $\lambda_{K\alpha}$ is the K- α photon wavelength (related to the photon energy) and d is the crystal spacing. The focal length of the crystal is given by its radius of curvature, the geometry of which is illustrated in Figure 4.18(b). These Cu K- α x-ray measurements are presented in combination with bremsstrahlung x-ray yield measurements in Chapter 7 to diagnose the electron populations generated by laser-solid interactions with intensities above 10^{21} Wcm $^{-2}$, and to guide the development of an x-ray spectrometer that can be used at such intensities.

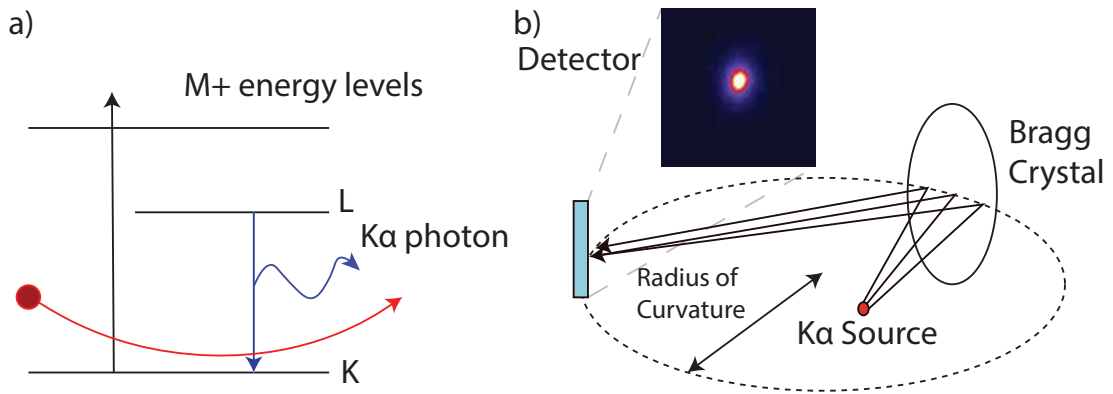


Figure 4.18: (a): electron energy transitions leading to K- α emission. An electron is freed from the atom by a collision with a fast electron, represented by the red circle and arrow, and an L-shell electron decays to the empty K-shell. (b): geometry of the Cu K- α detector, showing the spherically bent Bragg crystal that directs and focuses the x-ray radiation from the K- α source to the image plate detector.

4.4 Numerical modelling

In the study of laser-solid interactions, modelling is a necessary and powerful tool to aid the understanding of experimental measurements. The interaction between lasers and solids, including x-ray emission, can be modelled using particle-in-cell (PIC) codes. Additionally, Monte-Carlo modelling is an important diagnostic in modelling both x-ray emission and energy deposition, and is used in this work both to simulate bremsstrahlung x-ray spectra from solid targets and to model the energy deposition of x-rays into the absorption-based x-ray spectrometer, described above.

4.4.1 Monte Carlo modelling

Monte Carlo methods operate by using repeated random sampling alongside random number generation. The intent is to use randomness, typically pseudo-random numbers generated by a deterministic algorithm, to solve problems that are deterministic in nature [203]. The Monte Carlo code, GEANT4 [204], is used throughout the work presented here to simulate the emission and absorption of bremsstrahlung x-rays. GEANT4 uses pseudo-randomness, in combination with known probabilities of physical events, to calculate the scattering and energy loss of particles as they propagate through a medium. Whilst these codes do not

explicitly model laser-plasma interactions, they can be a useful tool to simulate the scattering and energy loss of electrons as they pass through a target. In the work in this thesis, Monte Carlo codes are used to model the propagation of hot electrons through material and, more specifically, the x-ray photons that are produced in such a process [187]. In addition, the deposition of energy by electrons and x-rays into scintillator arrays was also modelled using this method.

In GEANT4, detector geometries, material geometries, and particle inputs can be user-defined, which allows for the simulation of complex geometries (such as the x-ray spectrometer used for measurements presented in Chapters 6 and 7). Each particle is inputted one at a time and is tracked as it passes through the defined material and detector geometries. Particles, and any secondary or ‘daughter’ particles produced, are tracked until the particle reaches a minimum energy or exits the simulation box. To simulate the interactions of these particles, GEANT4 contains a range of physics tables which cover a wide range of nuclear processes and interaction cross-sections for particle energies from tens of eV to tens of GeV. Random number generation, alongside a large number of input particles, is used in combination with these tables to model electron behaviour and the resulting x-ray emission for the work in this thesis.

The disadvantage of using GEANT4 is that collective behaviours, such as electron beam filamentation, cannot be modelled as input particles are each individually considered. Nor can behaviours such as electron refluxing, which would require the inclusion of electric fields around the target. As the bremsstrahlung spectra generated using GEANT4 reported in this thesis are informed by electron spectra produced using laser-plasma simulation tools (Section 4.4.2), electron refluxing is independently modelled. It is also shown in Chapter 7, that the numerical modelling of electron spectral distributions due to refluxing can be combined with Monte-Carlo modelling to produce more ‘realistic’ x-ray spectra.

4.4.2 Particle-in-cell modelling

In the study of ultra-intense laser plasma interactions it would be ideal to fully and completely model plasma dynamics. With the large numbers of particles in-

volved, with particle densities around 10^{29} m^{-3} for a solid density target, alongside the collective behaviours due to the electromagnetic fields produced by dynamic charged particles, this is computationally impossible. A solution to this is provided by particle-in-cell (PIC) codes. In such codes, the distribution function is split into so-called macro-particles, which act as a collection of many real particles. The motion of said macro-particles, which are defined to have the same properties as the constituent particles, e.g. charge to mass ratio, is then approximated by the Lorentz force.

In PIC codes, the plasma is modelled using a kinetic description within which a distribution function of the form $f_s(\vec{r}, \vec{p}, t)$ is used to describe the probability that a particle will be found at a certain point in position-momentum space at any point in time. The Vlasov equation gives the evolution of this function where the effect of collisions can be ignored which, in a plasma where the plasma frequency is much greater than the collision frequency of the constituent particles, is appropriate [205]. The Vlasov equation is given by

$$\frac{\partial f_s}{\partial t} + \vec{v} \cdot \nabla f_s + \frac{q}{m} \left(\vec{E} + \vec{v} \times \vec{B} \right) \cdot \frac{\partial f_s}{\partial \vec{p}} = 0 \quad (4.7)$$

Still, solving this equation for each particle remains computationally expensive due to the number of particles and number of dimensions in both position and momentum space. As previously noted, this is solved by splitting the function into macro-particles, to which the Lorentz force can then be applied.

As collisions are neglected by the Vlasov equation, collisions are typically not treated within the PIC code, although modules can exist to calculate collisions, and macro-particles can occupy the same space without perturbation. Macro-particle motion and the associated electromagnetic fields are described using the following equations:

$$\frac{d\vec{r}}{dt} = \vec{p} \quad (4.8)$$

$$\frac{d\vec{u}}{dt} = \frac{q}{m} \left(\vec{E} + \vec{v} \times \vec{B} \right) \quad (4.9)$$

$$\frac{\partial \vec{B}}{\partial t} = -\nabla \times \vec{E} \quad (4.10)$$

$$\frac{\partial \vec{E}}{dt} = c^2 \nabla \times \vec{B} - \frac{\vec{j}}{\epsilon_0} \quad (4.11)$$

where $\vec{u} = \gamma \vec{v}$ and \vec{j} is the current density. Provided that $\nabla \cdot \vec{B}$ is true at the beginning of the simulation it will remain satisfied throughout. Within the code, these macroparticles are distributed about the grid and can be defined by different ‘shape-functions’ or distributions. Such shape-functions can take the form of discrete top-hat functions or, in the case of this work, splines which take the form of triangles [206]. More complex particle shapes are required to limit self-heating within the code as these have the effect of smoothing particle currents on the grid [207].

The electric and magnetic fields are defined on a Yee staggered grid [208]. In this process, a cyclical method known as the finite difference time domain (FDTD) is used to determine the evolution of the electric and magnetic fields, and the evolving particle trajectories by approximation. In the PIC code EPOCH, which is used in this thesis, the fields are calculated on half-integer and integer time-steps [206]. The electric and magnetic fields are first advanced from n to $n + 1/2$ using the current density at time-step n using the following equations

$$\frac{\vec{E}^{n+1/2} - \vec{E}^n}{\Delta t/2} = c^2 \nabla \times \vec{B}^n - \frac{\vec{j}^n}{\epsilon_0} \quad (4.12)$$

$$\frac{\vec{B}^{n+1/2} - \vec{B}^n}{\Delta t/2} = -\nabla \times \vec{E}^{n+1/2} \quad (4.13)$$

where Δt is the time-step size defined by the Courant-Friedrichs-Lewy (CFL) condition. These fields can then be inserted into the equations of motion, which pushes the macro-particles to a new position, updating the current density, \vec{j}^{n+1} . With this new current density value the fields can then be updated for the $n + 1$ time-step.

The new particle positions can then be interpolated onto the grid, with a particle ‘weight’ defining the fraction of a macro-particle at a given grid position, shown in Figure 4.19(a). The flux of macro-particles on the grid gives the current density, which means the cycle can begin again and repeat iteratively. Through

this method, all fields can be defined simultaneously within the same time-step, whilst also obtaining the half-integer time-step values required for the particles to be pushed. A flowchart of this algorithm is shown in Figure 4.19(b).

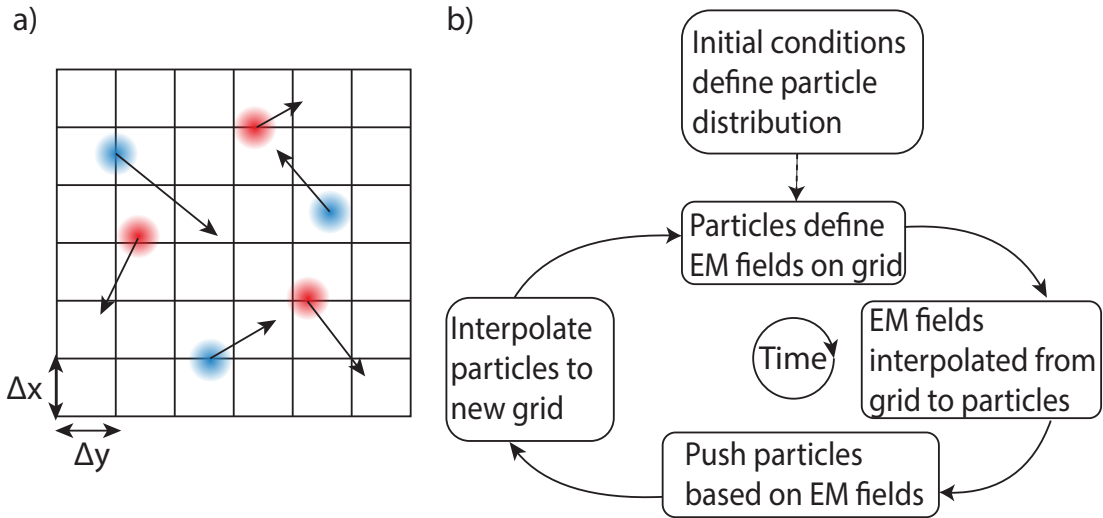


Figure 4.19: (a): an illustration of macroparticles on the PIC grid, where positive and negative macroparticles are represented by the red and blue points, respectively and (b), a flowchart of an example PIC algorithm.

While PIC simulations are a powerful tool for investigating and diagnosing laser-plasma interactions, there are a number of potential problems and limitations that need to be considered. Firstly, there are spatial and temporal resolutions that must be met within the simulation. Spatially, the simulation must resolve the Debye length so that the plasma is accurately modelled. Otherwise, numerical heating can occur, which is an artificial heating of the plasma that results from the electric fields being aliased over multiple adjacent cells so that the Debye length can be resolved. In the temporal domain, the resolution has to be high enough to resolve the highest frequencies of the system. In laser-plasma interactions, it is of utmost importance that the electron plasma frequency is resolved as this is key to the plasma dynamics. Therefore, the time-step criterion that must be obeyed at all times is $\Delta t \leq \omega_p$. Also of importance is the cyclotron frequency, ω_c , which, when strong magnetic fields are present, must also be resolved.

Another issue is that of excess numerical noise that can be introduced when the number of particles per cell is too low. There is no definitive criterion to

reach here, but the validity of the code can be determined by convergence testing the code by adding additional particles until the output remains fixed. Numerical noise will always exist in PIC simulations, for example in the low-flux, high-energy tails of particle distributions which are represented by very few macroparticles.

Additional limitations are placed on PIC simulations by their computationally expensive nature. Due to the above requirements on spatial and temporal resolution, alongside the restrictions on available computational resource, it can be prohibitively expensive to fully simulate a laser-plasma interaction in 3D. As such, it is often necessary to lower the number of spatial dimensions and simulate the interaction in 2D. This can have a number of effects on the interaction, for example affecting plasma expansion and the scaling of laser intensity with focal spot size due to the distribution of laser energy in 2D. Additionally, the significant effects of pre-pulses and ASE pedestals cannot be modelled in PIC simulations as the timescales are too long and the intensities are too low. However, a pre-plasma can be manually added to the simulation to simulate the effects of preheating by pre-pulses and ASE on the target.

The bremsstrahlung and synchrotron modules within the PIC code EPOCH are used to generate x-ray spectra for ultra-intense laser pulses. In the bremsstrahlung module, a Monte Carlo algorithm is used to simulate the processes of x-ray emission, using the methods in Wu *et al.* [209] and Vyskocil *et al.* [210]. The bremsstrahlung emission is modelled as a transport process where an electron propagates through a medium and undergoes scattering events, wherein the final electron energy, $\epsilon_{e,1}$ is equal to the difference of the initial electron energy, $\epsilon_{e,0}$ and the photon energy, ϵ_γ . These events are determined by a probability distribution function (PDF) and the differential cross section (DCS) for bremsstrahlung emission, the integral of which diverges as the photon energy, ϵ_γ , approaches zero. Due to this, a minimum, or cut-off, photon energy must be specified, ϵ_{cut} . The DCS is given by

$$\frac{d\sigma}{d\epsilon_\gamma} = \frac{Z^2}{\beta^2} \frac{1}{\epsilon_\gamma} \chi(Z, \epsilon_{e,0}, \kappa) \quad (4.14)$$

where Z is the atomic number, $\beta = v_e/c$, v_e is the electron velocity, and $\kappa = \epsilon_\gamma/\epsilon_{e,0}$

is the reduced photon energy [210]. The scaled DCS, $\chi(Z, \epsilon_{e,0}, \kappa)$, is read from a pre-calculated table and integrated over the photon energy to obtain a cross section, σ , for each ion species in the simulation.

Within the PIC loop, the ion density, n_i , is calculated for each cell and, for each electron velocity, v_e , a random number (between 0 and 1) is compared to the the emission probability, $g = n_i v_e \sigma \Delta t$, where Δt is the length of the simulation step. If the probability is larger than the random number generated, a photon is produced with a momentum parallel to the electron motion and a reduced energy, κ , according to the PDF:

$$p(\epsilon_{e,0}, \kappa) = \frac{1}{\kappa} \chi(Z, \epsilon_{e,0}, \kappa) \Theta(\kappa - \kappa_{cut}) \Theta(1 - \kappa) \quad (4.15)$$

where Θ is the Heaviside step function – $\Theta(x) = 0$ for $x < 0$, and $\Theta = 1$ for $x \geq 0$ [211], and $\kappa_{cut} = \epsilon_{cut}/\epsilon_{e,0}$ is the reduced cut-off energy. The PDF value is interpolated from the pre-calculated tables of $\chi(Z, \epsilon_{e,0}, \kappa)$, and κ is evaluated using the methods in [212]. The electron momentum is then modified and the process is repeated for each ion species in a random order. This process is evaluated in each time step.

The QED synchrotron module works similarly, using a Monte-Carlo method, first realised in [213], to determine whether a photon is emitted in each time step [145]. In this algorithm, the probability of a photon emission event with optical depth, τ_{em} , is calculated and is given by

$$P(t) = 1 - e^{-\tau_{em}} \quad (4.16)$$

The optical depth for each particle is given by $\tau(t) = \int_0^t \lambda_{em}[\eta_s(t')] dt'$, where λ_{em} is the appropriate rate of emission, and η_s is a parameter that determines the importance of quantum effects and is a ratio of the electric field in the direction of the electron's rest frame, E_{RF} and the Schwinger field, E_S . When $\tau = \tau_{em}$, the particle emits a photon of an energy again calculated by tabulated probability, $P_{\chi_S} = (\eta_s, \chi_S)$, where $\chi_S = (\gamma' - \gamma)(cB/2E_S)$ and γ is the Lorentz or relativistic factor. The recoil for the emitting positron or electron is then calculated and the

particle momentum is updated in the PIC code.

4.4.3 Summary

In summary, the laser systems and diagnostics used to make measurements of laser-solid interactions reported in this thesis, are described. It is shown that, to perform a laser-solid experiment and explore the underlying physics, it requires an array of different technologies, including well-optimised laser systems and a plethora of diagnostic equipment. As such, modelling is shown to be a necessary technique to complement the array of diagnostic equipment which helps to resolve the underlying physics. In the following chapters, the use of the modelling and experimental methods described within this chapter are reported with a view to diagnosing x-ray emission from laser-solid interactions and improving existing x-ray diagnostics.

Chapter 5

The role of focal spot size and pulse energy in bremsstrahlung and synchrotron production in thick targets

5.1 Introduction

Laser plasma interactions have long been identified as a source of high energy x-rays [9, 35, 55]. With the recent development of high-power, high-repetition rate lasers it has become possible to probe and image matter using x-rays from a high repetition-rate source [214, 215]. Laser-driven x-ray sources have also long been seen as an alternative to cathode-ray x-ray tubes and linac sources, due to their ability to achieve high brightness, high photon energy, ultra-short pulse duration, and small source size simultaneously [36]. In laser-solid interactions at currently available laser intensities, up to 10^{21} Wcm⁻², the bremsstrahlung mechanism is the dominant effect for generating high energy x-rays and has been studied with the intent of exploring industrial applications [36, 37, 216, 217]. However, as new facilities come online that can achieve intensities up to 10^{22} - 10^{23} Wcm⁻², such as the ELI-Nuclear Physics 10 PW laser in Romania [20, 21, 218], the synchrotron x-ray production mechanism becomes relevant, but not dominant. With both the

bremsstrahlung and synchrotron emission mechanisms present, it is important to optimise for synchrotron emission and to distinguish between the signals of each.

Partially laser-driven synchrotron sources have been used before, however, they typically use the interaction between a laser pulse and an underdense, counterpropagating electron beam from a more conventional accelerator. Eggl *et al.* [219] reported the use of a laser and counterpropagating linac electron beam to generate bright flashes of synchrotron x-rays to image a mouse embryo. It is therefore feasible that a laser-driven synchrotron source can be used to image not only dense matter but biological matter. The downside of this methodology is that an electron beam generated by a linac, or other RF accelerator, is required, which is expensive and large in size. Additionally, the brightness of the source is limited by the amount of charge in the electron bunch. True laser-driven synchrotron sources would remove the need for a linac. The benefit of the synchrotron emission mechanism is that it can be highly directional, due to the nature of the interaction. Since the electron quantum parameter is maximised when electrons counterpropagate with the laser pulse, synchrotron emission can be highly directional in either the forwards or backwards direction. Having a small and highly directional source has the desired effect of achieving higher imaging resolutions.

In addition, it is becoming more common to see shorter pulse durations and tighter focusing geometry used to achieve higher laser intensities. Increasing the pulse energy requires larger beam optics and gratings in order to keep the fluence below the damage threshold, which has a limit both in cost and manufacturability. The largest grating optics currently available are around one meter in diameter, which constrains the beam size and, therefore, increasing laser intensity by increasing the pulse energy is not available. Tighter focusing and lower pulse durations are therefore used to increase the laser intensity. Achieving an additional order of magnitude in intensity requires only a $3.3\times$ reduction in spot size, assuming the encircled energy remains the same, whereas increasing the energy by a factor of 10 requires a huge development. As higher laser intensities are required to examine the mechanisms of synchrotron emission, it is important to understand the effects of achieving higher intensities, i.e. by increasing laser

pulse energy and decreasing focal spot size, on laser-plasma interactions and, specifically, x-ray production.

5.1.1 Optimising synchrotron emission

At higher laser intensities the electron quantum parameter, χ_e , outlined in Equation 3.26. increases and the electrons can become increasingly relativistic. Additionally, as the electric field strengths present approach the Schwinger limit ($E_S = 1.32 \times 10^{18} \text{ Vm}^{-1}$) [25], the field strength at which electron-positron pairs can be produced from vacuum, QED effects and gamma-ray production can start to dominate the interaction. It is important to note that this field corresponds to an intensity of $4.6 \times 10^{29} \text{ Wcm}^{-2}$, which is many orders of magnitude greater than laser intensities achievable in the near future. Accelerating electrons to high energies means that intensities where quantum processes start to occur are becoming accessible in the centre of mass frame of reference when electrons counterpropagate with the strong laser field. At high intensities of 10^{21} Wcm^{-2} , both the synchrotron and bremsstrahlung emission mechanisms are present, producing broadband x-ray spectra over very similar energy ranges [73]. At higher intensities, above 10^{22} Wcm^{-2} , synchrotron emission dominates over bremsstrahlung in numbers as the bremsstrahlung mechanism saturates, due to electrons at higher energies becoming radiative as opposed to collisional, but at the lower laser intensities typically experimentally available the signals can be equivalent, depending on the choice of target material and thickness [71–73, 220]. For investigations of synchrotron radiation on present laser systems, the bremsstrahlung emission therefore acts as a strong source of experimental background, hiding an underlying synchrotron signal.

There have been many computational studies focused on the optimisation and detection of synchrotron radiation in the presence of a simultaneously abundant bremsstrahlung x-ray source [73, 220]. In Goodman *et al.* [73] a computational study of the effects of several laser parameters on synchrotron and bremsstrahlung emission is reported, using a combination of PIC modelling and Bayesian optimisation. This work was concentrated on the use of ultra-thin targets undergoing

transparency, and target thickness, pulse duration, focal spot FWHM, and laser intensity were varied over multi-parameter scans. For the laser intensities studied ($3.16 \times 10^{21} - 10^{23} \text{ Wcm}^{-2}$) it was found that the synchrotron emission was most efficient for the smallest spot size and shortest pulse durations as these resulted in the highest incident laser intensities. Of the two parameters, the spot size has a more notable effect on the laser-to-synchrotron conversion efficiency as the spot FWHM has an inverse square relationship to the laser intensity. Conversely, the laser energy-to-bremsstrahlung conversion efficiency is higher for the thickest targets (micron-thick), but still increases in efficiency with increasing laser intensity.

This enhanced energy conversion efficiency for synchrotron production is likely due to a phenomenon reported in Ridgers *et al.* [28]. The the EPOCH PIC code was used to simulate the interaction of a laser pulse of intensity $4 \times 10^{23} \text{ Wcm}^{-2}$ with a $1 \mu\text{m}$ -thick Al target. The spot size used in the simulation was equal to the laser wavelength, $1 \mu\text{m}$. In these conditions, “prolific” γ -ray production was reported at the holeboring front, where the laser is reflected from the critical surface. This is later attributed [70] to skin-depth emission wherein a standing wave is established within a few skin depths of the target, the backward component of which interacts with ponderomotively accelerated, forward-moving electrons. Not only laser focal spot size but also the spatial intensity profile will have an effect on the holeboring front, which can be expected to have an impact on synchrotron production.

Generally, modelling-based work on synchrotron emission uses near-diffraction-limited spots sizes around a micrometer FWHM, due to the strong relationship between energy conversion efficiency and intensity. As shown in the work reported in Wilson *et al.* [109], small spots achieved experimentally by tight focusing optics have large and relativistically intense airy disks, when the peak intensity is of the order of 10^{21} Wcm^{-2} or greater, which significantly affect the interaction. In another study, Dover *et al.* [110], electron and ion acceleration was found to be limited when near-diffraction-limited spots were used to increase the laser intensity. This highlights the importance of investigating the effects of tight focusing

to increase laser intensity when further increasing the pulse energy is intrinsically limited. There is limited experimental evidence on the influence of small spot sizes on bremsstrahlung emission and, in this chapter, the influence of focusing geometry, spot size, and pulse energy on bremsstrahlung and synchrotron emission is investigated through modelling.

5.1.2 Laser focal spot size and pulse energy in LPIs

With many mechanisms present within laser-solid interactions it is becoming apparent that laser intensity is not the only parameter dictating the dynamics: the quantities of laser focal spot size, pulse duration, and pulse energy, which all contribute to the magnitude of the laser intensity, each have their own effects on the interaction. Many existing models, especially those governing electron temperature scaling with laser intensity, only consider intensity.

It was reported in Dover *et al.* [110] that the use of near-diffraction limited laser focal spot sizes influences electron heating and proton acceleration. The 1.5 μm spot of the J-KAREN-P laser was defocused to produce on-target laser intensities between 1×10^{19} and 1×10^{21} Wcm^{-2} , which was compared to a similar intensity range, achieved by varying the pulse energy. It was found that, for the intensity range achieved by utilising a small focal spot and decreasing energy, the achieved electron temperatures were lower than for the same intensities but larger spots. Through tracing 1500 electrons in two PIC simulations of the same intensity but 1.5 and 5 μm spot sizes, it was found that the transverse acceleration lengths were smaller for the smaller focal spot radii, indicating that the electrons could not experience the full laser potential before being ejected from the spot ponderomotively. An adjustment to the transverse electron momentum, p_f , gained as a function of spot radius (r_L), for spot radii smaller than the transverse acceleration length, y_0 , was presented:

$$p_f = a_0 m_e c \left[1 - \left(1 - \frac{r_L}{y_0} \right)^2 \right]^{\frac{1}{2}}, \quad (5.1)$$

which predicted the electron temperature saturation that was seen experimen-

tally.

In Armstrong *et al.* [101], the effects of focal spot size on bremsstrahlung emission were considered to investigate the behaviour of recirculating electrons within the target, again by moving the target into the focusing and expanding beam. A penumbral foil [221, 222] was used to determine the profile of the x-ray emission from the target. Two emission regions were found: a small central region and a wider substrate emission. The overall x-ray yield was found to stay relatively constant over the full defocus range, however at larger magnitude defocus values the substrate emission was significantly brighter than the central region. The central x-ray emission is attributed to electrons emitting in their first pass of the target, whereas the wider substrate emission is produced by recirculating, or refluxing, electrons [97]. This was determined by combining x-ray yields generated using Nist ESTAR electron stopping tables and the Mora [223] sheath model to determine which electrons can escape the target.

5.1.3 ‘Defocusing’ to investigate spot size effects

Laser intensity scans are frequently achieved in the literature by moving the target out of the focal plane of the laser, a method known as ‘defocusing’. This method is typically used over using different focusing geometries to achieve differently-sized best focus laser focal spots, as this would generally require switching out the main focusing optic in the laser path, which would be both timely and expensive considering these optics are typically larger than 30 cm in diameter. The consideration to be made is how the laser wavefront changes away from focus. At focus, the beam should adhere to a Gaussian spatial intensity profile wherein the wavefront is flat. However, away from focus the spatial profile can resemble more of a flat top distribution if the beam is not perfectly Gaussian [156]. This has the potential to drastically change the spatial intensity profile and change the dynamics of the interaction. Here, the objective is to quantify the lesser-considered effects of spatial intensity profile on electron heating and x-ray production, which become relevant when defocusing the laser beam.

There have been many studies about the effects of defocusing the beam to

decrease the laser intensity on target [111, 224–226]. In Rusby *et al.* [196] an experiment was performed using the PHELIX laser whereby the intensity was varied from 10^{17} to mid- 10^{20} Wcm^{-2} by moving the target into the focusing beam. Escaping electron numbers and temperature were measured using a wraparound IP stack, with Fe filtering representing four different electron energies. The IP signal was compared to the Monte-Carlo-simulated diagnostic response in order to estimate electron temperature. A peak in electron signal at an intensity between 10^{18} and 10^{19} Wcm^{-2} was found, attributed to optimal self-focusing within the preplasma, leading to a peak intensity on target. Additionally, studies have found increased laser energy absorption for larger defocus spots. In Gray *et al.* [98], the fraction of absorbed laser energy was measured using an integrating sphere within which the target was placed. It was found that the absorption of laser energy was higher for larger spots at the same intensities. In Brenner *et al.* [106], like intensities with either higher energies or smaller spots were employed to consider the effects of both on ion production. It was found that a ten times increase in energy led to a 500 times increase in proton numbers, whereas decreasing the spot size to reach the same intensity only led to a less than tenfold increase in numbers. Considering these studies, it becomes clear that both spot size and pulse energy play an important role in the dynamics of laser plasma interactions. A larger spot size obtained by defocusing the beam clearly allows for the laser field to interact with more electrons on the target surface, which causes an increase in the absorption of laser energy. However, the amount of pulse energy available to those electrons, which will then produce x-ray radiation, dictates the amount of energy that can be transferred to secondary radiation. These two constituents of laser intensity are often as important as the peak intensity with regards to secondary radiation generation. It dictates whether, in the case of high pulse energy, electrons are accelerated to higher energies or, in the case of a larger focal spot, higher numbers of electrons are accelerated due to the increased size of the interaction volume.

It is therefore important to understand how to utilise this knowledge to minimise emission produced by the bremsstrahlung mechanism and optimise syn-

chrotron emission, in order to enhance our ability to measure the source of synchrotron radiation. In this chapter, experimental and numerical investigations of the production of bremsstrahlung and synchrotron radiation are reported. The role of the focal spot size, focusing geometry, and pulse energy on the production of secondary radiation is discussed.

5.2 Modelling

To first investigate the effect of F -number on the absorption of laser energy by the electrons and, in turn, x-ray emission, modelling was performed using the PIC code EPOCH 2D [206]. 2D PIC modelling was used to investigate the effects of focusing geometry on electron dynamics and bremsstrahlung emission. Separately, the laser energy and intensity were varied by manipulating the laser spot size and keeping either the intensity or pulse energy constant. The laser spot size was changed via two methods: by moving the laser focus away from the target and thus moving the target plane into the focusing beam, and by effectively changing the F -number of the focusing. Those two methods will be referred to as ‘defocus’ and ‘best focus’, respectively. The full range of spot sizes, F -numbers, and intensities used are shown in Table 5.1.

For these simulations, the parameters are outlined in Table 5.2. The laser FWHM was $2\ \mu\text{m}$ at best focus and, by moving the target into the incoming beam, on-target spot sizes of $5\ \mu\text{m}$, $15\ \mu\text{m}$, and $30\ \mu\text{m}$ were achieved (aside from the ‘negative’ defocus simulations where the target was moved *away* from the laser focal plane). In the best focus simulations, the FWHM at focus was changed to the same spot sizes as in the defocus simulations. The laser pulse has a Gaussian temporal profile with a pulse duration of 40 fs.

F -number	Spot Size (μm)	Fixed E Intensity (Wcm^{-2})
f/2	2 at best focus & 5, 15, 30 defocus	2.5×10^{19}
f/4.7	5 at best focus	1×10^{19}
f/7.8	15 at best focus	3.33×10^{18}
f/23.5	30 at best focus	1.67×10^{18}

Table 5.1: The spot size parameters for fixed energy and intensity EPOCH 2D simulations

These best focus and defocus simulations were run with a maximum intensity of $2.5 \times 10^{19} \text{ Wcm}^{-2}$ and independent intensity and energy scans were run by either keeping a constant intensity with changing spot size (Table 5.1) or by adjusting the intensity to keep the energy within the spot constant.

2D PIC Simulation Parameters	
Box Size	$35 \times 20 \times 20 \mu\text{m}^3$
Number of Cells	17500×8192 cells
Pulse Duration	40 fs
Simulation Duration	150 fs
Particle Shape	b-spline
Target Thickness	$10 \mu\text{m}$
Target Density	$60n_c$
Preplasma Scale Length	$1 \mu\text{m}$
3D PIC Simulation Parameters	
Box Size	$30 \times 20 \times 20 \mu\text{m}^3$
Number of Cells	$4000 \times 720 \times 720$ cells
Pulse Duration	100 fs
Simulation Duration	150 fs
Particle Shape	b-spline
Target Thickness	$10 \mu\text{m}$
Target Density	$9n_c$
Preplasma Scale Length	$1 \mu\text{m}$

Table 5.2: Parameters for the 2D and 3D EPOCH simulations performed.

Electron spectra corresponding to the peak of the laser pulse interacting with the target were extracted from the simulations according to their spatial position. For example, electrons from the front of the target, electrons from within the target, and rear target escaping electrons (with momentum ≥ 0) were sampled. Additionally, bremsstrahlung spectra, generated by EPOCH's bremsstrahlung module (outlined in Chapter 4), were also extracted.

To further investigate the effects of pulse energy and spot size on x-ray production at higher intensities, the PIC code EPOCH 3D was used. This enabled the full 3D focal spot size effects for a few intensity ranges to be investigated. This modelling was used to quantify bremsstrahlung and synchrotron x-ray emission for two spot sizes, at three intensity ranges. The simulation parameters are presented in Table 5.2. The spot size was varied between 1.5 and $5 \mu\text{m}$ in order to change the intensity by a factor of around 11 times, for constant pulse energy.

Fixed Energy	
Intensity (Wcm^{-2})	Spot Size (μm)
$4.5 \times 10^{19}, 5 \times 10^{20}$	5 (Defocus), 1.5 (Best Focus)
$4.5 \times 10^{20}, 5 \times 10^{21}$	5 (Defocus), 1.5 (Best Focus)
$4.5 \times 10^{21}, 5 \times 10^{22}$	5 (Defocus), 1.5 (Best Focus)
Fixed Intensity	
Intensity (Wcm^{-2})	Spot Size (μm)
5×10^{20}	1.5 (Best Focus), 5 (Best Focus)
5×10^{21}	1.5 (Best Focus), 5 (Best Focus)

Table 5.3: Parameters for the EPOCH 3D simulations performed, for both the fixed energy and fixed intensity scans.

For each energy-conserved pair of simulations, the intensities used were $5 \times 10^{22} \text{ Wcm}^{-2}$ and $4.5 \times 10^{21} \text{ Wcm}^{-2}$; $5 \times 10^{21} \text{ Wcm}^{-2}$ and $4.5 \times 10^{20} \text{ Wcm}^{-2}$; and $5 \times 10^{20} \text{ Wcm}^{-2}$ and $4.5 \times 10^{19} \text{ Wcm}^{-2}$. Intensity-conserved larger spot ($5 \mu\text{m}$) simulations were also performed at $5 \times 10^{21} \text{ Wcm}^{-2}$ and $5 \times 10^{22} \text{ Wcm}^{-2}$, made possible by increasing the pulse energy compared to the equivalent-intensity simulations with $2 \mu\text{m}$ focal spots. A larger target thickness of $20 \mu\text{m}$ was used for this set of simulations as, at the highest intensities, deep holeboring occurred due to the lower densities needed to model in 3D, required to stop numerical heating. This has the effect of increasing the numbers of bremsstrahlung emission compared to the thinner target simulations. The EPOCH QED and Bremsstrahlung modules were used to simulate the synchrotron and bremsstrahlung emission in each of the above cases. For both modules a lower energy threshold of 50 keV was used to limit detection of lower energy photons emitted by the lowest energy target electrons.

It is important to note that bremsstrahlung emission can continue long after the peak of the pulse arrives as the electron motion and collisions within the target continue until their energy is depleted. Synchrotron emission, however, tends to be limited to the interaction time as the laser field needs to be present [146]. In these simulations, particularly in 3D, it was not computationally possible to extend the simulation durations to picoseconds and, as such, some of the bremsstrahlung emission may be missed. This has been quantified by extrapolating the bremsstrahlung emission using a power-law fit out to 5 ps . It was found

to add an order of magnitude to the bremsstrahlung photon yield.

Uncertainties are provided for this data and are the result of the post processing of the simulation data,. Uncertainties in temperature values given are from the errors in fitting to the electron spectra, while errors in maximum electron energies arise from the discrete nature of the histogrammed energy spectra. As the maximum energy is taken from the histogrammed spectrum, there is an error associated with the bin size. Large bins are required at this end of the spectrum because the number of electrons is significantly lower and with more noise.

5.2.1 Spot size and energy dependence of electron acceleration and bremsstrahlung emission

In this section, the results of the 2D modelling investigating x-ray emission with spot size and focusing geometry are presented. Here, the effects of varying spot size and pulse energy on electron acceleration and x-ray production via bremsstrahlung are considered.

5.2.2 Fixed Intensity Modelling

In this series of simulations, the laser intensity is fixed as the laser focal spot size was changed but compensated by increasing the pulse energy. These simulations were performed for two focusing regimes, with best focus and defocus geometries, in order to establish if effects of spatial intensity profile are present.

Figure 5.1 shows the electron spectra for the fixed intensity 2D PIC simulations, taken when the peak of the laser pulse interacts with the target at 90 fs. Here, the spectra of different electron populations are presented: the front surface population, Figure 5.1(a), the rear-target escaping electron population, Figure 5.1(b), and the population internal to the target, Figure 5.1(c). The front surface population sampled the electrons with an x -position less than $0 \mu\text{m}$, as this is where the front surface of the target is defined to be. The internal target population is defined as those between $x = 0 \mu\text{m}$ and $x = 20 \mu\text{m}$. The rear surface escaping electrons have an x position greater than $20 \mu\text{m}$ and an x -momentum

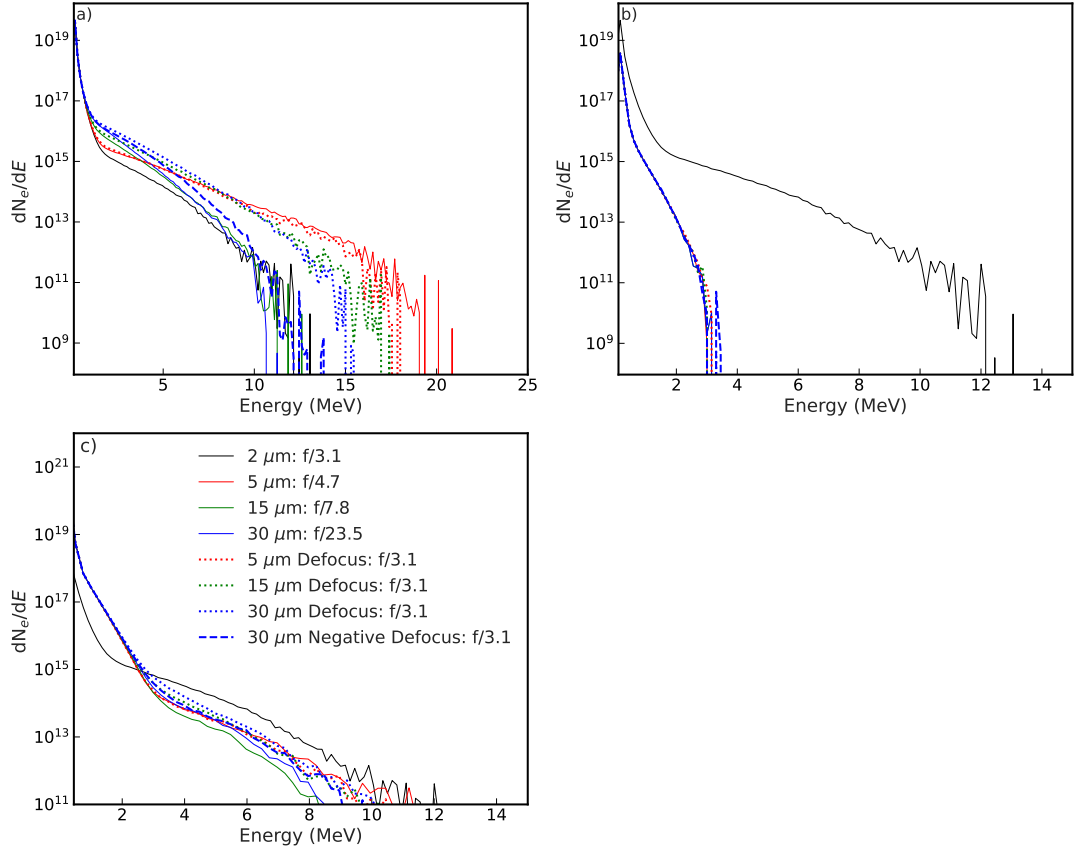


Figure 5.1: (a) Front surface, (b), rear surface escaping, (c), and internal electron spectra for fixed intensity ($2.5 \times 10^{19} \text{ Wcm}^{-2}$), for best-focus spots (solid) with focusing geometries of F -number $f/4.7$, $f/7.8$, and $f/23.5$. and defocus spots (dotted and dashed) for a $f/3.1$ focusing geometry.

greater than zero. In Figure 5.1, the best focus and defocus cases are shown by solid or dashed lines, respectively.

In ultra-intense laser-solid interactions, there are typically two temperature components to the electron energy distributions [54]. The simulated electron spectra in Figure 5.1(c) show two clear temperature components, the first ranging up to around 3 MeV, and the second ranging from 3 MeV to around 10 MeV. Throughout this thesis, these two components, each corresponding to a lower and higher temperature, will be labelled T_1 and T_2 , respectively.

The largest differences visible in the electron spectra between focusing geometries are found in the front surface electron population. Here, clear differences in both electron numbers and higher electron temperature, T_2 , are present, shown in Figure 5.2. The largest differences in T_2 are seen for the larger focal spots,

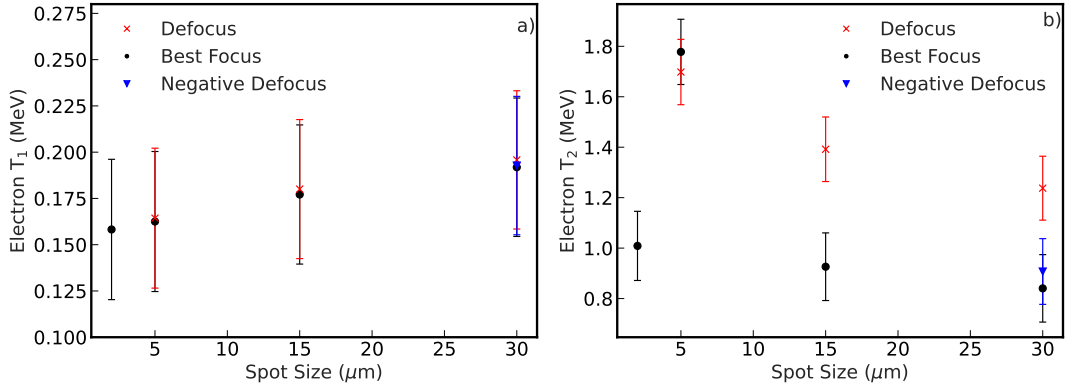


Figure 5.2: (a) Lower electron temperatures, T_1 , and (b) higher electron temperatures, T_2 , as a function of laser focal spot size for best focus and defocusing geometries for front surface electron population.

with increases of 400 keV for the defocus compared to the best focus geometries. The highest electron temperatures are seen for the 5 μm spot size, which has the second highest pulse energy of the data points. The lower electron temperature, T_1 , also increases slightly with increasing spot size and pulse energy, although this effect is minimal as it is around an order of magnitude in keV, within the bounds of uncertainty and is therefore not conclusive. There is a clear optimum in higher electron temperature in the 5 μm case, which is consistent with the relative decrease in electron temperature for tight focusing reported in Dover *et al.* [110]. There is a clear limit to electron acceleration for the tight focusing case, which occurs due to the decreased electron acceleration length for smaller focal spots. To further investigate the effects of spot size and pulse energy on the front surface electron population, the electron numbers and total energy within the front surface electron spectrum are shown in Figures 5.3(a) and 5.3(b), respectively. Within this figure, the best focus geometries are indicated by black circles, the defocus cases are shown by red crosses, and the special negative defocus case is shown as blue triangles. The numbers and total energies are summed for electron energies above 750 keV, to avoid sampling the lower energy preplasma population. However, the numbers remain constant when sampled across all energies.

Whilst the electron numbers remains constant for all spot sizes and pulse energies (Figure 5.3(a)), the total energy (Figure 5.3(b)) contained within the spectrum clearly increases with focal spot size and pulse energy. As the laser

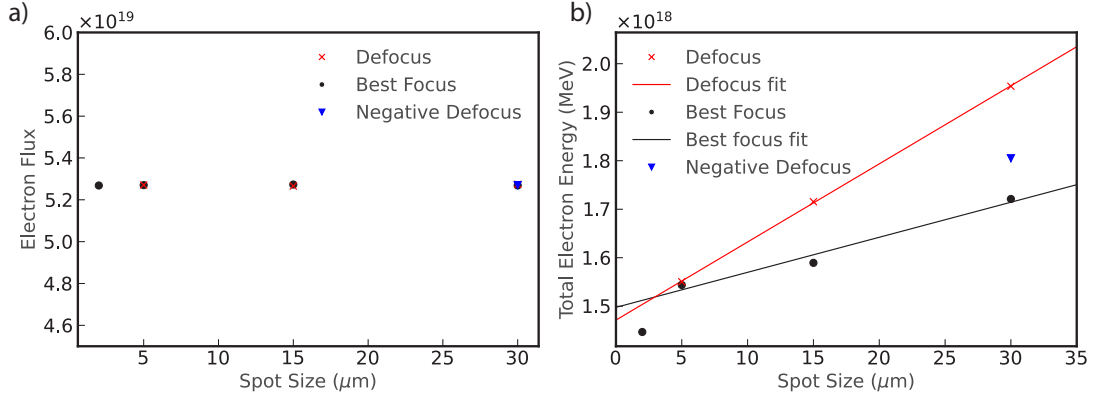


Figure 5.3: (a), Front surface electron numbers and, (b), total front surface electron energy as a function of laser focal spot size for best focus and defocusing geometries for fixed intensity simulations ($2.5 \times 10^{19} \text{ Wcm}^{-2}$). Fits to 5 to 30 μm points (excluding 2 μm points) are shown in red and black for the defocus and best focus cases.

focal spot size increases, so too does the pulse energy to keep the laser intensity constant: between the 2 μm and 30 μm focal spots there is a 15 times increase in pulse energy. The increase in energy absorption by the front surface electrons is steeper between the 2 μm and 5 μm focal spots than between those with larger spots, which remains more linear with increasing spot size and energy. This implies that there is a limitation to energy absorption in the 2 μm , tight-focusing case. This is further exemplified by the linear fits to the $r_L = 5$ to 30 μm points shown in Figure 5.3(b), which both exclude the 2 μm data point. For the larger spots, the relationship between total electron energy and spot size is linear, for both focusing geometries. This, again, is consistent with the limitation of electron heating for tight focusing reported in Dover *et al.* [110].

There is also a clear increase in the absorption of laser energy for defocused spots compared to the best focus spots, which is also shown in Figure 5.3(b). The pulse energy is the same for data points of the same spot size. However, there is clearly an increase in energy within the electron spectra for the defocus spots, with a maximum increase in energy absorption of 15% for the largest spots. This is due to the increased spatial intensity spread for the defocus spots due to the flat-top-like spatial intensity profile.

It is logical that the front surface population of electrons is affected not only by pulse energy and spot size, but by focusing geometry also. However, it is

not this population of electrons that predominantly generates bremsstrahlung - the population of electrons that is internal to the target and is most able to interact with target ions drives this mechanism. The electron population internal to the target, with spectra shown in Figure 5.1(c), experiences the next largest increase in heating, with the larger defocus focal spots producing high energy tails similar to those achieved by using the smaller $5 \mu\text{m}$ spots. The internal electron temperatures are shown in Figure 5.4. There, again, is an optimum in higher electron temperature in the $5 \mu\text{m}$ case, which is not conclusive due to the uncertainties, that suggests a limit to electron heating in for the tighter focusing. The uncertainty in T_2 for the $5 \mu\text{m}$ point lies close to the other temperatures, so this result is by no means conclusive but does suggest that there is an optimum in temperature. An increase in electron temperature between the defocus and best focus geometries is also suggested by the data but is not conclusive. The increases are smaller here than for the front surface electron population, with maximum increases of 100 keV as opposed to the several hundreds of keV seen in the front surface population temperatures. Again, within the uncertainties in T_2 , it is not possible to conclude that there is an increase. However, the data suggests that there may be a difference in temperature for differing focusing geometries.

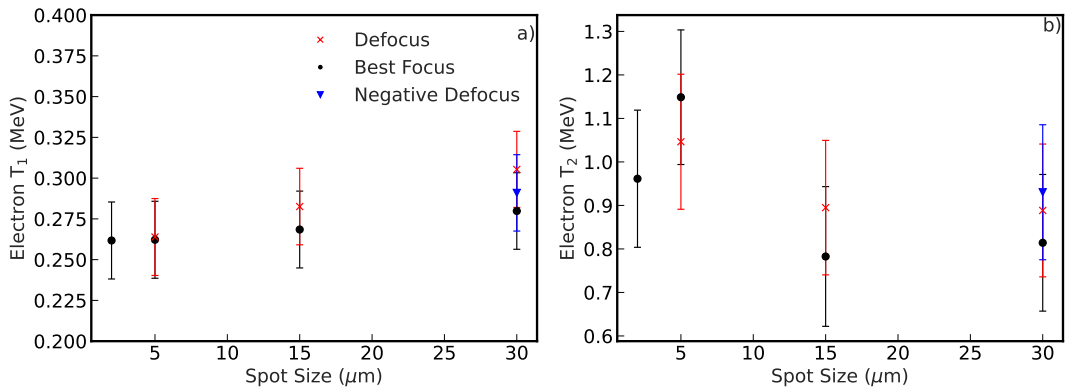


Figure 5.4: (a) Lower electron temperatures, T_1 , and (b) higher electron temperatures, T_2 , as a function of laser focal spot size for best focus and defocusing geometries for electron population internal to target.

The numbers and total energies for the electrons internal to the target as a function of laser focal spot size are shown in Figure 5.5(a) and 5.5(b), respectively. The numbers and total energies are summed for electron energies above 750 keV ,

to avoid sampling the lower energy target population (again, the numbers remain constant when sampled across the full energy range). The numbers slightly increase as a function of increasing spot size and pulse energy. The difference in numbers between the smallest and largest spot sizes is low, at 3%, however this corresponds to an increase of 3.5×10^{16} electrons with energies above 750 keV across the spot size range. The total energies within the spectra, shown in Figure 5.5(b), increase as a function of laser focal spot size, but only increase by a maximum of 4% across the spot size (and pulse energy) range. There is a suggested increase in heating between the best and defocus spots. However, this is again minimal at around 3% for the largest focal spot.

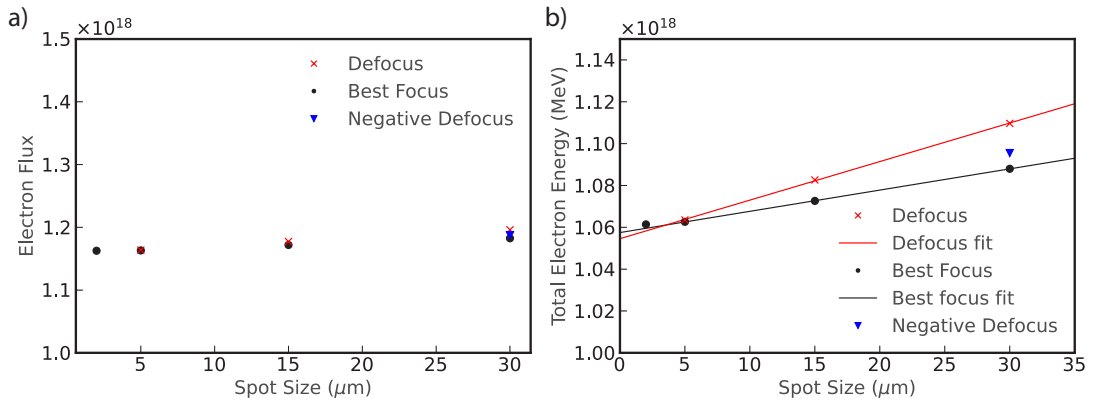


Figure 5.5: (a), Internal to target electron numbers and, (b), total internal to target electron energy as a function of laser focal spot size for best focus and defocusing geometries for fixed intensity simulations ($2.5 \times 10^{19} \text{ Wcm}^{-2}$). Fits to 5 to 30 μm points (excluding 2 μm points) are shown in red and black for the defocus and best focus cases.

The tight-focusing led limitation to electron heating is not seen in the total electron energy for the internal electron population. Linear fits to the total electron energies for best and defocus spots are shown in Figure 5.5(b). Unlike the front surface population, the relationship between total energy and spot size remains linear for all spot sizes. Whilst the energy absorbed by the target internal electrons is not relatively decreased at smaller spot sizes, as it is for the front surface population, the numbers and temperature are still minimally lower than for larger spots and pulse energies.

For the electron population internal to the target, the data suggests that the total energy contained within the spectrum increases with increasing spot size

and pulse energy. The effect of this on resulting bremsstrahlung emission will be discussed later in this section.

To summarise, pulse energy and spot size have been found to have individual effects on front surface and internal electron populations. For fixed intensity and changing spot size (with pulse energy adjusted to compensate), it is found that the lower electron temperatures (T_1) increases linearly with pulse energy. The higher electron temperatures (T_2) however, for both electron populations, feature an optimum at a spot size of 5 μm which corresponds to the second-highest intensity. The T_2 value at the highest intensity and smallest spot size (2 μm) is consistently lower than for the 5 μm data points, which indicates a limitation to electron heating for near diffraction-limited spot sizes, a phenomenon also reported in [110]. For the front surface population, there is a clear decrease in laser energy absorption, shown by the lower total energies seen for the 2 μm spot, which clearly results in a lower T_2 value. Conversely, the internal electron population shows a linear relationship between pulse energy and total energy but a small increase in electron numbers with increasing pulse energy and spot size and overall higher T_1 values. The data suggests that the T_2 electron population still experiences the same spot size limitations to acceleration as the front surface population, and that the relatively higher fraction of energy absorption instead results in higher T_1 values and overall electron numbers.

5.2.3 Fixed Energy Simulations

Figure 5.6 shows the complementary fixed pulse energy electron spectra 2D PIC simulations, corresponding to intensities of 1.67×10^{18} - 2.5×10^{19} Wcm^{-2} . The rear target electron population, shown in Figure 5.6(b), show no differences with intensity or spot size, which suggests that the escaping electron population is not sensitive to either. Again, the populations affected by spot size appear to be those internal to the target (Figure 5.6(c)) and those in front of the target (Figure 5.6(a)) which are directly interacting with the laser. Both groups are accelerated to higher maximum energies and temperatures for the smallest spot sizes and highest intensities.

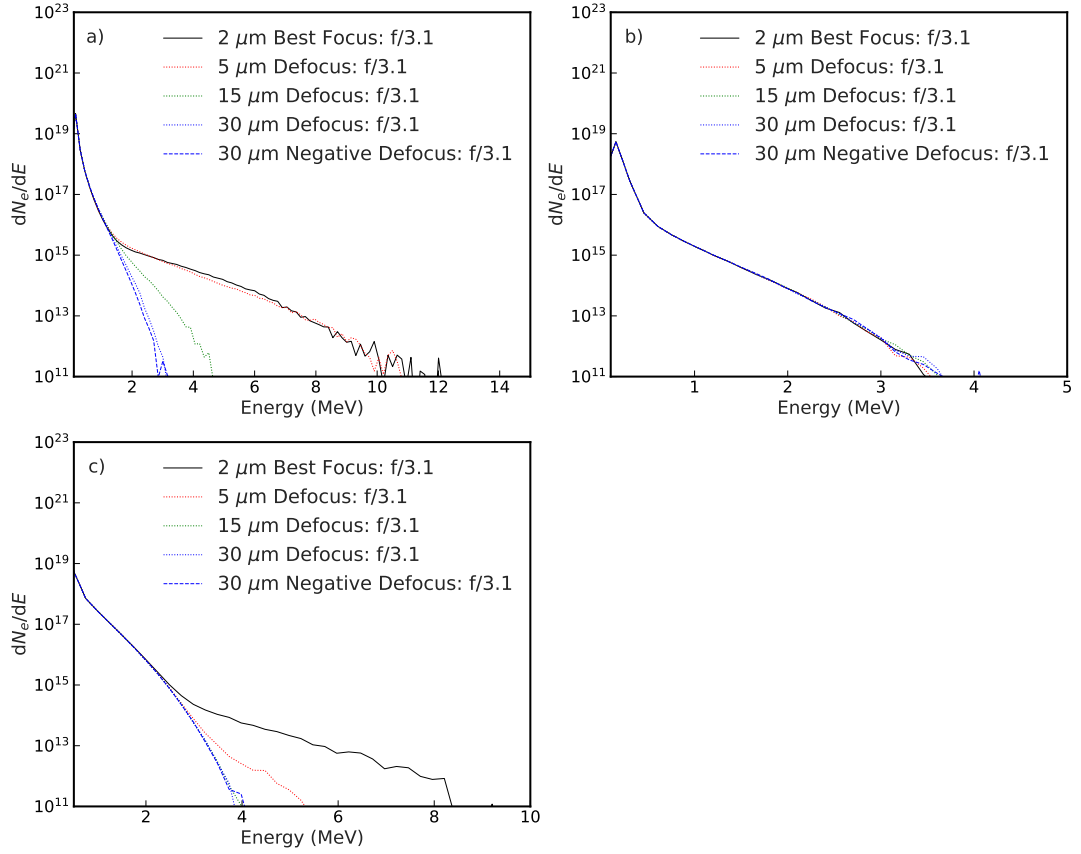


Figure 5.6: (a), Front surface, (b) rear surface escaping, and (c) internal electron spectra for fixed energy EPOCH 2D simulations.

The front surface electron population, with spectral distributions shown in Figure 5.6(a), experiences no increase in maximum energy or temperature between the smallest, 2 μm and 5 μm spots, which correspond to laser intensities of $2.5 \times 10^{19} \text{ Wcm}^{-2}$ and $1 \times 10^{19} \text{ Wcm}^{-2}$, respectively. This shows that there is not an increased heating of front surface electrons at the highest intensity. Studies [98, 106, 227, 228] have suggested that increasing the laser intensity should increase laser energy absorption and as such, either a higher number of electrons or a higher total energy of electrons would be expected. This is not seen in this population, which suggests there is a limit to laser energy absorption when tight focusing is applied.

The fast electron temperatures, electron numbers, and total electron energies for the front surface population are shown in Figure 5.7. An optimum in lower electron temperature (T_1 in Figure 5.7(a)) and total electron energy (Fig-

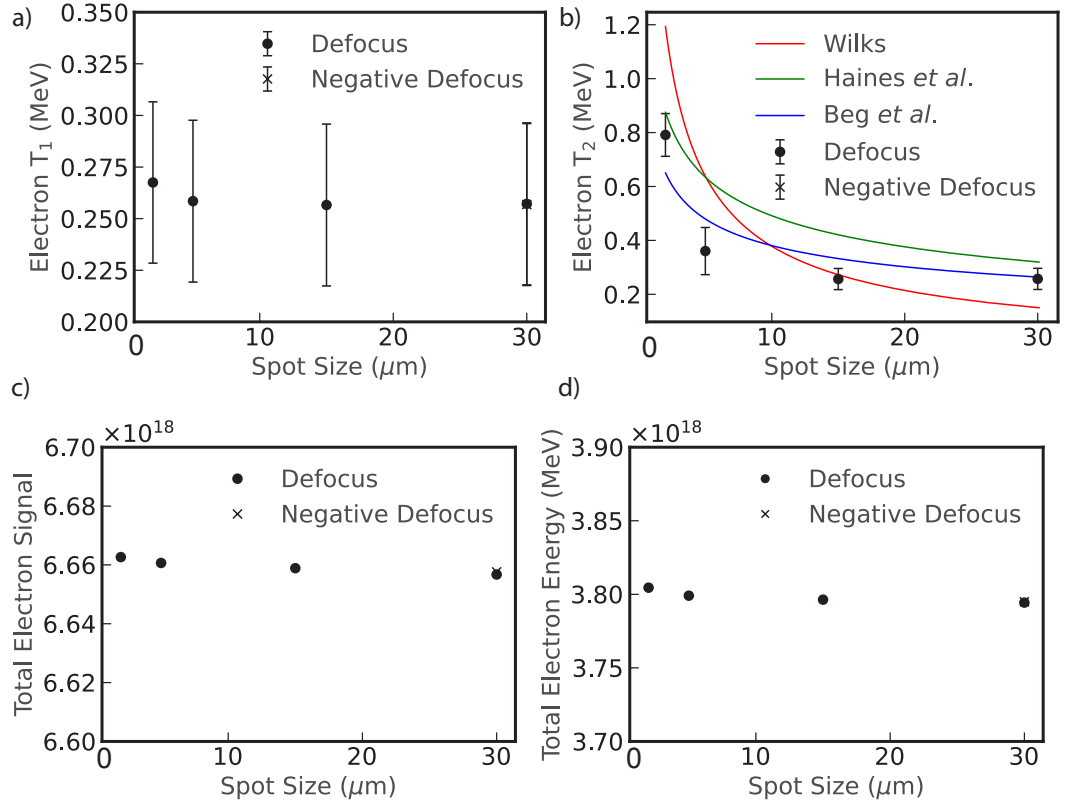


Figure 5.7: (a), Lower temperature, T_1 , (b), higher temperature, T_2 , and Wilks (red) [47], Beg *et al.* (blue) [54], and Haines *et al.* (green) [48] fast electron temperature scalings, (c), front surface electron numbers and, (d) total electron energy for front surface electron population as a function of laser focal spot size for fixed energy EPOCH 2D simulations.

Figure 5.7(d) for the 5 μm data point can be seen. Figure 5.7(c) shows the electron numbers within the front surface electron population, for electrons with energies above 100 keV, which remains constant (to within half a percent) across the spot size and intensity range. The total energy (Figure 5.7(d)) shows an increase in laser energy absorption with decreasing spot size, however, there is a lower than expected energy absorption for the 2 μm spot. This is reflected in the lower T_1 and T_2 values for this data point, which occur due to the lower amount of energy absorbed by the electron population. The electron acceleration appears to be limited for the smallest spot size, which is in agreement with the findings in [110].

The higher electron temperature, T_2 , of the electron population internal to the target, shown in Figure 5.6(c), has a dependence on spot size and, by extension, laser intensity. The corresponding temperatures are shown in Figures 5.8(a) and

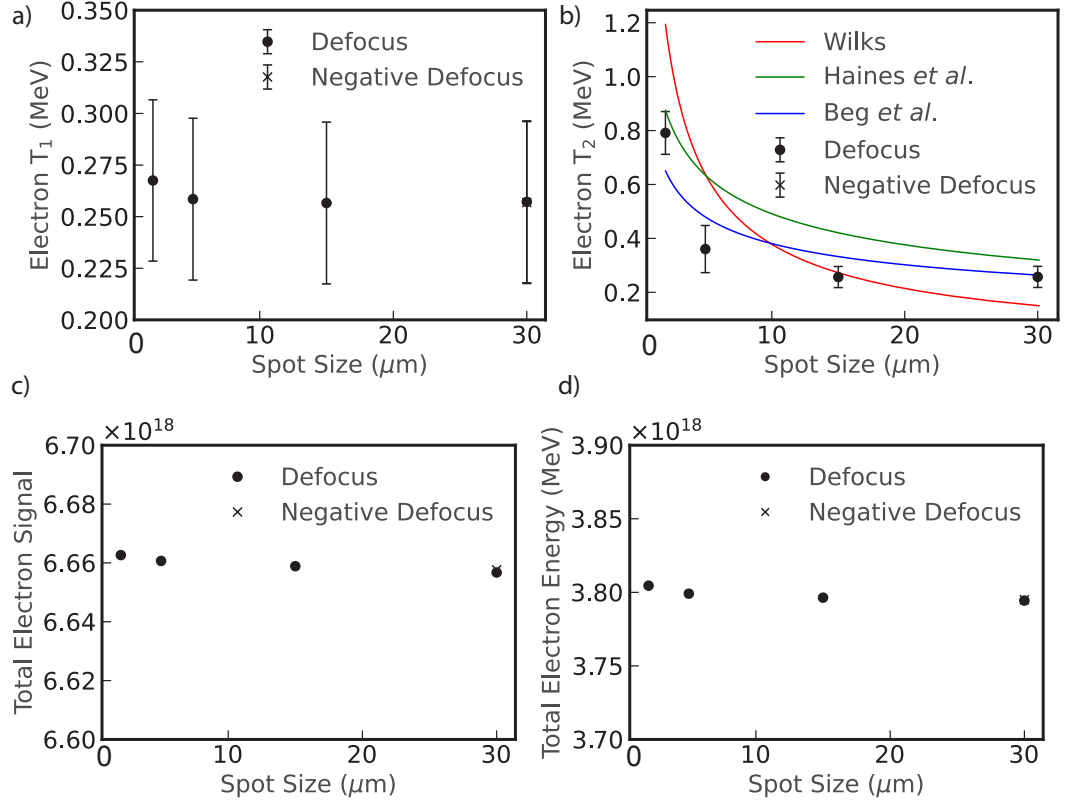


Figure 5.8: (a), Lower temperature, T_1 , (b), higher temperature, T_2 , and Wilks (red) [47], Beg *et al.* (blue) [54], and Haines *et al.* (green) [48] fast electron temperature scalings, (c), internal electron numbers and, (d) total electron energy for internal electron population as a function of laser focal spot size for fixed energy EPOCH 2D simulations.

5.8(b) as a function of spot size, wherein the intensity is decreasing linearly. The lower electron temperature, T_1 , remains largely unchanged across the spot size and intensity range with a 5 keV increase for the smallest spot/highest intensity. In combination with the results from the fixed intensity simulations it is apparent that the lower electron temperature, T_1 , is mostly affected by pulse energy, as it increases with increasing pulse energy and spot size. The higher electron temperature, T_2 , has a clear dependence on both spot size and laser intensity. At these intensities ($1.67 \times 10^{18} - 2.5 \times 10^{19} \text{ Wcm}^{-2}$), the Wilks [47] and Haines *et al.* [48] fast electron temperature scalings, shown in Figure 5.8(b), cross over at around 10^{19} Wcm^{-2} . Neither are a particularly good fit to the electron temperatures, however it is clear that the 2 μm data point is significantly below the temperature predicted by the Wilks scaling. The Haines *et al.* scaling assumes 100% absorption of laser energy whereas the absorption of laser energy as a function of

intensity with changing spot size and fixed pulse energy is reported to be around 40 - 60% in Gray *et al.* [98], which explains why the resulting temperatures are consistently lower than predicted by this scaling, as the electrons are gaining less energy. The Beg *et al.* [54] fast electron temperature scaling provides a better visual fit to the simulation temperatures, but underestimates the temperature for the highest intensity, which is better described by the Haines *et al.* scaling. The fast electron temperature scaling reported by Wilks [47] was derived through PIC simulations wherein the pulse energy was increased as the spot size was kept constant. It is clear that spot size and energy both have individual effects on the interaction and that, by keeping the pulse energy constant, the resulting electron temperatures are much flatter and largely lower than expected.

Figures 5.8(c) and 5.8(d) show the total electron numbers and total electron energy for the internal electron population. There is a 1% increase in both the total electron numbers and total electron energy for the 2 μm simulation compared to the larger spots. This suggests that there is a slight increase in laser energy absorption at the smallest spot compared to the larger spots. An increase in laser energy absorption is expected with increasing laser intensity, which was reported in Gray *et al.* [98], however, a larger increase of around 8% was shown across the same intensity range, for fixed pulse energy and varying spot size. It is this lower than expected increase in laser energy absorption that is causing the flatter temperature scaling. The energy absorbed by the electron population is not increasing with intensity as rapidly as expected and therefore the number of accelerated electrons and their temperature are also not increasing as rapidly as expected. With a fixed amount of energy available, it is logical that the total electron energies are relatively static across the intensity range.

With the fixed pulse energy simulations it has been possible to investigate how much energy is absorbed by the front surface and target electron populations. The front surface population showed clear limiting effects on electron heating at the smallest spot size (2 μm) with lower absorbed energies and electron temperatures for fixed pulse energy. Optima in energy absorption and T_1 , and a higher than predicted T_2 , were observed for the 5 μm data point, which suggests there is a

trade off between intensity and spot size. As the spot size approaches the diffraction limit, we see electron acceleration limiting effects, such as those reported in [110].

The total energy of the internal population decreases with laser spot size and intensity by a small amount, which supports the idea that the decrease in laser energy absorption with decreasing intensity is less steep for changing spot size than changing pulse energy, seen in [98, 106]. The total electron energies and numbers are only slightly influenced by spot size and intensity, which suggests that bulk electron acceleration, and therefore bremsstrahlung emission, is largely pulse energy dependent. Only at the highest intensities is there a high energy tail to the electron spectra featuring a second electron temperature, with temperatures lower than predicted by both the Wilks [47] and Haines *et al.* [48] scalings.

Both spot size and pulse energy are shown to affect electron acceleration. For both fixed and varying pulse energies, electron acceleration is found to be limited at near diffraction-limited spot sizes, with lower than expected electron temperatures (T_2) for both the front surface and target populations in particular. By increasing the pulse energy and keeping the intensity fixed, the lower electron temperatures (T_1) are found to increase as a function of pulse energy. The higher temperature tail of the spectra, however, are found to have an optimum temperature (T_2), at a spot size of $5 \mu\text{m}$. This shows that there is a trade off between spot size and pulse energy affecting the highest-energy part of the spectrum. In the next section, the effects of pulse energy and spot size on bremsstrahlung emission are investigated through 2D PIC modelling.

5.2.4 Bremsstrahlung modelling for fixed energy and fixed intensity pulses

The 2D PIC code EPOCH was used to generate bremsstrahlung emission spectra for the above simulations. Figure 5.9 shows the bremsstrahlung x-ray numbers for the fixed-intensity and fixed-energy simulations. In the fixed intensity simu-

lations, the pulse energy is increasing with increasing spot size, with a 15 times higher energy content within the 30 μm spot compared to the 2 μm (energy scales linearly with spot size in 2D PIC simulations). The photon numbers for the fixed energy simulations are almost constant with spot size, with only an increase of one percent between the smallest and largest spot sizes. This highlights the large pulse-energy dependence of bremsstrahlung x-ray photon numbers compared to spot-size. There is a small difference in x-ray numbers for the best focus and defocus geometries that appears to be up to 15% higher for the defocusing geometries than the best focus spots. With like-spot size simulations containing the same amount of energy within the pulse, this indicates that there is a perhaps a higher absorption of laser energy by the target for the defocus cases. As the target is moved further from focus, the spatial intensity profile of the laser pulse at the target shifts from being Gaussian to more of a flat-top distribution. This allows the still relativistic laser pulse to interact with a larger area of the target, generating more fast electrons.

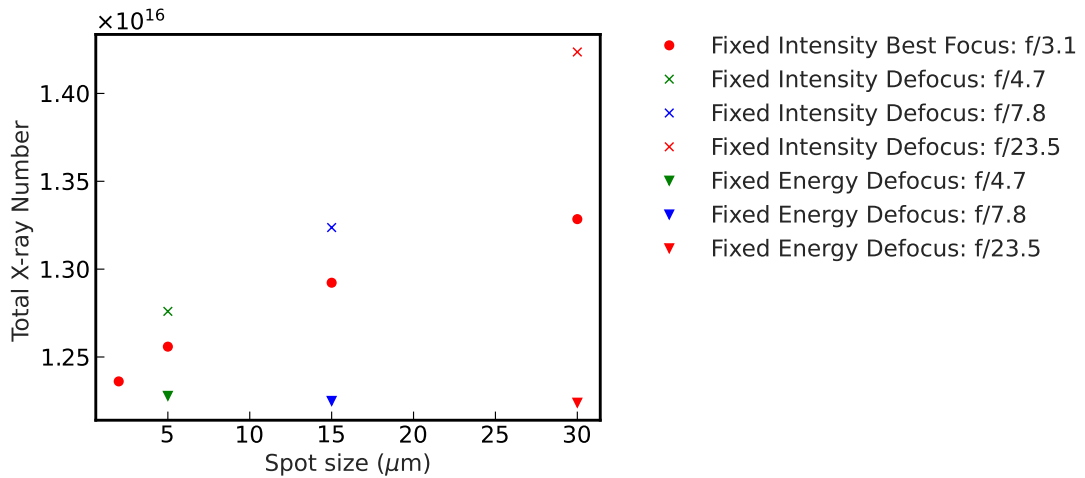


Figure 5.9: Total x-ray numbers as a function of spot size for each of the 2D PIC simulations, with the fixed intensity simulations in represented by crosses (defocus) and circles (best focus), and the fixed energy by triangles (defocus).

Bremsstrahlung x-ray numbers are found to scale strongly with pulse energy. The lower electron temperatures, total energies, and numbers (in Figures 5.4 and 5.5) were also found to scale with increasing pulse energy. As the energy within the electron spectrum increases along with the electron numbers and

temperatures, it is expected that bremsstrahlung numbers should also increase. As the bulk of the electron spectrum, contained within the high-flux and lower temperature component, increases in temperature, the electrons are of higher average energy and generate more bremsstrahlung photons [136]. For the fixed energy simulations, the total internal electron energies and lower temperatures remained fairly constant across the intensity range, resulting in largely unchanging bremsstrahlung numbers.

It is shown that the numbers of bremsstrahlung photons emitted by target electrons are largely influenced by laser pulse energy, whereas laser focal spot size has little effect. However, it is shown that pulse energy, spot size, and intensity influence the front of target electron population that is responsible for synchrotron x-ray emission. In the next section, the effects of spot size and pulse energy on both synchrotron and bremsstrahlung x-ray emission are considered, with a view to optimising synchrotron emission and minimising bremsstrahlung.

5.2.5 Spot size and energy dependence of bremsstrahlung and synchrotron emission

The influence of spot size and pulse energy on synchrotron and bremsstrahlung x-ray emission for intensities between $4.5 \times 10^{19} \text{ Wcm}^{-2}$ and $5 \times 10^{22} \text{ Wcm}^{-2}$, is investigated through 3D PIC modelling. In order to compare the above effects, modelling was performed with varying spot sizes and intensities, for both constant and increasing pulse energy. As outlined above, 3D PIC simulations were performed at two spot sizes for three intensity scans, with maximum intensities of $5 \times 10^{20} \text{ Wcm}^{-2}$, $5 \times 10^{21} \text{ Wcm}^{-2}$, and $5 \times 10^{22} \text{ Wcm}^{-2}$. These configurations are also described in Table 5.3. The photon numbers from both synchrotron, n_{sync} , and bremsstrahlung, n_{brem} , emission are extracted across the entire simulation box and are considered for each intensity case. In the simulations, the bremsstrahlung and synchrotron photons are generated by two separate modules and are defined as different photon species.

Figure 5.10 shows the photon numbers for two distinct spot sizes for both the

fixed intensity, 5.10(a), and fixed pulse energy, 5.10(b), simulations. In the fixed intensity case, in Figure 5.10(a), there is found to be a smaller drop in synchrotron numbers, n_{sync} , when decreasing the pulse energy and spot size from 5 to 1.5 μm compared to the bremsstrahlung numbers, n_{brem} , at the same intensities. For fixed energy, n_{sync} is much higher for the small spot, higher intensity data points, whereas the change in bremsstrahlung numbers is minimal with spot size and intensity.

In Vyskocil *et al.* [71], synchrotron and bremsstrahlung emission are compared at intensities of $3 \times 10^{21} \text{ Wcm}^{-2}$ and above. For CH targets, synchrotron emission is reported to have higher numbers of photons than bremsstrahlung, although the bremsstrahlung spectrum extends to higher energies. In the work presented here, a thicker target and higher- Z material is used compared to CH, for which higher bremsstrahlung photon numbers might be expected. As mentioned before, the short simulation duration will have the effect of cutting out later-time bremsstrahlung emission as the electrons continue to recirculate. Additionally, the target simulated in this work had a density of $9n_c$, which would also decrease the bremsstrahlung yield. In practice, the disparity in photon numbers between the two processes may be smaller. However, the relative dependencies on focal spot and energy demonstrated represent a significant insight and are not expected to change.

To quantify these changes, the ratios of n_{sync} and n_{brem} for each spot size are shown in Figures 5.10(c) and 5.10(d), for the fixed intensity and fixed energy simulations, respectively. The ratio of synchrotron and bremsstrahlung numbers for the fixed intensity data points, in Figure 5.10(c), show that, in all cases, the numbers are higher for the higher pulse energy, 5 μm spot. However, at $5 \times 10^{21} \text{ Wcm}^{-2}$, the synchrotron numbers are relatively higher for the lower energy, 1.5 μm spot. This suggests, particularly at the lower intensity, that there is a relationship between synchrotron emission and spot size. Figure 5.10(d) shows the same ratios for the fixed energy simulations. For each simulation pair, with maximum intensities of $5 \times 10^{20} \text{ Wcm}^{-2}$, $5 \times 10^{21} \text{ Wcm}^{-2}$, and $5 \times 10^{22} \text{ Wcm}^{-2}$, the energy is fixed whilst the spot size is changed. For each intensity pair, the

synchrotron numbers are much higher for the small spot than the larger. This, again, indicates not only an intensity dependence but a spot size dependence for synchrotron emission. Conversely, the bremsstrahlung numbers change by less than an order of magnitude in each simulation pair. The bremsstrahlung numbers are found to be less than an order of magnitude higher for the smaller spots and higher intensities. This aligns with the findings in the previous section, that bremsstrahlung emission is highly dependent on pulse energy.

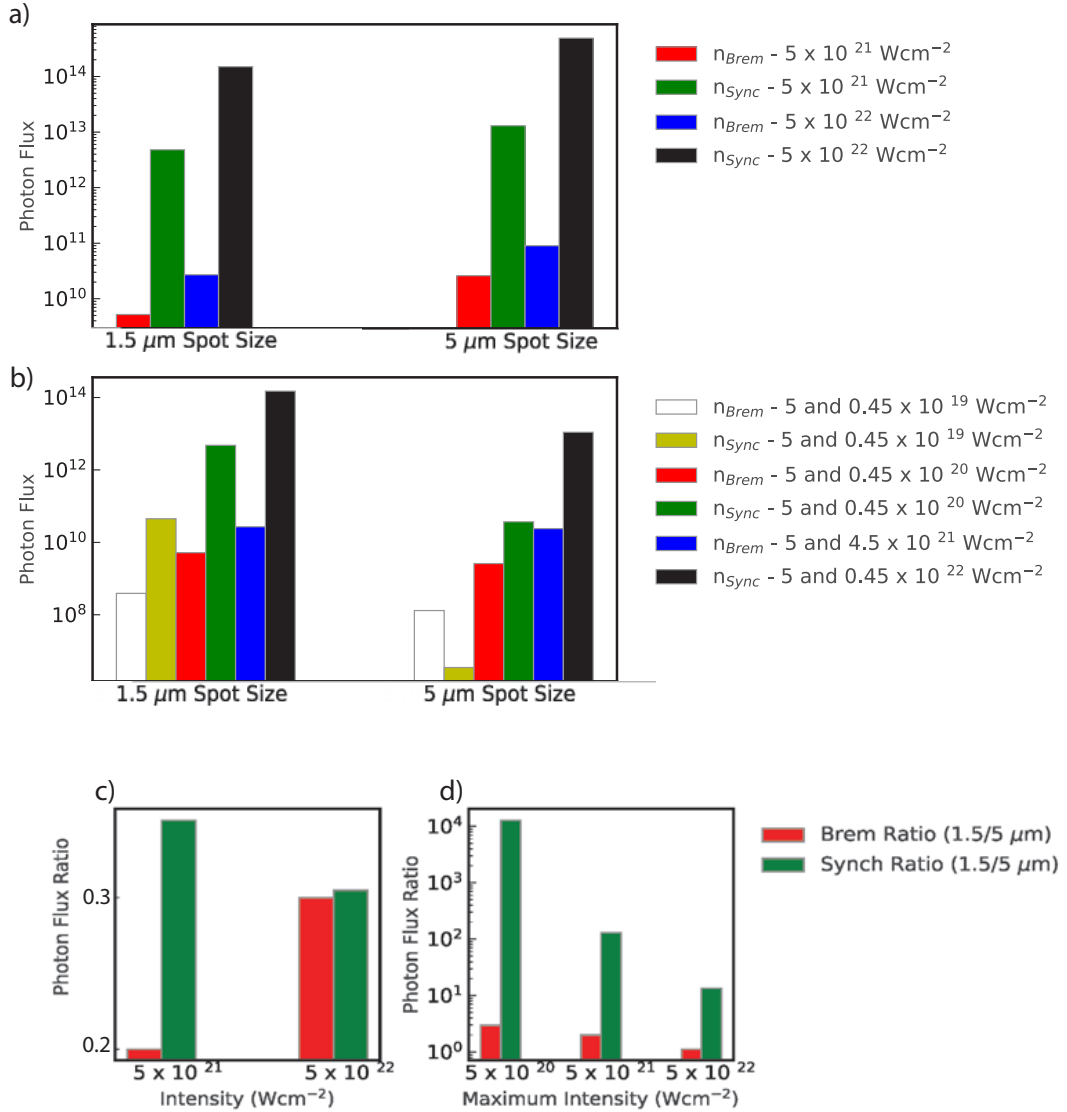


Figure 5.10: (a), photon numbers for $r_L = 1.5$ and $5 \mu\text{m}$ fixed intensity EPOCH 3D simulations, and (b), photon numbers for $r_L = 1.5$ and $5 \mu\text{m}$ fixed energy pair EPOCH 3D simulations (as outlined in Table 5.3). Ratio of photon numbers as a function of intensity for $r_L = 1.5 \mu\text{m}$ and $5 \mu\text{m}$ spot sizes, with bremsstrahlung emission in red and synchrotron emission in green from the (c), fixed intensity simulations, and (d), fixed energy pair (with maximum intensities labelled) simulations.

In order to investigate what is driving the differences in synchrotron numbers for different spot sizes, it is relevant to observe the electron density profiles within the simulations. The density profiles are taken along the $z=0$ plane, which cuts through the target along the laser axis. The final timestep electron density plots for each fixed energy simulation are shown in Figure 5.11. In these plots the front surface of the target can be seen at $x=0$. It is apparent that more holeboring occurs in the smaller spot cases, shown in Figures 5.11(b), 5.11(d), and 5.11(f), compared to the larger spot simulations on the left which experience this to a far lower level, Figures 5.11(a), 5.11(c), and 5.11(e). Notably, the lowest intensity case, shown in Figure 5.11(a), shows little holeboring. This is also the simulation for which there is almost no synchrotron emission. There is a clear link between synchrotron emission and holebore volume, as reported in Ridgers *et al.* [28].

To investigate this apparent trend between holeboring front and synchrotron numbers, one can map the photons onto the simulation grid and observe the spatial emission of each photon generation mechanism. Figure 5.12 shows the spatial emission of synchrotron, 5.12(b), and bremsstrahlung, 5.12(c), radiation alongside the electron density plot, 5.12(a), for the highest intensity case. As suspected, the synchrotron photons are emitted almost exclusively within the underdense holebore volume, whereas the bremsstrahlung emission occurs throughout the simulation (although largely along the critical surface boundary). Though not shown, this is apparent in each of the fixed energy simulations, aside from the lowest intensity which exhibits almost no synchrotron emission. This aligns with the nature of the two mechanisms: bremsstrahlung occurs due to the interaction of electrons and ions so it is intuitive that this emission occurs largely within the overdense target. Synchrotron emission in laser plasma interactions occurs due to electrons interacting with the relativistic laser fields, as such, this emission occurs where the laser is able to penetrate into underdense regions, such as the holebore regions seen here. This is shown in Figure 5.13, where the electron density and electric field strength are combined into one plot. It can be seen that the laser propagates into the holebore region within the target. Such a phenomenon is reported in Ridgers *et al.* [28], wherein synchrotron emission is produced by a

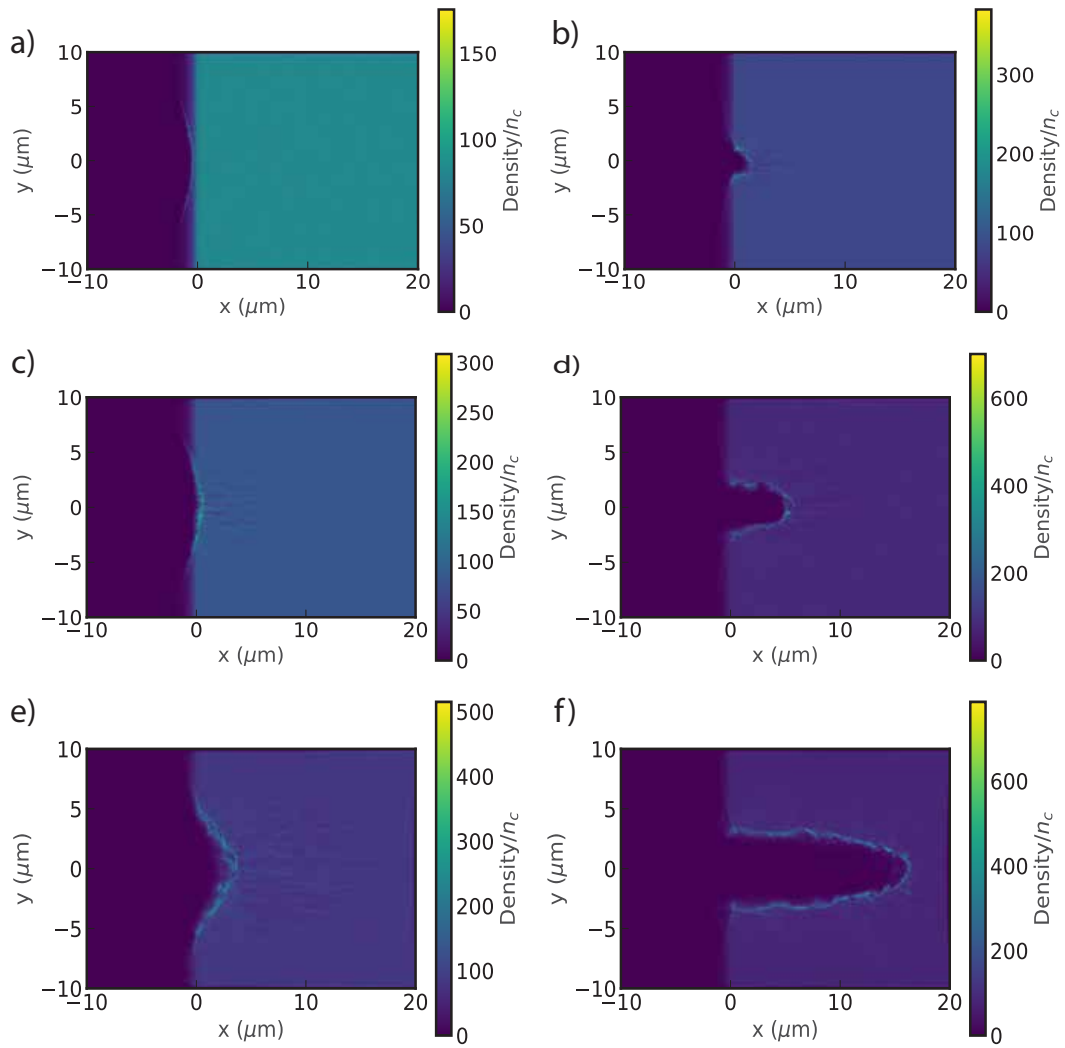


Figure 5.11: Final timestep electron density plots for pairs of fixed energy 3D simulations, with spot sizes of 5 and 1.5 μm , at the following intensities: (a), 4.5×10^{19} and (b), $5 \times 10^{20} \text{ Wcm}^{-2}$, (c), 4.5×10^{20} and (d), $5 \times 10^{21} \text{ Wcm}^{-2}$, and (e), 4.5×10^{21} and (f), $5 \times 10^{22} \text{ Wcm}^{-2}$

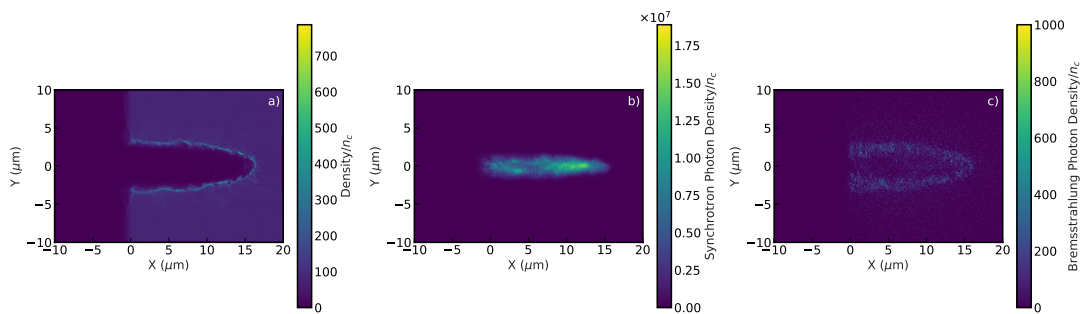


Figure 5.12: (a) electron density, (b) synchrotron emission density, (c) bremsstrahlung emission density for $5 \times 10^{22} \text{ Wcm}^{-2}$ simulation.

standing wave that is set up by the laser reflecting from the critical surface.

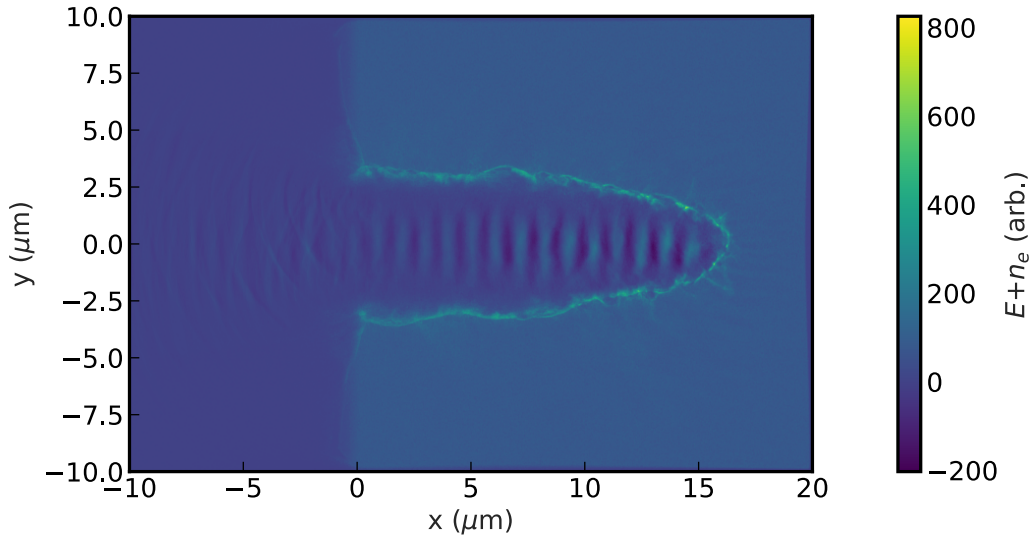


Figure 5.13: Combined E -field and electron density plot for final time step of $5 \times 10^{22} \text{ Wcm}^{-2}$ simulation.

As both the hole volumes and synchrotron numbers appear to increase with increasing laser intensity and decreasing spot size, it is important to quantify the relationship between the two. Here, the holebore volume is defined as the volume past the front target surface, at $x=0$, where the electron density is below the relativistic critical density. These volumes were measured by generating a binary mask which was equal to one where the electron density was below critical, and equal to zero for higher densities. The mask values for coordinates above $x=0$ were then summed to find the holebore volume in terms of simulation cells. The resolution of the simulation could then be used to determine the hole volume in terms of micrometers cubed. Figure 5.14(a) shows the volumes of each bored-out region, which increases with intensity for both spot sizes. Figure 5.14(b) shows the synchrotron numbers for each fixed energy simulation as a function of holebore volume. It is important to note that between each pair of fixed energy points there is a ten times energy increase. It is clear that pulse energy has less of an effect in the production of synchrotron x-rays and instead it is entirely spot size/intensity related, which is a result found in the majority of work on synchrotron emission [73, 139].

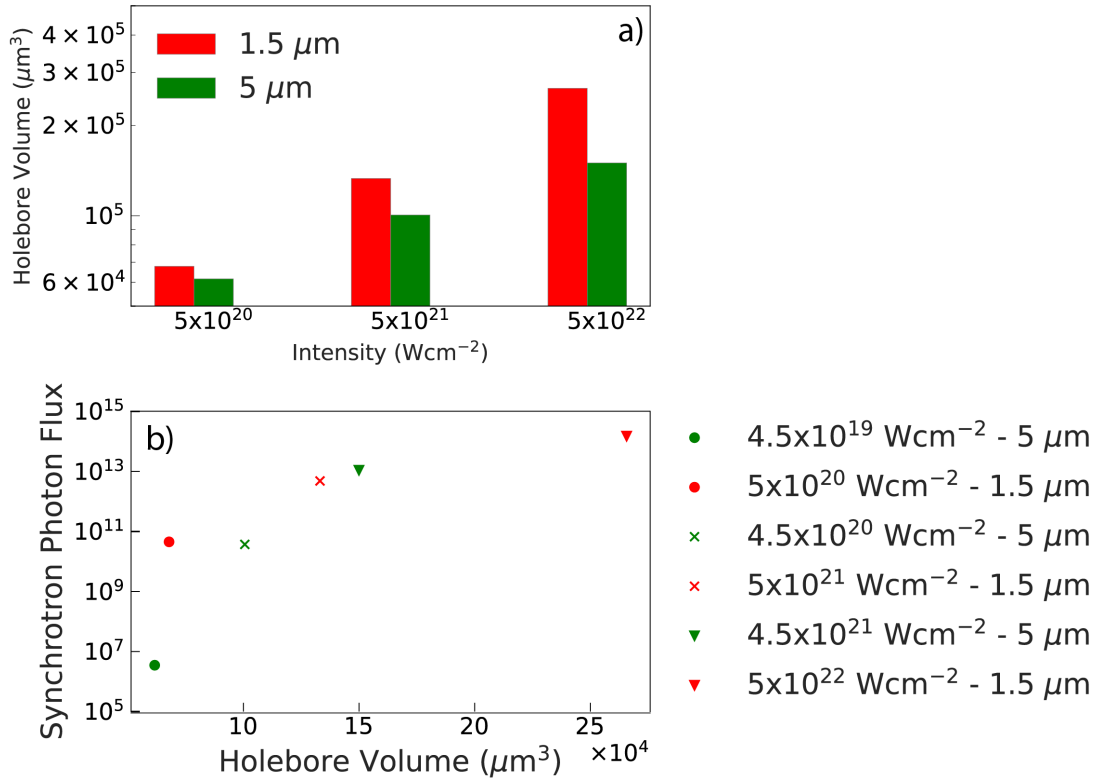


Figure 5.14: (a): Holebore volumes for fixed energy simulations with spot sizes of $1.5 \mu\text{m}$ (red) and $5 \mu\text{m}$ (green). Intensity axis shows maximum intensity of fixed-energy simulation pair. (b): numbers of synchrotron photons as a function of simulation holebore volume for fixed energy simulations. Spot sizes shown in red, $1.5 \mu\text{m}$, and green, $5 \mu\text{m}$. Intensity ranges represented by circles, $4.5 \times 10^{19} - 5 \times 10^{20} \text{ Wcm}^{-2}$, crosses, $4.5 \times 10^{20} - 5 \times 10^{21} \text{ Wcm}^{-2}$, and triangles, $4.5 \times 10^{21} - 5 \times 10^{22} \text{ Wcm}^{-2}$.

The smaller focal spots induce significantly deeper and larger-volume underdense holes within the target. Within these underdense regions, the laser can continue to propagate and, as the holes are both deeper and wider, the laser field has the opportunity to directly interact with a higher number of electrons. It is the higher number of fast electrons oscillating directly in the laser field that is generating a higher numbers of synchrotron photons. Not only are there more electrons for the laser to interact with, but there is a higher field strength accelerating the electrons, which is leading to higher numbers and energies of synchrotron photons, shown in Figure 5.15, which shows synchrotron spectra for the $1.5 \mu\text{m}$, $5 \times 10^{20} \text{ Wcm}^{-2}$ simulation (red) and $5 \mu\text{m}$, $4.5 \times 10^{20} \text{ Wcm}^{-2}$ simulation (green). Within these data points, the $5 \mu\text{m}$ simulation has ten times more energy in the laser pulse compared to the $1.5 \mu\text{m}$. Despite this, the $1.5 \mu\text{m}$ case with a similar intensity clearly has a far higher numbers but also reaches

higher photon energies compared to the $5 \mu\text{m}$ case. This further emphasises the spot size and field strength enhancement of synchrotron emission, even at lower laser intensities.

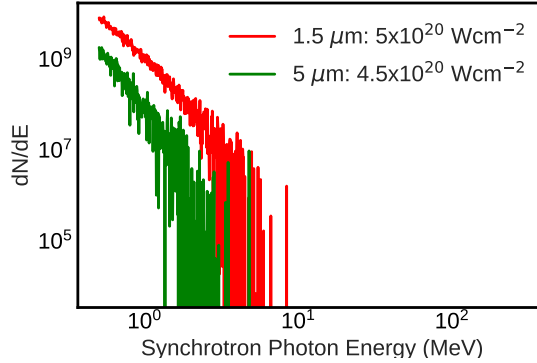


Figure 5.15: Synchrotron spectra for $1.5 \mu\text{m}$, $5 \times 10^{20} \text{ Wcm}^{-2}$ simulation (red) and $5 \mu\text{m}$, $4.5 \times 10^{20} \text{ Wcm}^{-2}$ simulation (green). The $5 \mu\text{m}$ simulation has ten times more energy in the pulse compared to the $1.5 \mu\text{m}$.

To enhance synchrotron emission, particularly at lower laser intensities, it is shown to be important to use as small a focal spot as possible. It is shown that the majority of bremsstrahlung emission occurs just past the critical surface where electrons are ponderomotively ejected into the target, whereas synchrotron photons are emitted where electrons can directly interact with the laser in underdense regions. By using a smaller focal spot and lower pulse energy, the underdense region where synchrotron emission occurs is maximised and the more energy-dependent bremsstrahlung process is minimised in comparison. In combination with the results from the previous section, it is shown that to use a small, best focus spot, is advantageous for minimising bremsstrahlung emission as lower pulse energies can be used to reach the same intensity and the extent of the spot encompasses a smaller volume of the target within which electrons can be driven into the overdense target and interact with target ions.

5.3 Conclusion

The influence of laser focal spot size and focusing geometry on x-ray production and electron acceleration is considered. PIC simulations were performed to fur-

ther investigate the effects of energy, spot size and focusing geometry on x-ray generation. It is found that there are very few focusing geometry effects on the interaction, with only the front surface and internal target electron spectra experiencing changes between corresponding best focus and defocus cases. While there are differences in interactions between best focus and defocus laser focal spots and solid targets, these differences in electron and x-ray spectra are not large enough to be seen experimentally. The bremsstrahlung module in EPOCH was used to generate x-ray spectra in these simulations. In both the fixed energy and fixed intensity cases the bremsstrahlung spectra are similar, although slight differences in x-ray numbers between the best focus and defocus cases are found, up to 15% for the largest spots. However, still, the most prominent effect is that of increasing pulse energy to maintain the fixed intensity.

3D PIC simulations were also performed to probe the effects of spot size and pulse energy not only on bremsstrahlung production but also synchrotron emission, for fixed energy and fixed intensity independently. It is found, again, that x-ray emission due to the bremsstrahlung mechanism is highly pulse energy dependent, with a much smaller dependence on spot size. However, synchrotron emission is highly spot-size and intensity dependent. Through further analysis of the simulation electron densities and spatial photon emission, it is found that synchrotron photons were emitted almost exclusively within the relativistically underdense volume that the laser pulse bores through the target. It is also found that the number of synchrotron photons is related to the size of this volume, which is in turn dictated by the size of the laser focal spot and laser intensity. Additionally, despite having a $10\times$ lower pulse energy than the like-intensity $r_L = 5 \mu\text{m}$ simulations, the $r_L = 1.5 \mu\text{m}$ simulations resulted in increased maximum synchrotron photon energies as well as higher synchrotron photon numbers compared to the larger spot simulations of the same laser intensity. To summarise, it is found that to enhance synchrotron emission, it is best to use not only a higher laser intensity but also the smallest spot possible to enhance holeboring.

This can be advantageous in the attempt to experimentally measure synchrotron radiation. In such campaigns there is the difficulty of distinguishing

synchrotron photons from bremsstrahlung photons, which are generally abundant in laser-plasma interactions, particularly for thick targets. In the new, high repetition-rate regime of ultra-intense lasers which may require the use of thicker, high repetition-rate targets, the results presented here offer an approach to achieve enhanced synchrotron production. The findings here suggest that, by increasing the laser intensity through decreasing spot size, rather than by increasing the pulse energy, one can enhance synchrotron emission and suppress bremsstrahlung emission.

In the next chapter, experimental work to investigate the influence of spot size and pulse energy on bremsstrahlung emission is presented. The next chapter aims to test the conclusions reached in this chapter regarding bremsstrahlung production.

Chapter 6

Experimental investigation of the role of focal spot size and pulse energy in bremsstrahlung production in thick targets

6.1 Introduction

In the last chapter, the effects of laser pulse energy and spot size on electron acceleration and the bremsstrahlung and synchrotron x-ray emission mechanisms were investigated through 2D and 3D PIC simulations. This chapter reports on the experimental investigation of the effects of pulse energy and spot size on electron heating and bremsstrahlung production. Bremsstrahlung emission was found to be largely dependent on laser pulse energy, whereas the synchrotron emission mechanism was found to be highly dependent on laser intensity and spot size, due to the presence of holeboring by the laser into the overdense target. Whilst this is difficult to experimentally investigate, as current laser intensities are not high enough for efficient synchrotron x-ray production, the effects of pulse energy and spot size on bremsstrahlung emission can be verified.

The overarching purpose of this work is to ascertain whether bremsstrahlung production can be minimised in future experiments to investigate synchrotron

generation. Bremsstrahlung spectra, even at the higher experimentally available laser intensities of $5 \times 10^{21} \text{ Wcm}^{-2}$, can be similar in spectral shape and flux to synchrotron emission spectra, and can therefore be difficult to differentiate. The results reported in the previous chapter indicate that the best way to achieve maximum synchrotron emission and minimise bremsstrahlung emission, for thick targets, is to reduce the laser focal spot size to increase the laser intensity, rather than by increasing the pulse energy.

The work in this chapter investigates how varying laser focal spot size and pulse energy influences energy absorption, particle acceleration, and bremsstrahlung x-ray production. It is shown that smaller laser spot areas lead to larger increases in both x-ray and electron spectrometer signals, as well as maximum electron energies, when increasing laser intensity. It also shows that pulse energy plays a more critical role in bremsstrahlung production, with higher energies on target resulting in significantly higher x-ray and escaping electron fluxes. These results, supported by experimental data and previous numerical modeling, suggest that experiments using future high-intensity laser systems can minimise bremsstrahlung signal by lowering pulse energies.

6.2 Experimental method

The purpose of this work is to investigate the effects of spot size and focusing geometry on bremsstrahlung x-ray emission. Studies investigating the effect of changing spot size by defocusing the target have been performed and, given the work in Dover *et al.* [110] on spot size limiting effects, it is imperative to understand how focusing geometry, and hence spatial intensity profile affects electron acceleration and bremsstrahlung x-ray emission. As the target moves into the focusing beam, the spatial intensity profile moves from a Gaussian shape to a flat top, which is typical for a beam that is not perfectly Gaussian in nature [156]. With a flat-top distribution, and therefore a more uniform spatial intensity, it is important to understand whether the same limiting effects are present.

In order to experimentally achieve this aim, a technique was used to effectively

Beam Diameter (mm)	$F/\#$
270	1.7
180	2.6
90	4.6

Table 6.1: Beam sizes and F -numbers ($F/\#$) achieved through the use of apodisers.

change the F -number without changing the main focusing optic. To achieve this, apodisers were used to decrease the beam size. With a focusing optic of constant F -number, and a decreasing beam size, larger F -numbers are obtained. A description of Gaussian beam expansion is provided in Chapter 4. The F -number ($f/\#$) of a focusing optic is defined as $f/\# = f/D$, where f is the focal length of the focusing optic and D is the optic diameter. To achieve higher F -numbers, the collimated beam was apodised to beam diameters of 180 and 90 mm, from a diameter of 270 mm and an F -number of 1.7, corresponding to F -numbers of 2.6 and 4.6.

This experiment was performed using the PHELIX laser near Darmstadt, Germany, which was chosen because of its low F -number, $F/1.7$ off-axis parabola (OAP) focusing optic, high available pulse energy, and relative stability in pulse energy [183, 184]. S-polarised pulses, with varied energy according to the unfocused beam diameter, a central wavelength of $1.053 \mu\text{m}$ and an angle of incidence of 20 degrees to target normal were delivered onto $25 \mu\text{m}$ thick Cu targets. The temporal laser intensity contrast was measured previously to be 10^{-12} at 1 ns and 10^{-10} at 10 ps, prior to the peak of the pulse [183].

By changing the effective F -number of the system, the focal spot was varied in the range of 3.5 to $8 \mu\text{m}$ (FWHM) at focus and, by defocusing the beam, spot sizes in the range of 10 - $35 \mu\text{m}$ (FWHM) were achieved. The focal spot distributions of the low power alignment beam, the main beam with some of the amplifiers switched off, were recorded during target alignment before each shot. The spots varied in spatial distribution between the at-focus and defocus shots, wherein the defocus spots had a top-hat-like distribution as opposed to the approximately Gaussian spatial distributions of the at-focus spots, shown in Figure 6.1.

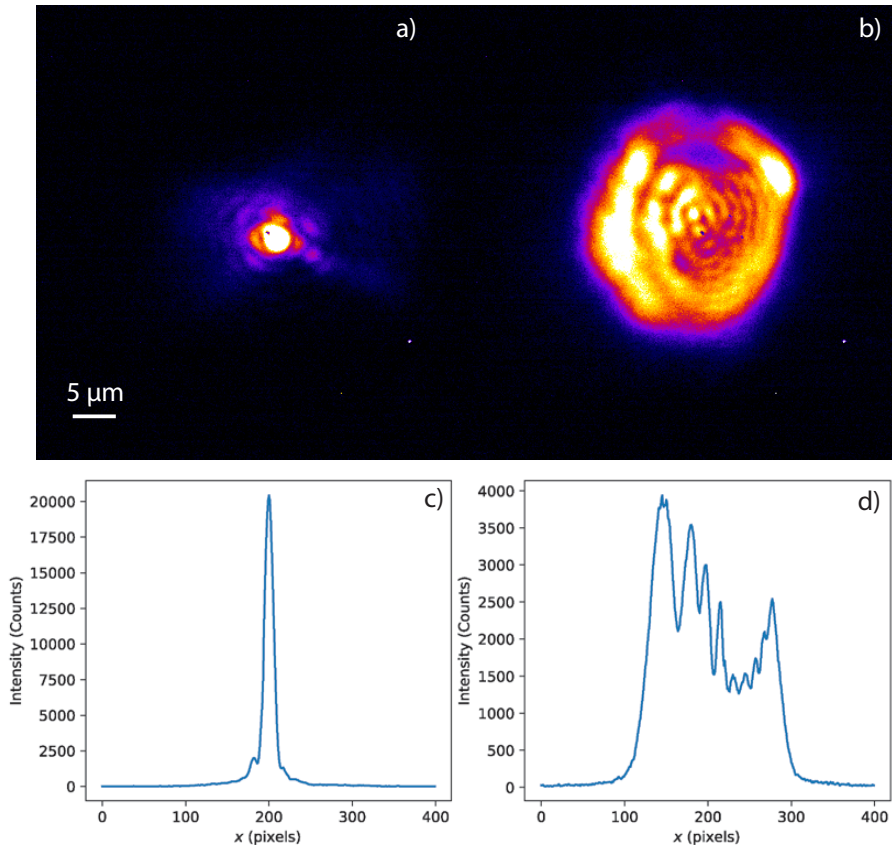


Figure 6.1: (a) Best focus focal spot with Gaussian spatial distribution, (b) defocus focal spot with approximate top-hat distribution, (c) intensity profile of best focus focal spot, showing Gaussian spatial distribution, (d) intensity profile of defocus focal spot, showing approximately top-hat spatial distribution.

The energy was changed for each beam size/apodiser, wherein the energy was decreased as the beam diameter was decreased in order to keep the intensity constant between F -number geometries. For the $F/1.7$ geometry, the pre-compressor energy was around 140 J, the $F/2.6$: 50 J and the $F/4.6$: 23 J. The variation in laser energy was achieved by rotating a calibrated wave plate between two crossed polarisers between the front end and preamplifier. Through this, an intensity range of between 1×10^{18} and $2 \times 10^{20} \text{ Wcm}^{-2}$ was achieved. The range of F -numbers available, compared to the simulations from the previous chapter, was much smaller, as the beam could only be apodised a finite amount, with the smallest beam size of 90 μm.

The x-ray signal measurements reported in this chapter were made using a linear absorption x-ray spectrometer. The diagnostic consists of one-dimensional array of LYSO scintillators which are attenuated by tungsten deeper into the

array. The array is imaged with a CMOS camera and the sum of the crystal signals is used as a measure of energy within the incident x-ray spectrum. Chapter 6 will focus on the use of this diagnostic to resolve x-ray spectra. Here, the spectrometer is used as a measure of the total x-ray flux as, at the intensity range explored within this work, the uncertainty in spectral measurements with this spectrometer design are high, as discussed in Chapter 7.

Measurements of the electron fluxes were also made. The magnetic field strength in the electron spectrometer was 0.07 T and was not large enough to accurately resolve electron energies, however the total electron signals could be recovered. A more detailed description of this diagnostic can be found in Chapter 4.

6.2.1 Laser focal spot size measurements

Step	Operation
1.	Laplacian operator applied to image
2.	Image threshold applied
3.	Contours of gradient found
4.	Outermost contour filled
5.	Mask created
6.	Mask applied to measure encircled energy
7.	Mask area calculated to find spot size

Table 6.2: Flow of code used to calculate laser focal spot areas and encircled energies from focal spot data.

Gaussian fitting was used to quantify the sizes and encircled energies of the focal spot measured close to best focus, given that they had an approximately Gaussian spatial intensity profile. This approach was found not to be suitable for the top-hat-like distributions of the defocused focal spots as the spatial intensity distributions were no longer Gaussian. Due to this, a code incorporating an edge detection function was developed to detect the edges of the focal spot. The main steps within the focal spot measurement code are outlined in Table 6.2. A Laplacian operator, which returns the divergence of the intensity gradients within the image, is applied to the image before a threshold is applied, such that the contours of each sharp gradient in the image are returned. The outermost

contour of the image is selected in order to create a mask wherein the values within the contour are equal to 255, and the values outside this area are equal to zero. This mask can be summed to calculate the spot area in image pixels. It can also be multiplied by the focal spot image to retrieve the signal within the defined area. This can be used to calculate the percentage of energy encircled within the masked focal spot. The transformation of the focal spot image with each step of the process can be seen in Figure 6.3. The asymmetric nature of the large focal spots and the resulting method of measuring their size dictates that a more appropriate description of laser focal spot size is ‘spot area’, as there is no singular, defining radius of the spot. As such, the experimental results in this chapter will be reported in terms of spot area, in units of μm^2 .

In order to test the focal spot measurement code a series of images with flat top distributions of varying radii were generated, some example 1D spatial distributions are shown in Figure 6.2(a). It was found that, as long as the outermost Laplacian gradient contour stayed within the confines of the image, the area containing 99.7% of the signal in the image was reliably retrieved. This was compared to a calculation of the width of the distribution which was calculated at 1% of the total cumulative signal, which is shown in Figure 6.2(b). Example images of the algorithm are shown in Figures 6.2(c)-6.2(f), corresponding to steps 1., 2., 3., and 5. in Table 6.2. The uncertainties associated with this measurement are the difference in areas between the contour found and the next smallest contour. This also gives the uncertainty in the encircled energy measurement, as the difference in encircled energies between these two contours is also calculated for each focal spot. Using these calculations, and the associated uncertainties in the laser energy, compressor throughput, and pulse duration measurements, the intensity uncertainties are calculated.

6.3 Experimental results

Presented here are the results from the PHELIX experimental campaign. The signals from x-ray and electron spectrometers are discussed with respect to the

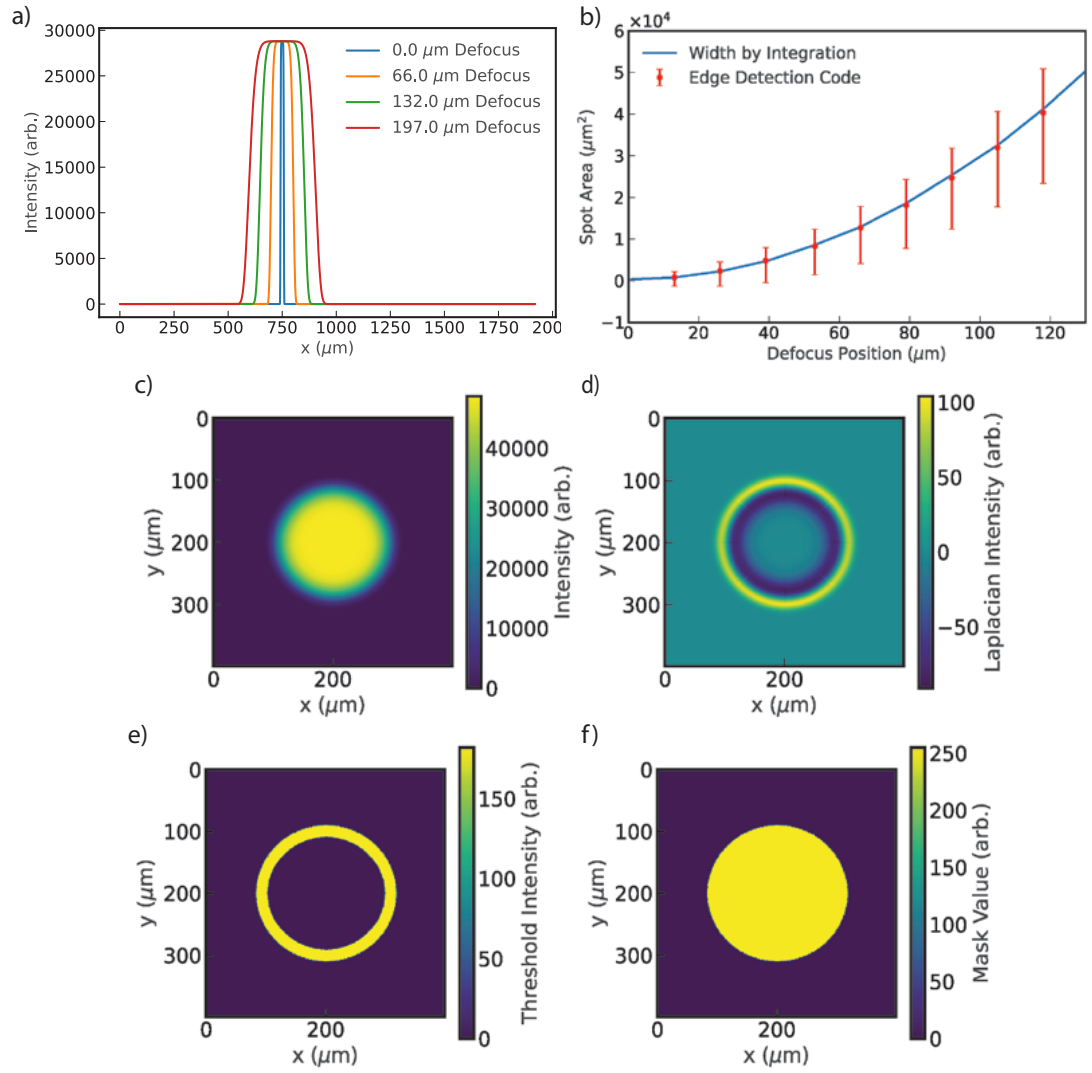


Figure 6.2: In (a), intensity profiles as a function of space in x for flat-top-like distributions at 0, 66, 132, and 197 μm from focus, (b), spot areas as a function of distance from focus for integration method of finding spot size (blue line) and the developed edge detection code (red circles), (c), image of test focal spot with flat-top-like distribution, (d), Laplacian differential of the test image, (e) thresholded Laplacian gradient showing contours, and, (f), mask generated using outermost contour.

laser focal spot-sizes, focusing geometries, and energies probed within the experimental campaign. Firstly, the effects of using different focusing geometries on emitted radiation are reported, with energy-normalised comparisons of signal as a function of laser intensity. Then, the effects of spot-size and pulse energy are compared with respect to x-ray and electron production.

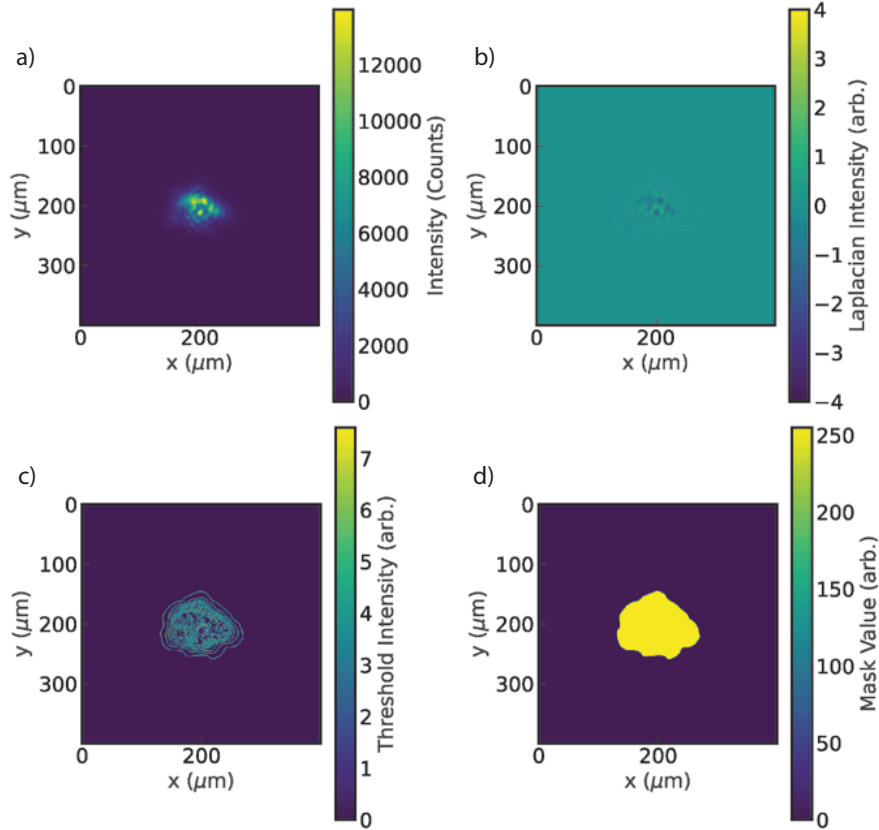


Figure 6.3: (a), image of focal spot, (b), Laplacian differential of the focal spot image, (c), thresholded Laplacian gradient showing contours, and, (d), binary mask generated using outermost contour.

6.3.1 Focusing geometry

A parameter space featuring a large range of best focus and defocus spot-sizes for three distinct focusing geometries ($F/1.7$, $F/2.6$ and $F/4.6$) was investigated. The range of experimental energy on target values and spot sizes are presented as a function of experimental shot number in Figures 6.4(a) and 6.4(b). The range of focal spot sizes measured span from 10 to 2500 μm^2 , corresponding to the best focus $F/1.7$ shots and defocused $F/1.7$ and $F/2.6$ shots with the target positioned at a maximum distance of 150 μm from the focal plane. Overall, 50 shots were taken however, the data sets reported in this chapter require the use of like-energy and spot size data points, which narrows down the number of usable measurements. The full range of energies and spot areas from the campaign are shown in Figure 6.4.

As previously noted, the pulse energy was decreased as the beam was apodised

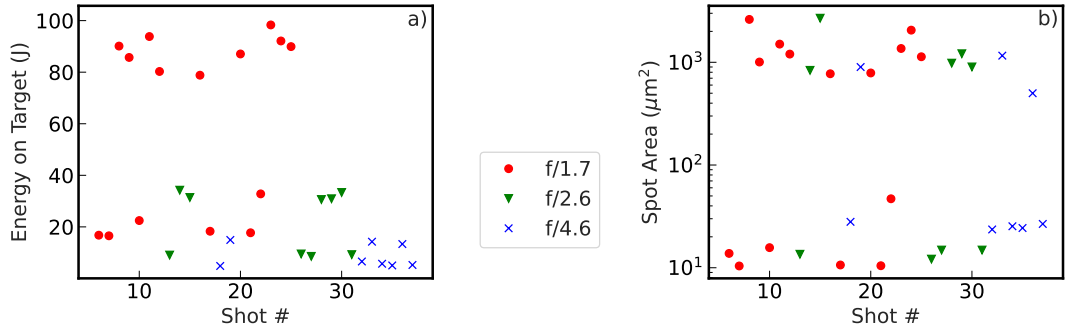


Figure 6.4: Plots illustrating the investigated pulse energy and focal spot size ranges: in (a), energy on target as a function of experimental shot number, (b), laser focal spot area as a function of experimental shot number, each for three different focusing geometries: $F/1.7$ (red circles), $F/2.6$ (green triangles), and $F/4.6$ (blue crosses).

in order to keep the intensity constant between focusing geometries. Therefore, to compare only the spot-size and focusing geometry effects for similar intensity data points, the signals were normalised for energy on target. The energy on target is calculated using the pre-compressor energy value, calibrations performed during the experiment using a calorimeter to measure compressor efficiency, and a measurement of the amount of energy contained within the focal spot (within the FWHM for the at-focus Gaussian spots and within the total spot area for the defocused spots). It will be seen later in this section that there is a relatively linear relationship between the spectrometer signals and energy on target.

Figure 6.5 shows the x-ray spectrometer signal, background-subtracted (see Chapter 4) and normalised for energy on target, plotted as a function of laser intensity for all three focusing geometries. Shown here are both best focus and defocus data points, which gives a larger range of intensities. When energy-normalised, the relationship between x-ray spectrometer signal and intensity is not linear. There is a large amount of scatter in the points, with two similar intensity data points around $1 \times 10^{21} \text{ Wcm}^2$ showing a doubling in signal. This could be caused by any of the contributing factors constituting laser intensity, such as the pulse duration or different relative spot size, or by some other parameter such as the pre-plasma scale length, which is shown to heavily affect energy absorption by the target [229–231]. This would be an important consideration for future experiments.

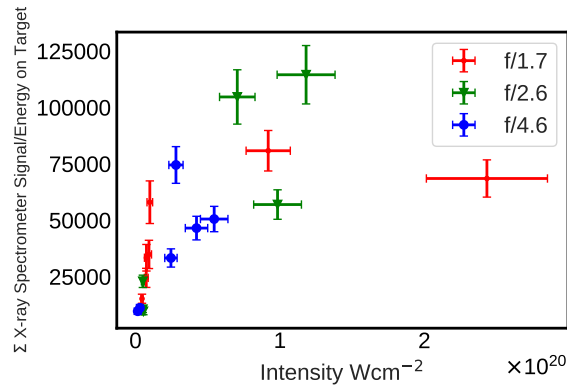


Figure 6.5: Experimental sum of x-ray spectrometer signal as a function of incident laser intensity for 3 different F -numbers: $F/1.7$ (red points), $F/2.6$ (green triangles), and $F/4.6$ (larger blue points).

With the scatter of the points, it is unclear whether there is an effect of focusing geometry on bremsstrahlung x-ray production. One issue is that, because the pulse energy was decreased as the beam was apodised, further apodising the beam would leave too little energy in the pulse for bremsstrahlung x-ray emission to be reliably bright enough on the x-ray spectrometers. Due to this, only a small range of best focus spot sizes could be probed, with very few similarly sized best focus and defocus spots to compare. To truly probe this parameter space, a higher number of data points is likely required, alongside a larger range of F -numbers, requiring a higher energy system or diagnostics of a much higher dynamic range.

In cases where there is a large scattering of points, it can be important to consider whether there are unquantified laser parameters, such as temporal intensity contrast, that are driving changes in the pre-plasma conditions. The pre-plasma or density gradient at the front of the target has been shown to strongly affect laser energy absorption [227, 228, 231] and can also affect the transport of electrons [232, 233]. It is important to note that it was not possible to make direct pre-plasma measurements and this may be contributing to the uncertainty in x-ray and electron measurements.

6.3.2 Energy on target for fixed spot size

A key parameter to consider when increasing laser intensity is the pulse energy. In order to consider the effects of pulse energy and, more specifically, energy on

target on x-ray generation and electron production, data points of fixed spot size and pulse duration were considered. Shown in Figure 6.6 are the x-ray spectrometer signals as a function of energy on target for best focus shots with three focusing geometries. The data points shown here have a pulse duration of (850 ± 130) fs, which is the average pulse duration ($\pm 15\%$) for the entire experimental campaign. The y-axis error bars are given by the standard deviation of the signal, measured across the area of the crystal, and, where energy normalised, the error in the energy on target fit, as outlined in Section 6.2.1. The x-axis error bars are given by the uncertainties in the measurements of laser parameters contributing to the calculated intensity, namely the pulse duration, pulse energy, and spot size calculations, also outlined in Section 6.2.1. Although there is some scatter present, there is a clear relationship between x-ray flux and energy on target regardless of focusing geometry and spot size, with an R^2 value of 0.72. It is logical that the energy deposited into the x-ray spectrometer, given by the

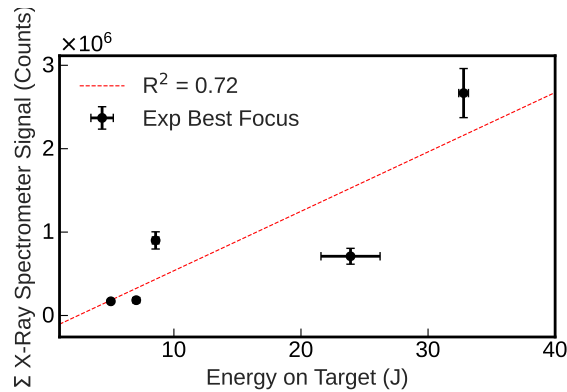


Figure 6.6: Experimental sum of x-ray spectrometer signal as a function of energy on target.

signal on the spectrometer, and therefore the amount of energy present in the bremsstrahlung spectrum, increases as the energy on target increases. If there is more energy present for target electrons to absorb, it is reasonable that they will also have more energy to emit in the form of bremsstrahlung x-ray radiation. To further investigate the behaviour of electrons accelerated during the interaction, the total electron signal from the electron spectrometer was measured. The electron numbers are calculated using a calibration of the signal loss with each rescan of the IP (method described in Chapter 4), a conversion between IP signal

and PSL intensity, and the efficiency of BAS-TR IP for electrons in the roughly 1 - 30 MeV range measured by Bonnet *et al.* [189]. In Figure 6.7, the electron flux/signal is presented as a function of energy on target for two different F -numbers: $F/1.7$ and $F/2.6$. The escaping electron flux is also seen to be closely related to energy on target: a linear fit with an R^2 value of 0.85 was applied to the data. This suggests that, as the energy in the interaction increases, so too does the number of escaping electrons. As the escaping electron flux increases, the temperature of the spectrum is likely also increasing, as more electrons are able to escape the sheath field on the rear surface of the target. The relationship

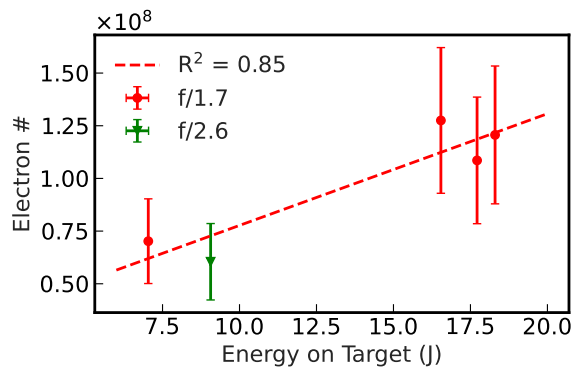


Figure 6.7: Experimental electron signal as a function of energy on target for 2 different effective F -numbers: $F/1.7$ (red points) and $F/2.6$ (green triangles).

between secondary particle flux and energy on target is clear. As the amount of energy available to the interaction increases, more energy is absorbed by the electrons which then emit bremsstrahlung x-rays and escape the target in larger numbers. However, given the work reported in Gray *et al.* [98] and Brenner *et al.* [106], it is important to consider the efficiency of absorption of energy available given the other variables in the interaction. These studies show that increasing laser focal spot size by defocusing the beam increases laser energy absorption and higher available pulse energies provide more energy to transfer the to electrons. To characterise the impacts of both parameters in the context of varying laser intensity, experimental points where the spot size was fixed or where the laser energy was fixed are considered.

6.3.3 Comparison of spot size and energy effects

With many new laser facilities opting for tighter focusing and shorter pulse lengths to achieve higher intensities, as opposed to increasing the pulse energy, which brings the risk of damaging optics within the laser chain, it is imperative to quantify the effects of each method on electron acceleration and secondary radiation production. In this chapter, the effects of changing spot size and pulse energy are considered. In order to further quantify the scaling of bremsstrahlung x-ray flux with fixed spot size laser intensity change, the bremsstrahlung x-ray flux from constant spot area (15 ± 1.5) μm^2 and pulse duration (850 ± 130) fs data points were considered, with on target pulse energies varied in the range of 7 - 18 J. In addition to the energy scaling we have observed, we investigate the bremsstrahlung x-ray flux scaling with spot size, considering constant energy ((30 ± 4.5) J on-target) and pulse duration (850 ± 130) data points.

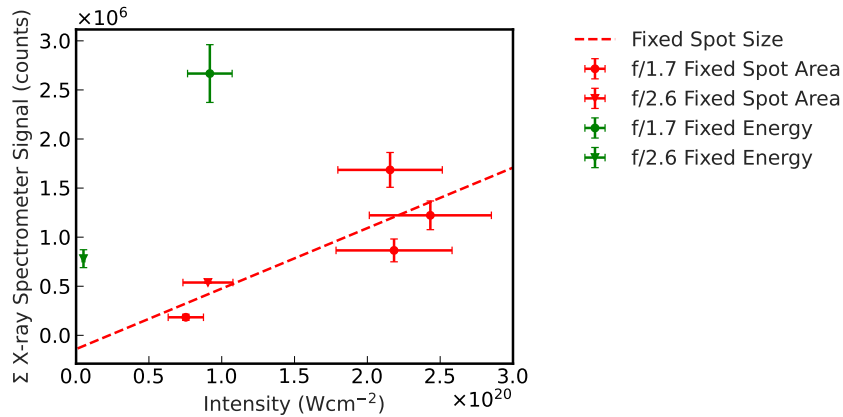


Figure 6.8: Experimental sum of x-ray spectrometer signal as a function of intensity for fixed pulse energy (green) and fixed spot area (red) on target for different effective F -numbers: $F/1.7$ (circles) and $F/2.6$ (triangles). Energy on target for green points is 33 J whereas energy on target for red points is 7-18 J.

The x-ray spectrometer signal for these points is shown as a function of laser intensity in Figure 6.8, with the constant spot area points in red and constant pulse energy in green. The uncertainty of these signals is given by the total of crystal standard deviation. In this figure, data points using different focusing geometries were used, with $F/1.7$ points indicated by circles and $F/2.6$ points indicated by triangles. Measurements using similar focusing geometries were

used in order to increase the number of data points available for analysis, as it is shown that such similar focusing geometries have no measurable influence on the secondary radiation produced. The x-ray spectrometer signal appears to increase faster with intensity when decreasing the spot size. However, this trend is not very well defined given the small number of data points. Within the bounds of experimental uncertainty there are essentially two data points. Thus, while the exact nature of the trend cannot be determined, it is evident that the signal is increasing faster with focal spot-size-driven intensity changes. The data shows that the points with the highest pulse energies (fixed energy in green) have the highest bremsstrahlung x-ray signals, which suggests that there are higher x-ray yields for higher pulse energies. This is in accordance with the results from the previous chapter. Gray *et al.* [98] reports that the absorption of laser energy with varying pulse focus has a higher absorption fraction at lower laser intensities than for varying pulse energy, with which a shallower increase in bremsstrahlung x-ray energy with intensity might be expected. However, the overriding result is that the bremsstrahlung x-ray flux is higher for higher pulse energy at the same laser intensity. It is worth noting here that the increase in x-ray spectrometer signal with laser intensity increases, when decreasing spot size, is likely to plateau as, given by the work in Dover *et al.* [110], the acceleration of electrons will become limited by near diffraction-limited spot sizes.

To further investigate the absorption of laser energy by the fast electron population, the measured electron flux and maximum energy are considered. A similar trend is found in the escaping electron signal, shown as a function of intensity in Figure 6.9. Again, a steeper scaling with varying spot area is found compared to the energy-driven intensity increase, but the overall escaping electron numbers are higher for the larger pulse energies of the fixed energy data points. To further test this hypothesis, the relationship between maximum electron energy and laser intensity was investigated. The measured maximum electron energies are plotted as a function of laser intensity in Figure 6.10, for fixed pulse energy (green) and fixed spot area (red). The uncertainties for this measurement are calculated using the image plate resolution and the energy resolution of the spectrometer, which is

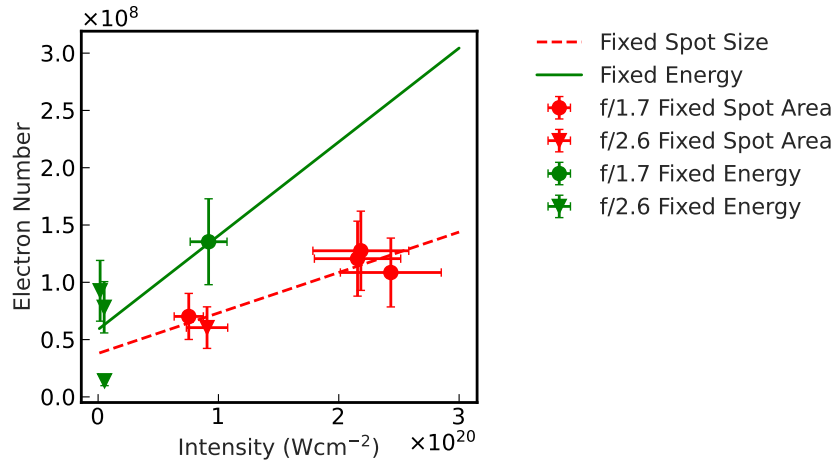


Figure 6.9: Signal from electron spectrometer as a function of intensity for fixed pulse energy (green) and fixed spot area (red) on target for different effective F -numbers: $F/1.7$ (circles) and $F/2.6$ (triangles).

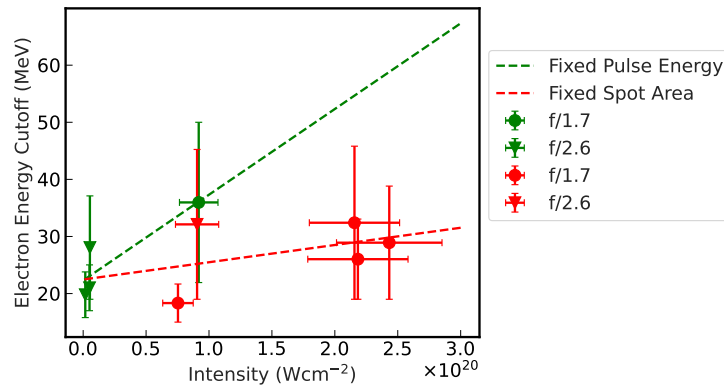


Figure 6.10: Experimental maximum electron energies from electron spectrometer as a function of intensity for fixed pulse energy (green) and fixed spot area (red) on target for different effective F -numbers: $F/1.7$ (circles) and $F/2.6$ (triangles).

large due to the low magnetic field used. It can be seen that, although the errors are large, the general trend in maximum electron energy is steeper with intensity for the fixed energy data points. Although the discrepancy is smaller here, there are still higher maximum electron energies for the higher pulse energy data points in green. These relatively smaller increases in maximum escaping electron energy are in accordance with the results from the previous chapter. It is found that the higher-energy escaping population does not vary with pulse energy and is instead purely intensity driven.

6.4 Conclusion

The effects of varying intensity by changing spot area and pulse energy were studied, with larger x-ray and electron spectrometer signal increases with laser intensity for smaller spot areas. A similar effect is also seen in the maximum electron energy. Particularly for the fixed pulse energy data set, it is clear that there is an increase in the absorption of laser energy that is seen in the bremsstrahlung x-ray and electron signals and maximum electron energies, due to the increase in available energy. For the intensity range investigated here, this is expected given the results reported in Gray *et al.* [98]. However, for higher intensities and smaller spot areas this trend is not likely to continue as the electron acceleration becomes limited by the small spot size [110]. The biggest influence seen on bremsstrahlung x-ray and electron production is the energy on target, with higher bremsstrahlung and electron fluxes for similar intensity data points with higher pulse energies.

In the previous chapter it was found, through 2D and 3D PIC modelling, that bremsstrahlung production is highly pulse energy-dependent, a result that has been experimentally verified here. This suggests that, in future experiments using higher-intensity laser systems, the use of lower pulse energies can inhibit bremsstrahlung production.

Chapter 7

Linear absorption spectrometer characterisation using bremsstrahlung x-rays

7.1 Introduction

At the time of writing, new ultrahigh intensity laser facilities are being brought online, with the ELI-Nuclear Physics 10 PW laser in Romania reaching intensities of 10^{23} Wcm^{-2} , we are about to reach new frontiers of high-field laser-plasma physics [21]. The fast electron temperature scaling with laser intensity is of great interest, as the characteristics of this population will define many of the other processes and mechanisms, such as those governing ion and x-ray production. Electron temperatures cannot be directly measured as escaping electrons are not a direct measure of the electron temperature within the target due to electron deceleration by the external sheath field. A method to infer the electron temperature is to make spectral measurements of the x-rays they produce.

At lower intensities, of 10^{19} Wcm^{-2} , the electron and x-ray spectra have been found to have two temperature components. This is likely due to the presence of more than one electron population: a fast population that exits the target, which initially sets up sheath fields on the target surfaces, and another that does not have enough energy to leave the target due to the sheath fields that were set

up. This population remains recirculating within the target until their energy has been lost, through conversion to bremsstrahlung x-rays and other processes. The resulting electron spectra tend to have two distinct temperatures: a higher defined by the escaping electrons and a lower defined by the lower-energy electrons that remain within the target. This was confirmed in Beg *et al.* [54], where x-ray measurements indicated that, at intensities of 10^{19} Wcm⁻², there are at least two Boltzmann-like temperature components to the electron and x-ray spectra [54]. It was predicted in Chen [198], La Fontaine *et al.* [234], and Courtois *et al.* [235] that there is the presence of multiple temperatures in x-ray spectra and proposed a method of two-temperature deconvolution for absorption spectrometers.

Laser plasma interactions generate x-rays through a range of different processes, predominantly through the bremsstrahlung mechanism at the laser intensities explored in this thesis, as discussed in Chapter 3. At intensities of 10^{21} Wcm⁻², the ponderomotive electron temperature scaling [47] has already begun to diverge from other scalings, such as the Haines *et al.* [48] model and the Beg *et al.* [54] empirical scaling. Regardless of which scaling is applicable, the electron temperature is expected to increase with increasing laser intensity. With increasing electron temperature one would expect x-ray photons of increasing temperatures to be produced [236]. With the potential to reach electron temperatures above 10 MeV, there is a likelihood that similar x-ray temperatures will be generated. There is a lack of detector options for these mid-energy (1-10 MeV) x-rays, due to the reduced, flat absorption cross sections at these energies. Figure 7.1, showing the attenuation curves for tungsten, exemplifies this. At lower photon energies, below 1 MeV, absorption is dominated by the photoelectric effect and coherent scattering. At around 4 MeV, pair production overtakes photoelectric absorption, however there is no gradient in the overall attenuation. For other materials this crossover occurs at much lower energies however, at lower overall absorption efficiencies. This means that it is difficult to distinguish the energy deposited by photons of different energies within this range, which makes the deconvolution of spectral information difficult.

For lower photon energies, line emission detectors can be used. A commonly

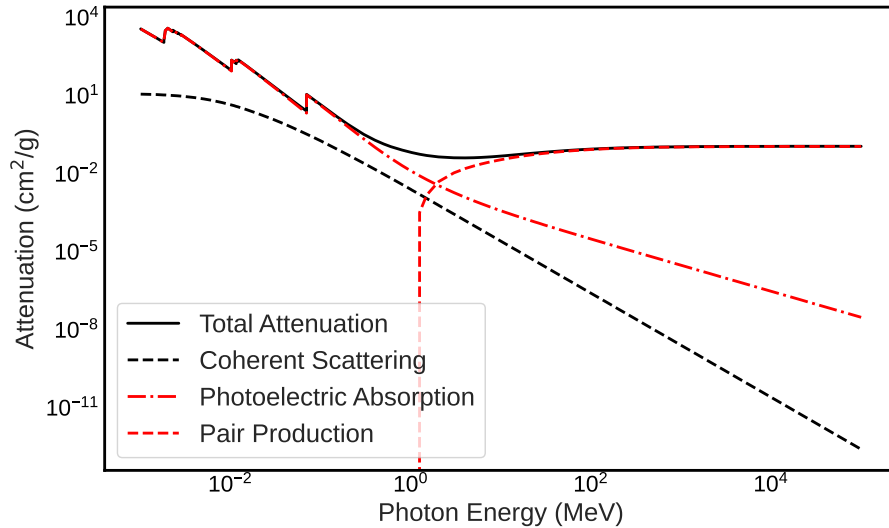


Figure 7.1: X-ray attenuation curves for tungsten, generated using NIST data tables [133]. Attenuation due to coherent scattering (black dashed), photoelectric absorption (red dot-dashed), and pair production (red dashed) are shown.

used emission line is the Cu K- α line at 8.04 keV with one of the highest energy emission lines being that of uranium at 94 to 105 keV [35]. Far above this range, one can monitor the activation of material caused by photo nuclear reactions [237]. In Courtois *et al.* [235], the $^{63}\text{Cu}(\gamma, n)^{62}\text{Cu}$ and $^{12}\text{C}(\gamma, n)^{11}\text{C}$ reactions are utilised, which have different thresholds of around 10 and 19 MeV. The ratio of the two activation measurements can then be used to infer a temperature, assuming a Maxwellian distribution of the form $S(E) \propto K_h \exp(-E/T_h)$, where K_h is a normalisation term, E is the electron energy and T_h is the fast electron temperature. These methods, however, are only applicable for x-ray measurements at higher (tens of MeV) and lower energy bands (keV) and are not useful for photon energies in the gap between 1 and 10 MeV.

Because of the lack of emission lines and inability to activate material within the 1-10 MeV region, many have used absorption-based techniques that apply filtering in front of the detector, both to increase the energy range detectable and to obtain more spectral information than possible with only a few points in the spectrum. Earlier designs, reported in Chen *et al.* [55], combined filtering of different Z materials with layers of imaging plate (IP). Spectral information can be extracted by calculating the response of each detector layer to incident photons using a Monte Carlo code. This method is common to all absorption-

based spectrometers.

Whilst this method was appropriate for laser systems with long cool-down periods, the recently developed high repetition-rate systems require online diagnostics that do not have detecting media that require processing after each use. Such diagnostics typically feature a series of scintillating crystal in the place of IP, with some method of detecting the light emitted when radiation is incident upon them.

In Behm *et al.* [238], a Caesium Iodide (CsI) based detector is reported, wherein a camera is used to image the 33 x 47 scintillator array. X-ray photons pass through the array of scintillators, which act to both attenuate the beam and detect the photons. Similarly, one can extract the input spectrum by generating a response matrix with a Monte Carlo code.

A similar spectrometer is reported in Rusby *et al.* [196] and Armstrong *et al.* [101, 197]. In contrast to the diagnostic developed in Behm *et al.* [238], the design comprised a single linear array of Lutetium-Yttrium Oxyorthosilicate ($\text{Lu}_{1.8}\text{Y}_{0.2}\text{SiO}_5$ or LYSO) scintillators separated by Tungsten (W) filtering. LYSO scintillators were chosen because of the high material density and tungsten filtering was used to increase the energy of x-rays that could be resolved by the diagnostic. It was this design that is used for data collection for the results presented in this thesis and was characterised for use in high-intensity laser-plasma interactions (above 10^{21} Wcm^{-2}).

Measurements of x-rays with an absorption-based spectrometer originating from laser-solid interactions with intensities above 10^{21} Wcm^{-2} have not been reported, to the author's knowledge. In Chen *et al.* [239], x-ray measurements for laser intensities up to 10^{20} Wcm^{-2} , made with the aforementioned image plate linear array, were reported. In Istokskaja *et al.* [240], a similar design to that reported in Rusby *et al.* [196] with plastic (EJ-200) and BGO crystal scintillators was developed, but was only used to measure photons for lower laser intensities (up to 10^{19} Wcm^{-2}). In Singh *et al.* [134], the current diagnostic design was used for laser intensities up to 10^{19} Wcm^{-2} . As will be shown in this chapter, linear absorption spectrometers begin to exhibit issues with non-

unicity of solutions due to the low and constant levels of absorption for mid-range x-rays. This presents as a large number, in the thousands (see Figure 7.14, which shows thousands of ‘valid’ temperature solutions), of different solutions that will accurately reconstruct the same input data because, especially in the range between 1-10 MeV, the material response to different energy photons cannot be distinguished.

This chapter presents a discussion of x-ray measurements made using laser intensities above 10^{21} Wcm⁻² and the method of characterising those spectra, given the issues outlined above. Firstly, analysis of the x-ray spectrometer signal as a function of intensity is presented, alongside analytical modelling performed to interpret these results. Then, two techniques to extract bremsstrahlung x-ray spectra, and thus the temperature values, from the experimental spectrometer measurements are presented. It is shown that the first technique, constraining solutions by merit value, does not provide accurate values, but the second, constraining the solutions by the experimental uncertainty of the individual crystals, does. Both methods, however are shown to exhibit large amounts of uncertainty. Numerical modelling is performed to generate simulated bremsstrahlung spectra and synthetic spectrometer data, which is used to characterise the x-ray spectrometer. Finally, two new spectrometer designs are considered, both featuring increased levels of filtering and numbers of crystals, with the objective of improving the spectrometer resolution for photon energies of 1-10 MeV.

7.2 Experimental method

The experiment was carried out using the Vulcan Petawatt laser at the Rutherford Appleton Laboratory. During this campaign, the laser energy on target, E_L , was (230 ± 30) J, with pulse duration, τ_L , equal to (900 ± 300) ps FWHM and wavelength equal to $1.053 \mu\text{m}$. The p-polarized pulses were focused initially using a $F/3.1$ OAP to a nominal focal spot size of $r_L = (4.5 \pm 1.0) \mu\text{m}$ (FWHM), measured using a low power, CW laser mode prior to the delivery of each high power pulse. Two plasma mirror configurations were used in the focusing beam to

enhance the laser temporal intensity contrast: a planar and an ellipsoidal focusing geometry.

7.2.1 Intensity enhancement using focusing plasma mirror

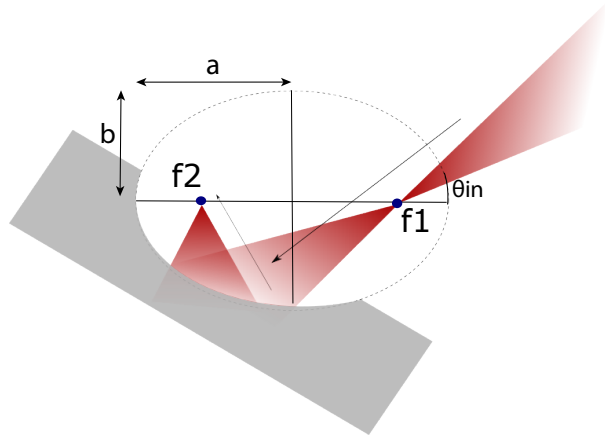


Figure 7.2: Schematic showing ellipsoidal focusing plasma mirror developed by Wilson *et al.* [38, 166, 172]. f_1 and f_2 marked on the diagram are the positions of the initial laser focus and the position of the second laser focus, induced by the FPM geometry. a and b are the lengths of the major and minor axes of the ellipse.

Focusing plasma mirrors rely on light being reflected by a thin layer of plasma on a curved surface. The design used for the work in this thesis, developed by Wilson *et al.* [38, 166, 172], utilises an ellipsoidal shape to refocus the incoming beam to a smaller focus than possible with larger F -number parabolas commonly used in laser beamlines. The geometry, shown in Figure 7.2, shows the two points of focus, f_1 and f_2 . The focal spot of the input beam is aligned to f_1 after which the expanding beam will interact with the plasma mirror surface and be focused down to a $1.7 \mu\text{m}$ focal spot at f_2 . The demagnification, m , is given by Equation 7.1, where e is the elliptical eccentricity and θ_{in} is the angle of incidence of the input beam from the major axis of the ellipse. The eccentricity is given by $e = \sqrt{1 - b^2/a^2}$, where a and b are the lengths of the major and minor axes, respectively. The magnification equation $m = v/u$, where the magnification is equal to the ratio of the image and object distances (v and u , respectively), applies here. In this case, v is given as the distance from f_1 to the optic surface and u is represented by the distance from the optic surface to f_2 [109, 179, 182]. This

modified magnification equation is given by

$$m = \frac{(1 + e^2) - 2e \cdot \cos \theta_{in}}{(1 - e^2)}. \quad (7.1)$$

It is important to note that the alignment of the plasma mirror must be optimal for intensity enhancement to occur. If the input focal spot is not spatially aligned with f_1 , to within $10 \mu\text{m}$ in the longitudinal direction and $30 \mu\text{m}$ in the transverse direction, then the optimum intensity enhancements cannot be achieved [179]. The likely sources of misalignment are spatial jitter and thermal lensing on shot [38, 179]. For the latter, it is imperative to have a control and measure of the laser defocus aberration. Equation 7.2 gives the maximum possible intensity enhancement (I_{enh}) and is dependent on the input and output focal spot sizes, r_{in} and r_{out} , the plasma mirror reflectivity (R_p), and the pulse energies before and after the optic, E_{in} and E_{out} .

$$I_{enh} = \left(\frac{r_{in}}{r_{out}} \right)^2 \cdot R_p \cdot \frac{E_{out}}{E_{in}} \quad (7.2)$$

In the planar plasma mirror case, the $r_L = 4.5 \mu\text{m}$ focal spot had a fractional encircled energy of $f_{EE} \approx 40\%$, wherein that portion of the pulse energy was found in the focal spot [179]. The focusing plasma mirror was used to form a smaller focal spot of size $r_L = (1.7 \pm 0.2) \mu\text{m}$ FWHM, with fractional encircled energy $f_{EE} \approx 30\%$ [179]. The focal spot achieved with the use of the ellipsoidal plasma mirror corresponds to a focusing geometry of approximately $F/1$. With the enhancement in intensity given by Equation 7.2, intensities above 10^{21} Wcm^{-2} were reached.

The peak calculated laser intensity when employing the PPM setup was $(5.0 \pm 2.0) \times 10^{20} \text{ Wcm}^{-2}$, which was increased to $(3.5 \pm 1.5) \times 10^{21} \text{ Wcm}^{-2}$ using the FPM setup. For both configurations, the plasma mirror reflectivity and temporal intensity contrast enhancement are similar. The intensity contrast ratio for both was 10^{-10} at 1 ns, 10^{-8} for the first pre-pulse at around 170 ps prior to the pulse, and 10^{-5} at 10 ps prior to the arrival of the peak of the pulse [180]. X-rays driven by the interaction of the laser pulse, in both focusing geometries, with 25

μm thick copper targets were measured using a linear absorption spectrometer, which was positioned at 30° with respect to rear target normal.

7.2.2 X-ray spectrometer deconvolution

In order to characterise the x-rays from the interaction an x-ray spectrometer was used. A 1D array of scintillators is imaged from the side by a CMOS camera. The design, developed in Rusby *et al.* [196] and later Armstrong *et al.* [101, 197], consists of an array of ten 2 mm LYSO scintillators separated by plastic spacers and, in the latter half of the array, 2 mm tungsten filtering. Each LYSO crystal is wrapped in white PTFE tape in order to increase light yield directed at the camera, and is held within a 3D printed frame that keeps the emission of each individual crystal optically separate. The lens used must have as high a numerical aperture as possible to maximise light collection, as such the lens used for this experiment is a high-speed 25mm, $F/0.95$ lens.

The rail is housed within a 1.6 cm thick lead enclosure, which is open to one side (facing the camera), the front and the back. The geometry of this can be seen in Figures 7.3(a) and 7.3(b). A strong magnetic field (0.6 T) is used to sweep away escaping electrons from the interaction to prevent them from hitting the spectrometer and a tungsten aperture is placed to isolate x-rays directly from the interaction.

The measured data in a scintillator array is the integral of the spectra and the energy-dependent absorption of x-rays. The difference in response for subsequent layers can then be generated, collectively these are referred to as the response matrix or response function. To reconstruct the incident x-ray spectra, one must first produce a response matrix for the spectrometer. In this case, the Monte Carlo code GEANT4 [204] is used to determine the energy deposited in each crystal as a function of incident photon energy. The initial response matrix for the design used in this thesis, shown in Figure 7.4, although later in this chapter other response matrices and spectrometer designs will be discussed. It can be seen that the energy deposited in the latter layers begins to exceed that of the first. This is due to the production of secondary x-rays in preceding crystals,

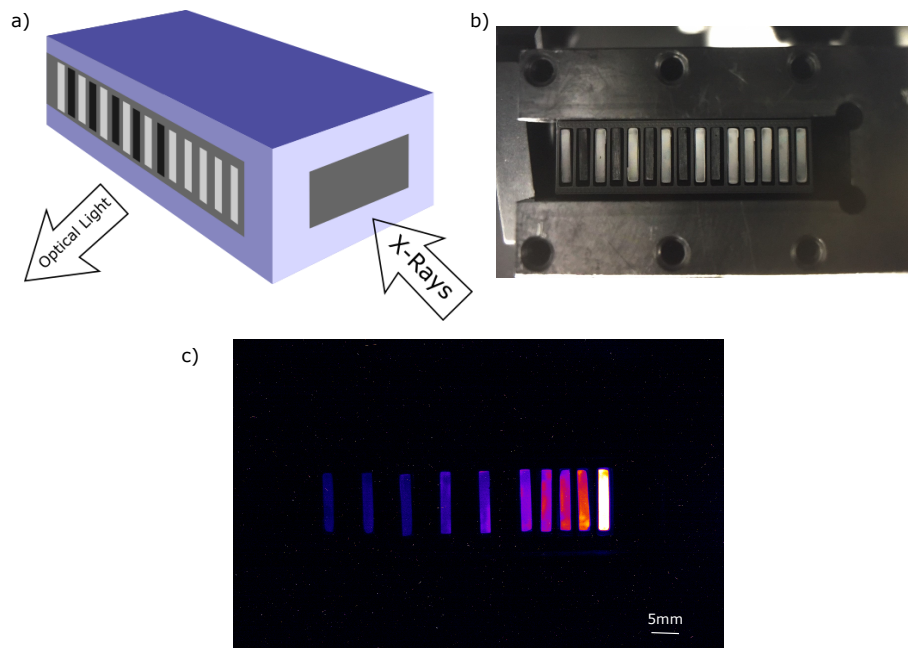


Figure 7.3: (a) a schematic showing the directions of photon input and output, (b) a photograph of the scintillator array, with the light-coloured PTFE-wrapped scintillators and darker tungsten filtering, and (c) an image of the scintillator array illuminated by x-rays.

largely through electron-positron annihilation. Secondly, a discontinuity is found at around 60 keV, which occurs due to the Lu K-edge of LYSO.

Chen *et al.* [198] proposed using a normalised ratio to express the relative weighting between different spectral components. However as this technique is normalised it is insensitive to variation in the total emitted flux and cannot scale directly to more components. To directly resolve the individual components, Armstrong *et al.* [197] describes an analytical method that directly computes the flux for different temperatures and spectral distributions. With this method it is possible to assess the impact of different spectral shapes and assess the total flux contributions on the measured spectrometer signal with minimal changes to the approach. Details of this approach, and extraction of the spectrometer data from the CMOS images, can be found in Chapter 4.

7.3 Experimental results

Here, measurements of x-rays generated by the interaction of ultra-high intensity laser pulses with 25 μm thick copper targets are presented. An analytical model

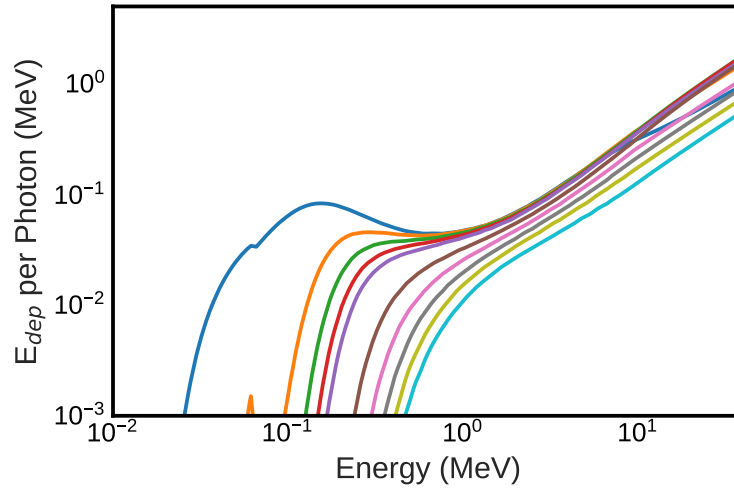


Figure 7.4: Spectrometer response matrix generated using Monte Carlo code GEANT4, showing energy deposited in each crystal layer per photon of a certain energy.

considering electron spectra with changing temperature components is outlined to explain the trend in x-ray flux with increasing electron temperature for constant laser energy. Then, spectral deconvolution is applied to the data, and the resulting solutions are discussed.

7.3.1 X-ray energy deposition scaling with incident laser intensity

The measurements of total scintillator signal can be correlated to the x-ray energy deposition within the scintillators. The main variation in intensity is achieved via two different focusing geometries: $F/3$ and $F/1$. Within each dataset there also is additional subtle variance due to slight variance in defocus and pulse duration. Each focusing geometry, for fixed energy, generates a difference in encircled energy due to the differences in spot size and spatial intensity distribution. It is important to separate the different effects of encircled energy and spot size on electron acceleration and therefore x-ray production. A smaller focal spot by its nature interacts with fewer target electrons due to the smaller interaction area, which will in turn decrease the flux of x-rays produced. However, a higher encircled energy will contribute more energy to the electron population, which will have effects on x-ray production by increasing the temperature of the spectrum

and overall photon flux.

In order to assess the effect of variances in encircled energy, the spectrometer signal was considered as a function of the energy on target. The energy on target encompasses the compressor and plasma mirror efficiencies, as the energies used in this calculation are pre-compressor energies, as well as the amount of energy encircled within the FWHM of the laser focal spot.

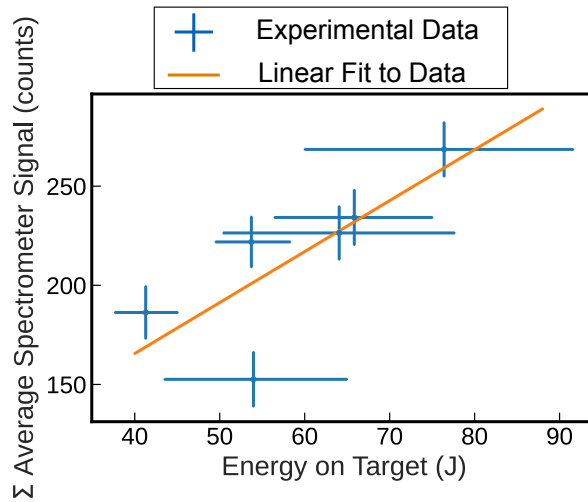


Figure 7.5: Average spectrometer signal as a function of laser energy on target (blue crosses), with a linear fit to the data (orange).

In Figure 7.6, the total of the average signals of each crystal within the spectrometer is shown as a function of incident laser intensity and is normalised to energy on target using the linear fit (in orange) in Figure 7.5. The uncertainty in these signals is given by the standard deviation of the crystal signals. As outlined in Chapter 4, the ‘hard hits’ have been filtered from the data and the signal has been background subtracted. The y-axis error bars are given by the standard deviation of the signal, measured across the area of the crystal, and, where energy normalised, the error in the energy on target fit. The x-axis error bars are given by the uncertainties in the measurements of laser parameters contributing to the calculated intensity, namely the pulse duration, pulse energy, plasma mirror reflectivity, and spot size calculations. The errors in pulse duration were determined from the autocorrelator traces and the errors in the spot size calculations are associated with the Gaussian fitting to the focal spot images. It can be seen from Figure 7.5 that there is a clear relationship between spectrometer

signal and energy on target. The increase in mean signal as a function of laser energy indicates that there is more energy being deposited in the scintillators. However, as the spectral shape and temperature is likely changing as the intensity is varied, it is not conclusive to state that the x-ray energy is increasing. It is also important to note that the linear fit seen in orange is not constrained to fit through zero and, as such, is not physical at low energies.

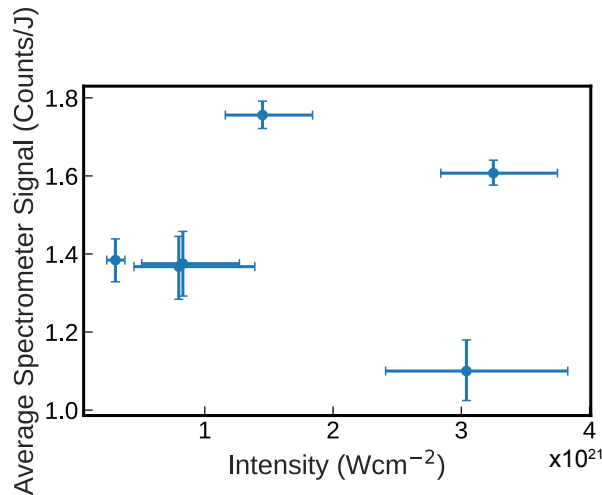


Figure 7.6: Average spectrometer signal normalised to energy on target as a function of laser intensity.

In order to ascertain the effect of laser intensity on x-ray emission, the above fit of spectrometer signal to energy on target was used to normalise the signal by energy. The energy normalised signal is plotted as a function of laser intensity in Figure 7.6. The spectrometer signal, albeit scattered, shows no particular trend with increasing laser intensity, ranging from roughly 1.1 to 1.8 counts per Joule of energy within the focal spot. It is perhaps intuitive that the total integrated x-ray signal, and therefore deposition of x-ray energy into the detector, is constant when energy normalised. However, when shifting to higher laser intensities with constant energy one might expect higher electron temperatures accompanied by a lower number of accelerated electrons, assuming the laser-to-electron energy conversion efficiency is constant, which would result in a lower flux of x-ray photons. Spectral information is required to ascertain whether the apparent constant energy deposition is masking a variation in x-ray fluence or temperature that would generate a constant spectrometer signal across the intensity range.

7.3.2 Cu K- α results

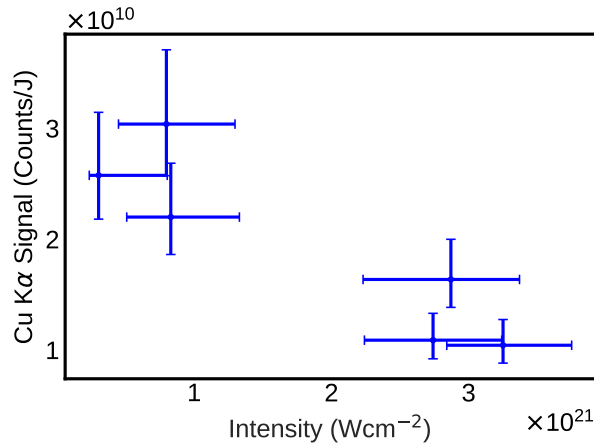


Figure 7.7: Cu K- α signal normalised to energy on target as a function of laser intensity.

Another x-ray diagnostic monitoring K- α emission from the copper target was employed and the data analysed by T. P. Frazer [179]. The details of this diagnostic are presented in Chapter 4. In a method similar to that employed to the spectrometer data, the copper K- α signal was extracted and the functional relationship with encircled energy was used to normalise the signals. The relationship between the energy normalised copper K- α signals and incident laser intensity is shown in Figure 7.7. The uncertainties in the K- α signals are determined from the uncertainty in the conversion from PSL to photon signal, and the x-axis error-bars are determined by the uncertainties in the measurement of the laser parameters contributing to the calculation of the peak laser intensity. The copper K- α signal, although slightly decreasing with increasing laser intensity, is still relatively flat. Despite the large difference in absolute signal between the two diagnostics, there is again a small range of signals, here only ranging from up to 3 times the minimum signal. A decrease in copper K- α signal is expected with an increase in laser intensity as, again, we expect the electron temperatures to rise and their collision frequencies to decrease. However, the decrease in K- α signal is not as high as it would be with electron temperatures predicted by either the Wilks [47] or Haines *et al.* [48] models.

Another consideration is the possibility of the emission lines shifting out of

the spectral bandwidth of the K- α spectrometer. A number of phenomena can cause this, including changes in the electron density and temperature [241, 242]. The shifting of the Cu K- α emission line, and therefore lower signal on the spectrometer, could wrongly be attributed to a drop in K- α x-ray yield.

Further analysis is required to ascertain whether the constant LAS spectrometer flux is caused by an increase in x-ray flux or an increase to higher temperatures. Conversely, it could show as a slower electron temperature scaling than those suggested in Wilks [47] and Haines *et al.* [48]. Further analysis will involve the consideration of x-ray and electron distributions with shifting temperatures and flux components, which will be described in the following section.

7.3.3 Analytical modelling

Two analytical modelling methods were employed in the consideration of the experimental spectrometer signal relation with incident laser intensity. Firstly, energy-normalised two temperature-component Boltzmann photon distributions were generated for different energy ratios within each component. Secondly, two temperature Boltzmann *electron* temperature component distributions were generated and passed into a model that simulates electron refluxing and the radiative losses associated with this process. Both models will be further explained in the coming paragraphs.

7.3.4 Consideration of two temperature component Boltzmann photon distributions

Photon distributions of the form

$$f(E) = \frac{1}{E_{tot}} [N_1 \exp(-E/kT_1) + N_2 \exp(-E/kT_2)] \quad (7.3)$$

were generated, where kT_1 and kT_2 are the temperatures of each component, which contain N_1 and N_2 numbers of particles. E_{tot} is the total energy contained in the spectrum covered by the two distributions, and as such the distributions are

each normalised to the energy contained within them. Each photon distribution, once generated, was then ‘folded in’ with the LAS spectrometer response matrix, shown in Figure 7.4, to generate a synthetic scintillator response for each x-ray distribution. By combining the photon distribution with the response function for each scintillator crystal, a synthetic signal can be found for each crystal when combined with the linear collection efficiency, and therefore an overall signal response for each input photon distribution.

This process was performed for a range of N_1 to N_2 ratios, representing different fluxes within each temperature component. Additionally, whilst the lower temperature was kept constant, a feature seen in the Monte Carlo simulations presented in a later section (Section 7.4.2), the higher temperature (kT_2) was varied according to the Wilks [47] and Haines *et al.* [48] fast electron temperature scalings for laser intensities between 1×10^{19} and 5×10^{21} Wcm⁻². These synthetic signals are compared to the experimental spectrometer signals, which, assuming isotropic x-ray emission from the target, have been multiplied by a factor to account for the solid angle subtended by the spectrometer to make the synthetic and experimental signals comparable.

The synthetic signals for photon distributions with higher temperatures given by the Wilks [47] and Haines *et al.* [48] temperature scalings, with different flux ratios, can be found in Figures 7.8 and 7.9. The same analysis was performed for the Beg *et al.* [54] temperature scaling. However, it is very similar to Haines and as such is not included here. In each figure, the experimental LAS spectrometer signals are plotted in blue on the right hand axis. For both temperature scalings, it is apparent that for distributions with larger higher temperature components, where the N_2/N_1 ratio is approaching or equal to unity, that the spectrometer signal should decrease quickly when the laser intensity increases into the 10^{21} Wcm⁻² range. It can be seen that this trend is not present in the experimental data, which remains relatively constant over the intensity range. This suggests that, even without deconvolving the x-ray spectra, the higher temperature components of the experimental spectra have lower fluxes, with fluxes two or three orders of magnitude smaller than the lower temperature component. This imme-

diately poses a problem for extracting spectral information, as it is difficult to deconvolve a component that contains such a small fraction of the total energy within the spectrum. This also suggests that, even if there is the presence of a fast electron population with a Wilks [47] or Haines *et al.* [48] temperature scaling which is generating the high energy component of the x-ray spectrum, it only comprises a very small fraction of the accelerated electron distribution.

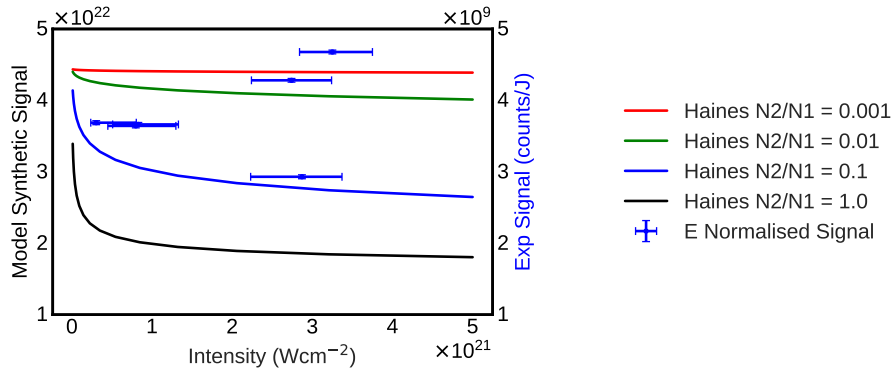


Figure 7.8: Energy normalised experimental average spectrometer signal as a function of experimental laser intensity (blue points). Synthetic spectrometer signals for photon distributions with changing higher temperature according to Haines *et al.* [48] electron temperature scaling and differing N_1/N_2 ratios.

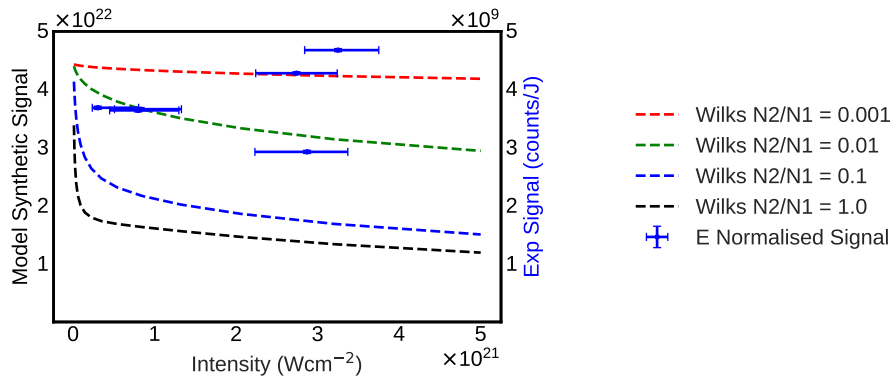


Figure 7.9: Energy normalised average spectrometer signal against experimental laser intensity (blue points). Synthetic spectrometer signals for photon distributions with changing higher temperature according to Wilks [47] fast electron temperature scaling and differing N_1/N_2 ratios.

In order to further investigate the implications for the generated electron distribution a radiative energy analytical model, adapted by the author from a Cu $K\alpha$ model reported in Quinn *et al.* [99], was used to assess the energy radiated for evolving electron spectra. The model uses radiative and collisional stopping

power tables to assess the energy lost by a refluxing electron with each pass of the target. Using this method it is assumed that there is no secondary particle generation as the electrons interact with the target. Later, this is addressed using Monte Carlo modelling. In this model an electron distribution of some defined shape is propagated through a target by considering the distribution at an integer number of steps through the target thickness. The electron distribution is modified at each step to include the attenuation of the electron distribution by radiative and collisional stopping, and the attenuated spectrum is then passed on to the next step. At the edges of the target this process is repeated and the escaping of fast electrons is simulated by losing a portion (10%) of the electron population above a certain energy (here, 2 MeV is used). In Myatt *et al.* [243], a capacitance model is used to predict the escaping electron fraction as a function of target size and laser intensity for circular targets. The escaping electron fraction spans a range of 10-30% across the intensity range investigated here and, for simplicity, the escaping fraction was taken to be 10% in the modelling. With each step the radiative energy loss is summed and a measure of the energy radiated by an initial electron spectrum as it recirculates can be estimated. This process is further illustrated in Figure 7.10

A two temperature component Boltzmann electron distribution of the form seen in Equation 7.3 was inserted into the model. A target thickness of 25 μm , step size of 1 μm , and number of steps equal to 1000 were used, meaning that the electrons passed through the target up to 40 times. Figure 7.11 shows the radiative energy loss for these two-temperature, evolving electron spectra, with a fixed lower temperature of 250 keV, chosen to reflect the later GEANT4 modelling, and higher temperatures that follow either the Beg *et al.* [54], Wilks [47] or Haines *et al.* [48] temperature scaling for intensities between 1×10^{19} and 5×10^{21} Wcm^{-2} . Here, the N_2/N_1 ratio is fixed to 0.01 as this looked to be a likely candidate given the experimental data and previous modelling (Figures 7.8 and 7.9). The radiative losses for each set of temperature distributions are normalised to one. Alongside this, the energy normalised experimental spectrometer signals, normalised to the maximum signal, are shown as a function of laser intensity.

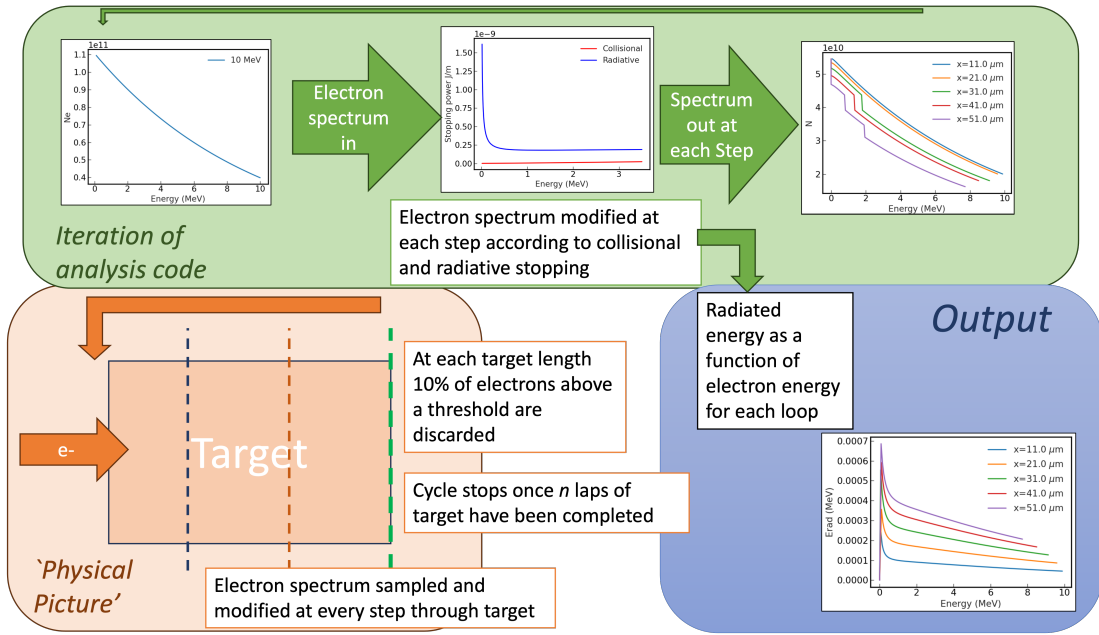


Figure 7.10: Flow chart illustrating the radiative numerical model. First, an electron population is injected into a target. Then, at periodic steps through the target, the electron spectrum is adjusted according to collisional and radiative stopping powers of the material. At every ‘target-thickness’, electron escaping is modelled by discarding 10% of the electron distribution above an energy threshold. The energy lost by the electrons by radiation production at each step is equivalent to energy radiated as bremsstrahlung radiation.

Although not a direct comparison, the total energy loss in the form of x-ray photons by the electron population and the spectrometer signal can be compared when it is considered that the spectrometer signal is a measure of energy deposited into the detector, and hence a measure of energy in the incident x-ray spectrum. A trend can be seen that is similar to that in the previous modelling: as the laser intensity increases, for the Beg *et al.* [54], Wilks [47] and Haines *et al.* [48] fast electron temperature scalings, the radiative loss by the electrons decreases. This is because the electrons have a higher average energy and are therefore experiencing lower stopping powers within the target material. This directly connects to the previous result. As the energy emitted in the form of x-ray photons decreases, the spectrometer signal (a measure of energy within the incident x-ray spectrum) will also decrease. This shows that, for a energy normalised, two-temperature electron distribution, the x-ray spectrometer signal should decrease with increasing laser intensity. Again, this trend is not seen in the experimental data.

The energy normalised experimental spectrometer signal, also shown in Figure

7.11, has a significantly flatter scaling with increasing laser intensity than the total radiative losses modelled using either the Beg *et al.* [54], Wilks [47] or Haines *et al.* [48] scaling electron distributions. The radiative losses indicated by the higher spectrometer signals indicate one of a few things. Either:

- the fast electron temperatures are lower and with a slower scaling than those indicated by Beg *et al.* [54], Wilks [47] or Haines *et al.* [48];
- the higher temperature component comprises an even smaller portion of the electron population or;
- there is a mechanism affecting the absorption of laser energy by the electron population which means there is a higher total energy within the electron population at higher laser intensities.

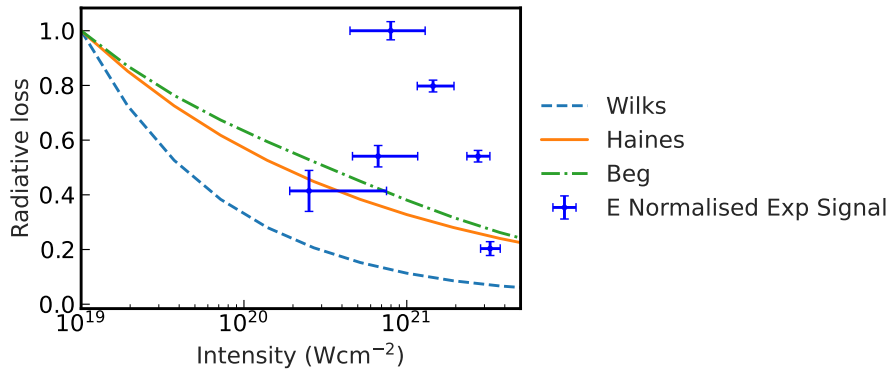


Figure 7.11: Energy normalised experimental average spectrometer signal (blue points) and radiative losses for electron distributions with higher temperatures predicted by Beg *et al.* [54], Haines *et al.* [48] and Wilks [47] temperature scalings (dashed green, solid orange and dashed blue lines, respectively) as a function of laser intensity.

Regarding the latter point, the work reported in Dover *et al.* [110] suggests something to the contrary. In the experimental study presented in this thesis, tight focusing was used to achieve high laser intensities, a method which was also investigated in Dover *et al.* [110]. It was found that, as the laser focal spot size is reduced it can become smaller than the transverse acceleration length of the accelerated electrons. Because of this, the ponderomotive force can very quickly force the electrons out of the focal spot of the laser and as such will gain a smaller fraction of energy from the laser. Additionally, in Wilson *et al.* [109], the

effect of spatial intensity contrast on electron heating and ion acceleration was investigated. It was found that, whilst using the same focusing plasma mirrors to achieve tightly focused laser pulses, the wings of the focal spot were of a high enough intensity to affect the interaction and through PIC simulation found that a pulse of the same intensity $2\ \mu\text{m}$ central spot with wings produced fewer higher energy electrons than a pulse of a larger spot size and same intensity ($5\ \mu\text{m}$, $2 \times 10^{20}\ \text{Wcm}^{-2}$). This was explained by the presence of the wings increasing the interaction area, which can accelerate a higher number of electrons, but spreads the pulse energy over a larger population of electrons.

Both of these studies indicate that the absorption of laser energy is limited by the laser focal spot sizes used to reach higher laser intensities, as both the spatial intensity contrast and the electron transverse acceleration distances can inhibit the acceleration of electrons to higher energies. If the findings in Dover *et al.* [110] apply to interactions featuring longer pulse durations, then the lower maximum electron energies and higher numbers of lower energy electrons would produce a x-ray spectrum containing relatively higher total energies. So, these studies, alongside the Cu K- α modelling from [179] and modelling presented here, suggest that there is a lower than expected fast electron temperature. In order to assess how prominent that fast electron population is within the distribution, spectral analysis is required to understand the way the x-ray emission, and therefore electrons, are energetically distributed. As suggested at the beginning of this chapter, this can be a challenging task.

7.3.5 X-ray temperature measurements

As discussed in the previous section, it is possible to gain insight into the dynamics of the intensity-dependent spectral evolution of fast electrons by characterising the x-ray emission. It was reported that the signals of both the x-ray spectrometer and copper K- α diagnostic both indicate a slower fast electron temperature scaling than expected with incident laser intensity. However, to gauge the magnitude of this, it is imperative that one is able to extract spectral information from the emitted x-ray spectrum. The x-ray spectrometer and accompanying al-

gorithm used in this experiment were intended to be able to deconvolve spectral information from the measured data. However, this design of spectrometer is yet to be tested at such high laser intensities where the resolution of x-ray temperatures in the tens of MeV is poorer. Therefore, the capability of this spectrometer to resolve bremsstrahlung x-ray spectra produced in laser-solid interactions with intensities above 10^{21} Wcm^{-2} is also investigated within this work.

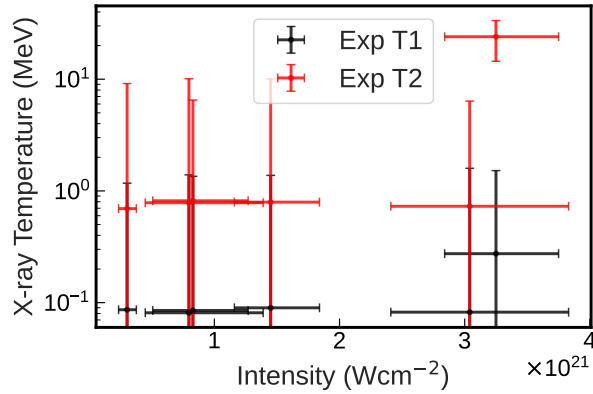


Figure 7.12: Initial experimental x-ray temperatures plotted as a function of incident laser intensity.

The initial two-temperature Boltzmann deconvolution temperatures are shown in Figure 7.12 for the data points in the previous section. The deconvolution algorithm is described in detail in Chapter 4. It can be seen that, for the most part, the deconvolved higher temperatures are below 1 MeV, with lower temperatures of 100 keV or less. However, the error bars for these data points span many orders of magnitude due to the large spread of solutions found when randomly modifying the response within the bounds of the standard deviation of the data. What can also be seen is a single data point that has significantly higher temperatures, with a T_1 of (0.3 ± 0.1) MeV and a T_2 of (25 ± 5) MeV. The fast electron temperature predicted by the Wilks [47] scaling is less than 20 MeV at these laser intensities. What becomes clear when analysing the distributions of the solution parameters is that this is a boundary solution. To assess the degree of uncertainty, the solutions found within the error analysis by making random small changes to the data and applying the deconvolution algorithm were histogrammed and plotted. The corresponding N_1 , T_1 , N_2 , and T_2 distributions for two experimental data points,

of intensities 3×10^{20} and $3 \times 10^{21} \text{ Wcm}^{-2}$, are shown in Figure 7.13. Due to the symmetry of the diagnostic merit function, T_1 and T_2 can either be higher or lower here, and as such temperatures up to 24 MeV are plotted for both. Despite the data points corresponding to laser intensities that are an order of magnitude apart, the solution distributions found for each are very similar. The key features shown in each temperature are an abundance of zero, or close to zero, MeV solutions and an almost equally numerous spike in upper boundary solutions at 24 MeV. This suggests that, in attempting to find a good quality fit, the algorithm is ‘running out of room’ in temperature space and is therefore returning boundary solutions. With the upper temperature of the scanning range set at 20 MeV, the algorithm is consistently returning a higher temperature value of 24 MeV, which is the upper limit of the fine-grid reconstruction phase which is $1.2 \times$ the temperature solution of the sparse-grid reconstruction phase. The same behaviour occurs when the upper temperature limit is increased up to 30 MeV. For both data points the algorithm is struggling to find a good fit for the experimental data and cannot find a two-temperature solution with any certainty. This trend is seen for all of the experimental data points. Not shown are the fits to the data retrieved using a single temperature function. The fits of these, too, are poor.

Given the similarity of solution distributions for all experimental points, it was appropriate to investigate the merit, or goodness of fit, for each solution within the 2D temperature grid that is scanned within the algorithm. The merit functions for this temperature scan from the first, sparse-grid, phase of reconstruction for the experimental data is shown in Figure 7.14. The merit functions, produced by scanning through the sparse temperature grid and calculating the merit of the fit at each point, are plotted with a maximum value equal to the experimental uncertainty, which is the standard deviation in each crystal signal divided by the average signal in the crystal. Above this value is plotted in black, as these merit values are deemed too high to give valid solutions. It is important to note here that a lower merit score is better, as it is a measure of the overall difference between the reconstructed and original signals.

Two things are immediately obvious: again, despite an order of magnitude

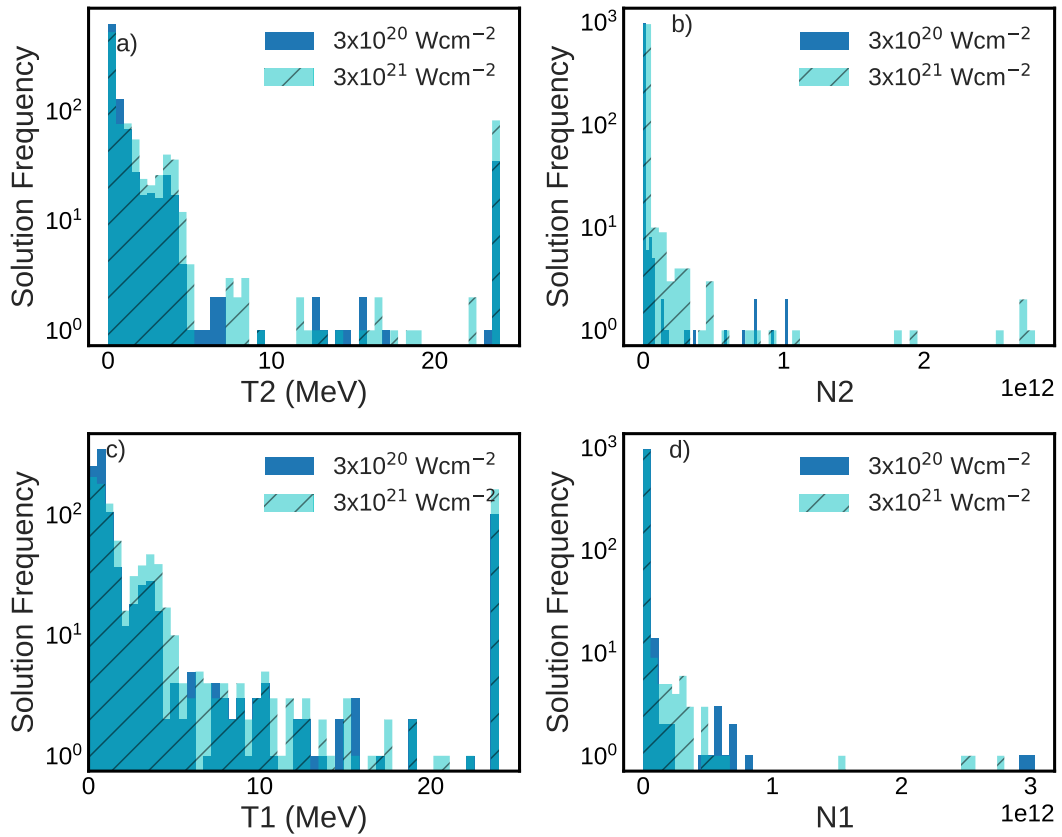


Figure 7.13: Distributions of spectral fitting parameters for two experimental points: 3×10^{20} , and 3×10^{21} Wcm^{-2} .

difference in laser intensity between the two points shown, the merit grids look almost identical; and the spread of lower merit solutions is vast for both which suggests a large uncertainty in the spectral reconstruction. It is also clear why the algorithm regularly returns boundary solutions, with the areas of lowest merit reaching the edges of the grid. In this first, sparse phase of reconstruction, the local area around the temperatures of lowest merit is selected for the second, fine-grid phase of reconstruction. With those areas appearing at the edges, boundary solutions are likely to be found. With such a large amount of uncertainty, it is not yet appropriate to assign a single solution to this data.

It is of interest to assess the data reconstructions in comparison to the original experimental data, which are constrained by possessing low merit values (which are shown as coloured regions in Figure 7.14). The reconstruction of the spectrometer signals for each of these solutions are shown in Figure 7.15, with the

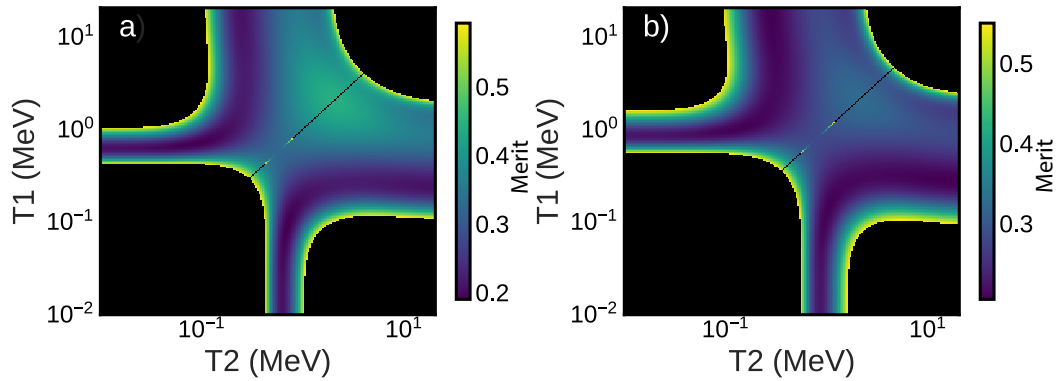


Figure 7.14: Merit grids for initial deconvolution of experimental data for intensities (a) 3×10^{20} and (b) 3×10^{21} Wcm^{-2} .

minimum merit, or ‘best’ solution plotted in red and the experimental data in blue. The standard deviation of the crystal signals is shaded around the experimental data line, in order to compare the reconstructions to the uncertainty in the experimental data. The reconstructions are plotted with a low opacity in black so that the distribution and number of solutions can be visualised according to density of colour. Some of the reconstructed scintillator signals appear to be many of orders of magnitude different to the experimental data and standard deviation, which shows that there are still a great number of solutions within our merit threshold that have very poor fits to the experimental data. This is likely because the merit function is only a measure of the *overall* difference between the reconstructed and actual signals and as such can allow a very good reconstruction of one crystal to compensate for a poor reconstruction of another.

The minimum merit solutions, plotted in red, are notably not a good fit to the experimental data, with around half the crystal signals in both not lying within the bounds of uncertainty in the experimental data. It can also be seen that the spread of solutions is larger for the higher laser intensity, shown in Figure 7.15(b), as opposed to the lower in Figure 7.15(a). The solutions span at least another order of magnitude in each direction, which suggests that there is an even greater uncertainty for the higher intensity point.

Given that this method of thresholding the merit function gives a vast spread of poor reconstructions, and perhaps unrealistically similar solutions for each

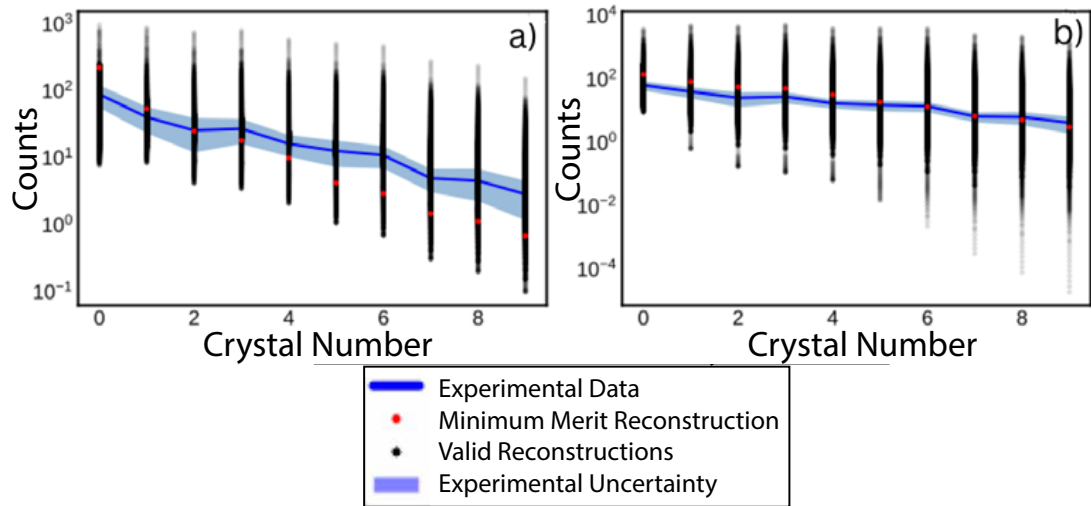


Figure 7.15: a): Reconstructed spectrometer signals corresponding to solutions constrained by merit value, for laser intensities of (a) 3×10^{20} and (b) 3×10^{21} Wcm^{-2} , constrained by merit value.

experimental point regardless of laser intensity, the solutions were instead constrained by reconstruction quality, or goodness of fit to each crystal. This occurs because the merit is only an average offset from the experimental data and does not take into account the individual values. One can achieve this by constraining the valid solutions to those that have reconstructions that fit within the bounds of uncertainty in the experimental data for each individual crystal. In Figure 7.16, it is shown how the solutions can be selected by ensuring that their reconstruction lies within the experimental standard deviation of the crystal signals. This significantly reduces the number of ‘valid’ temperature pairings and therefore the uncertainty.

The number of solutions for the higher intensity point is even more reduced than for the lower intensity data, as illustrated by the much-reduced opacity of plotted solutions in Figure 7.16(b) compared to Figure 7.16(a). This indicates that there are very few solutions that provide a satisfactory fit to the experimental data. Additionally, the only solutions that are valid within this method of constraint are those with an accurate first crystal signal and lower than experimental signals in the second and third crystals, which may predict the presence of a very low temperature component that deposits the majority of its energy

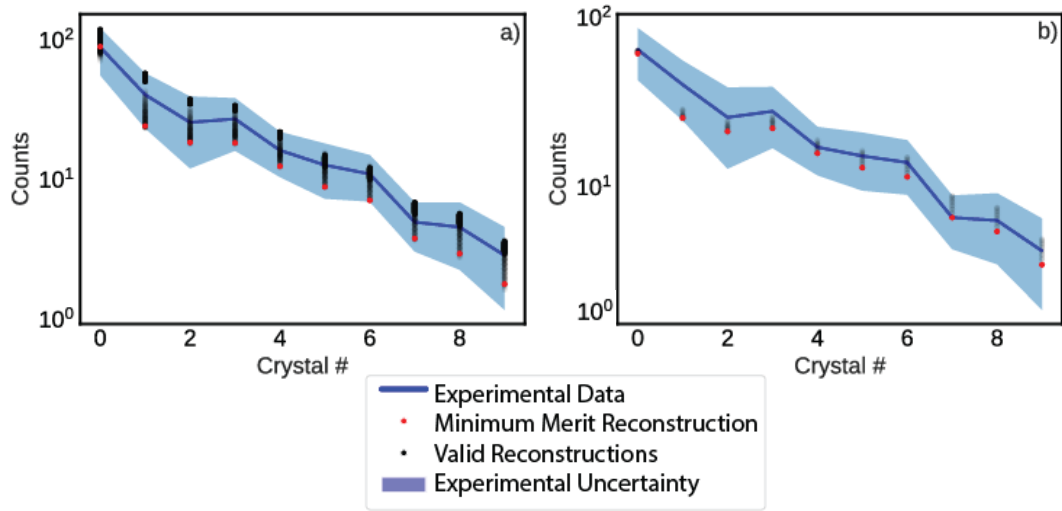


Figure 7.16: Reconstructed spectrometer signals corresponding to solutions constrained by experimental uncertainty for each crystal, for laser intensities of (a) 3×10^{20} and (b) 3×10^{21} Wcm^{-2} .

into the first crystal. This can be seen in the valid spectral solutions shown in Figure 7.16(b), where the reconstructions of the second and third crystals are consistently lower than the experimental data.

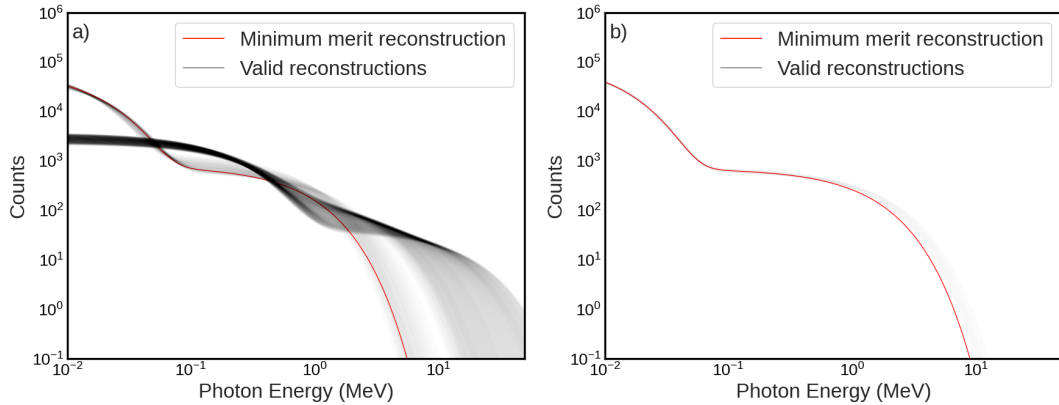


Figure 7.17: Reconstructed spectral distributions corresponding to solutions constrained by experimental uncertainty for each crystal, for laser intensities of (a) 3×10^{20} and (b) 3×10^{21} Wcm^{-2} . The transparent black lines each represent a ‘valid’ spectral solution and the red line represents the spectral solution with the lowest merit value.

These spectra, also plotted in black with a low opacity, shown in Figure 7.17, for laser intensities of 3×10^{20} , and 3×10^{21} Wcm^{-2} . Again, the minimum merit solution is plotted in red in each. The difference in the number of valid solutions for each intensity is again very apparent, as visualised by the density of solutions. What is also interesting is that the lower intensity point in Figure

7.17(a) features solutions of many different spectral shapes, whereas the higher (in Figure 7.16(b)) has only one. In both plots there is a similar solution that has both a lower T_1 and T_2 whereas, counter-intuitively, the lower intensity point in Figure 7.16(a) also features solutions with higher, multi-MeV temperatures, where the higher intensity point (in Figure 7.16(b)) does not. Higher x-ray temperature components are expected at both laser intensities according to the prevalent fast electron temperature scaling laws.

As higher electron, and therefore x-ray, temperatures are expected for the higher intensity point, whose solutions were not represented within the experimental reconstructions thus far, it is important to ascertain if the lack of higher temperature component at the highest intensity is real or a product of the spectrometer response. Another method was used to improve the number of solutions, with satisfactory fits to the experimental data, presented by the algorithm. Perhaps if the algorithm was presenting a low number of satisfactory fits for these higher temperatures it might be caused by a lack of resolution on the high energy region of the x-ray spectrum. For this reason, the first method involved extending the energy range of the spectrometer response matrix from 50 to 100 MeV in order to fully resolve the higher temperature component. Compared to the original response functions (Figure 7.4), the responses of the latter crystals become greater than the responses of the first crystal at the highest photon energies, which would have a small effect on the reconstructions. Moreover, it is important to note the problem with the detection of multi-MeV x-rays: the amount of energy deposited in each scintillator becomes very similar in the 1 to 20 MeV range, which is due to the intrinsic flattening in the gradient of absorption efficiency between the energy ranges of the Compton scattering and pair production mechanisms. Whilst the extension of the spectrometer response matrix might increase the number of solutions that are valid for the experimental data, it is likely that it will not increase the degree of certainty in the solutions.

Following the same method as before of constraining the solutions according to the signal reconstruction of each scintillator, reconstructed spectral distributions for the experimental data can be obtained. The reconstructed spectra for

experimental data points of intensities 3×10^{20} and $3 \times 10^{21} \text{ Wcm}^{-2}$ are shown in Figure 7.18, with the valid solutions plotted in black and the minimum merit solution in red. It can now be seen that there are significantly more valid solutions for the higher intensity (Figure 7.18(b)) when using the extended energy response matrix, which suggests that the higher temperatures can now be more accurately resolved. It is also apparent that the spectral distributions for the two cases are still very similar. Again, despite the order of magnitude difference in laser intensities between each experimental point, the reconstructed x-ray spectra have the potential to be very similar.

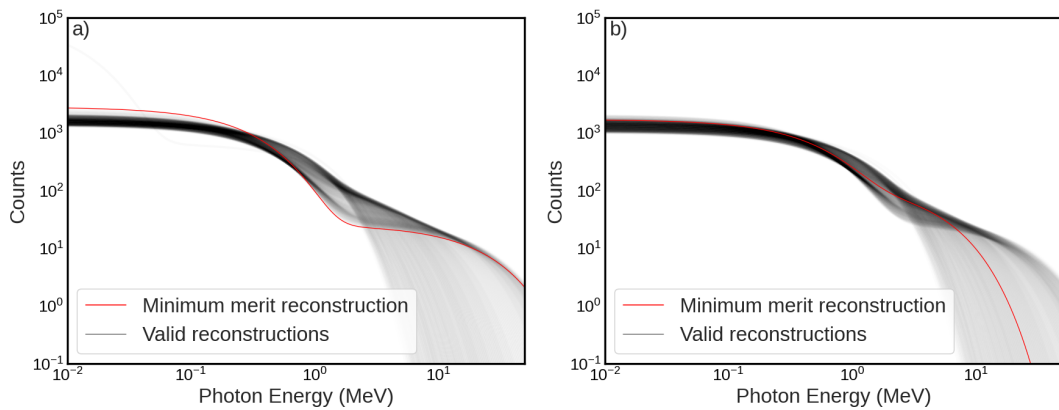


Figure 7.18: Reconstructed spectra using extended response function for laser intensities of (a) 3×10^{20} , and (b) $3 \times 10^{21} \text{ Wcm}^{-2}$. The transparent black lines each represent a ‘valid’ spectral solution and the red line represents the spectral solution with the lowest merit value.

The reconstructed spectral distributions for laser intensities of 3×10^{20} and $3 \times 10^{21} \text{ Wcm}^{-2}$, over an order of magnitude apart in intensity, are consistently very similar although with a significant amount of uncertainty. If the Wilks [47] temperature scaling is appropriate here then there should be considerable difference in the higher temperature components between the two points, which is not seen. However, it has also already been seen that it can be difficult to resolve the higher temperatures given the lack of differentiation in responses between each of the crystals at higher energy. The same conclusion is reached whether whilst considering either the total spectrometer signal or the spectral deconvolution of the individual spectrometer signals. To gain an insight into the spectral distributions that could be expected, more modelling is required and is presented in the

next section.

7.4 Modelling using PIC and Monte Carlo simulations

Because of the discrepancy between the experimental temperatures and modelling results, and large associated uncertainties, it is appropriate to examine the distributions of x-ray spectra that we might expect from similar experimental parameters and to test whether the spectrometer can be used to extract known x-ray spectra. In order to better understand the experimental measurements a series of 2D PIC and Monte Carlo simulations are performed to obtain electron and x-ray spectra.

7.4.1 Generation of electron spectra

A series of laser-plasma interactions with fixed energy are modelled in EPOCH 2D [206] wherein the intensity was varied via the spot size. The intensity was varied in the range of $1.5 \times 10^{20} \text{ Wcm}^{-2}$ to $3 \times 10^{21} \text{ Wcm}^{-2}$, with focal spots ranging from 2 to 40 μm . It is important to note that in 2D the energy does not scale as it would in reality and instead scales linearly with spot radius, so a larger range of spot sizes were required to simulate the full intensity range.

The $20 \times 40 \mu\text{m}$ simulation box consisted of 5000×12800 cells. The 1.054 μm , 500 fs laser pulse was incident onto a 10 μm thick copper target with a 0.5 μm density scale length. The maximum ion density was $8.4 \times 10^{28} \text{ m}^{-3}$. The electron and ion target populations were initialised with temperatures of 100 and 10 eV, respectively.

The electron spectra, shown in Figure 7.19, are sampled over the entirety of the simulation area at the time-step corresponding to the peak of the laser pulse interacting with the front of the target. Boltzmann spectra were fitted to extract the temperatures from the spectra which are shown in Figure 7.20. Uncertainties in these (and later) simulation temperatures are given by the associated uncer-

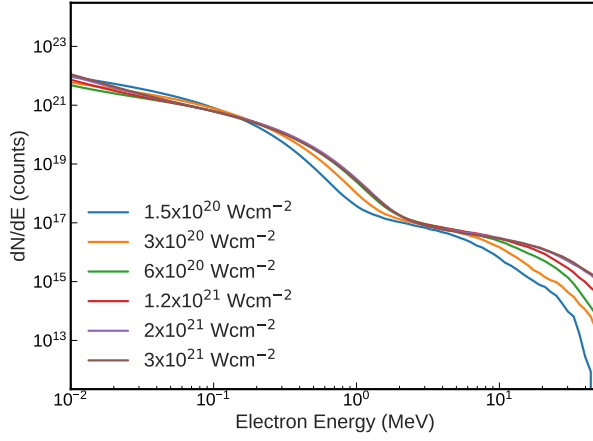


Figure 7.19: EPOCH 2D [206] electron spectra for fixed energy intensity scan, corresponding to laser intensities of 1.5×10^{20} , 3×10^{20} , 6×10^{20} , 1.2×10^{21} , 2×10^{21} , and 3×10^{21} Wcm^{-2} .

tainty in the temperature fit to the spectra. It is clear here that the electron spectra exhibit two well-defined temperatures. It can be seen that the lower electron temperature plateaus at intensities above 6×10^{20} Wcm^{-2} , whereas the higher electron temperature keeps increasing over the entire intensity range. Also shown are the fast electron temperatures given by the Wilks [47], Dover *et al.* [110], and Haines *et al.* [48] fast electron temperature scalings, described in Chapter 2. The Dover *et al.* [110] scaling is dependent on laser focal spot size. The Dover *et al.* [110] scaling shown in Figure 7.20 is calculated solely for the smallest spot sizes of 1.5 and 2 μm for simplicity, rather than full the full spot-size range. It can be seen, from Figure 7.20, that the 1.5 μm Dover *et al.* [110] scaling is a good fit for most of the simulation temperatures. Given that the minimum spot size in the simulations is 2 μm , this suggests that there is an additional limitation of electron heating in the simulations.

The higher electron temperatures are higher than the modelling in the previous section suggests, which followed a slower temperature scaling than all three established scalings shown in Figure 7.20. It is important to note that the simulation temperatures presented here are a snapshot of the peak electron temperatures, taken at the peak of the laser pulse interaction. In reality, especially with longer pulse lengths (≈ 1 ps), electrons will continue to interact with the laser light and absorb laser energy as they recirculate, providing the spot size is large enough [98]. It is largely the lower energy recirculating electrons that stay

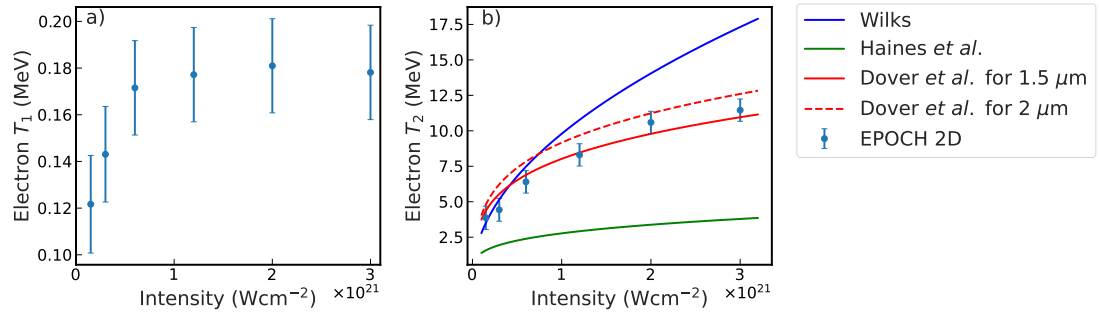


Figure 7.20: Lower (a) and higher (b) Boltzmann temperatures for EPOCH 2D electron spectra, with fitting errors. In (b) are the Wilks [47], Dover *et al.* [110], and Haines *et al.* [48] fast electron temperature scalings in blue, red, and green lines, respectively. The Dover *et al.* temperatures are calculated for both a 1.5 μm and 2 μm spot size for a 1.05 μm wavelength laser (dashed and solid lines, respectively).

trapped within the target that generate bremsstrahlung, although the higher energy electrons will contribute during their passage through the target. As such, it is possible that while higher electron temperatures may be present experimentally, many of the electrons in the higher temperature component will have less of a contribution to the x-ray emission, giving the signature of a lower electron temperature in the data. In Rusby *et al.* [244], it was found through PIC modelling that the temperature of the escaping and recirculating electron populations can be reduced by up to 50% of their initial temperatures after experiencing sheath fields on the rear of the target. This too suggests that, while higher temperatures may have initially been present, the evolution of sheath fields during the interaction have caused cooling of the electron temperatures. As the sheath field evolves, it tends to pull electrons back towards the target surface. The work done by the sheath field on the electrons as they interact with it can cause these electrons to lose kinetic energy, effectively cooling them.

7.4.2 Generation of x-ray spectra

The Monte Carlo code GEANT4 [204] is used to generate x-ray spectra for input electron distributions. This method involves independently inputting electrons of 100 different energies into a copper target simulated in GEANT4. This means that, for a single pass of the target for an electron of a certain energy, the emitted x-ray spectrum could be quantified. The purpose of doing this is to remove

the necessity to repeatedly perform incredibly computationally costly and time consuming simulations with 10^8 particles. The method used here allows for a single set of simulations to be run but with the ability to combine the mono-energetic simulations with different electron distributions without the additional computational cost, rather than performing a new set of Monte Carlo simulations for each distribution.

Mono-energetic electron beams containing 10^8 particles are injected into a 25 μm thick Cu target, for electron energies between 0.06 and 50 MeV. Collective effects are not present in the simulation as each electron is simulated one after the other. This means that particle collisions and collective effects, such as beam filamentation, are not modelled. The corresponding electron-to-x-ray spectral heat map is shown in Figure 7.21. It should be noted that the input electron energies were logarithmically spaced to achieve higher resolution at the lower energies and so the resulting spectra are normalised for bin size.

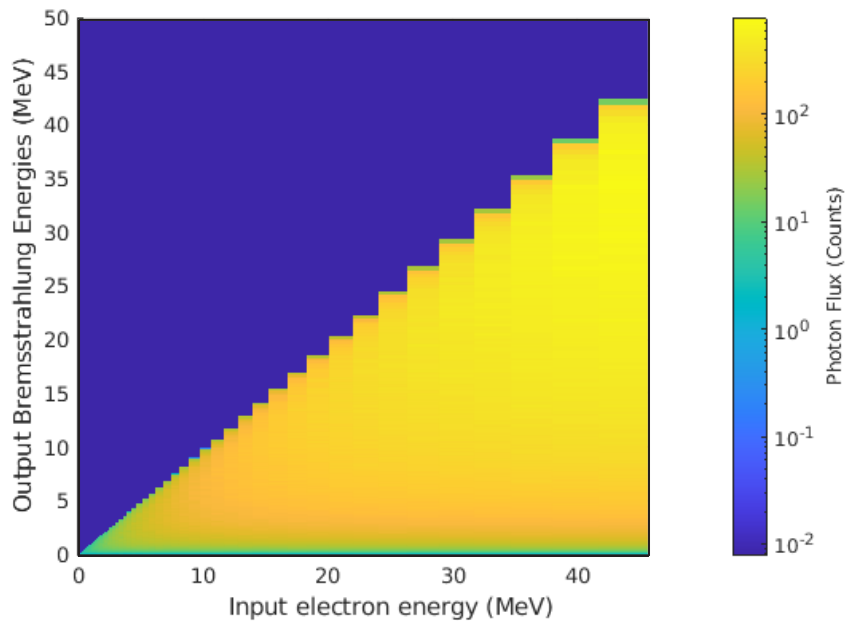


Figure 7.21: GEANT4-generated electron to x-ray spectral heatmap.

This method of generating x-ray spectra with monoenergetic electron inputs was compared to the work in Rusby *et al.* [244] and Fiorini *et al.* [245]. In both Rusby *et al.* [244] and Fiorini *et al.* [245], electron refluxing was simulated by inputting modified electron spectra into Monte Carlo codes to imitate the multiple

electron target-crossings that occur during electron refluxing. This method has the downside of being time consuming, both due to the nature of Monte Carlo codes and to the necessity of the electron inputs needing to be manually changed and resubmitted between each run. Here, the concept of the spectral heatmap was combined with the electron refluxing model outlined earlier in the chapter to generate x-ray spectra for refluxing electrons. In each case, single temperature Boltzmann electron distributions were inputted into the refluxing code. At each pass of the target an x-ray spectrum was produced by combining the modified electron distribution with the spectral heatmap. Whilst this is not entirely accurate as the electron distribution will change at each step within the refluxing code, which would marginally affect the resulting x-ray spectrum, the spectra generated via this method are comparable to the spectra reported in Rusby *et al.* [244] and Fiorini *et al.* [245] (Figure 7.22). The spectra generated by this method have fewer photons in the high energy end of the spectrum than those of Rusby *et al.* [244] and Fiorini *et al.* [245], which is likely due to the attenuation of high energy electrons in the first few passes of the target that the refluxing code is missing, and therefore fewer x-rays of those higher energies are being generated before those electrons lose their energy.

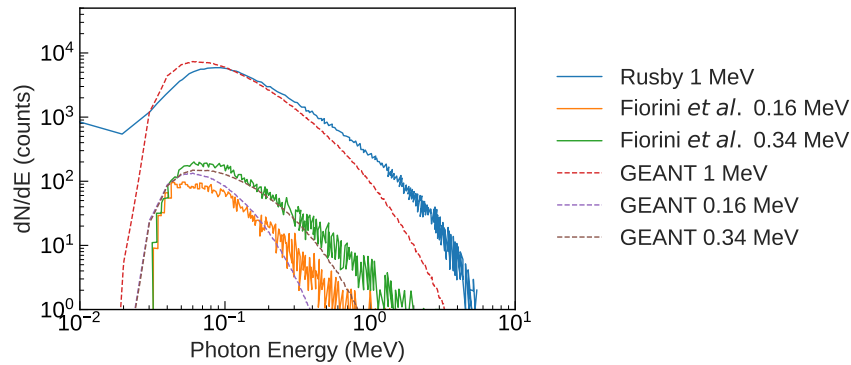


Figure 7.22: X-ray spectra generated using the method of combining mono-energetic GEANT4 x-ray spectra with input electron distributions, with temperatures of 0.16, 0.34, and 1 MeV (orange, green, and blue dashed lines, respectively) alongside the spectra reported in Rusby *et al.* [244] and Fiorini *et al.* [245] (0.16, 0.34, and 1 MeV (orange, green, and blue solid lines, respectively))

7.4.3 X-ray spectra

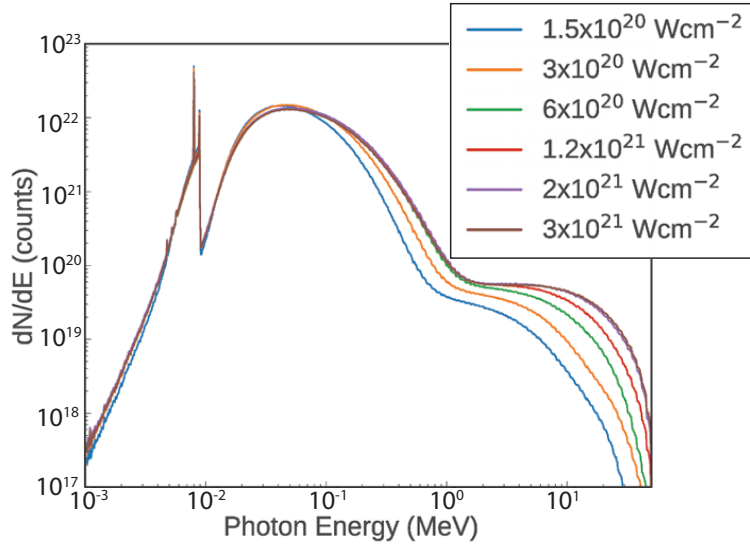


Figure 7.23: GEANT4 x-ray spectra corresponding to the six EPOCH 2D electron spectra corresponding to laser intensities of 1.5×10^{20} , 3×10^{20} , 6×10^{20} , 1.2×10^{21} , 2×10^{21} , and $3 \times 10^{21} \text{ Wcm}^{-2}$.

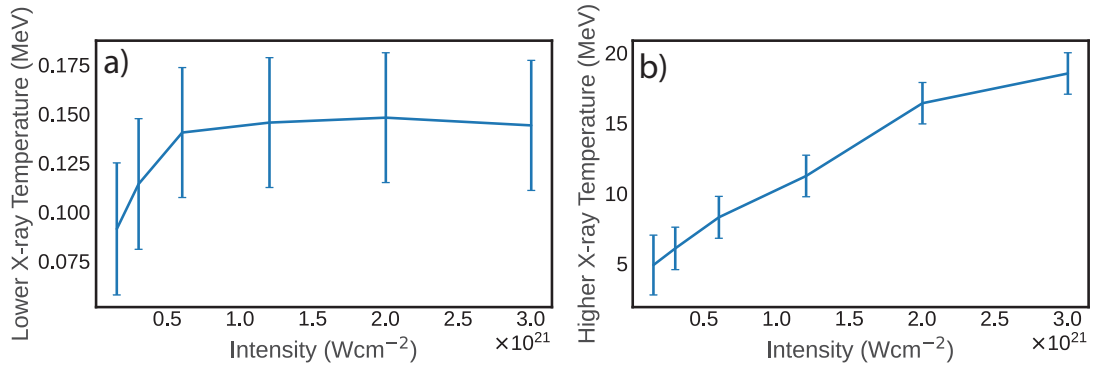


Figure 7.24: (a) Lower and (b) higher Boltzmann temperatures for GEANT4 x-ray spectra, with fitting errors, corresponding to the six EPOCH 2D electron spectra of laser intensities.

The spectral heat-map is then combined with the output EPOCH 2D electron spectra to produce complementary x-ray spectra for the intensity scan simulations. The x-ray spectra, shown in Figure 7.23, follow a similar shape to the electron spectra. Boltzmann temperature fits were also made to the resulting x-ray spectra, resulting in the fitted temperatures shown in Figure 7.24. There is a lower temperature that saturates at around 150 keV and a higher temperature that increases with intensity, in a manner similar to, but steeper than, the corresponding electron temperatures. The lower x-ray temperatures are continually

lower than the corresponding electron temperatures, however the higher x-ray temperatures appear to increase to become higher than the electron temperatures. This is due to the way we are defining x-ray temperatures. It is clear that this is not a perfect fit to the higher photon energies within the spectra, and fitting to most of the spectrum, here the fits are applied from 5-30 MeV before the highest energy section tails off, which is artificially increasing the temperature fit. It should be noted that the x-ray spectra cannot be perfectly defined by two Boltzmann temperature distributions as the electron spectra can.

The higher x-ray temperatures do not appear to saturate at the highest intensities as the electron temperatures do. However this is likely not physical and is a product of the temperature fitting. Figure 7.25 shows the linear Boltzmann fits to the x-ray spectra on a logarithmic y-axis, the highest of the two being applied up to 30 MeV. As the intensity increases, this fit becomes less appropriate as a higher energy tail becomes present, but is also not linear. This highlights the need for a better description of x-ray spectral distributions for higher-intensity interactions.

Another commonly used description of electron and x-ray spectra is the Maxwell-Boltzmann distribution. A Maxwell-Boltzmann distribution of the form

$$f(E) = 2\sqrt{E/\pi}(1/kT)^{\frac{3}{2}}e^{(-E/kT)} \quad (7.4)$$

can instead be used to describe the spectral components. In Figure 7.26, Maxwell-Boltzmann distributions have been fitted to the simulation x-ray spectra (only the extremes of intensities are shown here). It is shown that, in Figure 7.26(a), wherein the distributions have been fitted to the simulation spectrum corresponding to the lowest intensity of $1.5 \times 10^{20} \text{ Wcm}^{-2}$, the Maxwell-Boltzmann distribution is not a particularly good fit for either component. However, for the highest intensity spectrum, at $3 \times 10^{21} \text{ Wcm}^{-2}$, the distribution is a far better visual fit, especially for the higher temperature component. Another feature of the spectra that are easier to see in a logarithmic scale are the Cu K- α emission lines at 8.03 and 8.05 keV, which the spectrometer would not see due to attenuation caused

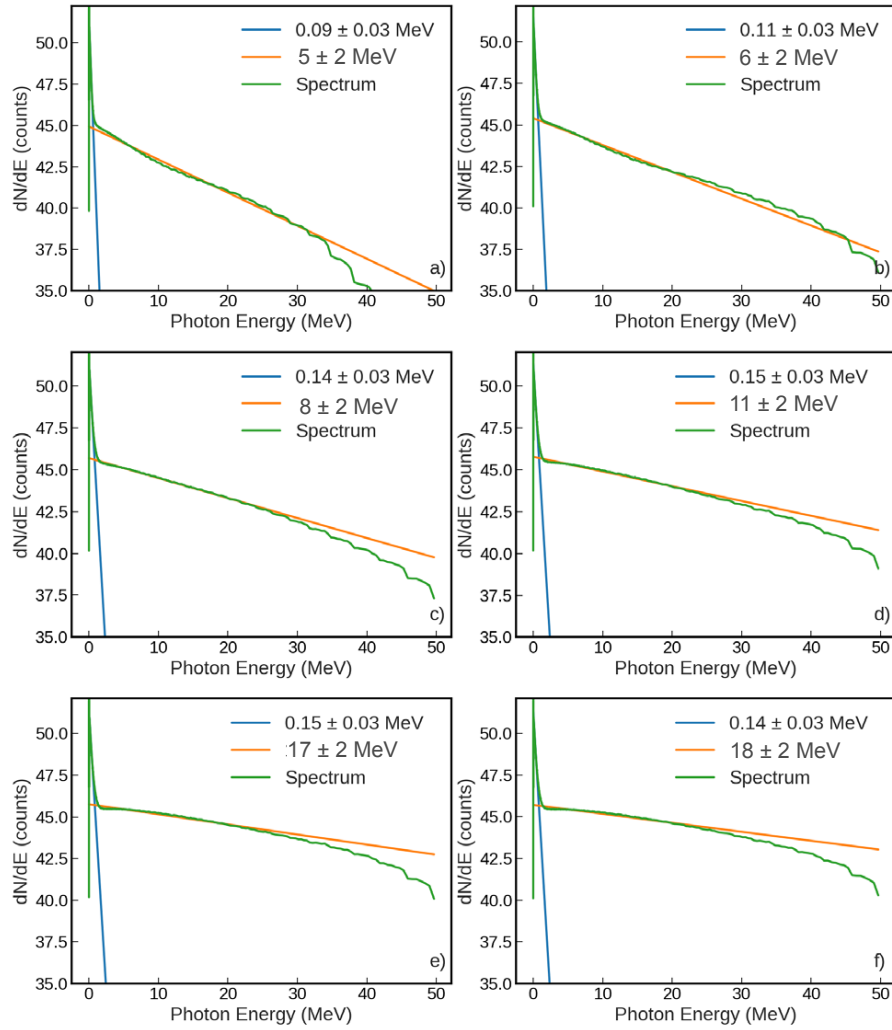


Figure 7.25: Boltzmann distributions fitted to GEANT 4 x-ray spectra for all simulated intensities: (a), $1.5 \times 10^{20} \text{ Wcm}^{-2}$, (b), $3 \times 10^{20} \text{ Wcm}^{-2}$, (c), $6 \times 10^{20} \text{ Wcm}^{-2}$, (d), $1.2 \times 10^{21} \text{ Wcm}^{-2}$, (e), 2×10^{21} , and (f) $3 \times 10^{21} \text{ Wcm}^{-2}$.

by the vacuum chamber and plastic housing of the diagnostic.

A comparison between the higher temperature Boltzmann and Maxwell-Boltzmann temperatures for the simulated x-ray spectra is shown in Figure 7.27. The uncertainties are generated by calculating the least squares error for each fit to the simulated spectra. At the lower intensities, the temperatures given by the two fitting methods do not differ much from each other, with the Maxwell-Boltzmann fits close to sitting within the bounds of uncertainty in the Boltzmann fits. At higher intensities, the temperatures appear to diverge. However, the magnitude of the difference remains the same, with the Boltzmann temperatures being around twice the Maxwell-Boltzmann temperatures. Given the evident difference

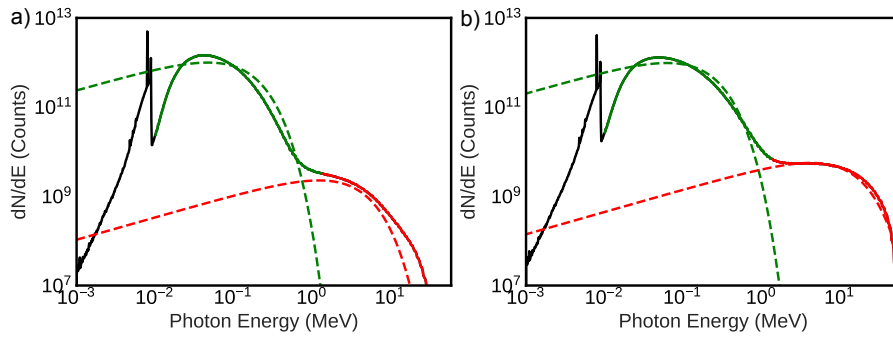


Figure 7.26: Maxwell-Boltzmann distributions fitted to GEANT 4 x-ray spectra for two intensities: (a) $1.5 \times 10^{20} \text{ Wcm}^{-2}$ and (b) $3 \times 10^{21} \text{ Wcm}^{-2}$. The dashed lines represent the Maxwell-Boltzmann temperature fits (green and red are the lower and higher temperatures, respectively), the solid lines indicate the portion of the spectrum included in each fit, and the black line is the GEANT4 bremsstrahlung spectra.

in quality of fit for the two methods, seen in Figures 7.25 and 7.26, the Maxwell-Boltzmann description gives a visibly better fit for higher laser intensities.

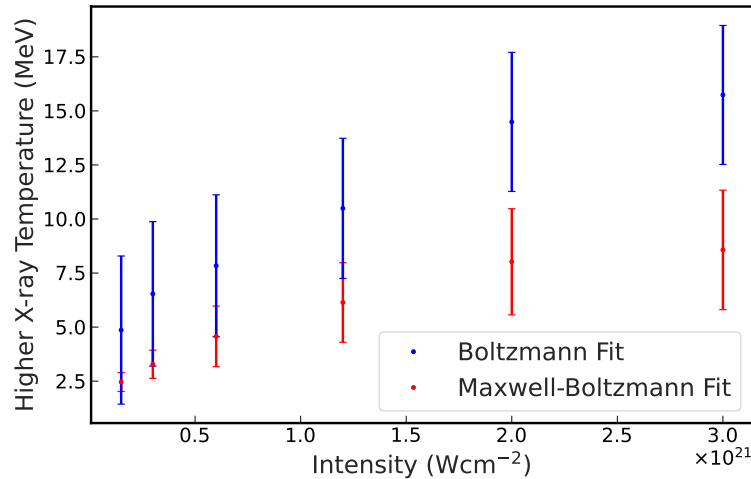


Figure 7.27: A comparison of the temperatures of the higher temperature components as of the GEANT4 x-ray spectra a function of laser intensity, for Boltzmann and Maxwell-Boltzmann fits.

The electron spectra, sampled at the time the peak of the pulse interacts with the front of the target, from the 2D PIC simulations and the output from mono-energetic input Monte Carlo simulations are combined. It is found that, for a set of increasing intensity and decreasing spot size simulations, the fast electron and Boltzmann-fit x-ray temperatures follow a scaling similar to that reported in Dover *et al.* [110]. These temperatures disagree with the experimental x-ray temperatures found initially with the absorption-based x-ray spectrometer. How-

ever, it was shown that the current design features a large amount of uncertainty in the deconvolution of input spectral distributions, particularly those extending to higher photon energies where the scintillator responses converge. Although it is known that such spectra may be difficult to resolve with this spectrometer, it is important to characterise the limitations of the current design, especially when applied to ‘real’ spectra that cannot be perfectly described by any of the common distributions. This will be explored in the next section.

7.5 The characterisation of the existing spectrometer design

7.5.1 Custom spectral fitting

It was shown in the previous section that a two-Boltzmann distribution may not be the best description of x-ray spectra generated in laser-plasma interactions. To test whether this might be an appropriate description for the experimental data, a Boltzmann temperature component and a Maxwell-Boltzmann temperature component was used for fitting to the spectrometer data, as opposed to two Boltzmann-like temperatures. The reconstructions for this Boltzmann/Maxwell-Boltzmann fitting are shown in Figure 7.28, where the distribution of solutions about the experimental data is very similar for both points. Neither cases possess a high number of solutions that are an appropriate fit for the data. This suggests that this spectral distribution is not likely to be a good fit for the experimental data.

The reconstructed Boltzmann/Maxwell-Boltzmann spectral distributions can be found in Figure 7.29. Again, the lower intensity data in Figure 7.29(a) appears to have more valid solutions than the higher intensity in Figure 7.29(b), as seen in the density of solutions in Figure 7.29(a). However, there appear to be a few very differently-shaped distributions, with differing N_1/N_2 ratios to match. The low number of solutions in Figure 7.29(b) also suggests some uncertainty in the solutions, as there are so few that can accurately reconstruct the experimental

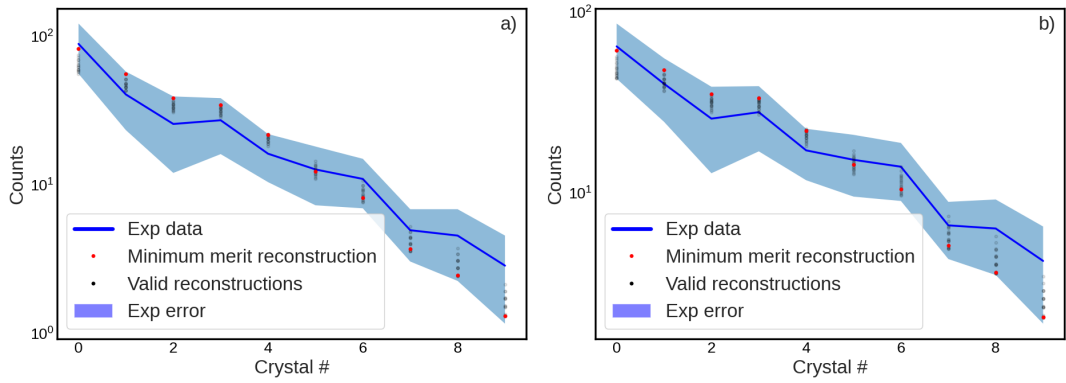


Figure 7.28: Reconstructed data for Boltzmann/Maxwell-Boltzmann fitting for two experimental intensities: (a) 3×10^{20} and (b) 3×10^{21} Wcm^{-2} .

data. In both cases this suggests that this description is not a good fit for the experimental data. It also indicates that the simulation spectra could be of a different distribution to the experimentally measured spectra. The simulation spectra appear to have higher x-ray temperatures than many of the reconstructions found for the experimental data, alongside fewer photon numbers within those higher-temperature components. Due to the uncertainty in the experimental distributions it is not yet possible to conclude whether this is indeed true. If it were true it would suggest that there is an electron heating mechanism that is not present as the intensity increases for there to be lower experimental fast electron and x-ray temperatures. In Frazer *et al.* [179], the presence of additional compression of the plasma skin depth at higher intensities is reported, which may limit the heating of electrons. This would have the observed effect of the experimentally measured x-ray and K- α distributions.

7.5.2 Generating synthetic data

The distributions of the simulated x-ray spectra from the previous section indicate the presence of a higher T_1 - T_2 temperature pairing for the experimental intensity range. Therefore, it is necessary to characterise the performance of the spectrometer for such spectra.

One such method is to test the diagnostic response for synthetic data. In Chen *et al.* [239], synthetic spectrometer data was generated using simulated

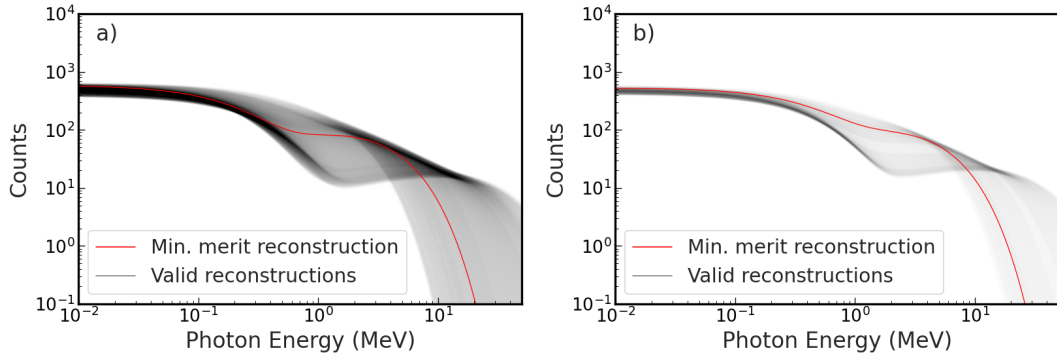


Figure 7.29: Reconstructed spectra for Boltzmann/Maxwell-Boltzmann fitting for two experimental intensities: (a) 3×10^{20} and (b) 3×10^{21} Wcm⁻². The transparent black lines each represent a ‘valid’ spectral solution and the red line represents the spectral solution with the lowest merit value.

x-ray spectra. Here, a similar technique is used. The simulation x-ray spectra presented in the previous section and the spectrometer response matrix were used to generate synthetic spectrometer data, which was then put through the same fitting algorithm as the experimental data. Through this method we can characterise the response of the spectrometer, given that the distributions of the input spectra are known.

The deconvolution merit functions for the fitting algorithm when applied to the synthetic data are shown in Figure 7.30. In comparison with the merit functions for the experimental data (in Figure 7.14), it can be seen that there is significantly less uncertainty in the lower temperature, particularly for the lowest intensities, as the ‘valid solutions’ with the lowest merit all feature a small range of T_1 centred roughly around 100 keV. However, there is a large amount of uncertainty in T_2 , with the lowest merit solutions stretching from below 1 MeV to the boundary at 20 MeV. The two-Boltzmann temperatures of the input spectra are shown in red, and can be seen to lie in the area of low merit. The solutions shown in the coloured areas of the merit grids may not be the best fit for the synthetic data, as seen previously, so the valid solutions will be constrained by the fit to each crystal.

As before, the valid solutions were constrained by the signal uncertainty, which in the case of the synthetic data is taken to be the cube root of the simulated signals. The reconstructed spectral distributions for simulation intensities 3×10^{20}

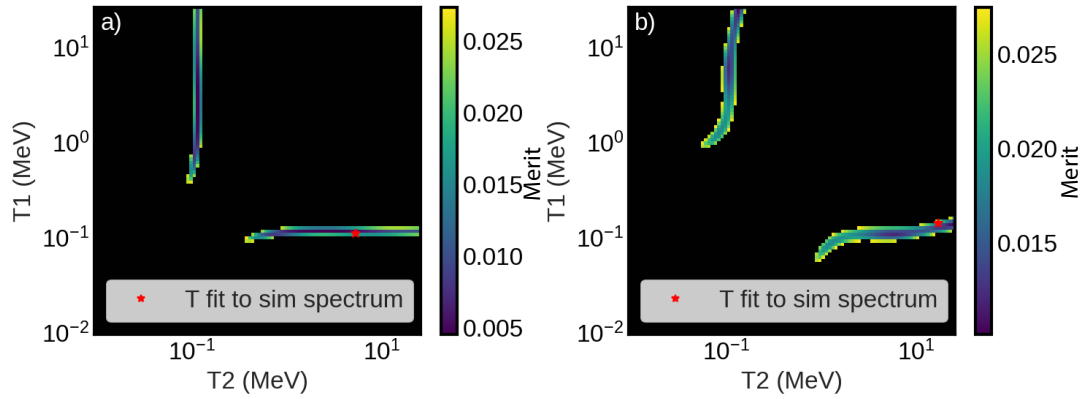


Figure 7.30: Merit functions for the deconvolution of synthetic data for the default, 10-layer, spectrometer design. Each merit grid corresponds to the above simulation x-ray spectra for intensities 3×10^{20} (a), and $3 \times 10^{21} \text{ Wcm}^{-2}$ (b).

and $3 \times 10^{21} \text{ Wcm}^{-2}$ is shown in Figure 7.31. Here, the merit function values, concerning the overall fit of the reconstruction rather than fits of the individual scintillators, are not used to constrain the solutions. As such, the certainty in T_1 seen in the merit grids is not reflected in the reconstructed spectral distributions. There are a great number of solutions than can be considered valid reconstructions of the input synthetic data, with hugely varying temperatures and fluxes. The input spectra are plotted in blue and, although difficult to see due to the high number of valid reconstructions, there are no reconstructions that fit the input spectra well. As before, the reconstructed spectrum corresponding to the solution with the lowest merit value is plotted in red. This solution is a particularly bad fit in Figure 7.31(a), and although it appears a better fit in Figure 7.31(b), this is not real as the solution presented is situated on the boundary of the temperature space.

The great uncertainty in the reconstructed spectral distributions is a reflection of the difficulty in deconvolving x-ray distributions with photon energies in the range of 1 to 10 MeV, where the scintillator responses converge. This also indicates that, even with a lack of experimental noise in the input spectra and non-uniformity in the scintillator output, the current spectrometer design has a significant amount of uncertainty that is intrinsic, due to the behaviour of x-ray energy deposition at this energy range.

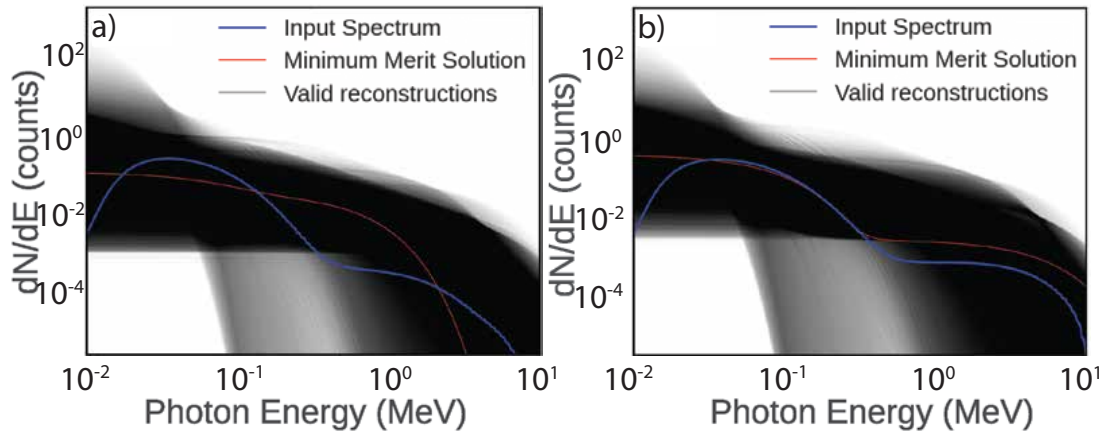


Figure 7.31: Reconstructed spectral distributions for synthetic data. Input spectra in blue correspond to laser intensities of (a) 3×10^{20} and (b) 3×10^{21} Wcm^{-2} . The transparent black lines each represent a ‘valid’ spectral solution, the red line represents the spectral solution with the lowest merit value, and the blue line represents the input spectrum.

Another reason for this poor spectral deconvolution is illustrated in Figure 7.32, which is the $N_1 T_1 / N_2 T_2$ ratio plotted as a function laser intensity for the simulated x-ray spectra. The $N_1 T_1 / N_2 T_2$ ratio is used in [197] to compare the uncertainties of reconstruction for differing temperature components. This gives an idea of the ratio of total energy contained in each temperature component. The ratio for all intensities is in the order of 200-300, and shows that there is significantly more energy stored in the lower temperature component than the higher. When x-ray distributions with so little energy in one of the components are to be deconvolved it leads to poor reconstructions, which is unfortunate given the distributions of x-ray spectra expected from high-intensity laser-plasma interactions.

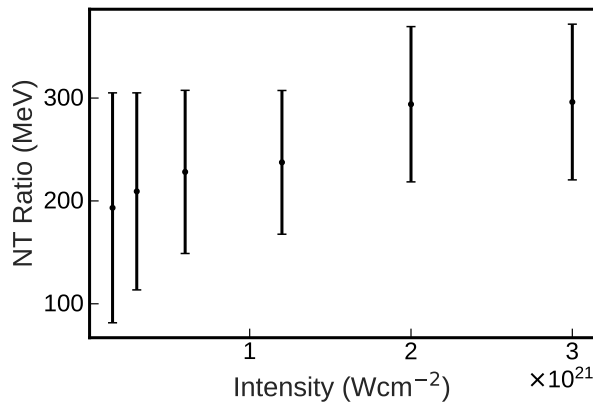


Figure 7.32: Ratio of $N_1 T_1$ to $N_2 T_2$ for simulated x-ray spectra as a function of intensity.

The combination of trying to detect spectral distributions with so little energy in the higher temperature component *and* the temperatures of interest (given by fast electron temperature scalings) being centred around the energy range of one to ten MeV where the scintillator responses converge, make it doubly difficult to deconvolve any kind of spectral information. A method to increase the certainty of reconstruction is to provide greater resolution for higher energy (1-10 MeV) x-ray photons. The method trialled in the next few sections involves providing more points to fit to and greater attenuation.

7.6 High-resolution hard x-ray spectrometer designs

The higher x-ray temperatures from laser-solid interactions at 10^{21} Wcm⁻² and above are, regardless of the relevant fast electron temperature scaling, expected to be in the multi-MeV range. It has been shown that temperatures in this range are difficult to resolve with x-ray diagnostics due to the nature of x-ray energy deposition within this energy range. In the current 10-layer spectrometer design, the responses of the scintillators converge in this energy range which makes it almost impossible to differentiate the diagnostic response for different energy photons in that range. In this section, several designs with a higher number of scintillators and larger amounts of attenuation, provided by more filtering, are tested using synthetic data.

7.6.1 Extension of current design

The first spectrometer design trialled was an extension of the current spectrometer design, incorporating more filtering and scintillators that would sit behind the spectrometer. This design was considered and characterised using the same method of generating synthetic data with the simulation x-ray spectra and the new design response matrix. Again, the deconvolution algorithm was applied to the synthetic data to characterise the performance of the design with known

input spectra.

The design consists of 20 LYSO scintillator crystals with increasing thicknesses of tungsten (W) filtering. The first part of the array is the same as the current design, however the latter ten crystals are in the configuration shown in Figure 7.33, with 5×2 mm LYSO, 5×2 mm LYSO and 2 mm W, 5×4 mm LYSO and 4 mm W and 5×6 mm LYSO and 6 mm W. As with the original design, the function of responses for each of the 20 scintillators to incident radiation was generated using the Monte Carlo code GEANT4.

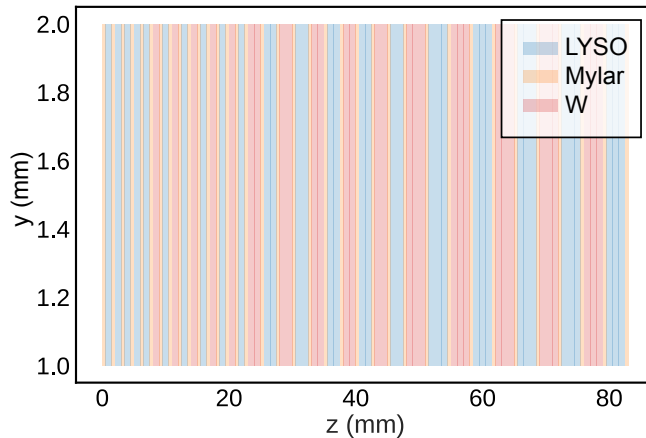


Figure 7.33: Schematic showing design of 20-layer spectrometer, with twenty LYSO layers (blue) and increasing thicknesses of tungsten filtering (red).

In the same manner as before, synthetic data was generated using the the simulation spectra and diagnostic response function. The merit functions generated when applying the synthetic data to the new extended design, for simulations of intensities 3×10^{20} and $3 \times 10^{21} \text{ Wcm}^{-2}$, are shown in Figures 7.34(a) and 7.34(b). Once again, the merit grids are plotted with a maximum value according to the uncertainty, which is taken to be the cube root of the synthetic signals, above which is in black and is not part of the colourmap. At a first glance, it appears as though the entire grid of solutions is invalid. However, there is one solution per grid that has a solution with a low enough merit value. The two-Boltzmann temperatures to the input simulation spectra are plotted in red. The valid solutions appear to come close to resolving the input temperatures, with the ‘valid’ solutions very close to the input distribution. However, for the higher intensity in Figure 7.34(b), the solution with the lowest merit value is again a boundary

solution and is not valid.

This design features far fewer solutions with a merit lower than the uncertainty in the data. Whilst the resolution for higher energy x-ray photons has been increased by having more attenuation and more layers, it has also doubled the number of constraints on the fitting. To see the influence of this on the constraining of reconstruction by individual crystals, the spectral distributions corresponding to solutions that fit the criteria were observed, shown in Figures 7.35(a) and 7.35(b) for simulation intensities of 3×10^{20} and 3×10^{21} Wcm^{-2} . The overall spread of distributions is not dissimilar to that for the original spectrometer design (Figure 7.31) however, the solutions with the lowest T_1 solutions have disappeared. The minimum merit solutions, plotted in red, are closer to resolving the input spectra (blue).

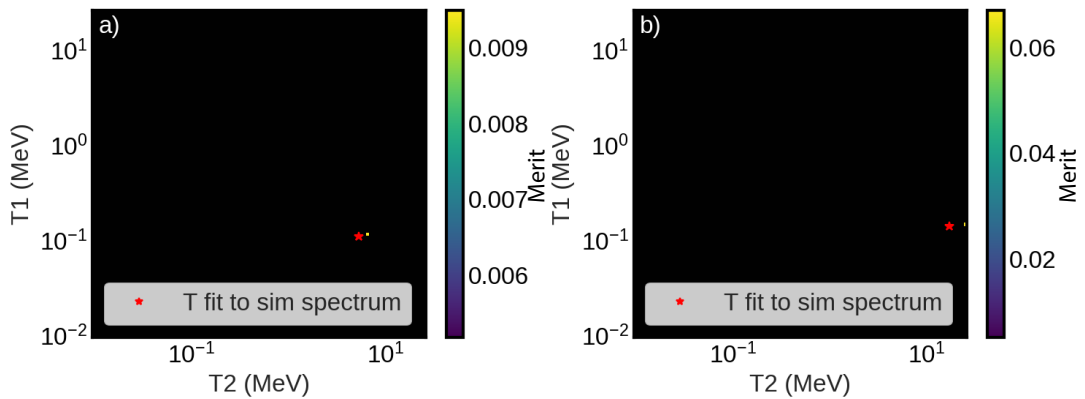


Figure 7.34: Extended-design merit grids for the reconstruction of synthetic data for two-Boltzmann fitting for two simulation intensities: (a) 3×10^{20} and (b) 3×10^{21} Wcm^{-2} .

The design certainly comes closer to resolving the input temperatures but a large amount of uncertainty is still present. To investigate how much of this is due to the poor fitting quality of Boltzmann distributions to some of the higher temperatures, the algorithm was also applied with the custom Boltzmann/Maxwell-Boltzmann distribution. The unconstrained merit grids for the synthetic data are shown in Figure 7.36, with the input Boltzmann and Maxwell-Boltzmann temperatures in red and the minimum merit solution in green. The merit functions for this spectral shape are not symmetrical as the two-Boltzmann functions are. The axis labelled T_2 corresponds to the Maxwell-Boltzmann temperature compo-

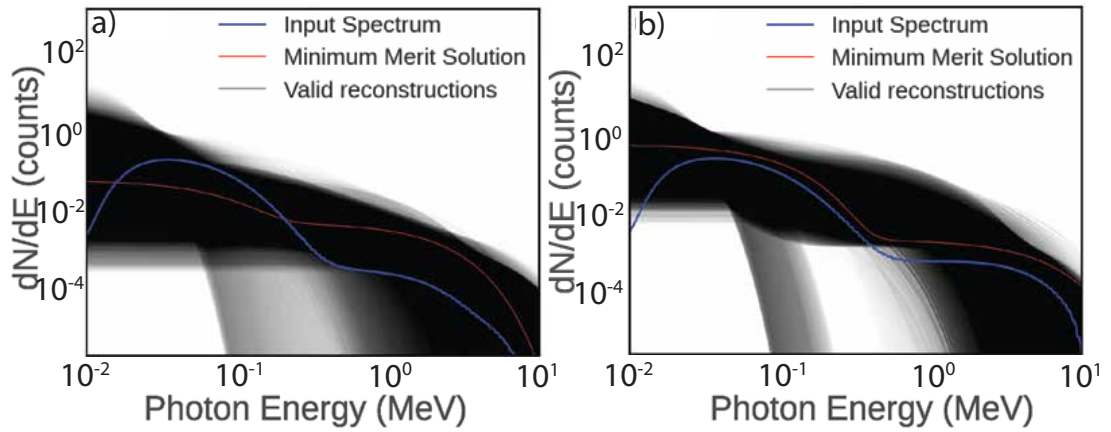


Figure 7.35: Reconstruction of x-ray spectra with two-Boltzmann fitting for two simulation intensities: (a) 3×10^{20} and (b) 3×10^{21} Wcm^{-2} . The transparent black lines each represent a ‘valid’ spectral solution, the red line represents the spectral solution with the lowest merit value, and the blue line represents the input spectrum.

ment, and the other to the Boltzmann component. The green point showing the minimum merit solution in Figure 7.36(a) indicates that the solution with minimum merit has a lower Maxwell-Boltzmann temperature and higher Boltzmann temperature. As seen in Figure 7.26(a), the Maxwell-Boltzmann distribution is not a good fit for either temperature component for the lower intensities, and it is likely a combination of this and a lack of energy within the higher temperature component that is causing the solution to be wrong. However, the minimum merit solution for the highest intensity, 3×10^{21} Wcm^{-2} in Figure 7.36(b), is relatively close to the input temperatures.

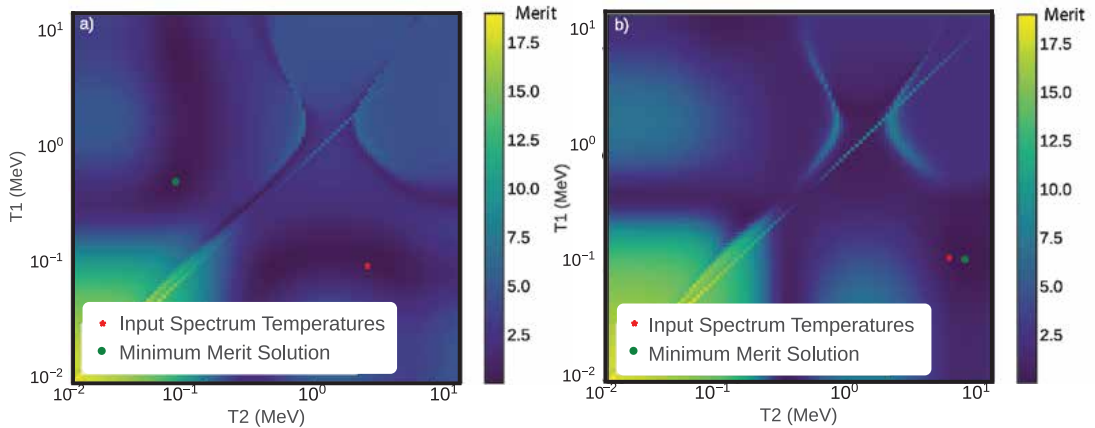


Figure 7.36: Extended-design merit grids for the reconstruction of synthetic data for Boltzmann/Maxwell-Boltzmann fitting for two simulation intensities: (a) 3×10^{20} and (b) 3×10^{21} Wcm^{-2} .

This is because of a few things: firstly the NT energy ratios shown in Figure 7.32 indicate that the energy contained within the higher temperature component at the higher intensities is higher than for the lower intensities which makes it easier to detect; the use of custom Boltzmann/Maxwell-Boltzmann fitting, which is a better fit for the synthetic spectral input and; the addition of more filtering and more detecting layers. This shows a great improvement compared to the original design in deconvolving the synthetic data.

7.6.2 Spectrometer signal and flux modelling

The analytical two-Boltzmann temperature x-ray photon distribution model used earlier to complement the experimental fluxes can also be used to predict what the spectrometer signals may have looked like on the extended spectrometer design. Figure 7.37. shows how the total spectrometer signal would scale with laser intensity for fixed energy with different x-ray temperature scalings (defined by the fast electron temperature scalings of Wilks [47] (dashed) and Haines *et al.* [48] (solid)). These photon distributions have a fixed lower temperature as before, and a higher temperature that scales with the laser intensity. Each distribution has a different ratio of photons in each component, from 1:1 to 1:1000. It can be seen that when the $N_2:N_1$ ratio is small ($\approx 1:1000$), it would be difficult to differentiate between a Wilks [47] and Haines *et al.* [48] temperature scaling with spectrometer signal alone. As this is the ratio seen in the simulation x-ray spectra it is likely that this kind of distribution is present in laser-solid interactions. This highlights the need for some certainty in the spectral deconvolution, even with the extended design of spectrometer. However, if there were an order of magnitude more photons in the higher temperature component then the difference in spectrometer signals as a function of laser intensity becomes more significant and could increase the certainty in spectral deconvolution.

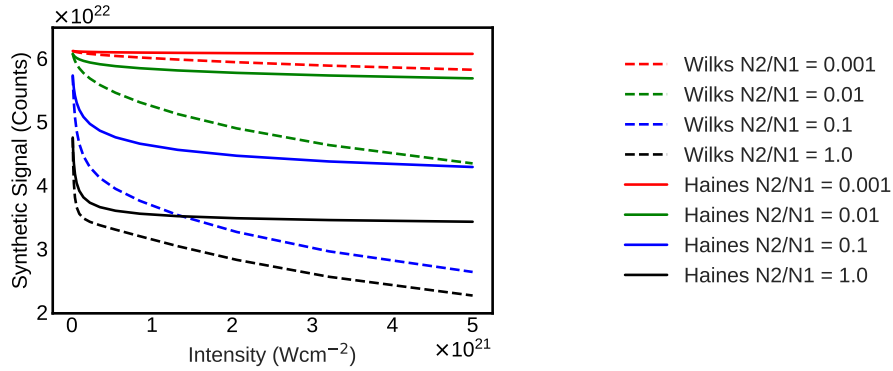


Figure 7.37: Synthetic spectrometer signals for extended spectrometer design using two-Boltzmann temperature distributions with fixed energy and differing $N_1:N_2$ ratios. The lower temperature is fixed and the higher temperature is given by the Haines *et al.* [48] (solid) and Wilks [47] (dashed) fast electron temperature scalings.

7.6.3 Extended spectrometer design summary

The highly-filtered, extended design provides better reconstruction of the input spectra overall, compared to the current 10-layer diagnostic design, with a somewhat better capability of measuring higher x-ray temperatures. However, the design and deconvolution struggles with the extremely low flux in the higher temperature and tends, instead, to find solutions with more equal-numbers of photons in each component. It is likely that the design would work well for x-ray spectra with temperature components that are more equal in flux.

The design, however, has drawbacks. The design itself is very large, with the array of filters and scintillators measuring 15 centimeters long without any spacers or housing. The problem this poses is two-fold: the detector would be difficult to place amongst other diagnostics due to its size and the whole array would be difficult to image on a single camera chip. Another issue, which is not isolated to this design, is that, with increasing thicknesses of filtering, the signal in the latter crystals would become incredibly dim and would require a higher-sensitivity camera or other detector, such as a photodiode, to detect.

7.6.4 Complementary high energy design (LAS-HX)

A more practical solution that solves the issue of size and camera chip space makes use of a heavily filtered design that can be placed in the same housing as

the current design. This would keep the diagnostic with the same footprint but utilise existing space within the camera image. This configuration is first filtered by 50 mm of tungsten, before an array of LYSO and tungsten layers, as shown in Figure 7.38(a). The combined response matrix for the two designs is shown in Figure 7.38(b) and, as long as the crystal regions of interest are inputted in the correct order, the design works no differently.

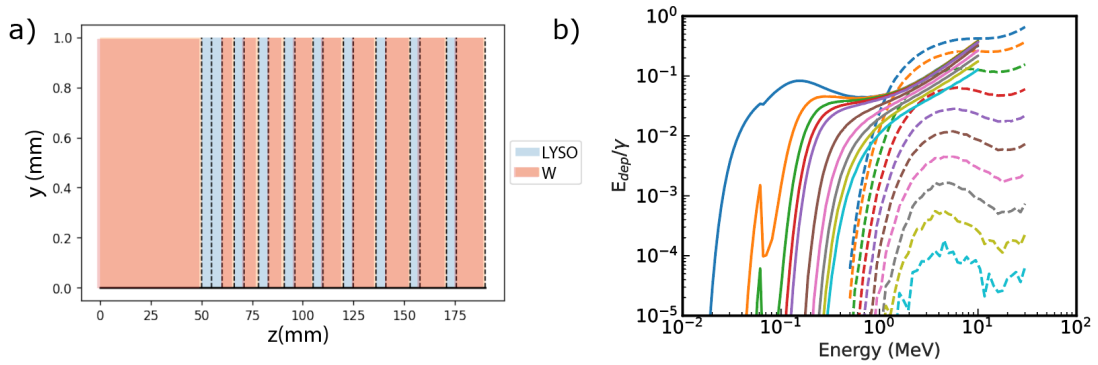


Figure 7.38: (a) Design of the heavily filtered addition to the current diagnostic, with 10 LYSO layers (blue) attenuated by increasing thicknesses of tungsten (orange), and, (b), the merged, high energy response matrix for the two arrays: the current design (solid) and the high-energy insert (dashed).

As before, this spectrometer design was tested by generating synthetic data with the simulation spectra and the diagnostic response matrix. The merit functions for two intensities ($3 \times 10^{20} \text{ Wcm}^{-2}$ and $3 \times 10^{21} \text{ Wcm}^{-2}$), generated with the Boltzmann/Maxwell-Boltzmann temperature fitting algorithm, can be found in Figure 7.39. Again, the low merit areas of the merit function for deconvolution with this design generally coincide with the input temperatures (green points), with the minimum merit solution shown in red. It can be seen that the deconvolved, minimum merit solution and actual input temperatures are in agreement in both intensity cases. This behaviour is also seen for two-Boltzmann temperature fitting.

As before, the response of the diagnostic to two-temperature spectra of increasing intensity but constant energy can be analysed. The synthetic signals for two-Boltzmann temperature distributions with higher temperatures defined by either the Wilks [47] or the Haines *et al.* [48] scaling, shown in Figure 7.40 show large differences in signal between the two scalings for higher laser intensities.

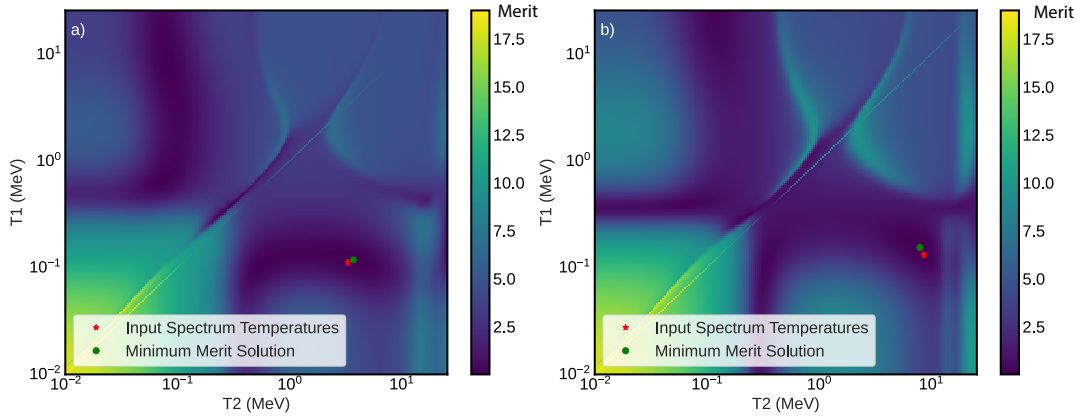


Figure 7.39: Reconstruction merit grids for the LAS-HX insert design reconstruction of synthetic data for Boltzmann/Maxwell-Boltzmann fitting at two simulation intensities: (a) 3×10^{20} and (b) $3 \times 10^{21} \text{ Wcm}^{-2}$.

Because of the heavily filtered addition it is possible to distinguish the decrease in x-ray flux due to the increase in x-ray temperatures for the higher Wilks [47] temperatures. Even with only 1:100 photons in the higher temperature component compared to the lower, there is a detectable decrease of a third of the total signal across the intensity range. Unfortunately, this is not seen with the lower temperature, slower Haines *et al.* [48] scaling. This scaling would not produce x-ray photons of high enough energy to make a difference to the signals of the filtered insert and as such this design would not be able to distinguish spectral distributions by total signal alone.

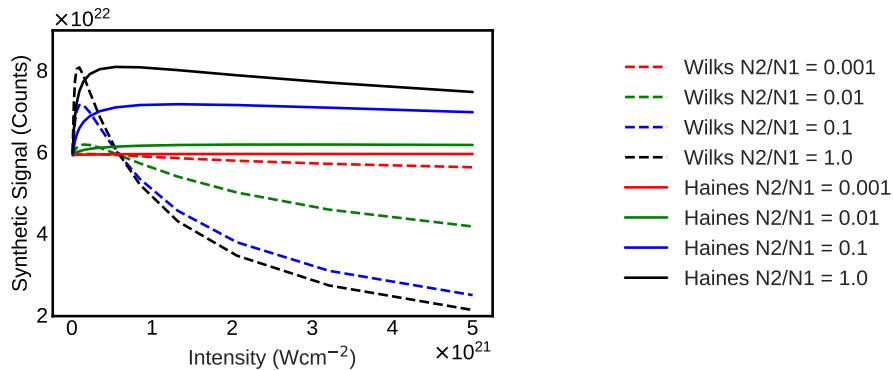


Figure 7.40: Synthetic spectrometer signals for LAS-HX spectrometer design using two-Boltzmann temperature distributions with fixed energy and differing $N_1:N_2$ ratios. The lower temperature is fixed and the higher temperature is given by the Haines *et al.* [48] and Wilks [47] (dashed) fast electron temperature scalings.

This design may experience some of the same practical issues as the 20-layer

design, with a large dynamic range of scintillator signals to detect and to fit to. However, this design removes the physical and image footprint issues. The main caveat to this design that each array is laterally sampling a different part of the beam, so it would not be useful if any highly energy-dependent directionality was expected within the beam, as each array could end up sampling different x-ray energies. For quasi-isotropic bremsstrahlung emission this would not be a problem however, for some of the more direction synchrotron emission mechanisms this may be an issue.

If this design of spectrometer were to have been used on the experiment described earlier, it is likely that some kind of spectral information would have been recovered. Without the addition of experimental noise (for example: emission from around the target chamber that is not filtered out by the collimator) the spectral deconvolution may have been more uncertain than for the synthetic data seen here. However, the performance would have been better than the original spectrometer design for this purpose.

7.7 Conclusions

In this chapter the measurement of x-rays from laser-solid interactions with intensities above 10^{21} Wcm⁻² were discussed, with consideration of a linear absorption spectrometer, as a means to test the electron temperature scaling at higher laser intensities. Such intensities were achieved through the use of focusing plasma optics.

Measurements of x-ray energy deposition and spectral distribution were made with the spectrometer. X-ray energy deposition into the spectrometer was found to be relatively constant with increasing laser intensity when normalised for energy on target. A similar trend in the Cu K- α signal was reported in [179]. Analytical modelling of x-ray and electron spectra was conducted to investigate this phenomenon.

The change in photon numbers given by an increasing higher x-ray temperature in a constant energy distribution was shown to have an influence on the

total signal measured on the spectrometer. It is found that, if the drop in photon numbers with increasing higher x-ray temperature in the system were the cause of decreasing x-ray energy depositions, then the ratio of fluxes within the components would have had to be lower than 10:1 between the lower temperature and higher temperature components, regardless of higher x-ray temperature. This was later found to be consistent with the x-ray spectra generated using input electron spectra from EPOCH 2D and the Monte Carlo code GEANT4, which had $N_1:N_2$ ratios of around 1000:1.

Analytical models using two electron temperature scalings, the Wilks [47] and Haines *et al.* [48] models, were applied to consider the decrease in electron numbers with increasing fast electron temperature for a fixed energy system, before a radiative loss refluxing model was applied. It is found that, if the laser energy absorbed by the electrons remained constant, it is likely that an electron temperature scaling slower than predicted by either the Haines *et al.* or Wilks models is causing the flat spectrometer signal with increasing laser intensity.

PIC modelling was used to generate electron spectra for laser pulses the intensity range of 1.2×10^{20} to 3×10^{21} Wcm^{-2} interacting with a Cu target. It was found that the higher temperature of the peak electron spectra agreed well with the fast electron temperature scaling reported by Dover *et al.* [110]. With those electron spectra and mono-energetic input GEANT4 simulations, x-ray spectra were generated. These spectra were found to have a higher temperature that followed a similar scaling to that of the electrons. For the higher laser intensities it was found that a Maxwell-Boltzmann spectral distribution was a better fit to the higher temperature component than a simple Boltzmann fit.

A deconvolution algorithm was applied to the spectrometer data in order to understand whether this change in electron, and therefore x-ray, temperature was the cause of the decrease in x-ray energy deposition. It was found that there was a great deal of uncertainty in the spectral deconvolution by assessing the algorithm merit functions. By exploring the areas of low merit within the temperature grid that is scanned through by the algorithm, it became apparent that many different input spectral shapes could provide a satisfactory fit to the exper-

imental data, within experimental uncertainty, which caused a large amount of uncertainty in the temperature measurements. Methods to improve the deconvolution of spectral information from the experimental data, such as extending the response matrix to higher photon energies and using custom hybrid Boltzmann and Maxwell-Boltzmann temperature fitting, were used which acted to gain more certainty in the spectral measurements, but not enough for a single T_1 - T_2 solution to be found for the data.

To better understand the response of the spectrometer and understand the spectral distributions likely from ultra-intense laser-plasma interactions, a combination of PIC and Monte Carlo modelling was used to generate x-ray spectra for a fixed energy intensity scan performed in EPOCH 2D. The electron and x-ray distributions are found to be quite well described as two-temperature distributions, with either two Boltzmann temperature components or a single Boltzmann component and higher temperature Maxwell-Boltzmann component. With simulated x-ray spectra, we are able to generate synthetic spectrometer data in order to characterise the current spectrometer design.

The current spectrometer design was characterised using the synthetic spectrometer data, and similar issues with large uncertainties in the recovered spectral distributions were found. It is concluded that this is in part due to the large difference in photon numbers between (and therefore total energy contained within) the temperature components, wherein the higher temperature component simply did not contain enough energy and, due to the additional lack of convergence of the scintillator signals for photons between 1-10 MeV, there is also not enough resolution.

To attempt to alleviate the issues regarding large uncertainties within the recovered spectra, two new spectrometer designs were tested: a single, one-dimensional array of increasing thicknesses of filtering and scintillators which is an extension to the current design and another 2D array, that consists of a new, heavily-filtered insert into the existing design. The LAS-HX design with the heavily filtered insert proves to exhibit the most certainty in deconvolving the input, synthetic spectral distributions, with correctly resolved temperatures

for the lower and higher intensities. It seems likely that this design, if employed on an ultra-high intensity experiment, would be able to deconvolve some spectral information.

7.8 Future work

To progress this work further to be appropriate for even higher laser intensities, it would be appropriate to take synchrotron emission into account. The presence of synchrotron emission would almost certainly act to change the distribution of x-rays in a way that would prove challenging to resolve separately from the bremsstrahlung emission.

The other, more obvious progression of this work would be to experimentally test the filtered insert design of spectrometer to understand the impact of experimental noise on deconvolving spectral information. As mentioned before, the difficulties in realising this lie in detecting a large dynamic range of scintillator signals within a single image without saturation or losing data in the noise floor of the CMOS detector due to low crystal signal.

Chapter 8

Conclusions

The aim of the work presented in this thesis is to experimentally and numerically investigate the measurement and optimisation of x-rays, through both the bremsstrahlung and synchrotron emission mechanisms, in laser-solid interactions. As a means of detecting and differentiating bremsstrahlung and synchrotron emission, an existing absorption-based x-ray spectrometer is characterised and developed for x-ray emission spectra from laser-solid interactions at intensities above 10^{21} Wcm^{-2} .

Over two experimental campaigns, within which a wide range of diagnostic and numerical simulation techniques are employed, a greater understanding of the relative optimisation bremsstrahlung and synchrotron production has been developed, particularly with relevance to the influences of laser pulse energy and focal spot size. To complement these findings, an absorption based x-ray spectrometer is characterised and further developed for higher spectral resolution at the x-ray spectral temperatures expected in ultra-intense laser plasma interactions. The key findings and conclusions of each of these investigations are summarised in this final chapter, alongside discussions of future avenues of work.

8.1 The role of laser focal spot size and pulse energy in bremsstrahlung and synchrotron production in thick targets

The investigation presented in Chapter 5 builds upon the previous work related to the influence of near-wavelength focal spots on fast electron temperature scalings with laser intensity [110]. In Chapter 5, the influence of laser focal spot size and pulse energy on bremsstrahlung and synchrotron production is investigated. Through PIC simulations, using the code EPOCH with its in-built bremsstrahlung and synchrotron modules, the influence of intensity changes, where the spot size is fixed or where the laser energy is fixed, on the production of x-rays is investigated.

Additionally, that the influence of the F -number focusing geometry on the interaction is small, with only the front surface and internal target electron spectra experiencing changes between corresponding best focus and defocus cases.

It is found that, for the two temperature electron population, consisting of a lower temperature (T_1) component and a higher temperature (T_2) component, internal to the target, the electron T_1 and total electron energies increased with increasing pulse energy. Furthermore, it is found that there are spot-size limiting effects, for fixed laser intensity, with a lower than expected electron T_2 for the smallest ($2 \mu\text{m}$) spots. This is in agreement with the results reported in [110].

In both the fixed energy and fixed intensity cases, the bremsstrahlung spectra are very similar, although differences in bremsstrahlung x-ray flux between the best focus and defocus cases are found, up to 15% for the largest spots. However, the largest effect is still that of increasing pulse energy to maintain a fixed intensity.

3D PIC simulations are performed to probe the effects of spot size and pulse energy, not only on bremsstrahlung emission, but also synchrotron emission, for fixed energy and fixed intensity independently at three different intensity ranges. It is found, again, that x-ray emission due to the bremsstrahlung mechanism is

highly pulse energy dependent. Synchrotron emission is instead found to be highly spot-size and intensity dependent. Through deeper investigation of the simulation electron densities and spatial photon emission, it is found that synchrotron photons are emitted almost exclusively within the relativistically underdense region that the laser pulse bored through the target. It is also found that synchrotron flux is related to the size of this hole-bore volume, which is in turn dictated by the size of the laser focal spot. Additionally, despite the $r_L = 1.5 \mu\text{m}$ simulations having an order of magnitude lower pulse energy than the $r_L = 5 \mu\text{m}$ simulations in the fixed intensity cases, increased maximum synchrotron photon energies as well as higher synchrotron photon numbers are observed. To summarise, it is found that to enhance synchrotron emission, it is best to use not only a higher laser intensity, but also the smallest spot possible to enhance holeboring, even if this is at the expense of laser energy.

This points to an advantage in the experimental detection of synchrotron x-rays. In such campaigns there is a requirement to distinguish synchrotron photons from bremsstrahlung photons, which are generally abundant in laser-plasma interactions, particularly for thick targets. The results presented here offer an approach to achieve improved signal to noise ratio of synchrotron to bremsstrahlung. This indicates that studies of synchrotron radiation may be accessible with lower pulse energy laser systems where the focusing geometry is optimised. It also suggests that careful tuning of the pre-plasma conditions to induce controlled self-focusing could be a potential route forward to improve the synchrotron to bremsstrahlung signal to noise. This directly relates to the content of Chapter 7, which focuses on the development and optimisation of an x-ray spectrometer for high-energy x-rays.

8.2 Experimental investigation of the role of laser focal spot size and pulse energy in bremsstrahlung production in thick targets

The investigation presented in Chapter 6 builds on the work of the preceding chapter, and relates to the work in Dover *et al.* [110]. The effects of laser pulse energy, focal spot size, and focusing geometry on electron acceleration and bremsstrahlung x-ray emission are explored experimentally. This is achieved through apodisation of the laser beam to effectively increase the F -number of the focusing optic. An intensity range of between 1×10^{18} and 2×10^{20} Wcm^{-2} is achieved through varying the pulse energy and spot size.

It is unclear whether focusing geometry had an effect on bremsstrahlung x-ray production due to the shot-to-shot variability in the measurements. The x-ray and electron spectrometer signals are found to increase strongly with increasing energy on target. It is also observed that reducing the focal spot size causes the x-ray and electron spectrometer signals to increase more rapidly with intensity, though overall, these signals are higher for higher pulse energies. This trend is also found for the maximum energy of the electron spectra. This is attributed to an increase in laser energy absorption, due to the overall increase in the number of fast electrons.

The conclusions of Chapter 6 are in agreement with those of the preceding chapter. Bremsstrahlung emission is found to be highly dependent on pulse energy and is substantially less sensitive to laser focal spot size changes. Further avenues of this work could involve a deeper investigation of focusing geometry, and hence spatial intensity profile, on electron acceleration and bremsstrahlung x-ray production. As previously stated, this would require a larger range of F -number focusing geometries. If this were to be explored by apodising the laser beam, a larger range of apodisers would be required.

8.3 Linear absorption spectrometer characterisation using bremsstrahlung x-rays

In Chapter 7, the measurement of bremsstrahlung x-rays from laser-solid interactions with intensities above 10^{21} Wcm⁻² is discussed with consideration of a linear absorption spectrometer, as a means to measure the electron temperature scaling at higher laser intensities. Such intensities are achieved through the use of focusing plasma optics [38, 166, 172]. Measurements of x-ray energy deposition and spectral distribution are made with the spectrometer. X-ray energy deposition into the spectrometer is found to be relatively constant with increasing laser intensity, when normalised to the laser pulse energy on target. A similar trend in the Cu K- α signal is reported in [179]. Analytical modelling of x-ray and electron spectra is conducted to investigate this phenomenon. It is found that the flux ratio between the lower and higher temperature components, N_1 and N_2 respectively, had to be lower than 10:1 to explain the experimental x-ray spectrometer signals. Through separate analytical modelling of electron energy losses through refluxing, it is found that a lower electron temperature scaling with intensity than those reported in Wilks [47] and Haines *et al.* [48] would reproduce the experimental x-ray spectrometer signal.

Through PIC and Monte Carlo modelling, it is found that the electron and bremsstrahlung spectra for parameters similar to those of the experiment, exhibits two clear temperature components. For the higher temperature component of the electron distributions, a temperature scaling with laser intensity is found to be in good agreement with the scaling reported in Dover *et al.* [110]. The bremsstrahlung spectra produced for these electron distributions are also found to have a higher temperature, T_2 , which increases in a similar manner to the electron temperatures. At higher laser intensities, it is found that a Maxwell-Boltzmann distribution is a better fit to the higher temperature component than a Boltzmann distribution.

A deconvolution algorithm is used to analyze the experimental x-ray spec-

trometer data, but the results show significant uncertainty in the deconvolved spectral fits. Numerous spectral shapes are able to adequately match the experimental data, leading to substantial uncertainty in the derived temperature measurements. To improve confidence in these measurements, efforts are made to enhance the spectrometer resolution by broadening the energy range of the diagnostic response matrix and using customised spectral fits, such as Boltzmann or Maxwell-Boltzmann distributions. Despite these efforts, a single, definitive temperature solution (T_1-T_2) can not be determined from the data.

Characterisation of the linear absorption x-ray spectrometer is performed by applying the deconvolution algorithm to the simulated bremsstrahlung spectra. This produced simulated spectrometer data to which the deconvolution algorithm could be applied. Similar issues are found, again, with large uncertainties in the spectral deconvolution. This is attributed both to the lack of flux within the higher temperature component of the bremsstrahlung x-ray spectra and due to the lack of convergence of the scintillator crystals for photon energies between 1 and 10 MeV.

To increase the resolution of the diagnostic, two new designs are investigated, both with increased numbers of scintillator crystals and levels of filtering. A design (LAS-HX) that incorporated a heavily filtered rail of scintillators alongside the original spectrometer is found to exhibit the most certainty in deconvolving the synthetic spectral distributions, with correctly resolved higher and lower temperatures. This design utilises existing ‘empty’ space on the camera chip in the current design and has the most practical footprint for use in diagnosing laser-solid interactions. Due to the increased amounts of filtering, a more sensitive camera would be required to detect emission from the most heavily-filtered scintillator crystals.

A further avenue for extending this work would be to employ this design of spectrometer on a future ultra-high intensity experiment, to test its efficacy in resolving high-energy bremsstrahlung x-ray spectra. This relates directly to the work presented in Chapters 5 and 6. Whilst it is important to increase the signal to noise ratio of synchrotron emission to bremsstrahlung, it is also imperative to

be able to distinguish the different spectra, which requires high levels of resolution.

8.4 Further work

This thesis focuses on two primary objectives: optimizing synchrotron emission to enhance the signal-to-noise ratio relative to bremsstrahlung production, and improving the detection and characterisation of high-energy x-rays. The development of an x-ray spectrometer, described within this work, enables the spectral diagnosis of high-energy x-rays, laying the foundation for experimental characterisation of synchrotron emission. Furthermore, precise resolution of bremsstrahlung x-ray spectra presents a valuable opportunity to obtain more definitive measurements of fast electron temperatures in laser-solid interactions, which is crucial for advancing fast ignition research.

The findings presented in Chapters 5 and 6 suggest that synchrotron emission can be measured using lower-energy, high-repetition-rate ultra-intense laser systems, provided that optimal focusing conditions are achieved. By utilising high-repetition-rate systems, it becomes feasible to amass a significant volume of data within a relatively short timeframe. This increased data acquisition would allow for a more thorough investigation of the underlying physics, facilitate the identification of key trends, and enable the refinement of theoretical models.

However, if the synchrotron radiation generated at current laser intensities remains insufficient compared to bremsstrahlung production for consistent detection, it presents significant challenges for future experiments. The limited availability of high-energy, ultra-intense laser systems further complicates these efforts, implying that detection difficulties may persist in the near term. Such limitations could impede progress in areas of research dependent on synchrotron characterisation, particularly in the development of laser-driven synchrotron x-ray sources. This underscores the need for technological advancements in detection capabilities or access to more powerful laser systems.

To ensure continued progress in the study of synchrotron emission, future work should prioritise the development of more sensitive detection technologies

and explore alternative approaches for enhancing synchrotron signal strength. In the absence of these advancements, experimental exploration of synchrotron x-ray production may face considerable obstacles, limiting our ability to further understand and exploit these processes for practical applications.

Bibliography

- [1] T. H. Maiman. Stimulated Optical Radiation in Ruby. *Nature*, 187(4736): 493–494, 1960. ISSN 0028-0836. doi: 10.1038/187493a0.
- [2] D. Strickland and G. Mourou. Compression of amplified chirped optical pulses. *Optics Communications*, 56(3):219–221, 1985. ISSN 00304018. doi: 10.1016/0030-4018(85)90120-8.
- [3] Nobel Prize Organization. Donna Strickland, Nobel Prize in Physics 2018. URL <https://www.nobelprize.org/womenwhochangedscience/stories/donna-strickland>.
- [4] H. Daido, M. Nishiuchi, *et al.* Review of laser-driven ion sources and their applications. *Reports on Progress in Physics*, 75(5):056401, 2012. ISSN 0034-4885. doi: 10.1088/0034-4885/75/5/056401.
- [5] A. Macchi, M. Borghesi, *et al.* Ion acceleration by superintense laser-plasma interaction. *Reviews of Modern Physics*, 85(2):751–793, 2013. ISSN 00346861. doi: 10.1103/RevModPhys.85.751.
- [6] A. J. Mackinnon, Y. Sentoku, *et al.* Enhancement of proton acceleration by hot-electron recirculation in thin foils irradiated by ultraintense laser pulses. *Physical Review Letters*, 88(21):2150061–2150064, 2002. ISSN 00319007. doi: 10.1103/PhysRevLett.88.215006.
- [7] M. J. Bernstein and G. G. Comisar. X-Ray Production in Laser-Heated Plasmas. *Journal of Applied Physics*, 41(2):729–733, 1970. ISSN 0021-8979. doi: 10.1063/1.1658739.

- [8] M. D. Perry, D. Pennington, *et al.* Petawatt laser pulses. *Optics Letters*, 24(3):160, 1999. ISSN 0146-9592. doi: 10.1364/ol.24.000160.
- [9] P. A. Norreys, M. Santala, *et al.* Observation of a highly directional γ -ray beam from ultrashort, ultraintense laser pulse interactions with solids. *Physics of Plasmas*, 6(5):2150–2156, 1999. ISSN 1070664X. doi: 10.1063/1.873466.
- [10] B. Dromey, S. Kar, *et al.* The plasma mirror - A subpicosecond optical switch for ultrahigh power lasers. *Review of Scientific Instruments*, 75(3):645–649, 2004. ISSN 00346748. doi: 10.1063/1.1646737.
- [11] N. Booth, A. P. Robinson, *et al.* Laboratory measurements of resistivity in warm dense plasmas relevant to the microphysics of brown dwarfs. *Nature Communications*, 6(8742):4–8, 2015. ISSN 20411723. doi: 10.1038/ncomms9742.
- [12] G. Sarri, K. Poder, *et al.* Generation of neutral and high-density electron-positron pair plasmas in the laboratory. *Nature Communications*, 6(1):6747, 2015. ISSN 2041-1723. doi: 10.1038/ncomms7747.
- [13] S. V. Bulanov, T. Esirkepov, *et al.* Oncological hadrontherapy with laser ion accelerators. *Physics Letters, Section A: General, Atomic and Solid State Physics*, 299(2-3):240–247, 2002. ISSN 03759601. doi: 10.1016/S0375-9601(02)00521-2.
- [14] D. Doria, K. F. Kakolee, *et al.* Biological effectiveness on live cells of laser driven protons at dose rates exceeding 109 Gy/s. *AIP Advances*, 2(1):011209, 2012. ISSN 2158-3226. doi: 10.1063/1.3699063.
- [15] R. D. Edwards, M. A. Sinclair, *et al.* Characterization of a gamma-ray source based on a laser-plasma accelerator with applications to radiography. *Applied Physics Letters*, 80(12):2129–2131, 2002. ISSN 00036951. doi: 10.1063/1.1464221.

- [16] K. Vaughan, A. S. Moore, *et al.* High-resolution 22-52 keV backlighter sources and application to X-ray radiography. *High Energy Density Physics*, 9(3):635–641, 2013. ISSN 15741818. doi: 10.1016/j.hedp.2013.05.006.
- [17] J. Nuckolls, L. Wood, *et al.* Laser compression of matter to super-high densities: Thermonuclear (CTR) applications. *Nature*, 239(5368):139–142, 1972. ISSN 00280836. doi: 10.1038/239139a0.
- [18] R. Kidder. Application of lasers to the production of high-temperature and high-pressure plasma. *Nuclear Fusion*, 8(1):3–12, 1968. ISSN 0029-5515. doi: 10.1088/0029-5515/8/1/001.
- [19] M. Tabak, J. Hammer, *et al.* Ignition and high gain with ultrapowerful lasers*. *Physics of Plasmas*, 1(5):1626–1634, 1994. ISSN 1070-664X. doi: 10.1063/1.870664.
- [20] Thales. World’s most powerful laser developed by Thales and ELI-NP achieves record power level of 10 PW, 2019. URL <https://www.thalesgroup.com/en/group/journalist/press-release/worlds-most-powerful-laser-developed-thales-and-eli-np-achieves>.
- [21] C. Radier, O. Chalus, *et al.* 10 PW peak power femtosecond laser pulses at ELI-NP. *High Power Laser Science and Engineering*, 10(e21):1–5, 2022. ISSN 20523289. doi: 10.1017/hpl.2022.11.
- [22] S. Weinberg. *The Quantum Theory of Fields*. Cambridge University Press, 1995. ISBN 9780521670531. doi: 10.1017/CBO9781139644167.
- [23] R. P. Feynman. *Quantum Electrodynamics*. CRC Press, 1st edition, 2018. ISBN 9780429493249. doi: 10.1201/9780429493249.
- [24] F. Sauter. On the behavior of an electron in a homogeneous electric field in Dirac’s relativistic theory. *Zeit. f. Phys*, 69(1):742–764, 1931.
- [25] J. Schwinger. On gauge invariance and vacuum polarization. *Physical Review*, 82(5):664–679, 1951. ISSN 0031899X. doi: 10.1103/PhysRev.82.664.

- [26] A. Di Piazza, C. Müller, *et al.* Extremely high-intensity laser interactions with fundamental quantum systems. *Reviews of Modern Physics*, 84(3): 1177–1228, 2012. ISSN 00346861. doi: 10.1103/RevModPhys.84.1177.
- [27] A. Gonoskov, T. G. Blackburn, *et al.* Charged particle motion and radiation in strong electromagnetic fields. *Reviews of Modern Physics*, 94(4):45001, 2022. ISSN 15390756. doi: 10.1103/RevModPhys.94.045001.
- [28] C. P. Ridgers, C. S. Brady, *et al.* Dense electron-positron plasmas and ultraintense γ rays from laser-irradiated solids. *Physical Review Letters*, 108(16):1–5, 2012. ISSN 00319007. doi: 10.1103/PhysRevLett.108.165006.
- [29] X.-B. Wang, G.-Y. Hu, *et al.* Gamma-ray generation from ultraintense laser-irradiated solid targets with preplasma. *High Power Laser Science and Engineering*, 8(e34):1–8, 2020. ISSN 2095-4719. doi: 10.1017/hpl.2020.30.
- [30] T. Nakamura, J. K. Koga, *et al.* High-power γ -ray flash generation in ultraintense laser-plasma interactions. *Physical Review Letters*, 108(19): 1–5, 2012. ISSN 00319007. doi: 10.1103/PhysRevLett.108.195001.
- [31] R. Capdessus and P. McKenna. Influence of radiation reaction force on ultraintense laser-driven ion acceleration. *Physical Review E - Statistical, Nonlinear, and Soft Matter Physics*, 91(5):1–8, 2015. ISSN 15502376. doi: 10.1103/PhysRevE.91.053105.
- [32] M. Marklund and P. K. Shukla. Nonlinear collective effects in photon-photon and photon-plasma interactions. *Reviews of Modern Physics*, 78(2): 591–640, 2006. ISSN 00346861. doi: 10.1103/RevModPhys.78.591.
- [33] A. R. Bell and J. G. Kirk. Possibility of prolific pair production with high-power lasers. *Physical Review Letters*, 101(20):1–4, 2008. ISSN 00319007. doi: 10.1103/PhysRevLett.101.200403.
- [34] G. Breit and J. A. Wheeler. Collision of two light quanta. *Physical Review*, 46(12):1087–1091, 1934. ISSN 0031899X. doi: 10.1103/PhysRev.46.1087.

- [35] H. S. Park, D. M. Chambers, *et al.* High-energy $K\alpha$ radiography using high-intensity, short-pulse lasers. *Physics of Plasmas*, 13(5), 2006. ISSN 1070664X. doi: 10.1063/1.2178775.
- [36] C. M. Brenner, S. R. Mirfayzi, *et al.* Laser-driven x-ray and neutron source development for industrial applications of plasma accelerators. *Plasma Physics and Controlled Fusion*, 58(1):014039, 2016. ISSN 0741-3335. doi: 10.1088/0741-3335/58/1/014039.
- [37] D. R. Rusby, C. M. Brenner, *et al.* Pulsed x-ray imaging of high-density objects using a ten picosecond high-intensity laser driver. In K. L. Lewis and R. C. Hollins, editors, *SPIE*, volume 9992, page 99920E, 2016. ISBN 9781510603882. doi: 10.1117/12.2241776.
- [38] R. Wilson. *On the role of focal spot size in ultra-intense laser-solid interaction physics*. PhD thesis, University of Strathclyde, 2018. URL <http://ethos.bl.uk/OrderDetails.do?uin=uk.bl.ethos.742074>.
- [39] S. Atzeni and J. Meyer-Ter-Vehn. *The Physics of Inertial Fusion*. Oxford Science Publications, 2004. ISBN 978-0-19-956801-7.
- [40] J. P. Freidberg. *Plasma physics and fusion energy*, volume 1. Cambridge University Press, 2007. ISBN 0521851076. doi: 10.2277/0521851076.
- [41] C. Nührenberg. Compressional ideal magnetohydrodynamics: Unstable global modes, stable spectra, and Alfvén eigenmodes in Wendelstein 7-X-type equilibria. *Physics of Plasmas*, 6(1):137–147, 1999. ISSN 1070664X. doi: 10.1063/1.873268.
- [42] K. Toi, S. Ohdachi, *et al.* MHD instabilities and their effects on plasma confinement in Large Helical Device plasmas. *Nuclear Fusion*, 44(2):217–225, 2004. ISSN 0029-5515. doi: 10.1088/0029-5515/44/2/001.
- [43] A. L. Schawlow and C. H. Townes. Infrared and optical masers. *Physical Review*, 112(6):1940–1949, 1958. ISSN 0031899X. doi: 10.1103/PhysRev.112.1940.

- [44] R. S. Craxton, K. S. Anderson, *et al.* Direct-drive inertial confinement fusion: A review. *Physics of Plasmas*, 22(11):110501, 2015. ISSN 10897674. doi: 10.1063/1.4934714.
- [45] J. Lindl. Development of the indirect-drive approach to inertial confinement fusion and the target physics basis for ignition and gain. *Physics of Plasmas*, 2(11):3933, 1995. ISSN 1070664X. doi: 10.1063/1.871025.
- [46] A. R. Piriz, Y. B. Sun, *et al.* Rayleigh Taylor instability in accelerated solid media. *European Journal of Physics*, 38(1):015003, 2017.
- [47] S. C. Wilks. Simulations of ultraintense laserplasma interactions*. *Physics of Fluids B: Plasma Physics*, 5(7):2603–2608, 1993. ISSN 0899-8221. doi: 10.1063/1.860697.
- [48] M. G. Haines, M. S. Wei, *et al.* Hot-Electron Temperature and Laser-Light Absorption in Fast Ignition. *Physical review letters*, 102(4):1–4, 2009. doi: 10.1103/PhysRevLett.102.045008.
- [49] M. Tabak, D. S. Clark, *et al.* Review of progress in Fast Ignition. *Physics of Plasmas*, 12(5):1–8, 2005. ISSN 1070664X. doi: 10.1063/1.1871246.
- [50] I. A. Bush, A. G. R. Thomas, *et al.* Effect of defocusing on picosecond laser-coupling into gold cones. *Physics of Plasmas*, 21(1):012702, 2014. ISSN 1070-664X. doi: 10.1063/1.4861375.
- [51] S. Kar, D. Adams, *et al.* Magnetic collimation of petawatt driven fast electron beam for prospective fast ignition studies. *Journal of Physics: Conference Series*, 244(2):022041, 2010. ISSN 1742-6596. doi: 10.1088/1742-6596/244/2/022041.
- [52] X. H. Yang, M. Borghesi, *et al.* Fast-electron self-collimation in a plasma density gradient. *Physics of Plasmas*, 19(6):062702, 2012. ISSN 1070-664X. doi: 10.1063/1.4729322.

- [53] S. N. Hosseinimotlagh. The stopping power of relativistic electrons and laser-accelerated proton beams for fast ignition of DT and D₃He and P₁1B fuels. *International Journal of Hydrogen Energy*, 41(3):1775–1790, 2016. ISSN 03603199. doi: 10.1016/j.ijhydene.2015.11.098.
- [54] F. N. Beg, A. R. Bell, *et al.* A study of picosecond laser-solid interactions up to 10^{19} Wcm⁻². *Physics of Plasmas*, 4:447–457, 1997. ISSN 1070664X. doi: 10.1063/1.872103.
- [55] C. D. Chen, J. A. King, *et al.* A Bremsstrahlung spectrometer using k-edge and differential filters with image plate dosimeters. *Review of Scientific Instruments*, 79(10):1–4, 2008. ISSN 00346748. doi: 10.1063/1.2964231.
- [56] H. Sawada, Y. Sentoku, *et al.* Characterization of intense laser-produced fast electrons using hard x-rays via bremsstrahlung. *Journal of Physics B: Atomic, Molecular and Optical Physics*, 48(22):224008, 2015. ISSN 0953-4075. doi: 10.1088/0953-4075/48/22/224008.
- [57] K. L. Lancaster, J. S. Green, *et al.* Measurements of energy transport patterns in solid density laser plasma interactions at intensities of 5×10^{20} Wcm⁻². *Physical Review Letters*, 98(12):1–4, 2007. ISSN 00319007. doi: 10.1103/PhysRevLett.98.125002.
- [58] J. S. Green, V. M. Ovchinnikov, *et al.* Effect of laser intensity on fast-electron-beam divergence in solid-density plasmas. *Physical Review Letters*, 100(1):1–4, 2008. ISSN 00319007. doi: 10.1103/PhysRevLett.100.015003.
- [59] Y. Xiao, P. M. Weber, *et al.* Compact laser-driven x-ray sources for medical imaging. *Applied Physics Letters*, 106(8):083101, 2015. doi: 10.1063/1.4896360.
- [60] Y. Chen, K. S. Chung, *et al.* Ultra-bright femtosecond x-ray generation from laser wakefield accelerated electrons. *Physical Review Letters*, 118(17), 2017. doi: 10.1103/PhysRevLett.118.174801.

- [61] D. Margarone and et al. Extreme ultraviolet and x-ray sources from compact laser-plasma accelerators. *Nature*, 511(7509):451–455, 2014. doi: 10.1038/nature13667.
- [62] D. G. Hicks, N. B. Meezan, *et al.* Implosion dynamics measurements at the National Ignition Facility. *Physics of Plasmas*, 19(12):122702, 2012. ISSN 1070-664X. doi: 10.1063/1.4769268.
- [63] L. C. Jarrott, A. J. Kemp, *et al.* $K\alpha$ and bremsstrahlung x-ray radiation backlighter sources from short pulse laser driven silver targets as a function of laser pre-pulse energy. *Physics of Plasmas*, 21(3):031211, 2014. ISSN 1070-664X. doi: 10.1063/1.4865230.
- [64] J. E. Field, J. R. Rygg, *et al.* Reconstruction of 2D x-ray radiographs at the National Ignition Facility using pinhole tomography (invited). *Review of Scientific Instruments*, 85(11):1–7, 2014. ISSN 10897623. doi: 10.1063/1.4890395.
- [65] A. Korzhimanov, A. Gonoskov, *et al.* Horizons of petawatt laser technology. *Uspekhi Fizicheskikh Nauk*, 181(1):9, 2011. ISSN 0042-1294. doi: 10.3367/UFNr.0181.201101c.0009.
- [66] C. N. Danson, C. Haefner, *et al.* Petawatt and exawatt class lasers worldwide. *High Power Laser Science and Engineering*, 7(e54):1–54, 2019. ISSN 2095-4719. doi: 10.1017/hpl.2019.36.
- [67] L. Roso. High repetition rate Petawatt lasers. *EPJ Web of Conferences*, 167(1):01001, 2018. ISSN 2100-014X. doi: 10.1051/epjconf/201816701001.
- [68] C. Haefner. Advanced Laser Promises Exciting Applications, 2017. URL <https://str.llnl.gov/past-issues/julyaugust-2017/advanced-laser-promises-exciting-applications>.
- [69] E. Sistrunk, T. Spinka, *et al.* All Diode-Pumped, High-repetition-rate Advanced Petawatt Laser System (HAPLS). In *Conference on Lasers and*

- Electro-Optics*, Washington, D.C., 2017. OSA. ISBN 978-1-943580-27-9. doi: 10.1364/CLEO_SI.2017.STh1L.2.
- [70] C. S. Brady, C. P. Ridgers, *et al.* Synchrotron radiation, pair production, and longitudinal electron motion during 10-100 PW laser solid interactions. *Physics of Plasmas*, 21(3), 2014. ISSN 10897674. doi: 10.1063/1.4869245.
- [71] J. Vyskocil, E. Gelfer, *et al.* Inverse Compton scattering from solid targets irradiated by ultra-short laser pulses in the 10^{22} – 10^{23} W/cm² regime. *Plasma Physics and Controlled Fusion*, 62(6):064002, 2020. ISSN 0741-3335. doi: 10.1088/1361-6587/ab83cb.
- [72] B. Martinez, E. D’Humières, *et al.* Synchrotron radiation from ultrahigh-intensity laser-plasma interactions and competition with Bremsstrahlung in thin foil targets. *Physical Review Research*, 2(4), 2020. ISSN 26431564. doi: 10.1103/PhysRevResearch.2.043341.
- [73] J. Goodman, M. King, *et al.* Optimization and control of synchrotron emission in ultraintense laser-solid interactions using machine learning. *High Power Laser Science and Engineering*, 11(e34):1–17, 2023. ISSN 2095-4719. doi: 10.1017/hpl.2023.11.
- [74] P. Gibbon. *Short Pulse Laser Interactions with Matter*. Imperial College Press, 1st edition, 2005. ISBN 1-86094-135-4. doi: doi.org/10.1142/p116.
- [75] C. I. Moore, J. P. Knauer, *et al.* Observation of the transition from thomson to compton scattering in multiphoton interactions with low-energy electrons. *Physical Review Letters*, 74(13):2439–2442, 1995. ISSN 00319007. doi: 10.1103/PhysRevLett.74.2439.
- [76] V. T. Tikhonchuk. Interaction of a beam of fast electrons with solids. *Physics of Plasmas*, 9(4):1416, 2002. ISSN 1070664X. doi: 10.1063/1.1459061.

- [77] Y. K. Kim and M. E. Rudd. Binary-encounter-dipole model for electron-impact ionization. *Physical Review A*, 50(5):3954–3967, 1994. ISSN 10502947. doi: 10.1103/PhysRevA.50.3954.
- [78] G. D’Agostini. A multidimensional unfolding method based on Bayes’ theorem. *Nuclear Inst. and Methods in Physics Research, A*, 362(2-3):487–498, 1995. ISSN 01689002. doi: 10.1016/0168-9002(95)00274-X.
- [79] G. S. Voronov and N. B. Delone. Ionization of the xenon atom by the electric field of ruby laser emission, 1965. URL http://www.jetpletters.ac.ru/ps/1590/article_24398.pdf.
- [80] Y. Gontier and M. Trahin. Energetic electron generation by multiphoton absorption. *Journal of Physics B: Atomic and Molecular Physics*, 13(22):4383–4390, 1980. ISSN 00223700. doi: 10.1088/0022-3700/13/22/012.
- [81] H. B. Bebb and A. Gold. Multiphoton ionization of hydrogen and rare-gas atoms. *Physical Review*, 143(1):1–24, 1966. ISSN 0031899X. doi: 10.1103/PhysRev.143.1.
- [82] J. H. Posthumus, M. Thompson, *et al.* Molecular dissociative ionisation using a classical over-the-barrier approach. *IOP Conf. Ser.*, (154):298–307, 1997.
- [83] L. V. Keldysh. Ionization in the field of a strong electromagnetic wave. *Journal of Experimental and Theoretical Physics*, 20(5):1307–1314, 1965. doi: 20(5):13071314,1965.
- [84] A. M. Perelomov, V. S. Popov, *et al.* Ionization of atoms in an alternating electrical field. *Sov. Phys. JETP*, 23(5):924, 1966.
- [85] M. King, R. Wilson, *et al.* Perspectives on laser-plasma physics in the relativistic transparency regime. *The European Physical Journal A*, 59(6):132, 2023. ISSN 1434-601X. doi: 10.1140/epja/s10050-023-01043-2.

- [86] C. Hooker, Y. Tang, *et al.* Improving coherent contrast of petawatt laser pulses. *Optics Express*, 19(3):2193, 2011. ISSN 10944087. doi: 10.1364/oe.19.002193.
- [87] D. Neely, P. Foster, *et al.* Enhanced proton beams from ultrathin targets driven by high contrast laser pulses. *Applied Physics Letters*, 89(2):1–4, 2006. ISSN 00036951. doi: 10.1063/1.2220011.
- [88] G.-Z. Sun, E. Ott, *et al.* Self-focusing of short intense pulses in plasmas. *The Physics of Fluids*, 30(2):526–532, 1987. ISSN 0031-9171. doi: 10.1063/1.866349.
- [89] H. S. Brandi, C. Manus, *et al.* Relativistic self-focusing of ultraintense laser pulses in inhomogeneous underdense plasmas. *Physical Review E*, 47(5):3780–3783, 1993. ISSN 1063651X. doi: 10.1103/PhysRevE.47.3780.
- [90] W. L. Kruer. *The Physics of Laser Plasma Interactions*. CRC Press, Boca Raton, 1st edition, 2019. ISBN 9780429502798. doi: 10.1201/9780429502798.
- [91] F. Brunel. Not-So-Resonant, Resonant Absorption. *Physical Review Letters*, 59(1):52–55, 1987.
- [92] W. L. Kruer and K. Estabrook. $J \times B$ heating by very intense laser light. *Physics of Fluids*, 28(1):430–432, 1985. ISSN 10706631. doi: 10.1063/1.865171.
- [93] H. Alfvén. On the Motion of Cosmic Rays in Interstellar Space. *Physical Review*, 55(5):425–429, 1939.
- [94] A. R. Bell, J. R. Davies, *et al.* Fast-electron transport in high-intensity short-pulse laser - solid experiments. *Plasma Phys. Control. Fusion*, 39(653):652–659, 1997.
- [95] A. P. L. Robinson, H. Schmitz, *et al.* Guiding of laser-generated fast electrons by exploiting the resistivity-gradients around a conical guide element.

- Plasma Physics and Controlled Fusion*, 57(6):1–6, 2015. ISSN 0741-3335. doi: 10.1088/0741-3335/57/6/064004.
- [96] K. U. Akli, M. J. Storm, *et al.* Time dependence of fast electron beam divergence in ultraintense laser-plasma interactions. *Physical Review E - Statistical, Nonlinear, and Soft Matter Physics*, 86(2):1–4, 2012. ISSN 15393755. doi: 10.1103/PhysRevE.86.026404.
- [97] Y. Sentoku, T. E. Cowan, *et al.* High energy proton acceleration in interaction of short laser pulse with dense plasma target. *Physics of Plasmas*, 10(5):2009–2015, 2003. ISSN 1070664X. doi: 10.1063/1.1556298.
- [98] R. J. Gray, R. Wilson, *et al.* Enhanced laser-energy coupling to dense plasmas driven by recirculating electron currents. *New Journal of Physics*, 20(3), 2018. ISSN 13672630. doi: 10.1088/1367-2630/aab089.
- [99] M. N. Quinn. *Investigations of Fast Electron Transport in Intense Laser-Solid Interactions*. PhD thesis, University of Strathclyde, 2011.
- [100] M. N. Quinn, X. H. Yuan, *et al.* Refluxing of fast electrons in solid targets irradiated by intense, picosecond laser pulses. *Plasma Physics and Controlled Fusion*, 53(2):025007, 2011. ISSN 0741-3335. doi: 10.1088/0741-3335/53/2/025007.
- [101] C. D. Armstrong. *Bremsstrahlung radiation and fast electron transport in laser-plasma interactions*. PhD thesis, University of Strathclyde, 2019.
- [102] C. D. Armstrong, C. M. Brenner, *et al.* Bremsstrahlung emission profile from intense laser-solid interactions as a function of laser focal spot size. *Plasma Phys. Control. Fusion*, 61(3):9, 2019.
- [103] R. A. Snavely, M. H. Key, *et al.* Intense high-energy proton beams from petawatt-laser irradiation of solids. *Physical Review Letters*, 85(14):2945–2948, 2000. ISSN 00319007. doi: 10.1103/PhysRevLett.85.2945.

- [104] S. P. Hatchett, C. G. Brown, *et al.* Electron, photon, and ion beams from the relativistic interaction of Petawatt laser pulses with solid targets. *Physics of Plasmas*, 7(5):2076–2082, 2000. ISSN 10897674. doi: 10.1063/1.874030.
- [105] S. C. Wilks, A. B. Langdon, *et al.* Energetic proton generation in ultra-intense laser-solid interactions. *Physics of Plasmas*, 8(2):542–549, 2001. ISSN 1070664X. doi: 10.1063/1.1333697.
- [106] C. M. Brenner, J. S. Green, *et al.* Dependence of laser accelerated protons on laser energy following the interaction of defocused, intense laser pulses with ultra-thin targets. *Laser and Particle Beams*, 29(3):345–351, 2011. ISSN 02630346. doi: 10.1017/S0263034611000395.
- [107] C. M. Brenner, A. P. L. Robinson, *et al.* High energy conversion efficiency in laser-proton acceleration by controlling laser-energy deposition onto thin foil targets. *Applied Physics Letters*, 104(8):081123, 2014. ISSN 0003-6951. doi: 10.1063/1.4865812.
- [108] M. Passoni, L. Bertagna, *et al.* Target normal sheath acceleration: theory, comparison with experiments and future perspectives. *New Journal of Physics*, 12(4):045012, 2010. ISSN 1367-2630. doi: 10.1088/1367-2630/12/4/045012.
- [109] R. Wilson, M. King, *et al.* Influence of spatial-intensity contrast in ultraintense laserplasma interactions. *Scientific Reports*, 12(1):1–10, 2022. ISSN 20452322. doi: 10.1038/s41598-022-05655-4.
- [110] N. P. Dover, M. Nishiuchi, *et al.* Effect of Small Focus on Electron Heating and Proton Acceleration in Ultrarelativistic Laser-Solid Interactions. *Physical Review Letters*, 124(8):84802, 2020. ISSN 10797114. doi: 10.1103/PhysRevLett.124.084802.
- [111] M. Coury, D. C. Carroll, *et al.* Influence of laser irradiated spot size on energetic electron injection and proton acceleration in foil targets. *Applied Physics Letters*, 100(7), 2012. ISSN 00036951. doi: 10.1063/1.3685615.

- [112] A. Higginson, R. J. Gray, *et al.* Near-100 MeV protons via a laser-driven transparency-enhanced hybrid acceleration scheme. *Nature Communications*, 9(1):724, 2018. ISSN 2041-1723. doi: 10.1038/s41467-018-03063-9.
- [113] O. Tresca, D. C. Carroll, *et al.* Controlling the properties of ultraintense laserproton sources using transverse refluxing of hot electrons in shaped mass-limited targets. *Plasma Physics and Controlled Fusion*, 53(10):105008, 2011. ISSN 0741-3335. doi: 10.1088/0741-3335/53/10/105008.
- [114] M. Allen, P. K. Patel, *et al.* Direct experimental evidence of back-surface ion acceleration from laser-irradiated gold foils. *Physical Review Letters*, 93(26 I):1–4, 2004. ISSN 00319007. doi: 10.1103/PhysRevLett.93.265004.
- [115] L. Boltzmann. *Weitere studien über das Wärmegleichgewicht unter Gas-molekülen.*, volume 67. 1872.
- [116] J. C. Maxwell. V. Illustrations of the dynamical theory of gases. Part I. On the motions and collisions of perfectly elastic spheres. *The London, Edinburgh, and Dublin Philosophical Magazine and Journal of Science*, 19(124):19–32, 1860. ISSN 1941-5982. doi: 10.1080/14786446008642818.
- [117] J. C. Maxwell. *Illustrations of the dynamical theory of gases. Part II. On the process of diffusion of two or more kinds of moving particles among one another.*, volume 20. London, Taylor Francis, [1840-1944], 1860.
- [118] F. Jüttner. Das Maxwellsche Gesetz der Geschwindigkeitsverteilung in der Relativtheorie. *Annalen der Physik*, 339(5):856–882, 1911.
- [119] M. Schnürer, M. P. Kalashnikov, *et al.* Hard x-ray emission from intense short pulse laser plasmas. *Physics of Plasmas*, 2(8):3106–3110, 1995. ISSN 10897674. doi: 10.1063/1.871142.
- [120] A. Rousse, P. Audebert, *et al.* Efficient K α x-ray source from femtosecond laser-produced plasmas. *Physical Review E*, 50(3):2200–2207, 1994. ISSN 1063651X. doi: 10.1103/PhysRevE.50.2200.

- [121] U. Teubner, I. Uschmann, *et al.* Absorption and hot electron production by high intensity femtosecond uv-laser pulses in solid targets. *Physical Review E - Statistical Physics, Plasmas, Fluids, and Related Interdisciplinary Topics*, 54(4):4167–4177, 1996. ISSN 1063651X. doi: 10.1103/PhysRevE.54.4167.
- [122] S. C. Wilks, W. L. Kruer, *et al.* Absorption of Ultra-Intense Laser Pulses. *Physical Review Letters*, 69(9):1383–1386, 1992.
- [123] A. Macchi, S. Veghini, *et al.* Light Sail Acceleration Reexamined. *Physical Review Letters*, 103(8):085003, 2009. ISSN 0031-9007. doi: 10.1103/PhysRevLett.103.085003.
- [124] B. Hafizi, A. Ting, *et al.* Relativistic focusing and ponderomotive channeling of intense laser beams. *Physical Review E - Statistical Physics, Plasmas, Fluids, and Related Interdisciplinary Topics*, 62(3 B):4120–4125, 2000. ISSN 1063651X. doi: 10.1103/PhysRevE.62.4120.
- [125] N. Naseri, D. Pesme, *et al.* Ponderomotive laser channelling and multi-channelling in homogeneous underdense plasma. In *51st Annual Meeting of the APS Division of Plasma Physics*, volume 54, pages 1–10, 2016.
- [126] V. Vshivkov, N. Naumova, *et al.* Nonlinear interaction of ultra-intense laser pulses with a thin foil. *Nuclear Instruments and Methods in Physics Research, Section A: Accelerators, Spectrometers, Detectors and Associated Equipment*, 410(3):493–498, 1998. ISSN 01689002. doi: 10.1016/S0168-9002(98)00183-1.
- [127] C. Li, M. L. Zhou, *et al.* Effects of laser-plasma interactions on terahertz radiation from solid targets irradiated by ultrashort intense laser pulses. *Physical Review E - Statistical, Nonlinear, and Soft Matter Physics*, 84(3):1–6, 2011. ISSN 15393755. doi: 10.1103/PhysRevE.84.036405.
- [128] G. Q. Liao, Y. T. Li, *et al.* Intense terahertz radiation from relativistic

- laserplasma interactions. *Plasma Physics and Controlled Fusion*, 59(1):014039, 2017. ISSN 0741-3335. doi: 10.1088/0741-3335/59/1/014039.
- [129] P. A. Norreys, M. Zepf, *et al.* Efficient extreme UV harmonics generated from picosecond laser pulse interactions with solid targets. *Physical Review Letters*, 76(11):1832–1835, 1996. ISSN 10797114. doi: 10.1103/PhysRevLett.76.1832.
- [130] V. V. Kim, S. R. Konda, *et al.* Harmonics Generation in the Laser-Induced Plasmas of Metal and Semiconductor Carbide Nanoparticles. *Nanomaterials*, 12(23):1–12, 2022. ISSN 20794991. doi: 10.3390/nano12234228.
- [131] J. Larmor. LXIII. On the theory of the magnetic influence on spectra; and on the radiation from moving ions. *The London, Edinburgh, and Dublin Philosophical Magazine and Journal of Science*, 44(271):503–512, 1897. ISSN 1941-5982. doi: 10.1080/14786449708621095.
- [132] J. M. Matthews. *High Energy Astrophysics*. 1994. ISBN 9780521756181. doi: 10.1142/2280.
- [133] M. Berger, J. Hubbell, *et al.* XCOM: Photon Cross Sections Database, 1998. URL <https://dx.doi.org/10.18434/T48G6X>.
- [134] S. Singh, C. D. Armstrong, *et al.* Bremsstrahlung emission and plasma characterization driven by moderately relativistic laserplasma interactions. *Plasma Physics and Controlled Fusion*, 63(3):035004, 2021. ISSN 0741-3335. doi: 10.1088/1361-6587/abcf7e.
- [135] T. Boyd and J. Sanderson. *The Physics of Plasmas*, volume XXXIII. Cambridge University Press, 2012. ISBN 9780874216561. doi: 10.1007/s13398-014-0173-7.2.
- [136] M. Berger, J. Coursey, *et al.* Stopping-Power Range Tables for Electrons, Protons, and Helium Ions, 1998. URL <https://physics.nist.gov/PhysRefData/Star/Text/ESTAR.html>.

- [137] L. D. Landau and E. M. Lifshitz. *The classical theory of fields*, volume 2. Pergamon Press Ltd., 3rd edition, 1971. doi: 10.1016/0029-5582(59)90093-8.
- [138] A. M. Fedotov, N. B. Narozhny, *et al.* Limitations on the attainable intensity of high power lasers. *Physical Review Letters*, 105(8):1–4, 2010. ISSN 00319007. doi: 10.1103/PhysRevLett.105.080402.
- [139] C. S. Brady, C. P. Ridgers, *et al.* Laser absorption in relativistically underdense plasmas by synchrotron radiation. *Physical Review Letters*, 109(24):1–5, 2012. ISSN 00319007. doi: 10.1103/PhysRevLett.109.245006.
- [140] C. S. Brady, C. P. Ridgers, *et al.* Gamma-ray emission in near critical density plasmas. *Plasma Physics and Controlled Fusion*, 55(12):124016, 2013. ISSN 0741-3335. doi: 10.1088/0741-3335/55/12/124016.
- [141] P. Hadjisolomou, T. Jeong, *et al.* Gamma-ray flash in the interaction of a tightly focused single-cycle ultra-intense laser pulse with a solid target. *Journal of Plasma Physics*, 88(1):905880104, 2022. ISSN 0022-3778. doi: 10.1017/S0022377821001318.
- [142] A. P. Robinson, P. Gibbon, *et al.* Relativistically correct hole-boring and ion acceleration by circularly polarized laser pulses. *Plasma Physics and Controlled Fusion*, 51(2):024004, 2009. ISSN 07413335. doi: 10.1088/0741-3335/51/2/024004.
- [143] H. Hall, J. Als-Nielsen, *et al.* Elements of Modern X-ray Physics, Second Edition - Als-Nielsen - Wiley Online Library. *Review of Modern Physics*, 8(3):358–397, 1936. ISSN 14653915.
- [144] J. W. Motz, H. A. Olsen, *et al.* Pair production by photons. *Reviews of Modern Physics*, 41(4):581–639, 1969. ISSN 00346861. doi: 10.1103/RevModPhys.41.581.
- [145] C. P. Ridgers, J. G. Kirk, *et al.* Modelling gamma-ray photon emission and pair production in high-intensity laser-matter interactions. *Journal of*

- Computational Physics*, 260:273–285, 2014. ISSN 10902716. doi: 10.1016/j.jcp.2013.12.007.
- [146] S. Morris, A. Robinson, *et al.* Highly efficient conversion of laser energy to hard x-rays in high-intensity lasersolid simulations. *Physics of Plasmas*, 28(10):103304, 2021. doi: 10.1063/5.0055398.
- [147] D. D. Sorbo, D. Seipt, *et al.* Electron spin polarization in realistic trajectories around the magnetic node of two counter-propagating, circularly polarized, ultra-intense lasers. *Plasma Physics and Controlled Fusion*, 60(6):064003, 2018. doi: 10.1088/1361-6587/aab979.
- [148] F. Wan, Y. Wang, *et al.* High-energy γ -photon polarization in nonlinear breitt-wheeler pair production and polarimetry. *Physical Review Research*, 2(3):032049, 2020. doi: 10.1103/PhysRevResearch.2.032049.
- [149] M. Mack. Mode locking the ruby laser. *IEEE Journal of Quantum Electronics*, 4(12):1015–1016, 1968. ISSN 0018-9197. doi: 10.1109/JQE.1968.1075017.
- [150] F. Salin, M. Piché, *et al.* Mode locking of Ti:Al₂O₃ lasers and self-focusing: a Gaussian approximation. *Optics Letters*, 16(21):1674, 1991. ISSN 0146-9592. doi: 10.1364/OL.16.001674.
- [151] T. Brabec, C. Spielmann, *et al.* Kerr lens mode locking. *Optics Letters*, 17(18):1292, 1992. ISSN 0146-9592. doi: 10.1364/OL.17.001292.
- [152] F. J. McClung and R. W. Hellwarth. Giant Optical Pulsations from Ruby. *Journal of Applied Physics*, 33(3):828–829, 1962. ISSN 0021-8979. doi: 10.1063/1.1777174.
- [153] R. Paschotta. Q Switching - an encyclopedia article. In *RP Photonics Encyclopedia*. RP Photonics AG, 2006. doi: 10.61835/fdh. URL https://www.rp-photonics.com/q_switching.html.

- [154] R. Paschotta. Saturable Absorbers - an encyclopedia article. In *RP Photonics Encyclopedia*. RP Photonics AG, 2008. doi: 10.61835/43c. URL https://www.rp-photonics.com/saturable_absorbers.html.
- [155] N. M. Kroll. Parametric Amplification in Spatially Extended Media and Application to the Design of Tuneable Oscillators at Optical Frequencies. *Physical Review*, 127(4):1207–1211, 1962. ISSN 0031-899X. doi: 10.1103/PhysRev.127.1207.
- [156] A. E. Siegman. *Lasers*. University Science Books, 1986.
- [157] v. F. Zernike. Beugungstheorie des schneidenverfahrens und seiner verbesserten form, der phasenkontrastmethode. *Physica*, 1(7-12):689–704, 1934. ISSN 00318914. doi: 10.1016/S0031-8914(34)80259-5.
- [158] J. C. Wyant and K. Creath. *Basic Wavefront Aberration Theory for Optical Metrology (Zernike Auszug)*, volume XI. 1992. ISBN 9781466598324.
- [159] I. O. Musgrave, M. Galimberti, *et al.* Study of the Prompt Aberrations of the Vulcan TAP Beamline. Technical report, Central Laser Facility, 2018.
- [160] H.-M. Heuck, U. Wittrock, *et al.* Adaptive optics at the PHELIX laser. In G. Cheriaux, C. Hooker, *et al.*, editors, *Adaptive Optics for Laser Systems and Other Applications*, volume 6584, page 658402. SPIE, 2007. ISBN 081946712X. doi: 10.1117/12.723380.
- [161] J. Hartmann. Objektivuntersuchungen. *Zeitschrift für Instrumentenkunde*, 24(138816):1–25,33–47,97–117, 1904.
- [162] R. V. Shack. Production and use of a lenticular Hartmann screen. In F. Smith, editor, *1973 Spring Meeting of the Optical Society of America*, volume 61, page 471, Tuscon, 1973. doi: 10.1364/josa.63.000471.
- [163] H. Chen, X. Wang, *et al.* Research on the pre-pulses caused by post-pulses in the optical parametric chirped-pulse amplifier. *Optics Express*, 31(24):40285, 2023. ISSN 10944087. doi: 10.1364/oe.506896.

- [164] F. Wagner, C. P. João, *et al.* Temporal contrast control at the PHELIX petawatt laser facility by means of tunable sub-picosecond optical parametric amplification. *Applied Physics B: Lasers and Optics*, 116(2):429–435, 2014. ISSN 09462171. doi: 10.1007/s00340-013-5714-9.
- [165] C. Thaury, F. Quere, *et al.* Plasma mirrors for ultrahigh-intensity optics. *Nature Physics*, 3(June):424–429, 2007. doi: 10.1038/Nphys595.
- [166] R. Wilson, M. King, *et al.* Ellipsoidal plasma mirror focusing of high power laser pulses to ultra-high intensities. *Physics of Plasmas*, 23(3):033106, 2016. ISSN 1070-664X. doi: 10.1063/1.4943200.
- [167] P. Monot, G. Doumy, *et al.* High order harmonic generation by non-linear reflection of a pedestal-free intense laser pulse on a plasma. *Applied Physics B: Lasers and Optics*, 78(7-8):901–904, 2004. ISSN 09462171. doi: 10.1007/s00340-004-1483-9.
- [168] G. G. Scott, V. Bagnoud, *et al.* Optimization of plasma mirror reflectivity and optical quality using double laser pulses. *New Journal of Physics*, 17(3):033027, 2015. ISSN 1367-2630. doi: 10.1088/1367-2630/17/3/033027.
- [169] H. C. Kapteyn, A. Szoke, *et al.* Prepulse energy suppression for high-energy ultrashort pulses using self-induced plasma shuttering. *Optics Letters*, 16(7):490, 1991. ISSN 0146-9592. doi: 10.1364/ol.16.000490.
- [170] A. Kon, M. Nakatsutsumi, *et al.* Geometrical optimization of an ellipsoidal plasma mirror toward tight focusing of ultra-intense laser pulse. *Journal of Physics: Conference Series*, 244(3):032008, 2010. ISSN 1742-6596. doi: 10.1088/1742-6596/244/3/032008.
- [171] M. Nakatsutsumi, A. Kon, *et al.* Fast focusing of short-pulse lasers by innovative plasma optics toward extreme intensity. *Optics Letters*, 35(13):2314, 2010. ISSN 0146-9592. doi: 10.1364/ol.35.002314.
- [172] R. Wilson, M. King, *et al.* Development of Focusing Plasma Mirrors for

- Ultraintense Laser-Driven Particle and Radiation Sources. *Quantum Beam Science*, 2(1):1–14, 2018. ISSN 2412-382X. doi: 10.3390/qubs2010001.
- [173] I. O. Musgrave, D. Canny, *et al.* Characterization of a new fibre laser oscillator for the Vulcan laser. Technical report, Central Laser Facility, 2007.
- [174] I. Musgrave, M. Galimberti, *et al.* Review of laser diagnostics at the Vulcan laser facility. *High Power Laser Science and Engineering*, 3(e26):1–10, 2015. ISSN 2095-4719. doi: 10.1017/hpl.2015.27.
- [175] C. N. Danson, M. White, *et al.* A history of high-power laser research and development in the United Kingdom. *High Power Laser Science and Engineering*, 9, 2021. ISSN 20523289. doi: 10.1017/hpl.2021.5.
- [176] R. Clarke. Target Area Petawatt, 2015. URL [https://www.clf.stfc.ac.uk/Pages/Target-Area-Petawatt-\(TAP\).aspx](https://www.clf.stfc.ac.uk/Pages/Target-Area-Petawatt-(TAP).aspx).
- [177] C. N. Danson, P. A. Brummitt, *et al.* Vulcan Petawatt - an ultra-high-intensity interaction facility. *Nuclear Fusion*, 44(12):S239–S246, 2004. ISSN 0029-5515. doi: 10.1088/0029-5515/44/12/S15.
- [178] G. Cheriaux, B. Walker, *et al.* Aberration-free stretcher design for ultrashort-pulse amplification. *Optics Letters*, 21(6):414, 1996. ISSN 0146-9592. doi: 10.1364/ol.21.000414.
- [179] T. P. Frazer. *Investigation of laser-solid interaction physics with tightly focused, ultra-intense laser pulses by*. PhD thesis, University of Strathclyde, 2021.
- [180] L. Döhl. *High-contrast, ultra-intense laser-solid interaction physics with engineered targets*. PhD thesis, University of York, 2019.
- [181] L. E. Bradley, A. C. Aiken, *et al.* Comparing temporal contrast measurements taken in the Vulcan front-end and target area petawatt. Technical report, Central Laser Facility, 2019.

- [182] T. P. Frazer, R. Wilson, *et al.* Enhanced laser intensity and ion acceleration due to self-focusing in relativistically transparent ultrathin targets. *Physical Review Research*, 2(4):42015, 2020. ISSN 26431564. doi: 10.1103/PhysRevResearch.2.042015.
- [183] V. Bagnoud, B. Aurand, *et al.* Commissioning and early experiments of the PHELIX facility. *Applied Physics B: Lasers and Optics*, 100(1):137–150, 2010. ISSN 09462171. doi: 10.1007/s00340-009-3855-7.
- [184] V. Bagnoud and F. Wagner. Ultrahigh temporal contrast performance of the PHELIX petawatt facility. *High Power Laser Science and Engineering*, 4:1–8, 2016. ISSN 20523289. doi: 10.1017/hpl.2016.38.
- [185] S. Gotte. PHELIX Laser Facility, 2015.
- [186] V. A. Schanz, F. Wagner, *et al.* Noise reduction in third order cross-correlation by angle optimization of the interacting beams. *Optics Express*, 25(8):9252, 2017. ISSN 10944087. doi: 10.1364/oe.25.009252.
- [187] K. A. Tanaka, T. Yabuuchi, *et al.* Calibration of imaging plate for high energy electron spectrometer. *Review of Scientific Instruments*, 76(1):013507, 2005. ISSN 0034-6748. doi: 10.1063/1.1824371.
- [188] N. Rabhi, K. Bohacek, *et al.* Calibration of imaging plates to electrons between 40 and 180 MeV. *Review of Scientific Instruments*, 87(5):103 – 103, 2016. ISSN 0034-6748. doi: 10.1063/1.4950860.
- [189] T. Bonnet, M. Comet, *et al.* Response functions of imaging plates to photons, electrons and 4He particles. *Review of Scientific Instruments*, 84(10):103510, 2013. ISSN 0034-6748. doi: 10.1063/1.4826084.
- [190] S. G. Gales and C. D. Bentley. Image plates as x-ray detectors in plasma physics experiments. *Review of Scientific Instruments*, 75(10 II):4001–4003, 2004. ISSN 00346748. doi: 10.1063/1.1789256.

- [191] W. R. Leo. *Techniques for Nuclear and Particle Physics Experiments*. Springer Berlin Heidelberg, Berlin, Heidelberg, 1994. ISBN 978-3-540-57280-0. doi: 10.1007/978-3-642-57920-2.
- [192] F. Wanlass and C. Sah. Nanowatt logic using field-effect metal-oxide semiconductor triodes. In *1963 IEEE International Solid-State Circuits Conference. Digest of Technical Papers*, pages 32–33. IEEE, 1963. doi: 10.1109/ISSCC.1963.1157450.
- [193] W. S. Boyle and G. E. Smith. Charge Coupled Semiconductor Devices. *Bell System Technical Journal*, 49(4):587–593, 1970. ISSN 00058580. doi: 10.1002/j.1538-7305.1970.tb01790.x.
- [194] Allied Vision. Manta G-235, 2024. URL <https://www.alliedvision.com/en/camera-selector/detail/manta/g-235/>.
- [195] Stanford Advanced Materials. LYSO (Ce) Scintillation Crystal, 2024. URL <https://www.samaterials.com/scintillation-crystals/2640-lyso-ce-scintillation-crystal.html>.
- [196] D. R. Rusby, C. D. Armstrong, *et al.* Novel scintillator-based x-ray spectrometer for use on high repetition laser plasma interaction experiments. *Review of Scientific Instruments*, 89(7):073502, 2018. ISSN 0034-6748. doi: 10.1063/1.5019213.
- [197] C. D. Armstrong, D. Neely, *et al.* Deconvolution of multi-Boltzmann x-ray distribution from linear absorption spectrometer via analytical parameter reduction. *Review of Scientific Instruments*, 92(11):113102, 2021. ISSN 0034-6748. doi: 10.1063/5.0057486.
- [198] C. D. Chen. *Spectrum and Conversion Efficiency Measurements of Suprathermal Electrons from*. PhD thesis, Massachusetts Institute of Technology, 2009.
- [199] R. J. Gray, X. H. Yuan, *et al.* Surface transport of energetic electrons in

- intense picosecond laser-foil interactions. *Applied Physics Letters*, 99(17): 171502, 2011. ISSN 0003-6951. doi: 10.1063/1.3655909.
- [200] M. Coury, D. C. Carroll, *et al.* Injection and transport properties of fast electrons in ultraintense laser-solid interactions. *Physics of Plasmas*, 20(4): 043104, 2013. ISSN 1070-664X. doi: 10.1063/1.4799726.
- [201] J. C. Kieffer, Z. Jiang, *et al.* Picosecond dynamics of a hot solid-density plasma. *Journal of the Optical Society of America B*, 13(1):132, 1996. ISSN 0740-3224. doi: 10.1364/josab.13.000132.
- [202] E. Nardi, Z. Zinamon, *et al.* $K\alpha$ emission and secondary electrons in femtosecond laser target interactions. *Laser and Particle Beams*, 33(4):685–693, 2015. ISSN 1469803X. doi: 10.1017/S0263034615000798.
- [203] M. H. Kalos and P. A. Whitlock. *Monte Carlo Methods. Second Edition.*, volume 1. Wiley-VCH, Weinheim, 2nd edition, 2015. ISBN 978-3-527-40760-6.
- [204] S. Agostinelli, J. Allison, *et al.* Geant4a simulation toolkit. *Nuclear Instruments and Methods in Physics Research Section A: Accelerators, Spectrometers, Detectors and Associated Equipment*, 506(3):250–303, 2003. ISSN 01689002. doi: 10.1016/S0168-9002(03)01368-8.
- [205] A. Vlasov. The vibrational properties of an electron gas. *Uspekhi Fizicheskikh Nauk*, 93(11):444–470, 1967. ISSN 0042-1294. doi: 10.3367/ufnr.0093.1967.11f.0444.
- [206] T. D. Arber, K. Bennett, *et al.* Contemporary particle-in-cell approach to laser-plasma modelling. *Plasma Physics and Controlled Fusion*, 57(11): 113001, 2015. ISSN 0741-3335. doi: 10.1088/0741-3335/57/11/113001.
- [207] F. Fiuza, M. Marti, *et al.* Efficient modeling of laserplasma interactions in high energy density scenarios. *Plasma Physics and Controlled Fusion*, 53(7):074004, 2011. doi: 10.1088/0741-3335/53/7/074004.

- [208] K. Yee. Numerical solution of initial boundary value problems involving maxwell's equations in isotropic media. *IEEE Transactions on Antennas and Propagation*, 14(3):302–307, 1966. ISSN 0018-926X. doi: 10.1109/TA P.1966.1138693.
- [209] D. Wu, X. T. He, *et al.* Particle-in-cell simulations of laserplasma interactions at solid densities and relativistic intensities: the role of atomic processes. *High Power Laser Science and Engineering*, 6(e50):1–15, 2018. ISSN 2095-4719. doi: 10.1017/hpl.2018.41.
- [210] J. Vyskočil, O. Klimo, *et al.* Simulations of bremsstrahlung emission in ultra-intense laser interactions with foil targets. *Plasma Physics and Controlled Fusion*, 60(5):054013, 2018. ISSN 0741-3335. doi: 10.1088/1361-6587/aab4c3.
- [211] M. Abramowitz and I. Stegan. *Handbook of Mathematical Functions with Formulas, Graphs, and Mathematical Tables*. Dover Publications, Washington, D.C., 10th edition, 1972. ISBN 0486612724.
- [212] F. Salvat, M. Fern, *et al.* PENELOPE-2008 : A Code System for Monte Carlo Simulation. In *Workshop Proceedings NUCLEAR ENERGY AGENCY ORGANISATION FOR ECONOMIC CO-OPERATION AND DEVELOPMENT*, number 6416, 2009. ISBN 9789264990661.
- [213] J. G. Kirk, A. R. Bell, *et al.* Pair production in counter-propagating laser beams. *Plasma Physics and Controlled Fusion*, 51(8):085008, 2009. ISSN 0741-3335. doi: 10.1088/0741-3335/51/8/085008.
- [214] J. M. Cole, J. C. Wood, *et al.* Laser Driven X-ray Imaging of Human Trabecular Bone. Technical report, Central Laser Facility, 2014.
- [215] J. M. Cole, D. R. Symes, *et al.* High-resolution μ CT of a mouse embryo using a compact laser-driven X-ray betatron source. *Proceedings of the National Academy of Sciences of the United States of America*, 115(25):6335–6340, 2018. ISSN 10916490. doi: 10.1073/pnas.1802314115.

- [216] C. Courtois, R. Edwards, *et al.* Characterisation of a MeV Bremsstrahlung x-ray source produced from a high intensity laser for high areal density object radiography. *Physics of Plasmas*, 20(8), 2013. ISSN 1070-664X. doi: 10.1063/1.4818505.
- [217] C. D. Armstrong, C. M. Brenner, *et al.* Bremsstrahlung emission from high power laser interactions with constrained targets for industrial radiography. *High Power Laser Science and Engineering*, 7(24):21–27, 2019. ISSN 20523289. doi: 10.1017/hpl.2019.8.
- [218] ELI-NP. First 10 PW laser pulse was shot through the entire ELI-NP laser system, 2020. URL <https://www.eli-np.ro/article.php?id=22>.
- [219] E. Eggl, S. Schleede, *et al.* X-ray phase-contrast tomography with a compact laser-driven synchrotron source. *Proceedings of the National Academy of Sciences of the United States of America*, 112(18):5567–5572, 2015. ISSN 10916490. doi: 10.1073/pnas.1500938112.
- [220] R. R. Pandit and Y. Sentoku. Higher order terms of radiative damping in extreme intense laser-matter interaction. *Physics of Plasmas*, 19(7), 2012. ISSN 1070664X. doi: 10.1063/1.4739442.
- [221] A. Zigler, H. Zmora, *et al.* Spatial resolution of X-ray line emission in laser produced plasma by shadow techniques. *Physics Letters A*, 60(4):319–322, 1977. ISSN 03759601. doi: 10.1016/0375-9601(77)90112-8.
- [222] G. Gillman and I. Macleod. Reconstruction of X-ray sources from penumbral images. *Computer Graphics and Image Processing*, 11(3):227–241, 1979. ISSN 0146664X. doi: 10.1016/0146-664X(79)90090-X.
- [223] P. Mora. Plasma Expansion into a Vacuum. *Physical Review Letters*, 90(18):4, 2003. ISSN 10797114. doi: 10.1103/PhysRevLett.90.185002.
- [224] J. S. Green, D. C. Carroll, *et al.* Enhanced proton flux in the MeV range by defocused laser irradiation. *New Journal of Physics*, 12(8):085012, 2010. ISSN 1367-2630. doi: 10.1088/1367-2630/12/8/085012.

- [225] L. M. Chen, P. Forget, *et al.* Study of hard x-ray emission from intense femtosecond Ti:sapphire laser-solid target interactions. *Physics of Plasmas*, 11(9):4439–4445, 2004. ISSN 1070664X. doi: 10.1063/1.1781625.
- [226] L. Robson, P. T. Simpson, *et al.* Scaling of proton acceleration driven by petawatt-laser-plasma interactions. *Nature Physics*, 3(1):58–62, 2007. ISSN 17452481. doi: 10.1038/nphys476.
- [227] Y. Ping, R. Shepherd, *et al.* Absorption of short laser pulses on solid targets in the ultrarelativistic regime. *Physical Review Letters*, 100(8):6–9, 2008. ISSN 10797114. doi: 10.1103/PhysRevLett.100.085004.
- [228] J. R. Davies. Laser absorption by overdense plasmas in the relativistic regime. *Plasma Physics and Controlled Fusion*, 51(1):014006, 2009. ISSN 0741-3335. doi: 10.1088/0741-3335/51/1/014006.
- [229] M. I. K. Santala, M. Zepf, *et al.* Effect of the Plasma Density Scale Length on the Direction of Fast Electrons in Relativistic Laser-Solid Interactions. *Physical review letters*, 84(7):1459–1462, 2000.
- [230] C. Courtois, A. Compant La Fontaine, *et al.* Effect of plasma density scale length on the properties of bremsstrahlung x-ray sources created by picosecond laser pulses. *Physics of Plasmas*, 16(1):16–28, 2009. ISSN 1070664X. doi: 10.1063/1.3067825.
- [231] R. J. Gray, D. C. Carroll, *et al.* Laser pulse propagation and enhanced energy coupling to fast electrons in dense plasma gradients. *New Journal of Physics*, 16, 2014. ISSN 13672630. doi: 10.1088/1367-2630/16/11/113075.
- [232] P. McKenna, D. Carroll, *et al.* Effects of front surface plasma expansion on proton acceleration in ultraintense laser irradiation of foil targets. *Laser and Particle Beams*, 26(4):591596, 2008. doi: 10.1017/S0263034608000657.
- [233] D. A. MacLellan, D. C. Carroll, *et al.* Annular fast electron transport in silicon arising from low-temperature resistivity. *Phys. Rev. Lett.*, 111:095001, 2013. doi: 10.1103/PhysRevLett.111.095001.

- [234] A. Compant La Fontaine, C. Courtois, *et al.* Production of multi-MeV Bremsstrahlung x-ray sources by petawatt laser pulses on various targets. *Physics of Plasmas*, 19(2):023104, 2012. ISSN 1070-664X. doi: 10.1063/1.3680611.
- [235] C. Courtois, R. Edwards, *et al.* Characterisation of a MeV Bremsstrahlung x-ray source produced from a high intensity laser for high areal density object radiography. *Physics of Plasmas*, 20(8):083114, 2013. ISSN 1070-664X. doi: 10.1063/1.4818505.
- [236] A. L. Meadowcroft and R. D. Edwards. High-Energy Bremsstrahlung Diagnostics to Characterize Hot-Electron Production in Short-Pulse Laser-Plasma Experiments. *IEEE Transactions on Plasma Science*, 40(8):1992–2001, 2012. ISSN 0093-3813. doi: 10.1109/TPS.2012.2201175.
- [237] I. Spencer, K. W. Ledingham, *et al.* A nearly real-time high temperature laser-plasma diagnostic using photonuclear reactions in tantalum. *Review of Scientific Instruments*, 73(11):3801, 2002. ISSN 00346748. doi: 10.1063/1.1511802.
- [238] K. T. Behm, J. M. Cole, *et al.* A spectrometer for ultrashort gamma-ray pulses with photon energies greater than 10 MeV. *Review of Scientific Instruments*, 89(11), 2018. ISSN 0034-6748. doi: 10.1063/1.5056248.
- [239] C. D. Chen, A. J. Kemp, *et al.* Comparisons of angularly and spectrally resolved Bremsstrahlung measurements to two-dimensional multi-stage simulations of short-pulse laser-plasma interactions. *Physics of Plasmas*, 20(5):052703, 2013. ISSN 1070-664X. doi: 10.1063/1.4804348.
- [240] V. Istokskaja, V. Stránský, *et al.* Experimental tests and signal unfolding of a scintillator calorimeter for laser-plasma characterization. *Journal of Instrumentation*, 16(02):T02006–T02006, 2021. ISSN 1748-0221. doi: 10.1088/1748-0221/16/02/T02006.

- [241] Y. Inubushi, H. Nishimura, *et al.* X-ray spectroscopic measurements of energy transport in ultra-intense laser produced plasma. *J. Plasma Fusion Res. SERIES*, 6:337–340, 2004. doi: 10.1585/jpfr.6.337.
- [242] N. C. Woolsey, R. J. Clarke, *et al.* Precision x-ray spectroscopy of intense laser-plasma interactions. *High Energy Density Physics*, 7:105–109, 2011. doi: 10.1016/j.hedp.2011.03.001.
- [243] J. Myatt, W. Theobald, *et al.* High-intensity laser interactions with mass-limited solid targets and implications for fast-ignition experiments on omega epa). *Physics of Plasmas*, 14(5):056301, 2007. ISSN 1070-664X. doi: 10.1063/1.2472371.
- [244] D. R. Rusby, C. D. Armstrong, *et al.* Effect of rear surface fields on hot, refluxing and escaping electron populations via numerical simulations. *High Power Laser Science and Engineering*, 7(e45):1–11, 2019. ISSN 2095-4719. doi: 10.1017/hpl.2019.34.
- [245] F. Fiorini, D. Neely, *et al.* Characterization of laser-driven electron and photon beams using the Monte Carlo code FLUKA. *Laser and Particle Beams*, 32(02):233–241, 2014. ISSN 0263-0346. doi: 10.1017/S0263034614000044.